Functional Surfaces for Radiodecontamination

Mohamad Maaz

université PARIS-SACLAY

Conseil National de la Recherche Scientifique

UNIVERSITÉ PARIS SUD
Comprendre le monde, construire l'avenir

NNT : 2018SACLS159

Surfaces fonctionnalisées pour la radiodécontamination

Thèse de doctorat de l'Université Paris-Saclay
préparée à l'Université Paris-Sud

École doctorale n°571 Sciences chimiques : molécules, matériaux, instrumentation et biosystèmes (2MIB)
Spécialité : Chimie

Thèse présentée et soutenue à huis clos, à Orsay, le 12/07/2018, par

Mohamad MAAZ

Composition du Jury :

Juan RODRIGUEZ HERNANDEZ Chargé de recherche, Conseil Supérieur de la Recherche Scientifique - Espagne (ICTP- CSIC)	Rapporteur
Jean-Luc SIX Professeur, Université de Lorraine (UMR 7375)	Rapporteur
Maurice BROGLY Professeur, Université de Haute-Alsace (EA 4567)	Président
Eric SIMONI Professeur, Université Paris-Sud (UMR 8608)	Examinateur
Nadine AUBRY-BARROCA Maitre de conférences, Université Paris-Sud (UMR 8182)	Examinateur
Tamara ElZEIN Chercheur associé, Conseil National de la Recherche Scientifique - Liban (CLEA – CNRSL)	Examinateur
Philippe ROGER Professeur, Université Paris-Sud (UMR 8182)	Directeur de thèse
Bilal NSOULI Directeur de recherche, Conseil National de la Recherche Scientifique - Liban (CLEA – CNRSL)	Co-Directeur de thèse

Thèse de doctorat

Acknowledgements

Firstly, I would like to express my sincere gratitude to my advisor Prof. Philippe Roger for the continuous support of my Ph.D study and related research, for his patience, motivation, and immense knowledge. His guidance helped me in all the time of research and writing of this thesis. I could not have imagined having a better advisor and mentor for my Ph.D study. Sincere gratitude also to my co-advisor Dr. Bilal Nsouli for granting me his trust.

I would like to thank my thesis committee: Prof. Maurice Brogly, Prof. Jean-luc Six, Dr. Juan Rodriguez Hernandez and Prof. Eric Simoni, for their insightful comments and encouragement, also for the hard question which incented me to widen my research from various perspectives.

My sincere thanks also goes to Dr. Nadine Aubry-Barroca and Dr. Tamara Elzein, who provided me with continuous support. Without them it would not be possible to conduct this research. Thank you Dr. Benedicte Lepoittevin for setting up this collaboration project.

I thank the SM2B team, Dr. Caroline Aymes-Chodur, Dr. Hanène Salmi, Mr. Ludovic Costa, my fellow labmates, Thu, Nacim and all postdocs and interns for the stimulating discussions and for all the fun we had in the last three years.

A special thanks to all experts and engineers at ICMMO, LAEC, IPN and GEOPS for helping me in obtaining and interpreting experimental data.

I would like to thank the Lebanese CNRS, the SM_2B lab, the IAEA and the CEDRE program for funding this project.

Last but not the least, I would like to thank my father and all my family for supporting me spiritually throughout this thesis and my life in general. Perrine, thank you for being by my side through all ups and downs.

Thank you all

Mohamad Maaz

Orsay, July 2018

Table of Contents

Acronyms

4VP	4-vinyl pyridine
An	Actinide
AcN	Acetonitrile
AFM	Atomic force microscopy
APTES	3-aminopropyltriethoxysilane
ATR-FTIR	Attenuated total reflection Fourier transform infrared spectroscopy
ATRP	Atom Transfer Radical Polymerization
BnCl	Benzyl chloride
CPVC	Chlorinated polyvinyl chloride, also known as polyvinylidene chloride (PVDC)
CRP	Controlled radical polymerization
Đ	Polymer dispersity
DP	Degree of polymerization
DCM	Dichloromethane
DCTB	*trans*-2-[3-(4-tert-Butylphenyl)-2-methyl-2-propenylidene]malononitrile
DIAMEX	Diamide extraction
DLS	Dynamic light scattering
DMF	*N*,*N*-dimethyl-formamide
DMSO	Dimethyl sulfoxide
FP	Fission products
FWHM	Full width at half maximum
GANEX	Grouped actinide extraction
Ln	Lanthanide
MALDI-ToF	Matrix-assisted laser desorption/ionization time-of-flight
NMP	Nitroxide mediated polymerization
NMR	Nuclear magnetic resonance spectroscopy
NSF	Nuclear spent fuel
PALEX	Polymer assisted actinide lanthanide extraction
PEG	Polyethylene glycol
PEI	Polyethylenimine
PET	Polyethylene terephthalate
PMMA	Poly(methyl methacrylate)
PP	Polypropylene

PUREX	Plutonium Uranium Redox Extraction
PVC	Poly(vinyl chloride)
RAFT	Reversible addition fragmentation chain transfer
RDRP	Reversible-deactivation radical polymerization
RIGP	Radiation-induced graft polymerization
RMS	Root mean square
SANEX	Selective actinide extraction
SARA ATRP	Supplemental Activation Reducing Agent Atom Transfer Radical Polymerization
SEC	Size exclusion chromatography
SEM	Scanning electron microscopy
SI-CRP	Surface-initiated controlled radical polymerization
TBP	Tributyl phosphate
THF	Tetrahydrofuran
ToF-SIMS	Time of flight secondary ion mass spectroscopy
TPMA	Tris(2-pyridylmethyl)amine
TPMA	Tris(2-pyridylmethyl)amine
VDPA	4-vinyl dipicolinic acid
VDPM	4-vinyl dimethyl dipicolinate
WCA	Water contact angle
XPS	X-ray photoelectron spectroscopy

I. General introduction

I.1. Thesis objectives

I.1.1. Introduction

Following the industrial revolution, the rise in atmospheric CO_2 concentration combined with the increased frequency of severe weather events led to increasing concerns that global climate change was being fueled by fossil fuel consumption. Climatologists have agreed that continuous injection of fossil carbon into the atmosphere will have lethal effects even in the near future, and the development of alternative fuels that avoid the introduction of additional greenhouse gases into the atmosphere became more vital than ever.

Renewable resources, primarily wind and solar, along with nuclear power became favored topics for consideration and we witnessed a significant increase in wind and solar contributions to the overall energy production balance. The average greenhouse gases (GHG) emissions in tonnes of CO_2-equivalent per GWh (Gigawatt-hours) from different power sources were reviewed in a WNA (World Nuclear Association) report [1] and are compared in figure 1.

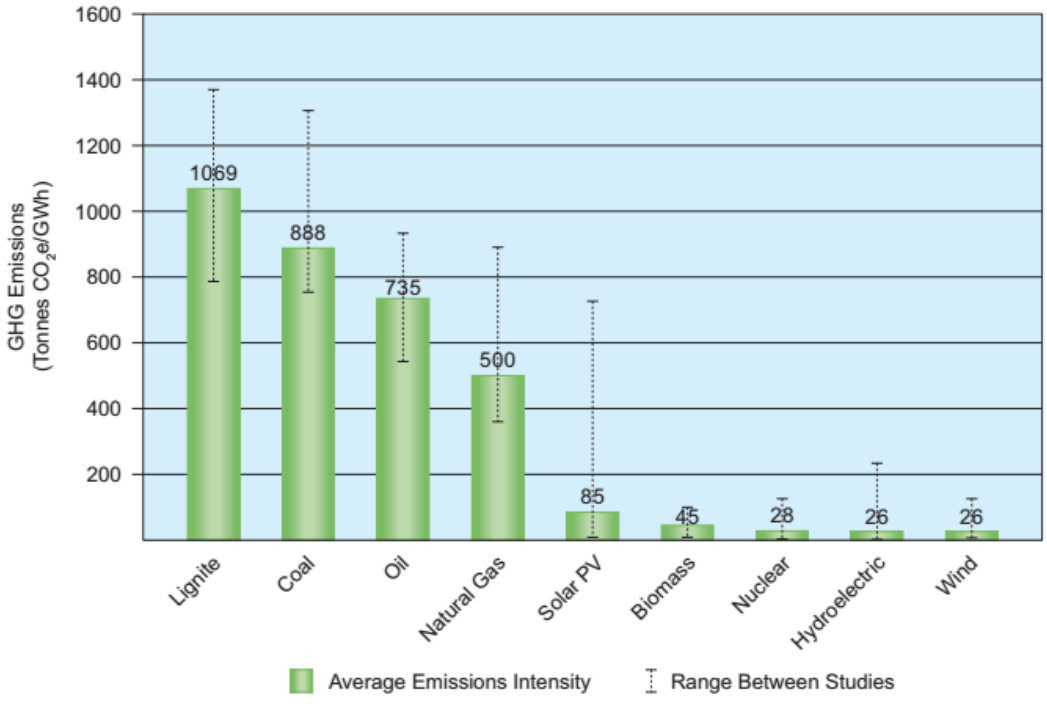

Figure I-1. GHG emissions from different power sources

However, the accelerating growth of population and industrial activities has resulted in a large increase in consumption of energy and effectively little displacement of fossil carbon combustion.

A growing global population means that energy demand will continue to grow, and it is impossible to overlook the fact that the wind does not always blow, nor does solar radiation always reach solar receptors, not to mention the overwhelming investment needed for the decentralization of power generation. Until now, nuclear plants that takes advantage of the energy released from uranium fission reaction, remain the only energy source that allows the reduction of carbon emissions while responding to our energy demands.

Uranium is one of earth's heaviest elements, with a density of 19.1 g/cm^3. Its two main isotopes are U-238 (99.283%) and U-235 (0.711%). The rare U-234 isotope is formed by the α-decay of U-238 and counts for only 0.005% of the total mass of uranium. U-235 is the only natural isotope which releases energy through fission chain reaction under neutrons bombardment, and finds important applications in the energy production industry, either for peaceful purposes like electrical energy production, or military purposes like nuclear weapons and nuclear-powered submarines.

Different forms of enriched, depleted or reprocessed uranium exist depending on the proportions of the three isotopes mentioned above. For example, enriched uranium comprises 3–5% U-235 for civilian applications, and more than 90% for military applications. Highly enriched U might induce radiological toxicity. Natural or depleted uranium is not considered to be a radiological hazard but can induce a non-negligible chemical toxicity.

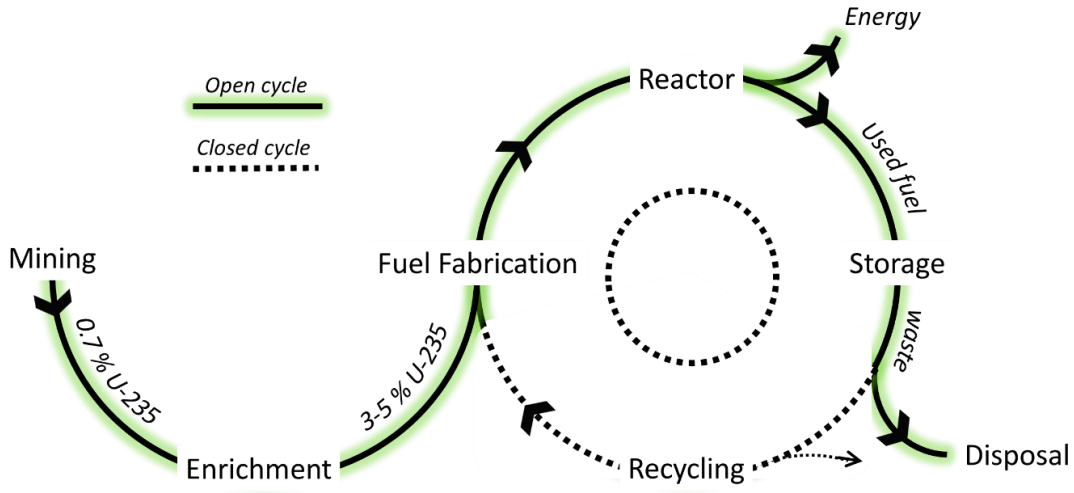

Scheme I-1. Simplified nuclear fuel cycle

The "nuclear fuel cycle" is the industrial process that includes various activities involved in the production of electricity from uranium in a nuclear power reactor. The nuclear fuel cycle starts

with the mining of uranium (front end) and ends with the management of nuclear waste (back end), either by disposal (open fuel cycle) or by recycling and reusing in a new energy production process (closed fuel cycle). The nuclear fuel cycle is briefly described in scheme 1.

The present project was initiated in 2015 by a collaboration between the Lebanese Atomic Energy Commission (LAEC) of the National Council for Scientific Research of Lebanon (CNRS-L), and the "Synthèse de Molécules et de Macromolécules Bioactives" (SM_2B) laboratory at the "Institut de Chimie Moléculaire et des Matériaux d'Orsay" (ICMMO) of Paris-Sud/Paris-Saclay university in France. This collaboration joins the knowledge of both parties, the LAEC expertise in the field of nuclear safety and nuclear analytical techniques, and the SM_2B know-how in the field of polymer science and surface modification. The aim of the present thesis, entitled "Functionalized surfaces for radio-decontamination", is to come up with innovative polymer materials with the ability to bind to radionuclides like uranium under a specific set of conditions, for a variety of applications with a focus on the nuclear industry and radiodecontamination.

In the nuclear industry, the new polymer materials will be proven promising in three fields of research. First of all, at the front end of the nuclear fuel cycle, they will contribute to the ongoing search for alternative uranium resources, namely the uranium extraction from seawater. Furthermore and at the back-end of the nuclear fuel cycle, they are potential candidate materials for nuclear waste treatment and recycling. Finally, facing the ever present risk on the environment following nuclear accidents and the release of hazardous radionuclides, these new materials can be possibly used in the field of radiodecontamination, also for the radiodetoxification of living beings following a radionuclides intoxication.

In this introductory chapter, we will briefly discuss the above mentioned fields of research and challenges they are facing, and we will try to justify the need for innovative solutions like ours. We will then present the state of art techniques used to synthesize those polymer materials, either in solution or on a solid substrate.

I.1.2. Uranium extraction from seawater

With over 4 billion tons, world's oceans count for 99.9 % of earth's uranium. Extracting some of this uranium was suggested shortly after the Second World War. However, because of the fast growing demand, it was decided that efforts should be directed towards the then known ores, mainly due to the overwhelming economic and technical challenges of extracting the extremely diluted uranium (3.3 ppb) from natural waters [2]. Nonetheless, at the current consumption rate, conventional reserves of uranium should dry out in roughly a century [3], making it inevitable to reconsider uranium harvesting from seawater.

The International Atomic Energy Agency (IAEA) estimated in a 2016 report [4] that nuclear power production may increase worldwide by up to 56% over the period 2015–2030. Because of the increasing demand of nuclear energy, and the fact that conventional uranium reserves could be depleted within a century, uranium recovery from seawater was listed as one of " Seven chemical separations to change the world " in a 2016 *Nature* article [5].

In the next few decades, the oceans can become a long sustainable resource for uranium. However, it is very challenging to extract uranium from seawater because of its extremely low concentration while many other elements are present in overwhelmingly higher or comparable concentrations (table 1). Therefore, the extraction process must be extremely efficient, highly selective and must be a passive process, meaning that no energy should be spent to force the extraction. This can be possible for example by taking advantage of tidal wave energy [6].

Table I-1. Various elements in seawater [7]

Element	Concentration (ppb)	Element	Concentration (ppb)
Cl	1.91×10^7	Fe	1-2
Na	1.08×10^7	Ni	0.5-1.7
Mg	1.33×10^6	V	1.5
Ca	4.22×10^5	Ti	1
K	3.8×10^5	Cu	0.6
Li	170	Mn	0.25
Zn	4	Co	0.05
U	3-3.3	Pb	0.03
Al	2		

The extremely low concentration of the uranyl ion (UO_2^{2+}) in seawater (~3.3 ppb) and the presence of competitive ions complicate the recovery process. Uranium recovery is hindered by the complex solution chemistry in seawater; uranium is present in multiple forms even if the dominant form (~85%) is the uranyl tricarbonate $UO_2(CO_3)_3^{4-}$ complex. Furthermore, seawater has varying solution characteristics in terms of pH (7.5–8.5), temperature (12 – 40 °C), complex ion speciation and high salt concentration (0.6–0.7 M). As a consequence, the extraction of uranium from seawater requires the development of a highly selective separation process.

For the uranium recovery from seawater by adsorption, the development of a highly selective adsorbent technology has been primarily focused on the interaction of an adsorbent (stationary phase) with seawater (mobile phase). Considering the dilute uranium concentration, adsorption by chelating polymers appears to be the most promising method for uranium recovery from seawater in terms of simplicity of operation, operating cost, environmental risk and uptake capacity [8], as compared to other separation methods such as coagulation, coprecipitation, and membrane filtration [9] which require additional sedimentation and filtration processes and high operating costs. Membranes tend also to foul during filtration [10].

Several adsorbing materials have been developed for that purpose. Those materials can be divided into three main categories, i.e. inorganic porous materials, biopolymers, and synthetic organic polymers [7].

Various inorganic materials have been considered as potential adsorbents for uranium recovery. Magnesium silicate [11] and oxyhydroxide [12], silicate [13], nanoporous alumina [13], iron (III) oxide [14], and hydrous titanium oxide ($TiO_2.nH_2O$) [15] have been studied, with hydrous titanium oxide receiving the most interest [16]. Advantages of these materials over polymeric adsorbents include high surface area, high porosity and tunable pore structure. However, transport limitations due to pore blockage can significantly reduce the accessible surface area. Moreover, adsorption of uranium has been affected by the solution pH [17], temperature [18], the presence of other ions [19], crystallographic form, morphology, surface area and grain size…[20]. The complexity of the above systems associated with high operating costs pushed scientists to look for alternative strategies.

Biological adsorbents have been also considered [21]. Ligands such as grafted DNA [22], starch-based hydrogels [23], unicellular cyanobacteria [24], chitosan resin [25] and various biomass [26] have been tested as potential adsorbents for the recovery of uranium from seawater. Biopolymers have the advantage of being renewable and environmentally friendly for marine systems. However they are more likely to be sensitive to changes of environmental conditions (e.g., temperature, pH, and biofouling). Biological adsorbents are still being considered for uranium harvesting from seawater, but a parallel search for more robust adsorbents is gaining momentum, namely synthetic polymers.

Synthetic polymers have received the most interest for the recovery of uranium from seawater [27-30] because selective functional groups can be readily added on polymer chains to enhance uranium capacity and affinity. Robust and ductile polymers can be chosen as a substrate for the adsorbent and various shapes of polymeric adsorbents can be fabricated in large quantities.

Adsorbents with amidoxime functional groups (scheme 2) are by far the most promising adsorbents because of their high affinity in chelating uranyl ions in seawater [28]. Over the last few decades, many efforts had been devoted to this topic and one of the most successful strategies among them was polymer fiber adsorbents synthesized via radiation-induced graft polymerization (RIGP) [7, 31]. Researchers at the Japanese Atomic Energy Agency (JAEA) developed polymeric fiber adsorbents, which contained polyethylene or polypropylene as a trunk polymer and amidoximated polyacrylonitrile (PAN) copolymerized with hydrophilic groups (e.g., poly(methacrylic acid)) as a graft chain. The incorporation of hydrophilic groups is crucial to allow seawater to access the amidoxime (AO) group on the graft chain [32, 33]. Japanese researchers also performed marine tests with stacked unwoven fabrics and braided fibers for different periods of time and at different locations [29]. Their pioneering work has established a good foundation to this research field.

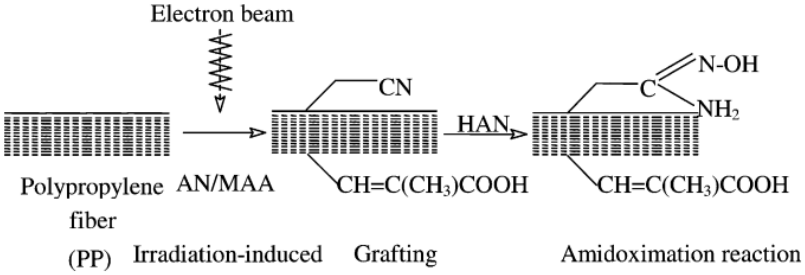

Scheme I-2. JAEA's amidoxime-based adsorbent [28]

More recently, researchers at the Oak Ridge National Laboratory (ORNL) employed a similar strategy (i.e., using RIGP) but with different geometry polyethylene fibers, which provided a high surface area, and demonstrated an improved uranium adsorption capacity [34]. Polymeric fiber adsorbents for uranium adsorption have several advantages, they are easily deployable in seawater, light weight and easy to fabricate into various shapes and lengths.

However, polymeric fiber adsorbents prepared solely via conventional RIGP have some limitations such as inability to tune its composition, degree of grafting, conformation, and morphology due to its ill controlled polymerization mechanism. Therefore, ORNL researchers utilized a hybrid approach, using RIGP and controlled atom-transfer radical polymerization (ATRP) [30] to prepare polymeric fiber adsorbents for uranium recovery from seawater.

In this strategy, RIGP-grafted poly-(vinylbenzyl chloride) (PVBC) were prepared in the first step then used for subsequent ATRP as shown in scheme 3.

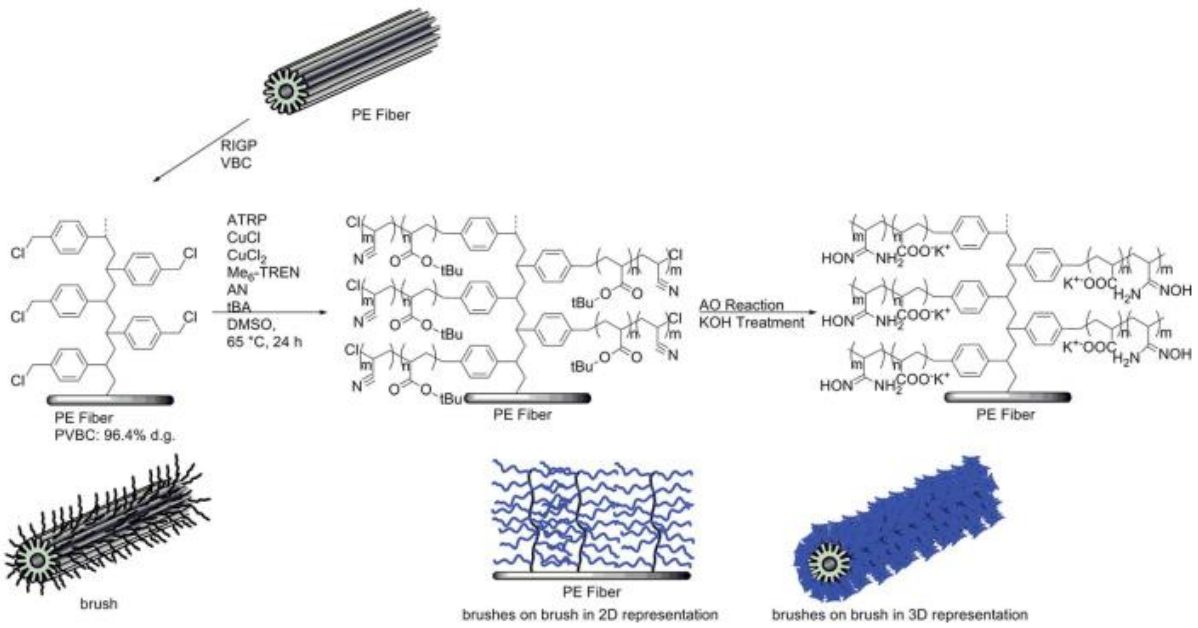

Scheme I-3. Reaction scheme for the preparation of fiber adsorbents via ATRP [30]

The use of the controlled radical polymerization allows to control the degree of polymerization (length of graft chains) in order to reach higher chain lengths and, once optimized, to reproduce the optimal degree of polymerization and architecture for best performance in aqueous systems.

Using this strategy, adsorbents made by the ORNL team are steadily approaching an adsorption capacity of 6 mg U/mg adsorbent, much higher than the average 1.1 mg U/mg adsorbent for that of JAEA.

Despite the high uranium adsorption capacity, poly(amidoxime)-based fiber still suffer from the following drawbacks:

1. The need for a hydrophilic comonomer (ex. acrylic acid) to allow seawater to access the ligand.
2. The use of a multiple step preparation strategy, increasing the adsorbent production cost, and consequently the overall extraction cost.
3. The use of classical ATRP polymerization in which reagents and solvents must be degassed, and heating is required (65 °C). A harmful solvent like DMSO is used and the unstable copper (I) catalyst should be purified prior to reaction.
4. Amidoxime, the main ligand responsible for uranium adsorption, exhibits a very high competitive affinity towards vanadium species [35]. In fact, vanadium is present at lower concentrations (1.5 ppb) than uranium (3.3 ppb) in seawater (table 1). Yet, vanadium uptake by poly(amidoxime) fibers is found to be twice higher than uranium's [34]. The vanadium species bind so strongly that stripping them under harsh acidic conditions irreversibly damages the amidoxime sorbent [36].

In the present work, and in order to overcome the problems associated with amidoxime-based adsorbents, we proposed the use of a 4-hydroxy-dipicolinic acid (chelidamic acid)-derived monomer as an alternative ligand. This approach offers the following advantages:

1. Dipicolinic acid is water soluble, eliminating the need for a hydrophilic comonomer.
2. This ligand has already proven to have a higher affinity towards uranium UO_2^{2+} (log K = 11.6) over VO_2^{+} (log K1 = 9.3) and VO^{2+} (log K2 = 8.0) cations [37].
3. The classical ATRP polymerization will be replaced by the Supplemental Activation Reducing Agent (SARA) ATRP. This way, the non-stable copper (I) catalyst will be replaced by the stable copper (II) and the catalyst load will be reduced by a factor of 100. DMSO will be replaced by acetonitrile, a green solvent. Furthermore, the polymerization will be achieved at room temperature, minimizing the energy consumption and eventually the overall cost. Finally, thanks to metallic copper added to the system, the reaction is

oxygen tolerant and no degassing will be needed. SARA ATRP will be discussed in detail in a later section.

4. The modification steps will be reduced to a single step using PVC-co-CPVC fiber as a substrate. PVC-based fibers were very recently used by the ORNL team to graft poly(amidoxime) adsorbent [38]. However, they still used classical ATRP, higher temperature (65 °C), and a high boiling point (244 °C) toxic ethylene carbonate (EC) solvent. Their strategy is described in scheme 4.

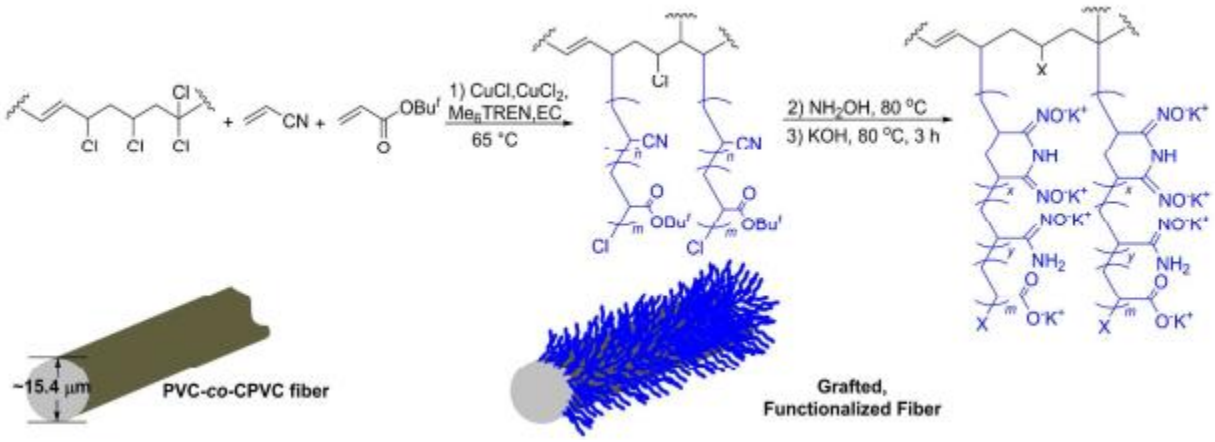

Scheme I-4. Synthesis steps of uranium adsorbent fibers from PVC-co-CPVC fibers [38]

Our proposed strategy is described in scheme 5, where SARA ATRP stands for Supplemental Activation Reducing Agent Atom Transfer Radical Polymerization and VDPM stand for the 4-vinyl dimethyl dipicolinate monomer, both terms will be described later in this manuscript. The monomer synthesis, surface-initiated polymerization and performance of the new adsorbent materials will be discussed in details throughout this manuscript.

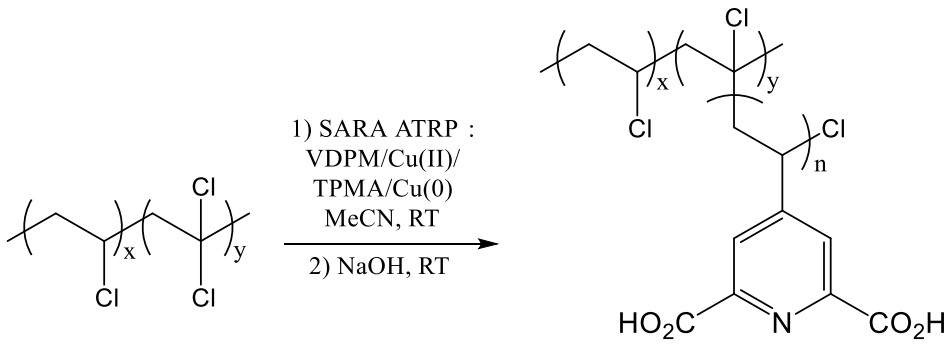

PVC-co-CPVC (PVC-co-CPVC) -*g*- PVDPA

Scheme I-5. Synthesis of the new (PVC-co-CPVC)-g-PVDPA adsorbents

I.1.3. Nuclear waste management

Given the intensity and persistence of the radiation field of discharged nuclear fuel, it is clear that significant handling precautions are needed for reasons of safety and security. Intact nuclear fuel has been considered to be “self-protecting” from intrusion because of the intense gamma radiation field. This philosophy was the driver for adoption of the open nuclear fuel cycle (scheme 1), especially in the United States. In this approach, the spent fuel is considered as waste to be deposited in a geological repository permanently.

This approach however, is very questionable and fuel recycling is now being used and developed for different reasons [39]. Spent fuel poses a serious danger on population upon exposure to ionizing radiation. For the direct disposal option, fuel must be isolated from the accessible environment for about 250,000 years, due mainly to the radiotoxicity of Pu-239. Building a repository system for a time greater than that of human civilization is challenging and is considered impossible. Reprocessing with actinide transmutation shifts the radiotoxicity to fission products like Sr-90 and Cs-137, acute radiotoxicity threat is then reduced to 300-400 years. Reprocessing can also help prevent nuclear weapons proliferation by limiting isolated uranium and plutonium reserves.

In term of financial cost, even though reprocessing is directly more expensive, this cost can be counterbalanced by a decreased safety margin needed in repository, the reuse of reprocessed fuel in closed nuclear cycle and the use of other partitioned materials like minor actinides, lanthanides, and other byproducts. Enhancing nuclear energy’s economic viability, and most importantly its security, will also favors its attractiveness compared to conventional carbon emitting fossil fuel as energy source.

Two options for spent fuel reprocessing exists today, the aqueous (solution) approach and the pyroelectrometallurgy (dry) approach [40]. The aqueous approach begins with the dissolution of used fuel rods in concentrated nitric acid, followed by solvent-extraction processes designed to extract the target metallic species. The dry method is achieved under inert atmosphere and in the absence of aqueous media. It mainly uses molten salts and/or liquid molten metals. Pyroprocessing has the benefit of being tolerant to high radiation doses, which allows the treatment of used fuel without having to wait for an extended period of time to let the material decay to lower levels of activity. Pyroprocessing will not be further discussed and is out of scope of our work.

I.1.3.1. Aqueous processing/recycling of nuclear spent fuel

Nuclear spent fuel (NSF) contains approximately 95% uranium, 1% plutonium, and 4% fission products (minor actinides, lanthanides and many other elements). Once dissolved in concentrated nitric acid, spent fuel reprocessing is carried out using PUREX (**P**lutonium **U**ranium **R**edox **Ex**traction) liquid-liquid extraction process to extract uranium and plutonium using a 30% tributyl phosphate (TBP) solution in kerosene. Remaining fission products and minor actinides are then sent for subsequent processing, or treated as wastes for disposal as high-level radioactive waste stored in a solid matrix like glass or ceramic. The uranium recovered by PUREX is stored for future use and plutonium is recycled to create MOX (mixed oxide) fuel by blending with natural uranium.

To assure the sustainability of the nuclear fuel cycles, both on the technical and economic levels, the PUREX process is continuously reviewed and possible improvement paths are investigated. In the American UREX (**UR**anium **EX**traction) process, uranium can be extracted along with technetium while leaving the plutonium to waste with the fission products and higher actinides. Since plutonium is not isolated, proliferation risks associated with PUREX are reduced [41]. Another American process, TRUEX (**TR**ans**U**ranic **EX**traction) allows the extraction of transuranic metals (americium and curium) by adding octyl(phenyl)(N,N-diisobutylcarbamoyl methyl)-phosphine oxide (CMPO) ligand to PUREX's TBP solution.

Alternatively in the French COEX process, used nuclear fuel is separated into three streams: uranium-plutonium, uranium, and fission products and minor actinides. Pure plutonium is never separated out and thus the risk of proliferation is reduced. The uranium-plutonium stream is extracted and then turned into MOX fuel. The uranium stream is sent to a separate facility for purification, conversion and re-enrichment and conversion into added recycled fuel. The fission products and minor actinides stream is vitrified and stored as high-level waste then disposed of [42].

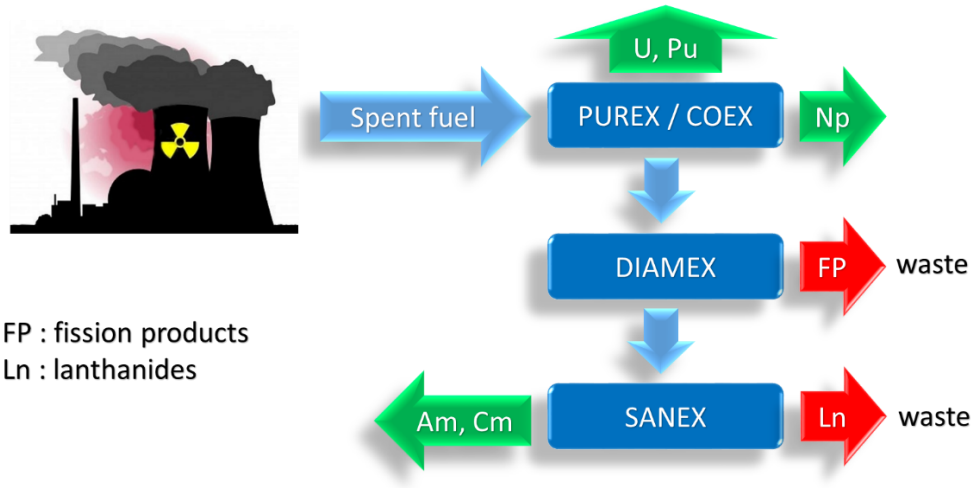

Scheme I-6. French multistage spent fuel recycling

Consequently, PUREX/COEX raffinate can be further processed and minor actinides separated using the french DIAMEX-SANEX process. After having been extracted with lanthanides by in the DIAMEX (**DIAM**ide **EX**traction) process using *N*,*N*'-dimethyl-*N*,*N*'-dioctylhexylethoxy malonamide (DMDOHEMA), minor actinides (mainly americium and curium) are separated in the SANEX (**S**elective **A**cti**N**ide **EX**traction) process [43]. Americium can also be extracted alone from the PUREX raffinate by the ExAm (**Ex**traction of **Am**ericium) [44] or the SESAME (**S**elective **E**xtraction and **S**eparation of **A**mericium by **M**eans of **E**lectrolysis) processes [45].

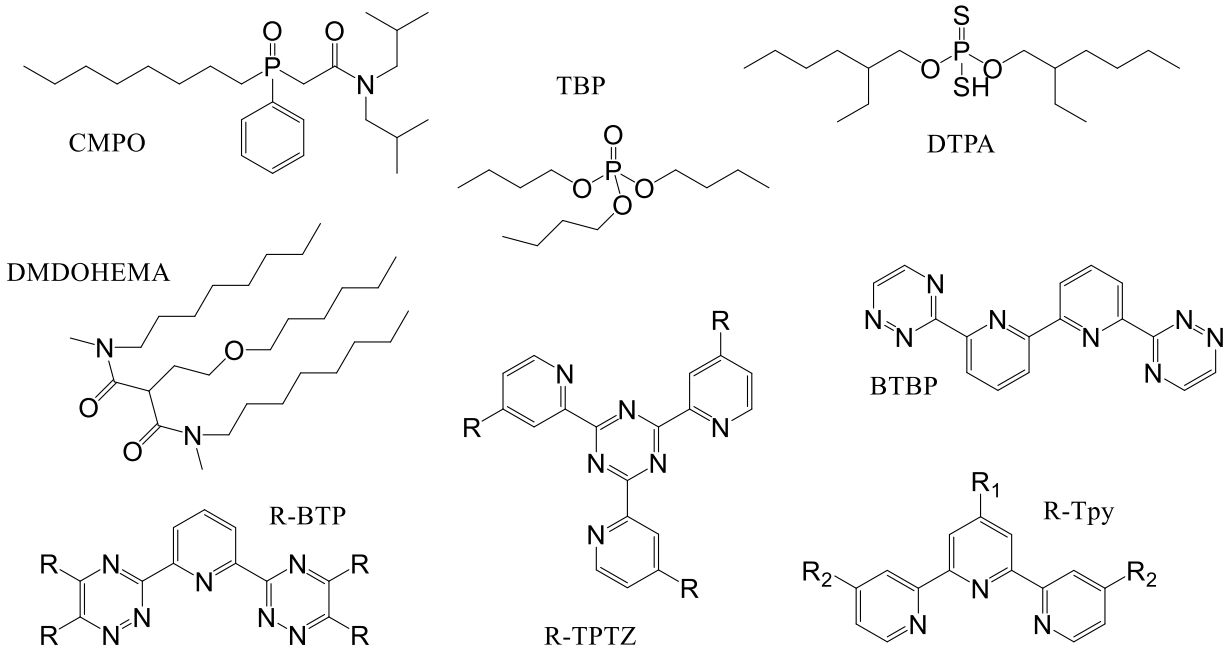

Figure I-2. Ligands used in different separation processes

In the future 4th generation nuclear reactors, a more homogeneous reprocessing plan will be needed to minimize the proliferation risk and to close the nuclear fuel cycle. This leads us to the GANEX (**G**rouped **A**cti**N**ide **EX**traction) concept where actinides (uranium, plutonium, neptunium, americium and curium) are extracted and reintegrated in a new fuel cycle. Lanthanides (Ln) and other fission products (FP) are sent as waste. In a GANEX process, this is done by adding a bis-triazinyl bipyridine (BTBP)-based ligand to the TBP organic solution [46].

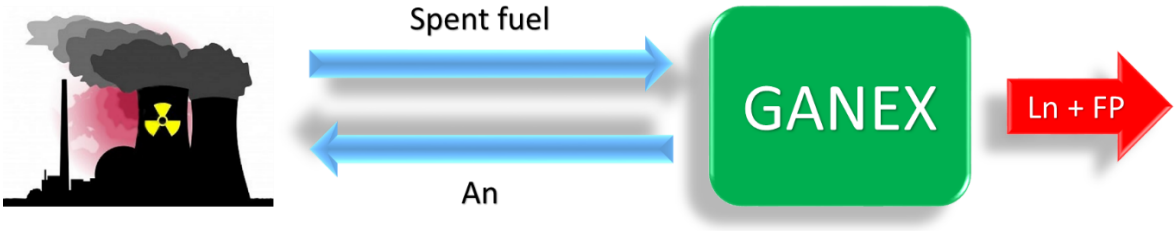

Scheme I-7. Homogeneous actinide recycling by GANEX process

I.1.3.2. Proposed polymer assisted reprocessing strategy

The development of the An/Ln separation strategy is of great importance, either for the DIAMEX-SANEX process or the future GANEX homogenous recycling concept. Nitrogen and sulfur donors was found to bind preferentially to trivalent actinides than to lanthanides [47], and promising extractants were suggested like 2,4,6-tri(2-pyridyl)-1,3,5-triazine (TPTZ) and di-(2-ethylhexyl)dithiophosphoric acid (DTPA) [48]. However, the CHON rule makes N-donors more preferred in a nuclear application because they can be incinerated, purified and released into the atmosphere. In contrast, incineration of S-donor phosphorus containing molecules leaves solid residue that contribute to the production of radioactive waste and can retain not easily recoverable residues of actinides [47].

A wide variety of N-donor ligands has been proposed for the An/Ln separation including terpyridines (Tpy) and bis-triazinylpyridines (BTP)-based ligands and many others [47]. The development of partitioning processes has attracted increased attention and the search for improved N-donors has become more intensive.

However, efforts have been focused on lipophilic extractants knowing that all strategies are based on liquid-liquid separation, the metallic species being in the aqueous phase (nitric acid) and the

extractant being in the organic phase. In this case, the basicity of the extractant is an important factor, because it determines the extent to which the H^+ ions compete with the Ln or An ions for the N-donor ligand. The complexant is only slightly soluble in water in the unprotonated form and it becomes more soluble with increasing concentration of H^+ ions (i.e. increasing degree of protonation). The distribution coefficient of the ligand between the organic and the aqueous phase is then dependent on pH. Decreasing the pH then leads to a loss of extractants to the aqueous phase and partially compromise the solvent extraction separation process.

In this scope, several studies have proposed the use of adsorbents in the form of ion exchange resins to trap elements of interest directly from nitric acid, then selectively eluting them from those resins. Compared to the conventional liquid-liquid extraction, adsorption separation process have the advantage of a minimal organic solvent utilization, smaller separation equipment and simultaneous separation of multi-components. In fact, ion exchange has been considered for spent fuel reprocessing long time ago, but ion exchanger were very sensitive to swelling/shrinking depending on solution composition and had poor performance.

Recent advances however in the field of organic ion-exchange, like porous silica-based resins, encouraged researchers to reconsider the use of ion exchange in reprocessing. For example, pyridine-type resin synthesized by copolymerizing 4-vinylpyridine with 20% divinylbenzene in porous silica proved capable of separating uranium from fission products in an acidic medium [49]. Another ion exchanger, named AR-01, where the resin, with benzimidazole groups (figure 3) as exchange sites, is embedded in porous silica particles, was successfully used to separate uranium from most fission products [50] in a 6 M nitric acid solution. Fission products were further separated in a CMPO and R-BTP based resins [51]. CMPO and R-BTP structures were shown earlier in figure 2.

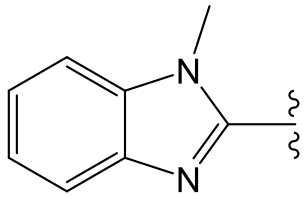

Figure I-3. N-methylbenzimidazol used in AR-01 ion-exchange resin

These suggestions try to overcome problems associated with a liquid-liquid extraction process. However, they still use concentrated nitric acid to dissolve spent fuel with which several other disadvantages are associated, including the increased emission of volatile fission products (e.g., I_2), the discharge of toxic NOx vapors, and the large plant footprint required to perform the fuel digestion [52].

Other researchers looked for alternative UO_2 dissolution processes in order to avoid some of the challenges associated with highly acidic reprocessing. The use of peroxide-containing carbonate solutions, for example, can open the door to a process with lower operating costs and improved safety relative to PUREX [52]. The oxidative dissolution of UO_2 by hydrogen peroxide H_2O_2 was studied as a function of peroxide concentration and pH and was proven feasible [53].

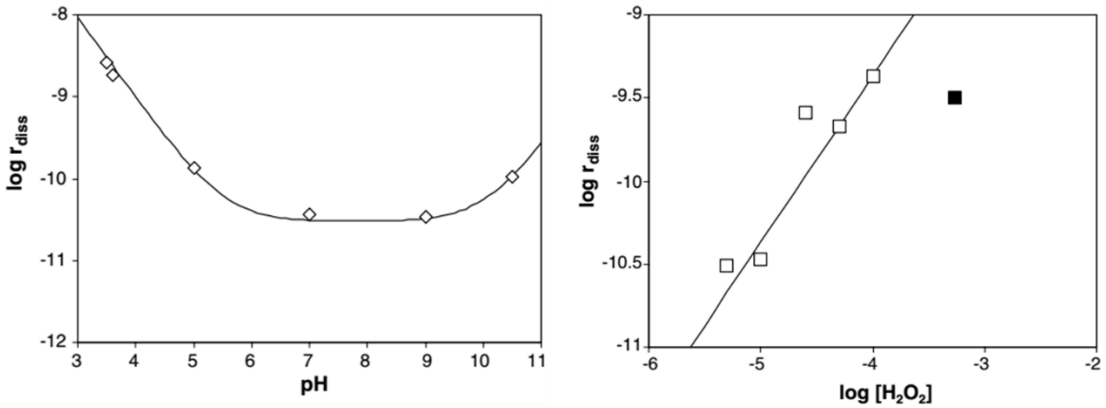

Figure I-4. UO_2 dissolution rates (in mol m^{-2} s^{-1}) as a function of pH at $[H_2O_2] = 10^{-5}$ M (left) and as a function of hydrogen peroxide concentration at pH 5.8 (right) (ref [53])

Moreover, the dissolution of the tetravalent UO_2 in sodium carbonate solutions was found to be straightforward in the presence of an oxidant according to the following equation [52], yielding a hexavalent uranyl carbonate complex.

$$U^{IV}O_2\ (s) + CO_3^{2-} + \text{oxidant} \rightarrow U^{VI}O_2(CO_3)_3^{4-}$$

To conclude, the above mentioned efforts suggest using ion exchange technology to extract different radionuclides (using lipophilic extractant fixed on silica) from nitric acid solutions on one side, or on the other hand, dissolving spent fuel in solvents other than nitric acid (like H_2O_2) before PUREX liquid-liquid extraction.

In this scope, we are proposing a new concept for spent fuel recycling, a strategy where actinides, lanthanides and other fission products can be separated directly from an aqueous solution even at

mild pH levels. In this strategy, both actinides and lanthanides will be trapped by a hydrophilic polymer and the rest of fission products will be eliminated by a first filtration. Afterwards, by decreasing the pH level, lanthanides will be released back into an aqueous solution and eliminated by a second filtration to leave actinides trapped in the polymer matrix. We called this strategy PALEX as in "**P**olymer assisted **A**ctinide **L**anthanide **EX**traction". Our proposed strategy is described in scheme 8.

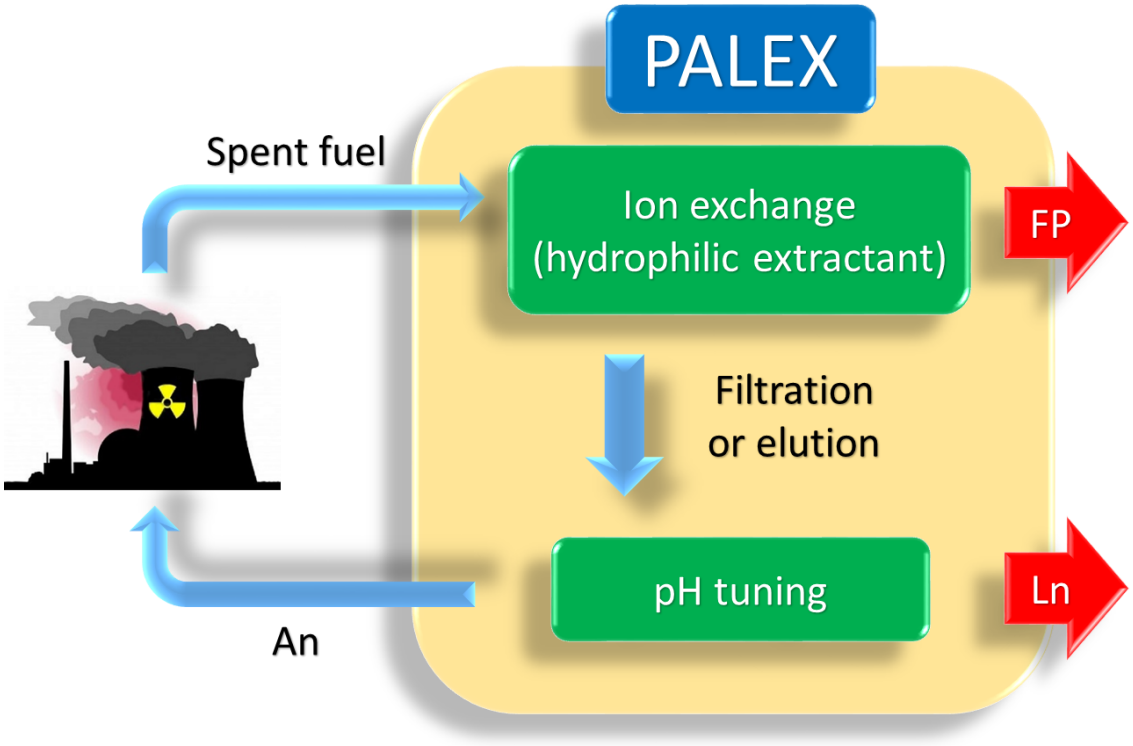

Scheme I-8. Proposed PALEX process

Later in this thesis (chapter IV), we will further discuss this strategy, its advantages compared to above mentioned liquid-liquid extraction processes, and the future challenges that needs to be eradicated if this strategy is ever to be considered for nuclear spent fuel recycling.

I.1.4. Radiotoxicity and radiodecontamination

I.1.4.1. Radiotoxicity

The radiological and chemical toxicity of uranium and other radionuclides are responsible for many public health issues. Exposure to radionuclides can be either external when the radionuclide remains outside or at the surface of the body, or internal when the radionuclide is absorbed into the body either by inhalation, ingestion or through skin [54].

Inhalation is considered as the most frequent mode of contamination in the industry. It can occur after an explosion or a fire, causing atmospheric dispersion of radionuclides in case of containment disruptions. The second most frequent mode of contamination after inhalation is skin exposure. This can occur especially on injured skin, after an explosion or improper handling of contaminated tools. The skin can also be contaminated by contact with aerosols or by contact with contaminated surfaces. Ingestion is unlikely to happen among workers in the nuclear industry thanks to strict health and safety instructions. However, it may be more critical for civilians in the case of an accidental release of radioactivity into the environment [55] after an accident such as the one that took place in Chernobyl or more recently in the Fukushima Dai-ichi Nuclear Power Plant [56].

The risk is also increased in geographic areas where uranium is mined, milled, processed and/or fabricated as well as in the vicinity of former battlefields where depleted uranium munitions were deployed. Several studies reported increased rates of cancer and congenital anomalies following the hostilities in conflict areas like Bosnia-Herzegovina [57] and Iraq [58, 59] and described the consequences arising from the inhalation of the uranium oxide aerosols generated when depleted uranium munitions are detonated [60].

High levels of uranium, thorium and plutonium were found in the bodies of deceased workers who have worked in mining and processing plants [61] and high cancer mortality was registered among employees working in these plants [62] and communities living nearby [63]. Exposure to uranium has several consequences on living species including humans, with variations in sensitivity among species. The chemical toxicity of uranium in kidneys is one of the consequences of the precipitation and binding of the radionuclide to the proximal tubular cells [64]. Radionuclides like radium and uranium are also retained in bones where they replaces the calcium in the hydroxyapatite structure and causes a decrease in osteogenesis and therefore of bone mass [65, 66]. The skin of rats exposed

to uranium was found to be 35-50% thinner and more permeable compared to controls [67]. Uranium can also induce the secretion of inflammation proteins, and cell death through the activation of kinase proteins [68]. It can also induce apoptosis and necrosis of macrophages and T lymphocytes and was found to deregulate the immune response even at non-cytotoxic concentrations [69]. Uranium can also accumulate in some parts of the brain like the striatum, hippocampus and frontal cortex [70].

I.1.4.2. Radiodecontamination

Uranium related hazards are treated either by limiting and controlling external exposure paths and contaminated sources like soil and water or, if uranium is already incorporated into a human body, by chelation therapy.

Uranium polluted environment can be treated by physical, chemical or biological means [71]. Physical methods (coagulation, precipitation, evaporation, extraction and membrane separation) are only suitable for small areas of water contaminated by uranium and have high operating cost. Chemical methods have high efficiency and low cost to remove the uranium, but most are still in the experimental stage. Bioremediation methods (bacteria, fungi, yeast and algae…) are appropriate for large areas of soil and water contaminated by low concentrations of uranium and don't produce secondary pollution, but their success depends largely on the geochemistry of contaminated sites [72].

Chelation therapy is the use of chelating agent capable of binding to a metal contaminant, uranium in this case, and guide it out of the human body, mainly through sweat and urine. For a chelating agent to be suitable for treatment of uranium intoxication, several factors have to be considered, like the solubility of the chelating agent at physiological pH (~7.4), its toxicity, its ability to bind to uranium and eventually the competitive chelation with other metals present in the human body like iron, zinc and manganese.

Many chelating agents were considered for the decorporation of uranium. Treatments with sodium bicarbonate [73], sodium citrate [60], ethylenediaminetetraacetic acid (EDTA) [74] and many other agents [75] were recommended to promote uranium mobilization and elimination. Among many chelating agents, Tiron™ (2,4,5-Trihydroxy-1,3- benzenedisulfonic acid) appears to be the most effective agent of those tested in the treatment of acute uranium intoxication [76].

Once again, our dipicolinic acid-based polymer materials could be a potential candidate for an improved radiodecontamination and radiodetoxification. In addition to its high chelating capability, dipicolinic acid has a proven biocompatibility and has been reported in pharmaceutical research articles [77].

It should be noted however, that this thesis is more of a precursor work. Field experiments in the three applications mentioned above are of extreme difficulty given the complexity of each field and the three years lifetime of a thesis work. An important prove-of-concept work was achieved at the laboratory scale level, and we hope that this work will be at the basis of future projects and collaborations with experts in each field for further development.

I.2. Controlled Radical Polymerization (CRP)

I.2.1. Introduction

Nowadays, conventional radical polymerization (RP) is employed to produce annually more than 100 million tons of polymer materials, with thousands of different compositions [78]. However, until the last two decades, the control of molecular architecture in a RP was considered impossible at a level similar to other living ionic systems because two radicals always terminate at a very fast rate [79]. In conventional RP, described in scheme 9, control over molecular structure is impossible because radical intermediates are very reactive with a lifetime less than 1 second [80], making it impossible to control macromolecular structure during such a short time.

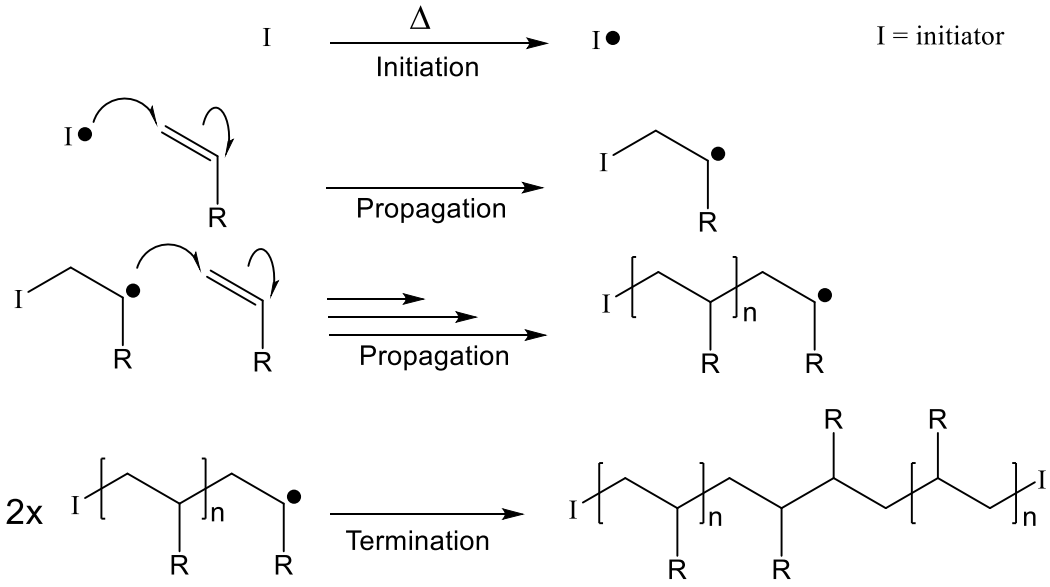

Scheme I-9. Conventional radical polymerization

The concept of controlled/living radical polymerization, or reversible-deactivation radical polymerization (RDRP) as IUPAC recommends, was introduced in order to domesticate this uncontrolled radical behavior. By inserting long periods of latency (~1 min) after each ~1 ms of activity, the overall life of propagating chains can be extended to minutes, hours or days, giving the time to "control" the molecular structure of the expanding polymer chains. This extension of the lifetime of growing chains was accomplished by insertion of multiple reversible radical deactivation steps and allowed the synthesis of well-defined, tailor-made polymers.

Even though the first "living" radical polymerization was introduced back in the early 80s by Otsu and coworkers [81], it got its real boost later in mid-90s following the independent work of Sawamoto [82] and Matyjaszewski [83]. Ever since, the Matyjaszewski team at Carnegie Mellon University pioneers the field of controlled radical polymerization.

The controlled radical polymerization (CRP), or reversible-deactivation radical polymerization (RDRP), has paved the way to a wide variety of advanced materials with precisely controlled molecular architecture [84, 85]. All of the RDRP methods are based on establishing a dynamic equilibrium between a limited amount of growing free radicals and a large majority of dormant species. The dormant chains may be alkyl halides, as in atom transfer radical polymerization (ATRP) [86], thioesters, as in reversible addition fragmentation chain transfer processes (RAFT) [87] or alkoxyamines, as in nitroxide mediated polymerization (NMP) [88]. These different mechanisms are described in scheme 10.

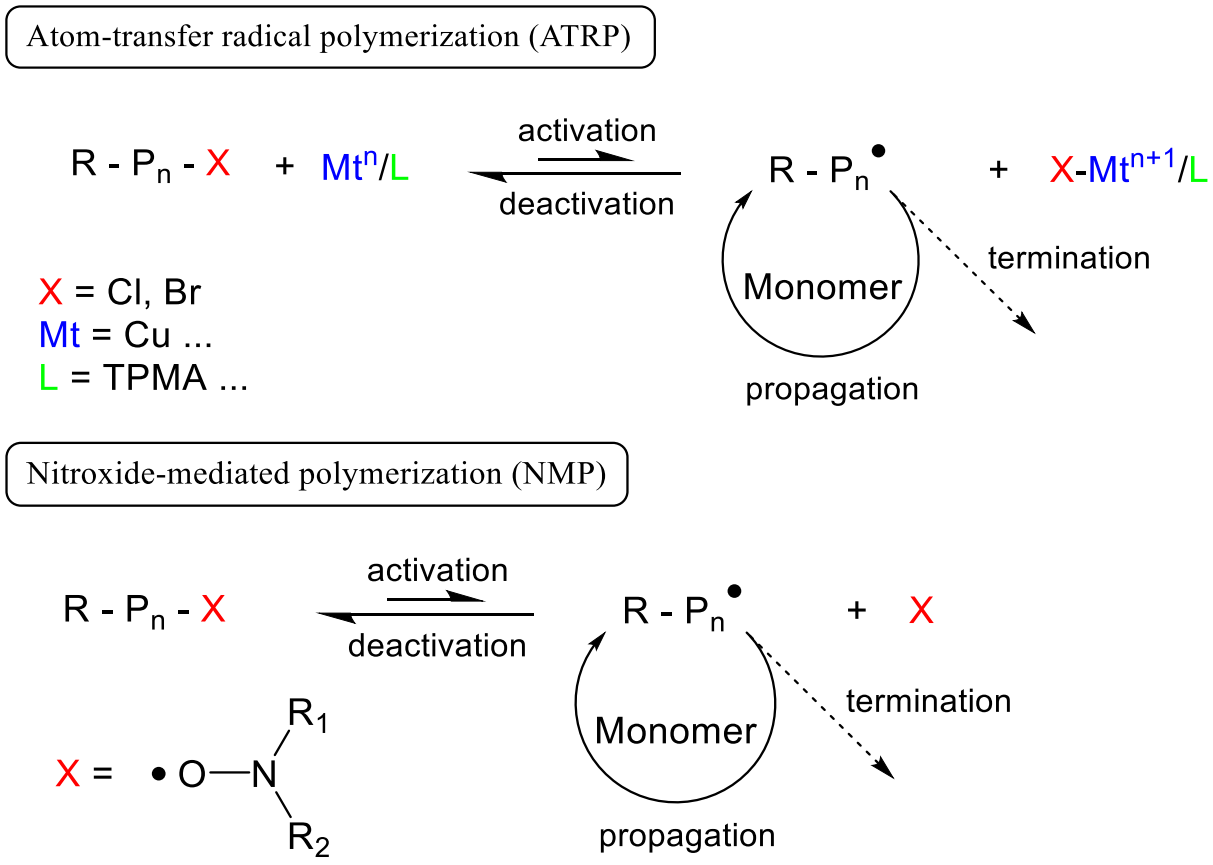

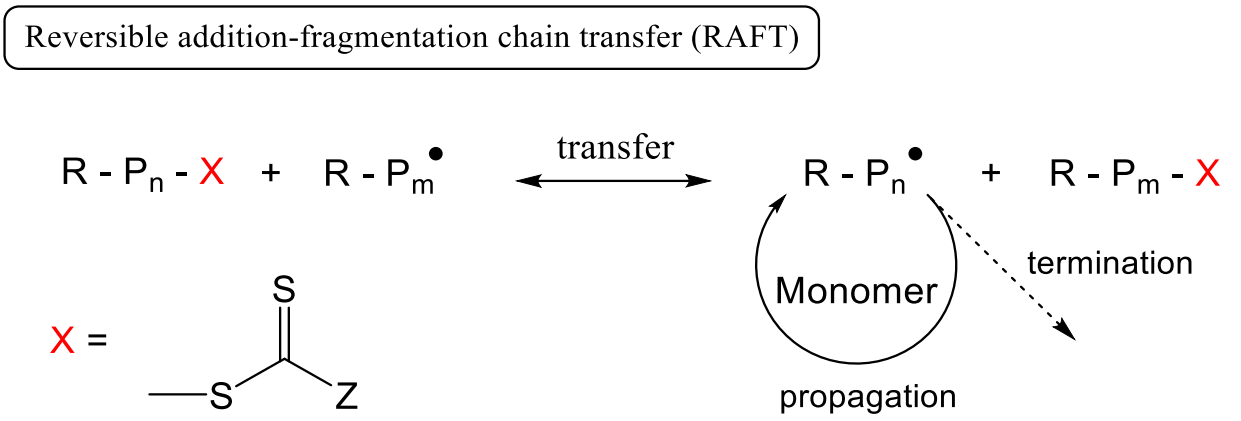

Scheme I-10. The three main types of RDRP

Each of these three highly successful CRP systems has its own set of advantages and limitations. The higher reaction temperatures of NMP can be harmful to a wide array of substrates and, high temperature makes NMP energy consuming. RAFT, on the other hand, has a versatile and robust reaction setups. However, its use has been hindered by the multistep reactions required for the synthesis of the chain transfer agent. ATRP is the most attractive and highly translational technique across laboratories, disciplines, and levels of chemical expertise, due to the simple experimental setup, broad range of monomers and solvents used and commercial availability of initiators (alkyl halides, which can also be easily attached to surfaces or biological molecules) and catalyst components, while maintaining exquisite control and versatility [85].

In the following section, we will further describe ATRP, its mechanism, advantages and limitations. We will also explain how its drawbacks can be further eradicated using a special kind of ATRP called Supplemental Activator and Reducing Agent (SARA) ATRP.

I.2.2. Atom transfer radical polymerization (ATRP)

ATRP is mechanistically related to transition metal mediated atom transfer radical addition (ATRA) reactions used to form a carbon-carbon bond through a transition metal catalyst [85]. In normal ATRP, the polymerization system components are composed of an organic halide species (R-X), known as the ATRP initiator, and a transition metal (most often copper)-ligand complex in the low oxidation state (Mt^n/ligand), known as the activator (scheme 11). The detachment of the halogen from R-X results in the generation of an oxidized halogenated transition metal complex (X-Mt^{n+1}/ligand), called the deactivator, in addition to the radical center, R•. The radical center can then undergo radical addition across double bonds of monomers, affording polymerization. The deactivator rapidly transfers the halogen back to the propagating radicals to reform the dormant alkyl halides and the activator.

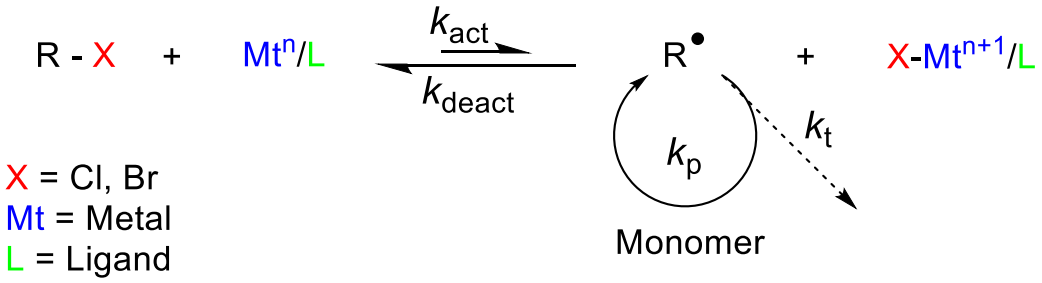

Scheme I-11. Atom transfer radical polymerization

The overall process occurs with a rate constant of activation, $\boldsymbol{k_{act}}$, and deactivation $\boldsymbol{k_{deact}}$. Polymer chains grow eventually by the addition of the intermediate radicals to monomers like in conventional radical polymerization, with the rate constant of propagation $\boldsymbol{k_p}$. Termination reactions $\boldsymbol{k_t}$ can also occur mainly through radical coupling and disproportionation; however, in a well-controlled ATRP, termination is limited to no more than a few percent of the polymer chains.

In a typical transition metal catalyzed ATRP, assuming that contribution of termination becomes insignificant due to the persistent radical effect [89], and using a fast equilibrium approximation, the polymerization rate law $\boldsymbol{R_p}$ can be expressed by the following equation [90]:

$$R_p = k_p[\mathrm{M}][\mathrm{P}^*] = k_p[\mathrm{M}]k_{eq}\,[\mathrm{P\text{-}X}] \times [\mathrm{Mt^nL}]/[\mathrm{X\text{-}Mt^{n+1}L}]$$

where [M] is the monomer concentration, [P*] the propagating chain radical, [P-X] the dormant chains concentration and $\boldsymbol{k_{eq}} = \boldsymbol{k_{act}/k_{deact}}$.

The number-average degree of polymerization (DP_n) of the produced polymers is determined by the initial concentration ratio of monomer to initiator $[M]_0/[R\text{-}X]_0$, and the monomer conversion. In a well-controlled ATRP with fast initiation, no chain-breaking reactions, and a small number of monomer units added during each activation step, the formed polymers are characterized by a narrow molecular weight distribution or low dispersity (Đ = Mw/Mn < 1.5), where Mn is the number-average molar mass and Mw is the mass-average molar mass.

I.2.2.1. ATRP components

A typical ATRP is composed of the monomer, an initiator and a catalyst/ligand complex. For a successful ATRP, these components, and other variables like solvent and temperature, have to be finely tuned.

The monomer:

A wide variety of monomers have been successfully polymerized using ATRP (styrenes, (meth)acrylates, (meth)acrylamides…). Each monomer possesses its own intrinsic radical propagation rate. Thus, for a specific monomer, the concentration of propagating radicals and the rate of radical deactivation need to be adjusted, among other parameters, to maintain good polymerization control.

The initiator:

It determines the number of growing polymer chains. If initiation is fast and transfer and termination negligible, then the number of growing chains is constant and equal to the initial initiator concentration. The theoretical molecular weight or degree of polymerization (DP) increases with the decrease of initial concentration of initiator in a living polymerization.

$$DP = [monomer]_0 \,/\, [initiator]_0 \times conversion$$

Alkyl halides (R-X) are typically used as initiators with the rate of the polymerization being at first order with respect to the concentration of R-X. In a well-controlled ATRP, the halide must rapidly and selectively migrate between the growing chain and the transition-metal complex. Typically, when either bromine or chlorine are used, the molecular weight control is the best, though iodine [91] and pseudohalogens like thiocyanates [92] can be used in certain cases.

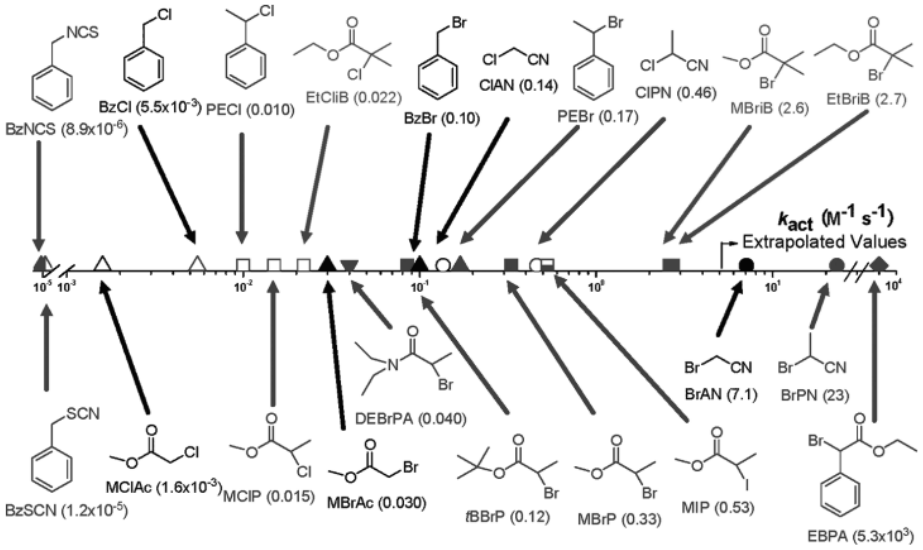

Figure I-5. ATRP activation rate constants for various initiators with Cu(I)-X/PMDETA (X = Br or Cl) in MeCN [93]

A selection of initiators is shown in figure 5 and placed as a function of activation rate constants in a certain ATRP system [93].

The catalyst:

A good choice of a metal/ligand complex is the key to a successful ATRP since it determines the position of the equilibrium and the dynamics of exchange between the dormant and active species. The metal center must have two (or more) accessible oxidation states separated by one electron. It should also have reasonable affinity toward a halogen and be able to bind strongly to the ligand. A number of transition metal complexes have been used in ATRP including molybdenum [94], chromium [95], rhenium [91], ruthenium [82], iron [96], rhodium [97], nickel [98], palladium [99], cobalt [100] osmium [101] and titanium [102]. However, copper is by far the most used transition metal catalyst due to its high versatility and low cost [90] and will be the metal of choice in this thesis.

As for the ligand, a long list of nitrogen based ligands commonly used for ATRP is available. Monodentate nitrogen ligands along with sulfur, oxygen, or phosphorus ligands are less effective due to the different electronic effects or weak binding constants [103]. Therefore, polydentate (N $\geq$ 2) nitrogen ligands are used. These ligands could be either amines or pyridine derivatives, linear, branched or cyclic.

The role of the ligand in ATRP is to solubilize the metal salt and to tune the catalytic activity. The choice of ligand greatly influences the effectiveness of the catalyst. The redox potential of the metal complex serves as a useful guideline for catalyst design. Polydentate nitrogen-based ligands generally work well for Cu-mediated ATRP. A selection of ligands is shown in figure 6 and placed as a function of activation rate constants in a certain ATRP system [104].

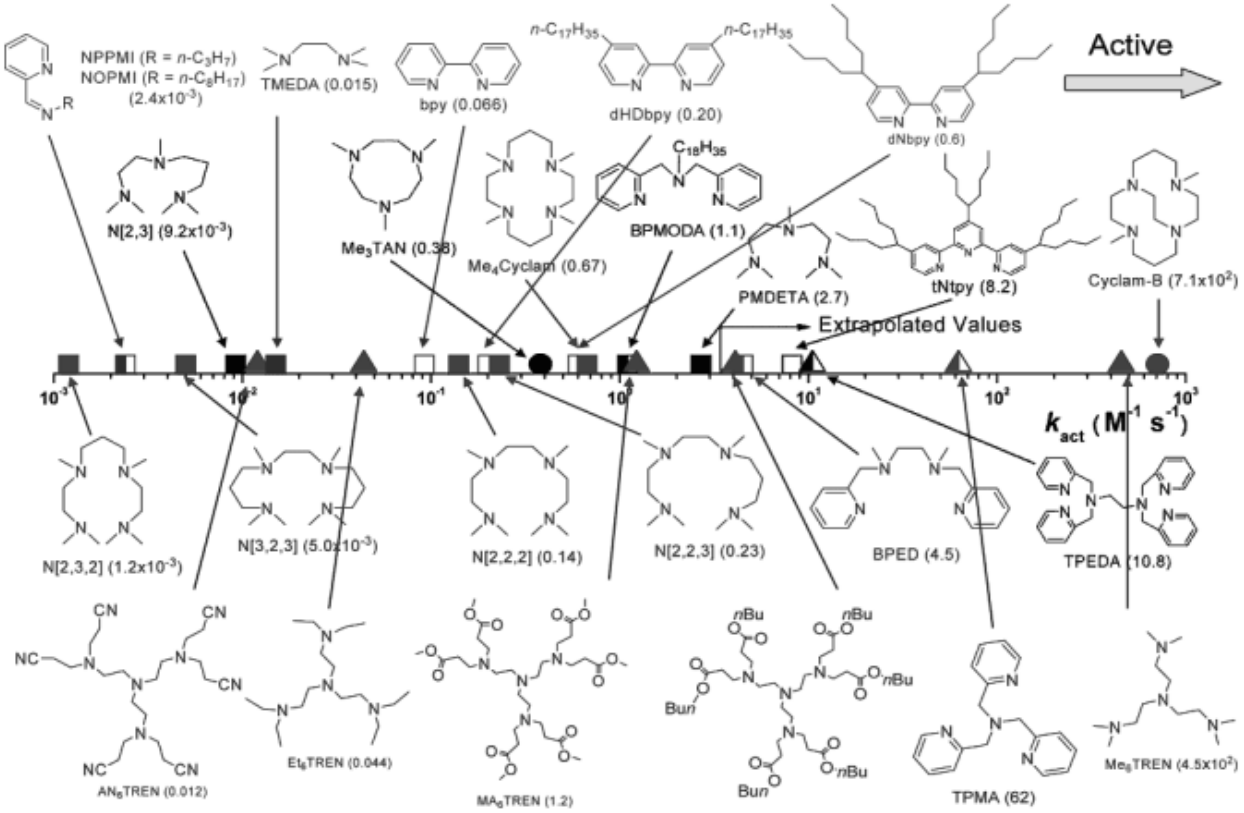

Figure I-6. ATRP activation rate constants for various ligands with EtBriB initiator and Cu(I)-X (X = Br or Cl) in MeCN [104]

The solvent:

ATRP can be carried out either in bulk, in solution, or in a heterogeneous system (e.g., emulsion, suspension). Various solvents, such as benzene, toluene, anisole, diphenyl ether, ethyl acetate, acetone, *N*,*N*-dimethyl-formamide (DMF), ethylene carbonate, alcohol, water, carbon dioxide, and many others, have been used for different monomers. A solvent is sometimes necessary, especially when the obtained polymer is insoluble in its monomer (e.g., polyacrylonitrile). Several factors affect the solvent choice [86]. Chain transfer to solvent should be minimal and interactions between the solvent and the catalytic system should be considered. Catalyst poisoning by the

solvent and solvent-assisted side reactions, such as elimination of HX from polystyryl halides should be minimized [105].

Temperature and reaction time:

The rate of polymerization in ATRP increases with temperature due to the increase of both the radical propagation rate constant and the atom transfer equilibrium constant. As a result of the higher activation energy for the radical propagation than for the radical termination, higher k_p/k_t ratios and better control may be observed at higher temperatures. However, chain transfer and other side reactions become more pronounced [105] as well as catalyst decomposition [97].

At high monomer conversions, the rate of propagation slows down considerably; however, the rate of monomer and concentration independent side reactions persists. Prolonged reaction times leading to nearly complete monomer conversion will induce loss of end groups [106]. Thus, to preserve high end-group functionality or to subsequently synthesize block copolymers, near total monomer conversion must be avoided to prevent end-group loss.

I.2.2.2. ATRP applications

ATRP, either in its conventional of its many modified forms that we will discuss in a later section, gives access to polymers with complex yet precisely controlled architectures in terms of chain topology (stars, cycles, combs, brushes, regular networks), composition (block, graft, alternating, gradient copolymers) and functionality, for different purposes or applications. Scheme 12 illustrates some of the recent advances in macromolecular engineering enabled by ATRP.

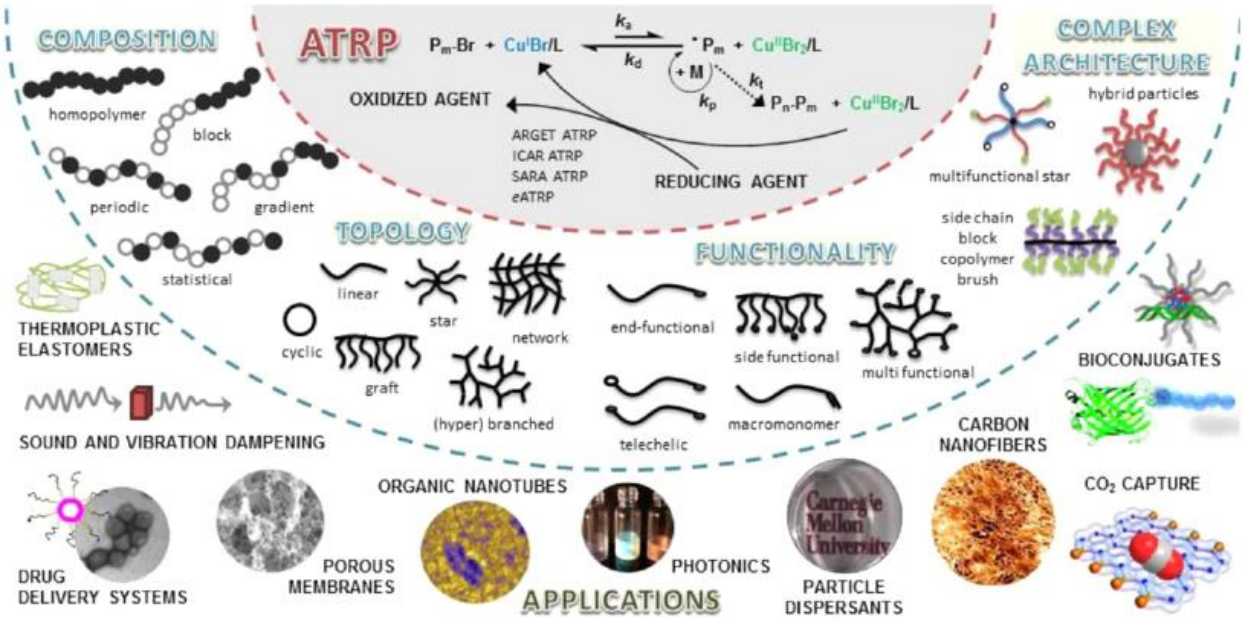

Scheme I-12. Macromolecular Architecture and Applications of polymers synthesized by ATRP [85]

Composition:

The living character of ATRP gives an easy access to block, gradient, and periodic/alternating copolymers not accessible by conventional RP. The efficient initiation, propagation and preservation of chain end functionalities allow the synthesis of block copolymers that can self-assemble in solution and find applications that range from thermoplastic elastomers to drug delivery systems, coatings, sealants, templates or membranes [107]. Gradient copolymers can be obtained by spontaneous copolymerization by ATRP [108], based on different reactivity ratios of comonomers or through continuous controlled feeding of one monomer. Gradient copolymers show very broad glass transition temperatures [109] and can be used as sound or vibration dampening materials [110]; they have high critical micelle concentrations and can be used as efficient surfactants for dispersed media and for polymer blends [111]. On the other hand, comonomer pairs with strongly different polarities, like a strong electron-accepting monomer and an electron-donating comonomer [112], have strong tendency to alternate and yield periodic/alternating copolymer, styrene-maleic anhydride and styrene-maleimides being classical examples [113]. Comonomers with a weak alternation like styrene/MMA with reactivity ratios ~0.5 form statistical copolymers but in the presence of complexing agents such as strong Lewis acids can also lead to alternating incorporation of the monomers [114].

Topology:

The use of a mono- or difunctional initiator leads to formation of linear polymers. The obtained mono- or difunctional macroinitiator can be used to form an AB diblock or ABA triblock copolymers, respectively. Multifunctional initiators can yield star [115] or graft polymers [116]. Branched polymers can also be obtained when a branching agent, like a divinyl monomer, is used [117]. Growth from polymer chains with several initiating sites leads to graft copolymers. This can be done by grafting-from, -through and -onto a polymer's backbone with multiple reactive sites. The majority of molecular brushes are prepared by the grafting-from procedure, and this is a particularly important technique that will be used in our project to build polymer brushes from a solid substrate, also known as surface-initiated ATRP (SI-ATRP) [118].

Functionalities:

Functional groups can be placed at the tail-end of the polymer chain when an initiator with the desired functionality or its precursor is used. The growing head (halide) of the polymer can be used to attach functional moieties via nucleophilic substitution [119, 120], click chemistry [121] or electrophilic addition [122]. Functional groups can also be incorporated into the polymer backbone by a direct polymerization of functional monomers [123-126] or by the post modification of the repeating units [127-131]. Their density and distribution can be designed by the type of copolymerization (block, statistical, gradient…) and/or reaction conditions (monomer feeding).

Applications:

The range of monomers polymerized by ATRP is ever expanding and many of these obtained polymers have been commercialized around the world [132]. They can be used for an endless list of applications, from lubricants, sealants and oil additives, to wetting agents, blend compatibilizers [133] pigment dispersants, surfactants and cosmetics. Oil resistant and recyclable polar thermoplastic elastomers were also prepared by bulk or emulsion ATRP [134].

ATRP was successfully used for "grafting-from" surfaces with controlled brushes thickness and grafting density [135]. Surface initiated ATRP can be used to tailor surface properties such as hydrophilicity/hydrophobicity, conductivity, biocompatibility, adhesion, adsorption, corrosion resistance, and friction. ATRP is used to synthesize antibacterial/antimicrobial surfaces [136] and nanoparticles [137]. ATRP-functionalized particles were used as the stationary phase for

chromatography columns for protein separation [138]. Biodegradable functional copolymers were used for drug [139] and gene delivery [140]. Various natural products were also successfully coupled to polymers prepared by ATRP [141].

Metal-complexing polymers like poly(4-vinylpyridine) were also prepared by ATRP [142] and poly(amidoxime) grafted polyethylene fibers were prepared via ATRP for uranium extracting from seawater [30], the latter being at the heart of the current thesis and will be later discussed in detail.

I.2.3. Supplemental activator and reducing agent (SARA) ATRP

Despite its enormous versatility, ATRP has several drawbacks that make it time and energy consuming, difficult to scale up and relatively expensive. Among these drawbacks, ATRP suffers from its oxygen sensitivity that leads to the unavoidable buildup of the higher oxidation state Cu^{II} and therefore hard degassing techniques like freeze-pump-thaw cycles are systematically used and the non-stable Cu^{I} has to be purified before each reaction to eliminate the oxidized fraction. Relatively high load of catalyst has to be used in order to compensate for the lost copper species during the reaction, increasing the cost of post-treatment to remove that excess catalyst. These drawbacks stand especially in the way of scaling up the reaction to industrial levels.

Several strategies have been proposed to make the reaction oxygen tolerant and minimize the copper load [86], where dissolved oxygen is removed from the system and accumulated Cu^{II} is reduced back to Cu^{I} using electric potential, photoreduction, or chemical reductant like conventional initiators, Sn^{II} species, ascorbic acid, hydrazine and zerovalent metals [143-151]. The process of continuously reducing the Cu^{II} is labeled under activator regenerated by electron transfer (ARGET) ATRP [148].

When considering the industrial viability of these different reducing agents, metallic copper is most interesting due to its low cost, compatibility with different polymerization systems and its simple removal especially when used in a heterogeneous form (wire, tube…), facilitating industrial scale employment. Metallic copper or Cu^{0}-mediated RDRP was investigated and two different reaction mechanisms were suggested (scheme 13). One proposed mechanism, supplemental activator and reducing agent atom transfer radical polymerization (SARA ATRP), has Cu^{I} as the major activator of alkyl halides, Cu^{0} acting as a supplemental activator and both by inner-sphere electron transfer (ISET). Another proposed mechanism called single electron transfer living radical

polymerization (SET-LRP) assumes that the Cu^{I} species do not activate alkyl halides, but undergo instantaneous disproportionation, and that the relatively rapid polymerization is due to a fast reaction between alkyl halides and Cu^{0} through an outer-sphere electron transfer (OSET).

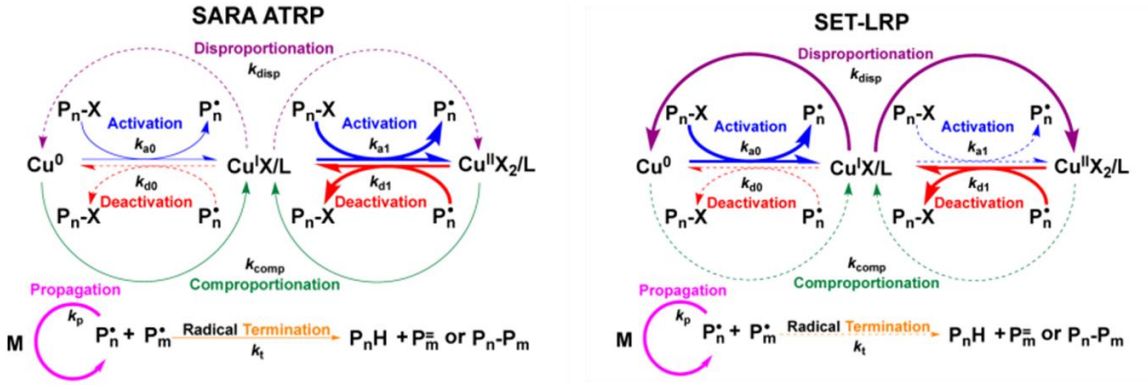

Scheme I-13. SARA ATRP and SET-LRP mechanisms. Line thickness reflects relative rates as in Ref [152]

Researchers have debated about the mechanism of copper-mediated RDRP in the presence of Cu^{0} [153-155]. A detailed study of the two mechanisms was conducted by the Matyjaszewski group [152, 156] where the kinetic experiments agreed more with SARA ATRP rather than SET-LRP. The SARA ATRP mechanism will be adopted in this thesis, though fully aware of the ongoing debate. SARA ATRP allows to use the stable Cu^{II} at the beginning of the reaction instead of the non-stable Cu^{I}. Cu^{0} and Cu^{II} can then comproportionate to generate the Cu^{I} activator in situ. As a results, the quantity of the copper catalyst is reduced by ~100 folds without the need for special precautions, a major advantage if the strategy is to be applied on industrial scale.

I.2.4. Surface-initiated CRP

To a certain extent, every type of CRP (ATRP, NMR, RAFT…) can be applied to graft polymer "brushes" on a surface by means of surface-initiated (SI)-CRP. Surface modification using polymer brushes has become a powerful tool to tailor the chemical and physical properties of interfaces [157-162].

Polymer brushes are thin polymer films where chains are attached by one end to an interface. These chains can adopt various conformations, "mushroom", "pancake" or a true "brush" conformation, depending on the density of anchoring sites, polymer's size (chain length) and the interaction between polymer chains and the surface. These conformations are described in scheme 14.

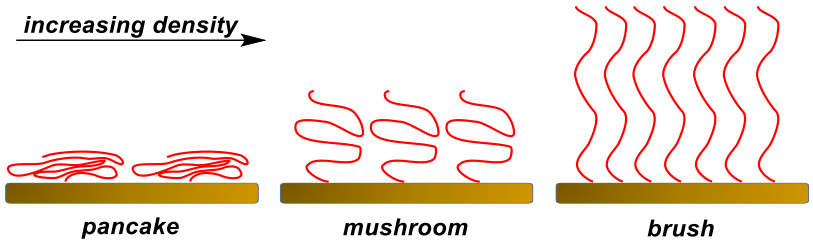

Scheme I-14. Conformations of surface-anchored polymers

Polymer brushes can be prepared mainly by "grafting-to" or "grafting-from" methods [163] as shown in scheme 15. In the "grafting-to" approach, a polymer is grafted to the surface through anchoring sites while in the "grafting-from" strategy, polymers are built from radical initiating sites present at the surface prior to polymerization. Grafting-from strategy is often preferred as it allows a higher grafting density and film thickness while having a simple experimental setup, mild reaction conditions, tolerance toward a variety of functional groups and compatibility with both aqueous and organic media [162].

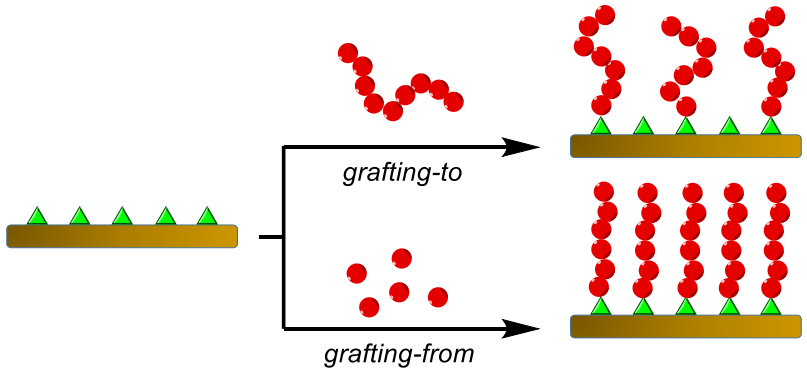

Scheme I-15. Building polymer brushes by "grafting-to" or "grafting-from" strategies

Surface-Initiated SARA ATRP (SI-SARA ATRP) is a fast method for the synthesis of polymer brushes with ultrahigh molecular weight, low dispersity, and high chain-end fidelity. It is also attractive thanks to its high tolerance to air and impurities, mild conditions, simple experimental setup and robustness [162].

It should be noted that while SI-CRP is already extensively used to produce polymer brushes for many applications, it still faces several challenges. Direct characterization of polymer brush molecular weight and dispersity, for example, is a difficult task. Consequently, calculating important parameters like the grafting density is not straightforward. The majority of published papers relies on characterization of free polymers produced via sacrificial initiators during polymer brush growth. This approach lacks accuracy because it doesn't take into account important

variables like substrate curvature and confinement [164, 165] on SI-CRP kinetics. Several studies suggest significant differences in the molecular weight and dispersity between bulk and surface-initiated polymers [166, 167] and indicate that the rate of termination of anchored chains depends on grafting density [168]. Local viscosity at the interface, known as the Trommsdorff gel effect [169], was found to enhance polymerization rates. Surface charge also appears to accelerate/decelerate propagation by influencing the concentration of the metal catalysts near the interface [170]. The type of initiator, the ligand and the solvent can also affect the rate of polymerization on the surface versus chains in solution. In the case of Cu^0-mediated CRP, the disproportionation/comproportionation equilibrium between copper species can also play a critical role in the brush growth kinetics. Overall, it seems that the chain length and distribution of polymer brushes rarely correspond to that of free polymers, however, it is difficult to draw a general conclusion because every case has its own set of variables that should be considered as a whole.

From silicon [171], silica [172], metals [173-175], metal oxides [176-178], carbon nanomaterials [179, 180] to polymer surfaces such PET [181], Nylon [182], PTFE [183], PP [184], PVDF [185] and many others, SI-CRP allows to grow polymer brushes from a wide variety of substrates [186]. These surfaces also include a variety of biobased substrates like cellulose in different forms [187-189], chitin nanofibers [190] and other natural fibers [191, 192], proteins [193-196] and microorganisms [197, 198], in addition to mesoporous materials [165, 199-202], graphene and related substrates [203-211]. It should be noted that even if one SI-CRP reaction can be applied on so many substrates, each surface needs to be carefully treated prior to polymerization in order to graft the halogenated initiator, in accordance with each surface's chemistry [162].

I.3. Conclusion and perspectives

In the following chapters, free and surface-initiated CRP, particularly SARA ATRP, will be used to synthesize innovative chelating materials. Different strategies will be first evaluated using a model monomer (4-vinylpyridine), to be then applied on a highly chelating dipicolinic acid-based monomer. Polymer brushes will be built from poly(ethylene terephthalate) (PET) surfaces, both films and fibers, silica films and microparticles and later from poly(vinyl chloride) (PVC)-based substrates. These new materials will be characterized, their interaction with rare earths and uranium species will be examined and their potential applications, especially in the nuclear industry, will be evaluated.

I.4. References

1. *Comparison of Lifecycle Greenhouse Gas Emissions of Various Electricity Generation Sources, World Nuclear Association.*
2. Davies, R., et al., *Extraction of uranium from sea water.* Nature, 1964. **203**(4950): p. 1110-1115.
3. *Uranium 2016: Resources, Production and Demand, NEA No. 7301, Organisation for Economic Co-operation and Development/Nuclear Energy Agency, International Atomic Energy Agency.*
4. *Energy, Electricity and Nuclear Power Estimates for the Period up to 2050.* IAEA-RDS-1/36, 2016.
5. Sholl, D.S. and R.P. Lively, *Seven chemical separations: to change the world: purifying mixtures without using heat would lower global energy use, emissions and pollution--and open up new routes to resources.* Nature, 2016. **532**(7600): p. 435-438.
6. Saxena, A., *Experiments for recovery of uranium from seawater by harnessing tidal energy.* BARC Newsl, 2004. **249**: p. 226-232.
7. Kim, J., et al., *Recovery of uranium from seawater: a review of current status and future research needs.* Separation Science and Technology, 2013. **48**(3): p. 367-387.
8. Kabay, N., *Preparation of amidoxime-fiber adsorbents based on poly (methacrylonitrile) for recovery of uranium from seawater.* Separation science and technology, 1994. **29**(3): p. 375-384.
9. Kanno, M., *Present status of study on extraction of uranium from sea water.* Journal of Nuclear Science and Technology, 1984. **21**(1): p. 1-9.
10. Van Reis, R. and A. Zydney, *Membrane separations in biotechnology.* Current Opinion in Biotechnology, 2001. **12**(2): p. 208-211.
11. Fan, F., et al., *Sorption of uranium (VI) from aqueous solution onto magnesium silicate hollow spheres.* Journal of Radioanalytical and Nuclear Chemistry, 2011. **289**(2): p. 367-374.
12. Brennecka, G.A., et al., *Uranium isotope fractionation during adsorption to Mn-oxyhydroxides.* Environmental science & technology, 2011. **45**(4): p. 1370-1375.
13. Sadeghi, S. and E. Sheikhzadeh, *Solid phase extraction using silica gel modified with murexide for preconcentration of uranium (VI) ions from water samples.* Journal of Hazardous Materials, 2009. **163**(2-3): p. 861-868.
14. Lefevre, G., S. Noinville, and M. Fédoroff, *Study of uranyl sorption onto hematite by in situ attenuated total reflection–infrared spectroscopy.* Journal of colloid and interface science, 2006. **296**(2): p. 608-613.
15. Lieser, K. and B. Thybusch, *Sorption of uranyl ions on hydrous titanium dioxideSorption von Uranylionen an wasserhaltigem Titandioxid.* Fresenius' Zeitschrift für analytische Chemie, 1988. **332**(4): p. 351-357.
16. Hori, T., M. Yamawaki, and M. Kanno, *Uranium adsorption properties of hydrous titanium oxides in seawater.* Journal of Nuclear Science and Technology, 1987. **24**(5): p. 377-384.
17. Yamashita, H., et al., *The collection of uranium from sea water with hydrous metal oxide. II. The mechanism of uranium adsorption on hydrous titanium (IV) oxide.* Bulletin of the Chemical Society of Japan, 1980. **53**(1): p. 1-5.
18. Yamashita, H., et al., *The Collection of Uranium from Sea Water with Hydrous Metal Oxide. IV. Physical Properties and Uranium Adsorption of Hydrous Titanium (IV) Oxide.* Bulletin of the Chemical Society of Japan, 1980. **53**(11): p. 3050-3053.
19. Yamashita, H., et al., *The collection of uranium from sea water with hydrous metal oxide. III. The effects of diverse ions in sea water on uranium adsorption by hydrous titanium (IV) oxide.* Bulletin of the Chemical Society of Japan, 1980. **53**(5): p. 1331-1334.
20. Comarmond, M.J., et al., *Uranium sorption on various forms of titanium dioxide–influence of surface area, surface charge, and impurities.* Environmental science & technology, 2011. **45**(13): p. 5536-5542.
21. Das, N., *Remediation of radionuclide pollutants through biosorption–an overview.* CLEAN–Soil, Air, Water, 2012. **40**(1): p. 16-23.
22. Kim, J., et al., *Binding of uranyl ion by a DNA aptamer attached to a solid support.* Bioorganic & medicinal chemistry letters, 2011. **21**(13): p. 4020-4022.
23. Chauhan, K. and G.S. Chauhan, *Separation of uranyl ions on starch-based functional hydrogels: mechanism and kinetics.* Separation Science and Technology, 2010. **46**(1): p. 172-178.
24. Acharya, C., D. Joseph, and S. Apte, *Uranium sequestration by a marine cyanobacterium, Synechococcus elongatus strain BDU/75042.* Bioresource technology, 2009. **100**(7): p. 2176-2181.

25. Oshita, K., et al., *Synthesis of chitosan resin possessing a phenylarsonic acid moiety for collection/concentration of uranium and its determination by ICP-AES.* Analytical and bioanalytical chemistry, 2008. **390**(7): p. 1927-1932.
26. Tsezos, M. and S. Noh, *Extraction of uranium from sea water using biological origin adsorbents.* The Canadian Journal of Chemical Engineering, 1984. **62**(4): p. 559-561.
27. Sugasaka, K., et al., *Recovery of uranium from seawater.* Separation Science and Technology, 1981. **16**(9): p. 971-985.
28. Zhang, A., T. Asakura, and G. Uchiyama, *The adsorption mechanism of uranium (VI) from seawater on a macroporous fibrous polymeric adsorbent containing amidoxime chelating functional group.* Reactive and Functional Polymers, 2003. **57**(1): p. 67-76.
29. Seko, N., et al., *Aquaculture of uranium in seawater by a fabric-adsorbent submerged system.* Nuclear Technology, 2003. **144**(2): p. 274-278.
30. Saito, T., et al., *Uranium recovery from seawater: development of fiber adsorbents prepared via atom-transfer radical polymerization.* Journal of Materials Chemistry A, 2014. **2**(35): p. 14674-14681.
31. Saito, K., et al., *Recovery of uranium from seawater using amidoxime hollow fibers.* AIChE journal, 1988. **34**(3): p. 411-416.
32. Kawai, T., et al., *Comparison of amidoxime adsorbents prepared by cografting methacrylic acid and 2-hydroxyethyl methacrylate with acrylonitrile onto polyethylene.* Industrial & engineering chemistry research, 2000. **39**(8): p. 2910-2915.
33. Kawai, T., et al., *Preparation of hydrophilic amidoxime fibers by cografting acrylonitrile and methacrylic acid from an optimized monomer composition.* Radiation Physics and Chemistry, 2000. **59**(4): p. 405-411.
34. Kim, J., et al., *Uptake of uranium from seawater by amidoxime-based polymeric adsorbent: field experiments, modeling, and updated economic assessment.* Industrial & Engineering Chemistry Research, 2014. **53**(14): p. 6076-6083.
35. Wang, C.-Z., et al., *Complexation of vanadium with amidoxime and carboxyl groups: uncovering the competitive role of vanadium in uranium extraction from seawater.* Radiochimica Acta, 2017. **105**(7): p. 541-553.
36. Suzuki, T., et al., *Fractional elution and determination of uranium and vanadium adsorbed on amidoxime fiber from seawater.* Analytical sciences, 2000. **16**(4): p. 429-432.
37. Martell, A.E. and R.M. Smith, *Critical Stability Constant Database, 46.* National Institute of Science and Technology (NIST), Gaithersburg, MD, USA, 2003.
38. Brown, S., et al., *Uranium adsorbent fibers prepared by ATRP from PVC-co-CPVC fiber.* Ind. Eng. Chem. Res, 2015.
39. Nash, K.L. and M. Nilsson, *Introduction to the reprocessing and recycling of spent nuclear fuels*, in *Reprocessing and Recycling of Spent Nuclear Fuel*. 2015, Elsevier. p. 3-25.
40. Nash, K.L., et al., *Actinide separation science and technology*, in *The chemistry of the actinide and transactinide elements*. 2008, Springer. p. 2622-2798.
41. Thompson, M., *Demonstration of the UREX solvent extraction process with Dresden reactor fuel solution*. 2002, Savannah River Site (United States). Funding organisation: US Department of Energy (United States).
42. Drain, F., et al. *COEX-process: cross-breeding between innovation and industrial experience*. 2008. WM Symposia, 1628 E. Southern Avenue, Suite 9-332, Tempe, AZ 85282 (United States).
43. Baron, P., et al., *Separation of the minor actinides: the DIAMEX-SANES concept.* 2001.
44. Montuir, M., et al., *Sensitivity of americium and curium splitting flowsheet and running procedure.* Procedia Chemistry, 2012. **7**: p. 275-281.
45. Chartier, D., L. Donnet, and J. Adnet, *Electrochemical oxidation of Am (III) with lacunary heteropolyanions and silver nitrate.* Radiochimica Acta, 1998. **83**(3): p. 129-134.
46. Aneheim, E., et al., *Development of a novel GANEX process*, in *Nuclear Energy and the Environment*. 2010, ACS Publications. p. 119-130.
47. Kolarik, Z., *Complexation and separation of lanthanides (III) and actinides (III) by heterocyclic N-donors in solutions.* Chem. Rev, 2008. **108**(10): p. 4208-4252.
48. Musikas, C., *Actinide-lanthanide group separation using sulfur and nitrogen donor extractants*. 1984, CEA Centre d'Etudes Nucleaires de Fontenay-aux-Roses.
49. Nogami, M., et al., *Ion-exchange selectivity of tertiary pyridine-type anion-exchange resin for treatment of spent nuclear fuels.* Nuclear technology, 1996. **115**(3): p. 293-297.
50. Wei, Y., et al., *The application of an advanced ion exchange process to reprocessing spent nuclear fuels,(I).* Journal of nuclear science and technology, 1998. **35**(5): p. 357-364.

51. Wei, Y.Z., et al. *Adsorption materials development for the separation of actinides and specific fission products from high level waste*. in *Advances in Science and Technology*. 2014. Trans Tech Publ.
52. Peper, S.M., et al., *A Green Approach to SNF Reprocessing: Are Common Household Reagents the Answer?* 2008, Pacific Northwest National Laboratory (PNNL), Richland, WA (US).
53. Clarens, F., et al., *The oxidative dissolution of unirradiated UO2 by hydrogen peroxide as a function of pH.* Journal of Nuclear Materials, 2005. **345**(2-3): p. 225-231.
54. Fattal, E., N. Tsapis, and G. Phan, *Novel drug delivery systems for actinides (uranium and plutonium) decontamination agents.* Advanced drug delivery reviews, 2015. **90**: p. 40-54.
55. Bhattacharyya, M., et al., *Guidebook for the treatment of accidental internal radionuclide contamination of workers.* Radiation Protection Dosimetry, 1992. **41**(1): p. 1-49.
56. Butler, D., *Radioactivity spreads in Japan*. 2011, Nature Publishing Group.
57. Sumanović-Glamuzina, D., et al., *Incidence of major congenital malformations in a region of Bosnia and Herzegovina allegedly polluted with depleted uranium.* Croatian medical journal, 2003. **44**(5): p. 579-584.
58. Busby, C., M. Hamdan, and E. Ariabi, *Cancer, infant mortality and birth sex-ratio in Fallujah, Iraq 2005–2009.* International journal of environmental research and public health, 2010. **7**(7): p. 2828-2837.
59. Alaani, S., et al., *Four polygamous families with congenital birth defects from Fallujah, Iraq.* International journal of environmental research and public health, 2010. **8**(1): p. 89-96.
60. Lawrence, G.D., K.S. Patel, and A. Nusbaum, *Uranium toxicity and chelation therapy.* Pure and Applied Chemistry, 2014. **86**(7): p. 1105-1110.
61. Hare, D., et al., *Elemental bio-imaging of thorium, uranium, and plutonium in tissues from occupationally exposed former nuclear workers.* Analytical chemistry, 2010. **82**(8): p. 3176-3182.
62. Figgs, L.W., *Lung cancer mortality among uranium gaseous diffusion plant workers: a cohort study 1952–2004.* The international journal of occupational and environmental medicine, 2013. **4**(3 July): p. 275-128-40.
63. Arzuaga, X., et al., *Renal effects of exposure to natural and depleted uranium: a review of the epidemiologic and experimental data.* Journal of Toxicology and Environmental Health, Part B, 2010. **13**(7-8): p. 527-545.
64. Wrenn, M., et al., *Metabolism of ingested uranium and radium*. 1983, Utah Univ., Salt Lake City (USA). Radiobiology Div.; Lawrence Berkeley Lab., CA (USA); Utah Dept. of Health, Salt Lake City (USA). Div. of Environmental Health Services; Instituto de Radioprotecao e Dosimetria, Rio de Janeiro (Brazil); Argonne National Lab., IL (USA); Kerr-McGee Corp., Oklahoma City, OK (USA). Environment and Health Management Div.
65. Arruda-Neto, J., et al., *Long-term accumulation of uranium in bones of Wistar rats as a function of intake dosages.* Radiation protection dosimetry, 2004. **112**(3): p. 385-393.
66. Priest, N., et al., *Autoradiographic studies of the distribution of radium-226 in rat bone: Their implications for human radiation dosimetry and toxicity.* Human toxicology, 1983. **2**(3): p. 479-496.
67. Ubios, A., M. Marzorati, and R. Cabrini, *Skin alterations induced by long-term exposure to uranium and their effect on permeability.* Health physics, 1997. **72**(5): p. 713-715.
68. Gazin, V., et al., *Uranium induces TNFα secretion and MAPK activation in a rat alveolar macrophage cell line.* Toxicology and applied pharmacology, 2004. **194**(1): p. 49-59.
69. Wan, B., et al., *In vitro immune toxicity of depleted uranium: effects on murine macrophages, CD4+ T cells, and gene expression profiles.* Environmental health perspectives, 2006. **114**(1): p. 85.
70. Lestaevel, P., et al., *The brain is a target organ after acute exposure to depleted uranium.* Toxicology, 2005. **212**(2-3): p. 219-226.
71. Li, J. and Y. Zhang, *Remediation technology for the uranium contaminated environment: a review.* Procedia Environmental Sciences, 2012. **13**: p. 1609-1615.
72. Belli, K.M., et al., *Effects of aqueous uranyl speciation on the kinetics of microbial uranium reduction.* Geochimica et Cosmochimica Acta, 2015. **157**: p. 109-124.
73. Ohmachi, Y., et al., *Sodium bicarbonate protects uranium-induced acute nephrotoxicity through uranium-decorporation by urinary alkalinization in rats.* Journal of toxicologic pathology, 2015. **28**(2): p. 65-71.
74. Dagirmanjian, R., E.A. Maynard, and H.C. Hodge, *THE EFFECTS OF CALCIUM DISODIUM ETHYLENEDIAMINE TETRAACETATE ON URANIUM POISONING IN RATS.* Journal of Pharmacology and Experimental Therapeutics, 1956. **117**(1): p. 20-28.
75. Šömen Joksić, A. and S.A. Katz, *Chelation therapy for treatment of systemic intoxication with uranium: A review.* Journal of Environmental Science and Health, Part A, 2015. **50**(14): p. 1479-1488.
76. Ortega, A., et al., *Treatment of Experimental Acute Uranium Poisoning by Chelating Agents.* Pharmacology & Toxicology, 1989. **64**(3): p. 247-251.

77. Celestine, M.J., et al., *Interesting properties of p-, d-, and f-block elements when coordinated with dipicolinic acid and its derivatives as ligands: their use as inorganic pharmaceuticals.* Reviews in Inorganic Chemistry, 2015. **35**(2): p. 57-67.
78. Matyjaszewski, K., *Atom transfer radical polymerization (ATRP): current status and future perspectives.* Macromolecules, 2012. **45**(10): p. 4015-4039.
79. Matyjaszewski, K. and T.P. Davis, *Handbook of radical polymerization*. 2003: John Wiley & Sons.
80. Goto, A. and T. Fukuda, *Kinetics of living radical polymerization.* Progress in Polymer Science, 2004. **29**(4): p. 329-385.
81. Otsu, T., M. Yoshida, and T. Tazaki, *A model for living radical polymerization.* Macromolecular Rapid Communications, 1982. **3**(2): p. 133-140.
82. Kato, M., et al., *Polymerization of methyl methacrylate with the carbon tetrachloride/dichlorotris-(triphenylphosphine) ruthenium (II)/methylaluminum bis (2, 6-di-tert-butylphenoxide) initiating system: possibility of living radical polymerization.* Macromolecules, 1995. **28**(5): p. 1721-1723.
83. Wang, J.-S. and K. Matyjaszewski, *Controlled/" living" radical polymerization. Atom transfer radical polymerization in the presence of transition-metal complexes.* Journal of the American Chemical Society, 1995. **117**(20): p. 5614-5615.
84. Braunecker, W.A. and K. Matyjaszewski, *Controlled/living radical polymerization: Features, developments, and perspectives.* Progress in Polymer Science, 2007. **32**(1): p. 93-146.
85. Matyjaszewski, K. and N.V. Tsarevsky, *Macromolecular engineering by atom transfer radical polymerization.* Journal of the American Chemical Society, 2014. **136**(18): p. 6513-6533.
86. Matyjaszewski, K. and J. Xia, *Atom transfer radical polymerization.* Chemical reviews, 2001. **101**(9): p. 2921-2990.
87. Chiefari, J., et al., *Living free-radical polymerization by reversible addition− fragmentation chain transfer: the RAFT process.* Macromolecules, 1998. **31**(16): p. 5559-5562.
88. Hawker, C.J., A.W. Bosman, and E. Harth, *New polymer synthesis by nitroxide mediated living radical polymerizations.* Chemical reviews, 2001. **101**(12): p. 3661-3688.
89. Fischer, H., *The persistent radical effect in "living" radical polymerization.* Macromolecules, 1997. **30**(19): p. 5666-5672.
90. Patten, T.E. and K. Matyjaszewski, *Copper (I)-catalyzed atom transfer radical polymerization.* Accounts of chemical research, 1999. **32**(10): p. 895-903.
91. Kotani, Y., M. Kamigaito, and M. Sawamoto, *Re (V)-Mediated Living Radical Polymerization of Styrene: ReO2I (PPh3) 2/R− I Initiating Systems.* Macromolecules, 1999. **32**(8): p. 2420-2424.
92. Singha, N.K. and B. Klumperman, *Atom-transfer radical polymerization of methyl methacrylate (MMA) using CuSCN as the catalyst.* Macromolecular rapid communications, 2000. **21**(16): p. 1116-1120.
93. Tang, W. and K. Matyjaszewski, *Effects of initiator structure on activation rate constants in ATRP*. Macromolecules, 2007. **40**(6): p. 1858-1863.
94. Brandts, J.A., et al., *Controlled radical polymerization of styrene in the presence of lithium molybdate (V) complexes and benzylic halides.* Journal of organometallic chemistry, 1999. **584**(2): p. 246-253.
95. Champouret, Y., et al., *Controlled radical polymerization of vinyl acetate with cyclopentadienyl chromium β-diketiminate complexes: ATRP vs OMRP.* Organometallics, 2010. **29**(14): p. 3125-3132.
96. Ando, T., M. Kamigaito, and M. Sawamoto, *Iron (II) chloride complex for living radical polymerization of methyl methacrylate.* Macromolecules, 1997. **30**(16): p. 4507-4510.
97. Percec, V., et al., *Metal-catalyzed "living" radical polymerization of styrene initiated with arenesulfonyl chlorides. From heterogeneous to homogeneous catalysis.* Macromolecules, 1996. **29**(10): p. 3665-3668.
98. Granel, C., et al., *Controlled radical polymerization of methacrylic monomers in the presence of a bis (ortho-chelated) arylnickel (II) complex and different activated alkyl halides.* Macromolecules, 1996. **29**(27): p. 8576-8582.
99. Lecomte, P., et al., *Controlled radical polymerization of methyl methacrylate in the presence of palladium acetate, triphenylphosphine, and carbon tetrachloride.* Macromolecules, 1997. **30**(24): p. 7631-7633.
100. Debuigne, A., et al., *Synthesis of poly (vinyl acetate) and poly (vinyl alcohol) containing block copolymers by combination of cobalt-mediated radical polymerization and ATRP.* Macromolecules, 2005. **38**(23): p. 9488-9496.
101. Braunecker, W.A., Y. Itami, and K. Matyjaszewski, *Osmium-mediated radical polymerization.* Macromolecules, 2005. **38**(23): p. 9402-9404.

102. Asandei, A.D., et al., *Titanium-mediated living radical styrene polymerizations. VI. Cp2TiCl-catalyzed initiation by epoxide radical ring opening: Effect of the reducing agents, temperature, and titanium/epoxide and titanium/zinc ratios.* Journal of Polymer Science Part A: Polymer Chemistry, 2006. **44**(7): p. 2156-2165.
103. Rorabacher, D.B., *Electron transfer by copper centers.* Chemical reviews, 2004. **104**(2): p. 651-698.
104. Tang, W. and K. Matyjaszewski, *Effect of ligand structure on activation rate constants in ATRP*. Macromolecules, 2006. **39**(15): p. 4953-4959.
105. Matyjaszewski, K., et al., *Observation and analysis of a slow termination process in the atom transfer radical polymerization of styrene.* Tetrahedron, 1997. **53**(45): p. 15321-15329.
106. Matyjaszewski, K., *Comparison and classification of controlled/living radical polymerizations*. 2000, ACS Publications.
107. Bates, F.S. and G. Fredrickson, *Block copolymers-designer soft materials.* Physics today, 2000.
108. Matyjaszewski, K., et al., *Gradient copolymers by atom transfer radical copolymerization.* Journal of Physical Organic Chemistry, 2000. **13**(12): p. 775-786.
109. Kim, J., et al., *Uniquely broad glass transition temperatures of gradient copolymers relative to random and block copolymers containing repulsive comonomers.* Macromolecules, 2006. **39**(18): p. 6152-6160.
110. Mok, M.M., J. Kim, and J.M. Torkelson, *Gradient copolymers with broad glass transition temperature regions: design of purely interphase compositions for damping applications.* Journal of Polymer Science Part B: Polymer Physics, 2008. **46**(1): p. 48-58.
111. Shull, K.R., *Interfacial activity of gradient copolymers.* Macromolecules, 2002. **35**(22): p. 8631-8639.
112. Zamfir, M. and J.-F. Lutz, *Ultra-precise insertion of functional monomers in chain-growth polymerizations.* Nature Communications, 2012. **3**: p. 1138.
113. Chen, G.-Q., et al., *Synthesis of alternating copolymers of N-substituted maleimides with styrene via atom transfer radical polymerization.* Macromolecules, 2000. **33**(2): p. 232-234.
114. Denizli, B.K., et al., *Properties of well-defined alternating and random copolymers of methacrylates and styrene prepared by controlled/living radical polymerization.* Journal of Polymer Science Part A: Polymer Chemistry, 2005. **43**(15): p. 3440-3446.
115. Gao, H. and K. Matyjaszewski, *Synthesis of star polymers by a new "core-first" method: sequential polymerization of cross-linker and monomer.* Macromolecules, 2008. **41**(4): p. 1118-1125.
116. Hester, J., et al., *ATRP of amphiphilic graft copolymers based on PVDF and their use as membrane additives.* Macromolecules, 2002. **35**(20): p. 7652-7661.
117. Li, Y. and S.P. Armes, *Synthesis and chemical degradation of branched vinyl polymers prepared via ATRP: use of a cleavable disulfide-based branching agent.* Macromolecules, 2005. **38**(20): p. 8155-8162.
118. Edmondson, S., V.L. Osborne, and W.T. Huck, *Polymer brushes via surface-initiated polymerizations.* Chemical society reviews, 2004. **33**(1): p. 14-22.
119. Matyjaszewski, K., Y. Nakagawa, and S.G. Gaynor, *Synthesis of well-defined azido and amino end-functionalized polystyrene by atom transfer radical polymerization.* Macromolecular rapid communications, 1997. **18**(12): p. 1057-1066.
120. Lepoittevin, B., et al., *Easy access to amphiphilic glycosylated-functionalized polystyrenes.* Carbohydrate polymers, 2011. **83**(3): p. 1174-1179.
121. Golas, P.L. and K. Matyjaszewski, *Marrying click chemistry with polymerization: expanding the scope of polymeric materials.* Chemical Society Reviews, 2010. **39**(4): p. 1338-1354.
122. Coessens, V., T. Pintauer, and K. Matyjaszewski, *Functional polymers by atom transfer radical polymerization.* Progress in polymer science, 2001. **26**(3): p. 337-377.
123. Li, Y., et al., *Direct synthesis of well-defined quaternized homopolymers and diblock copolymers via ATRP in protic media.* Macromolecules, 2003. **36**(22): p. 8268-8275.
124. Lobb, E.J., et al., *Facile synthesis of well-defined, biocompatible phosphorylcholine-based methacrylate copolymers via atom transfer radical polymerization at 20 C.* Journal of the American Chemical Society, 2001. **123**(32): p. 7913-7914.
125. Yao, K. and C. Tang, *Controlled polymerization of next-generation renewable monomers and beyond.* Macromolecules, 2013. **46**(5): p. 1689-1712.
126. Mosnácek, J. and K. Matyjaszewski, *Atom transfer radical polymerization of tulipalin A: a naturally renewable monomer.* Macromolecules, 2008. **41**(15): p. 5509-5511.
127. Tsarevsky, N.V., S.A. Bencherif, and K. Matyjaszewski, *Graft copolymers by a combination of ATRP and two different consecutive click reactions.* Macromolecules, 2007. **40**(13): p. 4439-4445.
128. Hoyle, C.E., T.Y. Lee, and T. Roper, *Thiol–enes: Chemistry of the past with promise for the future.* Journal of Polymer Science Part A: Polymer Chemistry, 2004. **42**(21): p. 5301-5338.

129. Kade, M.J., D.J. Burke, and C.J. Hawker, *The power of thiol-ene chemistry.* Journal of Polymer Science Part A: Polymer Chemistry, 2010. **48**(4): p. 743-750.
130. Iha, R.K., et al., *Applications of orthogonal "click" chemistries in the synthesis of functional soft materials.* Chemical reviews, 2009. **109**(11): p. 5620-5686.
131. Binder, W.H. and R. Sachsenhofer, *'Click'chemistry in polymer and materials science.* Macromolecular Rapid Communications, 2007. **28**(1): p. 15-54.
132. Matyjaszewski, K. and J. Spanswick, *Controlled/living radical polymerization.* Materials Today, 2005. **8**(3): p. 26-33.
133. Koulouri, E., J. Kallitsis, and G. Hadziioannou, *Terminal anhydride functionalized polystyrene by atom transfer radical polymerization used for the compatibilization of nylon 6/PS blends.* Macromolecules, 1999. **32**(19): p. 6242-6248.
134. Min, K., H. Gao, and K. Matyjaszewski, *Development of an ab initio emulsion atom transfer radical polymerization: from microemulsion to emulsion.* Journal of the American Chemical Society, 2006. **128**(32): p. 10521-10526.
135. Matyjaszewski, K., et al., *Grafting from surfaces for "everyone": ARGET ATRP in the presence of air.* Langmuir, 2007. **23**(8): p. 4528-4531.
136. Huang, J., et al., *Antibacterial polypropylene via surface-initiated atom transfer radical polymerization.* Biomacromolecules, 2007. **8**(5): p. 1396-1399.
137. Dong, H., et al., *Recyclable antibacterial magnetic nanoparticles grafted with quaternized poly (2-(dimethylamino) ethyl methacrylate) brushes.* Biomacromolecules, 2011. **12**(4): p. 1305-1311.
138. McCarthy, P., et al., *Nanoengineered analytical immobilized metal affinity chromatography stationary phase by atom transfer radical polymerization: Separation of synthetic prion peptides.* Analytical biochemistry, 2007. **366**(1): p. 1-8.
139. Siegwart, D.J., J.K. Oh, and K. Matyjaszewski, *ATRP in the design of functional materials for biomedical applications.* Progress in polymer science, 2012. **37**(1): p. 18-37.
140. Averick, S.E., et al., *Preparation of cationic nanogels for nucleic acid delivery.* Biomacromolecules, 2012. **13**(11): p. 3445-3449.
141. Lutz, J.-F. and H.G. Börner, *Modern trends in polymer bioconjugates design.* Progress in Polymer Science, 2008. **33**(1): p. 1-39.
142. Xia, J., X. Zhang, and K. Matyjaszewski, *Atom transfer radical polymerization of 4-vinylpyridine.* Macromolecules, 1999. **32**(10): p. 3531-3533.
143. Matyjaszewski, K., et al., *Diminishing catalyst concentration in atom transfer radical polymerization with reducing agents.* Proceedings of the National Academy of Sciences, 2006. **103**(42): p. 15309-15314.
144. Magenau, A.J., et al., *Electrochemically mediated atom transfer radical polymerization.* Science, 2011. **332**(6025): p. 81-84.
145. Tasdelen, M.A., M. Uygun, and Y. Yagci, *Photoinduced controlled radical polymerization in methanol*. Macromolecular Chemistry and Physics, 2010. **211**(21): p. 2271-2275.
146. Konkolewicz, D., et al., *Visible light and sunlight photoinduced ATRP with ppm of Cu catalyst.* ACS Macro Letters, 2012. **1**(10): p. 1219-1223.
147. Jakubowski, W., K. Min, and K. Matyjaszewski, *Activators regenerated by electron transfer for atom transfer radical polymerization of styrene.* Macromolecules, 2006. **39**(1): p. 39-45.
148. Jakubowski, W. and K. Matyjaszewski, *Activators Regenerated by Electron Transfer for Atom-Transfer Radical Polymerization of (Meth) acrylates and Related Block Copolymers.* Angewandte Chemie, 2006. **118**(27): p. 4594-4598.
149. Min, K., H. Gao, and K. Matyjaszewski, *Use of ascorbic acid as reducing agent for synthesis of well-defined polymers by ARGET ATRP.* Macromolecules, 2007. **40**(6): p. 1789-1791.
150. Zhang, Y., Y. Wang, and K. Matyjaszewski, *ATRP of methyl acrylate with metallic zinc, magnesium, and iron as reducing agents and supplemental activators.* Macromolecules, 2011. **44**(4): p. 683-685.
151. Matyjaszewski, K., et al., *Zerovalent metals in controlled/"living" radical polymerization.* Macromolecules, 1997. **30**(23): p. 7348-7350.
152. Konkolewicz, D., et al., *Aqueous RDRP in the presence of Cu0: the exceptional activity of CuI confirms the SARA ATRP mechanism.* Macromolecules, 2014. **47**(2): p. 560-570.
153. Percec, V., et al., *Ultrafast synthesis of ultrahigh molar mass polymers by metal-catalyzed living radical polymerization of acrylates, methacrylates, and vinyl chloride mediated by SET at 25 C.* Journal of the American Chemical Society, 2006. **128**(43): p. 14156-14165.

154. Matyjaszewski, K., et al., *Role of Cu0 in controlled/"living" radical polymerization.* Macromolecules, 2007. **40**(22): p. 7795-7806.
155. Lligadas, G., et al., *Solvent choice differentiates SET-LRP and Cu-mediated radical polymerization with non-first-order kinetics.* Macromolecules, 2008. **41**(22): p. 8360-8364.
156. Konkolewicz, D., et al., *Reversible-deactivation radical polymerization in the presence of metallic copper. A critical assessment of the SARA ATRP and SET-LRP mechanisms.* Macromolecules, 2013. **46**(22): p. 8749-8772.
157. Badri, A., M.R. Whittaker, and P.B. Zetterlund, *Modification of graphene/graphene oxide with polymer brushes using controlled/living radical polymerization.* Journal of Polymer Science Part A: Polymer Chemistry, 2012. **50**(15): p. 2981-2992.
158. Bünsow, J., T.S. Kelby, and W.T. Huck, *Polymer brushes: Routes toward mechanosensitive surfaces.* Accounts of chemical research, 2009. **43**(3): p. 466-474.
159. Krishnamoorthy, M., et al., *Surface-initiated polymer brushes in the biomedical field: applications in membrane science, biosensing, cell culture, regenerative medicine and antibacterial coatings.* Chemical reviews, 2014. **114**(21): p. 10976-11026.
160. Hui, C.M., et al., *Surface-initiated polymerization as an enabling tool for multifunctional (nano-) engineered hybrid materials.* Chemistry of Materials, 2013. **26**(1): p. 745-762.
161. Peng, S. and B. Bhushan, *Smart polymer brushes and their emerging applications.* Rsc Advances, 2012. **2**(23): p. 8557-8578.
162. Zoppe, J.O., et al., *Surface-initiated controlled radical polymerization: state-of-the-art, opportunities, and challenges in surface and interface engineering with polymer brushes.* Chemical reviews, 2017. **117**(3): p. 1105-1318.
163. Barbey, R., et al., *Polymer brushes via surface-initiated controlled radical polymerization: synthesis, characterization, properties, and applications.* Chemical reviews, 2009. **109**(11): p. 5437-5527.
164. Liu, H., et al., *Influence of Grafting Surface Curvature on Chain Polydispersity and Molecular Weight in Concave Surface-Initiated Polymerization.* ACS Macro Letters, 2012. **1**(11): p. 1249-1253.
165. Pasetto, P., et al., *Mechanistic Insight into Surface-Initiated Polymerization of Methyl Methacrylate and Styrene via ATRP from Ordered Mesoporous Silica Particles.* Macromolecules, 2009. **42**(16): p. 5983-5995.
166. Genzer, J., *In Silico Polymerization: Computer Simulation of Controlled Radical Polymerization in Bulk and on Flat Surfaces.* Macromolecules, 2006. **39**(20): p. 7157-7169.
167. Turgman-Cohen, S. and J. Genzer, *Simultaneous Bulk- and Surface-Initiated Controlled Radical Polymerization from Planar Substrates.* Journal of the American Chemical Society, 2011. **133**(44): p. 17567-17569.
168. Mastan, E., L. Xi, and S. Zhu, *What Limits the Chain Growth from Flat Surfaces in Surface-Initiated ATRP: Propagation, Termination or Both?* Macromolecular Theory and Simulations, 2015. **24**(2): p. 89-99.
169. Prucker, O. and J. Rühe, *Mechanism of Radical Chain Polymerizations Initiated by Azo Compounds Covalently Bound to the Surface of Spherical Particles.* Macromolecules, 1998. **31**(3): p. 602-613.
170. Zoppe, J.O., et al., *Effect of Surface Charge on Surface-Initiated Atom Transfer Radical Polymerization from Cellulose Nanocrystals in Aqueous Media.* Biomacromolecules, 2016. **17**(4): p. 1404-1413.
171. Yu, W., et al., *Controlled grafting of well-defined polymers on hydrogen-terminated silicon substrates by surface-initiated atom transfer radical polymerization.* The Journal of Physical Chemistry B, 2003. **107**(37): p. 10198-10205.
172. Kobayashi, M. and A. Takahara, *Synthesis and frictional properties of poly (2, 3-dihydroxypropyl methacrylate) brush prepared by surface-initiated atom transfer radical polymerization.* Chemistry letters, 2005. **34**(12): p. 1582-1583.
173. Ohno, K., et al., *Synthesis of gold nanoparticles coated with well-defined, high-density polymer brushes by surface-initiated living radical polymerization.* Macromolecules, 2002. **35**(24): p. 8989-8993.
174. Cai, Q.J., et al., *GaAs–Polymer Hybrids Formed by Surface-Initiated Atom-Transfer Radical Polymerization of Methyl Methacrylate.* Angewandte Chemie International Edition, 2005. **44**(7): p. 1104-1107.
175. Xu, F., et al., *Well-Defined Polymer− Germanium Hybrids via Surface-Initiated Atom Transfer Radical Polymerization on Hydrogen-Terminated Ge (100) Substrates.* Organometallics, 2005. **24**(7): p. 1768-1771.
176. Sun, L., G.L. Baker, and M.L. Bruening, *Polymer brush membranes for pervaporation of organic solvents from water.* Macromolecules, 2005. **38**(6): p. 2307-2314.
177. Snaith, H.J., et al., *Self-organization of nanocrystals in polymer brushes. Application in heterojunction photovoltaic diodes.* Nano letters, 2005. **5**(9): p. 1653-1657.

178. Babu, K. and R. Dhamodharan, *Grafting of poly (methyl methacrylate) brushes from magnetite nanoparticles using a phosphonic acid based initiator by ambient temperature atom transfer radical polymerization (ATATRP).* Nanoscale research letters, 2008. **3**(3): p. 109.
179. Yao, Z., et al., *Polymerization from the surface of single-walled carbon nanotubes− preparation and characterization of nanocomposites.* Journal of the American Chemical Society, 2003. **125**(51): p. 16015-16024.
180. Li, L., J. Davidson, and C.M. Lukehart, *Surface functionalization of nanodiamond particles via atom transfer radical polymerization.* Carbon, 2006. **44**(11): p. 2308-2315.
181. Bech, L., et al., *Atom transfer radical polymerization of styrene from different poly (ethylene terephthalate) surfaces: films, fibers and fabrics.* European Polymer Journal, 2009. **45**(1): p. 246-255.
182. Xu, F., et al., *Functionalization of nylon membranes via surface-initiated atom-transfer radical polymerization.* Langmuir, 2007. **23**(16): p. 8585-8592.
183. Liu, Y.L., M.T. Luo, and J.Y. Lai, *Poly (tetrafluoroethylene) Film Surface Functionalization with 2-Bromoisobutyryl Bromide as Initiator for Surface-Initiated Atom-Transfer Radical Polymerization.* Macromolecular rapid communications, 2007. **28**(3): p. 329-333.
184. Yao, F., et al., *Antibacterial effect of surface-functionalized polypropylene hollow fiber membrane from surface-initiated atom transfer radical polymerization.* Journal of Membrane Science, 2008. **319**(1-2): p. 149-157.
185. Liu, D., et al., *Controlled grafting of polymer brushes on poly (vinylidene fluoride) films by surface-initiated atom transfer radical polymerization.* Journal of applied polymer science, 2006. **101**(6): p. 3704-3712.
186. Olivier, A., et al., *Surface-initiated controlled polymerization as a convenient method for designing functional polymer brushes: From self-assembled monolayers to patterned surfaces.* Progress in polymer science, 2012. **37**(1): p. 157-181.
187. Yi, J., et al., *Chiral-nematic self-ordering of rodlike cellulose nanocrystals grafted with poly (styrene) in both thermotropic and lyotropic states.* Polymer, 2008. **49**(20): p. 4406-4412.
188. Xiao, M., et al., *Surface-initiated atom transfer radical polymerization of butyl acrylate on cellulose microfibrils.* Carbohydrate polymers, 2011. **83**(2): p. 512-519.
189. Lacerda, P.S., et al., *Nanostructured composites obtained by ATRP sleeving of bacterial cellulose nanofibers with acrylate polymers.* Biomacromolecules, 2013. **14**(6): p. 2063-2073.
190. Yamamoto, K., S. Yoshida, and J.-i. Kadokawa, *Surface-initiated atom transfer radical polymerization from chitin nanofiber macroinitiator film.* Carbohydrate polymers, 2014. **112**: p. 119-124.
191. Zhang, X.M., et al. *Wood Pulp Fibers Grafted with Polyacrylamide through Atom Transfer Radical Polymerization*. in *Advanced Materials Research*. 2012. Trans Tech Publ.
192. Gao, G., J.I. Dallmeyer, and J.F. Kadla, *Synthesis of lignin nanofibers with ionic-responsive shells: water-expandable lignin-based nanofibrous mats.* Biomacromolecules, 2012. **13**(11): p. 3602-3610.
193. Gokhale, R., J. Couet, and M. Biesalski, *In situ cross-linking of the shell of self-assembled peptide nanotubes.* physica status solidi (a), 2010. **207**(4): p. 878-883.
194. Goli, K.K., et al., *Generation of functional coatings on hydrophobic surfaces through deposition of denatured proteins followed by grafting from polymerization.* Biomacromolecules, 2012. **13**(5): p. 1371-1382.
195. Strozyk, M.S., et al., *Protein/Polymer-Based Dual-Responsive Gold Nanoparticles with pH-Dependent Thermal Sensitivity.* Advanced Functional Materials, 2012. **22**(7): p. 1436-1444.
196. Xing, T., et al., *Preparation, structure and properties of multi-functional silk via ATRP method.* Applied Surface Science, 2012. **258**(7): p. 3208-3213.
197. Pan, J., et al., *Fabrication and evaluation of temperature responsive molecularly imprinted sorbents based on surface of yeast via surface-initiated AGET ATRP.* Applied Surface Science, 2013. **287**: p. 211-217.
198. Pokorski, J.K., et al., *Functional virus-based polymer–protein nanoparticles by atom transfer radical polymerization.* Journal of the American Chemical Society, 2011. **133**(24): p. 9242-9245.
199. Ver Meer, M.A., et al., *Effect of mesoporosity on thermal and mechanical properties of polystyrene/silica composites.* ACS Applied Materials & Interfaces, 2009. **2**(1): p. 41-47.
200. Qin, L., et al., *Surface-modified polystyrene beads as photografting imprinted polymer matrix for chromatographic separation of proteins.* Journal of Chromatography A, 2009. **1216**(5): p. 807-814.
201. Karesoja, M., et al., *Mesoporous silica particles grafted with poly (ethyleneoxide-block-N-vinylcaprolactam).* Journal of Polymer Science Part A: Polymer Chemistry, 2013. **51**(23): p. 5012-5020.
202. Müllner, M., et al., *Surface-initiated polymerization within mesoporous silica spheres for the modular design of charge-neutral polymer particles.* Langmuir, 2014. **30**(21): p. 6286-6293.

203. Bak, J.M. and H.-i. Lee, *pH-tunable aqueous dispersion of graphene nanocomposites functionalized with poly (acrylic acid) brushes.* Polymer, 2012. **53**(22): p. 4955-4960.
204. Bak, J.M., et al., *Thermoresponsive graphene nanosheets by functionalization with polymer brushes.* Polymer, 2012. **53**(2): p. 316-323.
205. Gao, T., et al., *Noncovalent microcontact printing for grafting patterned polymer brushes on graphene films.* Langmuir, 2013. **29**(4): p. 1054-1060.
206. Wang, D., et al., *Graphene functionalized with azo polymer brushes: surface-initiated polymerization and photoresponsive properties.* Advanced Materials, 2011. **23**(9): p. 1122-1125.
207. Hu, J., et al., *Effect of interfacial interaction between graphene oxide derivatives and poly (vinyl chloride) upon the mechanical properties of their nanocomposites.* Journal of materials science, 2014. **49**(7): p. 2943-2951.
208. Lillethorup, M., et al., *High-versus Low-Quality Graphene: A Mechanistic Investigation of Electrografted Diazonium-Based Films for Growth of Polymer Brushes.* Small, 2014. **10**(5): p. 922-934.
209. Hong, D., et al., *Generation of Cellular Micropatterns on a Single-Layered Graphene Film.* Macromolecular bioscience, 2014. **14**(3): p. 314-319.
210. Deng, Y., et al., *Functionalization of graphene oxide towards thermo-sensitive nanocomposites via moderate in situ SET-LRP.* Journal of Polymer Science part A: polymer chemistry, 2011. **49**(22): p. 4747-4755.
211. Steenackers, M., et al., *Polymer brushes on graphene.* Journal of the American Chemical Society, 2011. **133**(27): p. 10490-10498.

II. Poly(4-vinylpyridine)

A model polymer

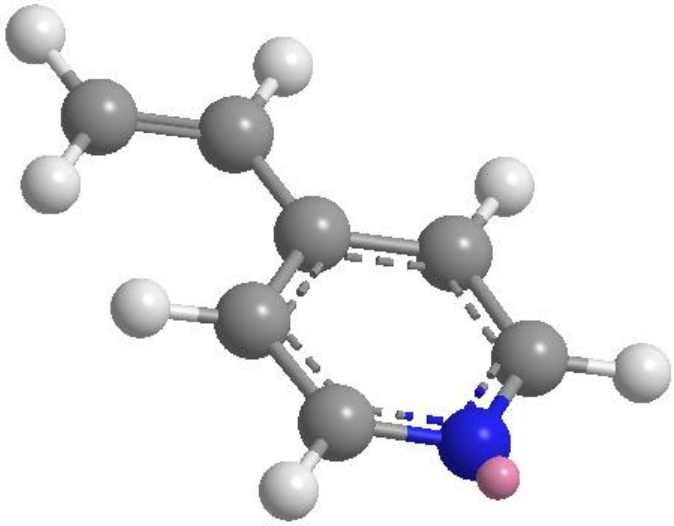

II.1. Introduction

During the first year of this thesis, the synthesis of the highly chelating dipicolinic-acid based monomer was under investigation. Meanwhile, the polymerization strategy that will be later used to synthesis the new polymer materials was being studied using a model monomer, the commercial 4-vinylpyridine (4VP). This monomer has some structural similarity with our targeted dipicolinic acid-based monomer bearing a pyridine center, and has indeed some affinity towards metals, including copper, that makes the polymerization more challenging because of the competition between the chelating monomer and the ligand used in the ATRP reaction. This will help us develop the polymerization system that will be later applied to dipicolinic acid-based monomer, both in solution and on a solid substrate.

In this chapter, the polymerization of 4VP will be investigated and optimized in solution, to be then applied to build P4VP polymer brush from polyethylene terephthalate (PET) and silica surfaces. Obtained materials will be characterized and assessed at each point.

II.2. Polymerization of 4VP in solution

Herein, the control and livingness of the ATRP polymerization of 4VP is examined in solution. The polymerization of 4VP by ATRP is quite challenging because 4VP is a coordinating monomer that competes for the binding of the metal catalysts. To avoid this problem, a strong ligand like tris(2-pyridylmethyl)amine (TPMA) should be used in the polymerization system.

Conventional ATRP of 4VP was reported before in different polymerization systems in term of different radical initiators, catalysts, ligands and solvents [1-5] and the Cu^0-mediated polymerization of 4VP was reported in the very expensive solvent of hexafluoropropan-2-ol (HFIP) [6]. The surface initiated ATRP (SI-ATRP) of 4VP was reported on polysulfone surface [7] and Cu^0-mediated surface initiated polymerization of 4VP was described on silicon wafer using a copper plate at 0.5 mm distance from the surface as a Cu^0 source and DMSO as solvent [8].

However, the above systems were either oxygen sensitive (in the case of classical ATRP), too expensive (in the case of HFIP solvent) or not feasible on an industrial scale (in the case of copper plate). A possible simplification of the polymerization system using SARA ATRP in 2-propanol

and a copper wire reducer is here considered. Benzyl chloride (BnCl) was used as initiator and $CuCl_2$/TPMA as a catalyst/ligand complex (scheme 1).

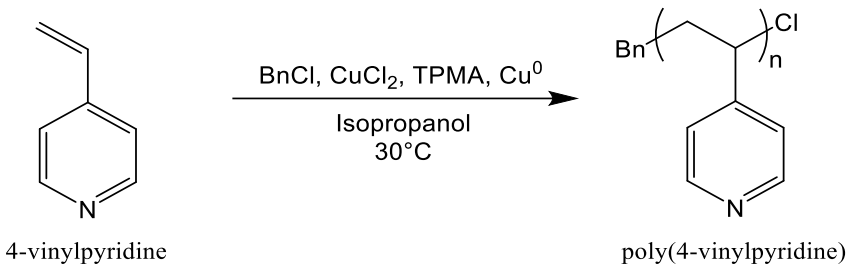

Scheme II-1. SARA ATRP of 4VP

Reaction protocols are detailed in "materials and methods" and the overall polymerization reaction is described as follows: 4VP / BnCl / $CuCl_2$ / TPMA = 100 / 1 / 0.05 / 0.2

The resulting P4VP was characterized with ^{1}H NMR and size exclusion chromatography (SEC). Monomer conversion was calculated from the ^{1}H NMR spectra of aliquots taken at different reaction times. Taking the monomer's vinyl protons at 5.5 and 6.1 ppm as 1 proton reference each, the 4VP monomer conversion was calculated as follows:

$$4VP\ monomer\ conversion\ (\%) = \frac{\mathcal{A}_{7.7-8.9\ ppm} - 2}{\mathcal{A}_{7.7-8.9\ ppm}} \times 100$$

$\mathcal{A}_{7.7-8.9\ ppm}$ being the peak area between 7.7 and 8.9 ppm attributed to the 2 protons at ortho position from the nitrogen atom. Figure 1 shows an example at 79 % 4VP conversion.

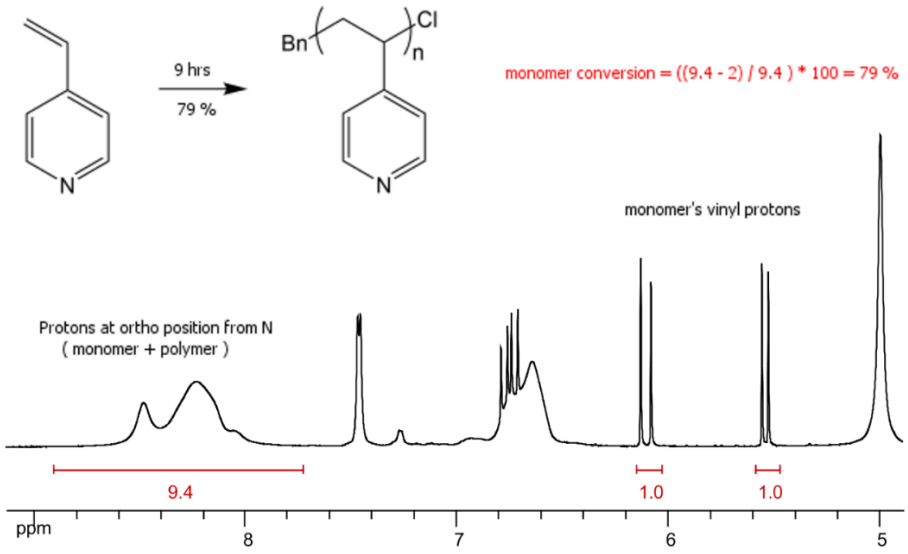

Figure II-1. ^{1}H NMR spectrum at 79 % 4VP monomer conversion

The reaction kinetics of the optimized polymerization system were studied. Between 1 and 9 hours of reaction time, the monomer conversion ranged between 13 and 79%, with calculated Mn (NMR) ranging between 1.4 10^3 and 8.3 10^3 g.mol^{-1}, measured Mn (SEC) between 4.1 10^3 and 13.4 10^3 g.mol^{-1} and dispersity Đ between 1.07 and 1.37. Results are summarized in table 1. Monomer conversion, molecular weight evolution, and SEC traces are plotted in figure 2.

Table II-1. 4VP polymerization kinetics

Time (h)	Conversion (%)	Mn (NMR) 10^3 g.mol^{-1}	Mn (SEC) 10^3 g.mol^{-1}	Đ (SEC)
1	13	1.4	4.1	1.07
3	35	3.7	8.1	1.21
5	52	5.5	8.7	1.33
7	71	7.5	12.8	1.37
9	79	8.3	13.4	1.34

4VP / BnCl / CuCl2 / TPMA = 100 / 1 / 0.05 / 0.2

T = 30 °C, solvent = 2-propanol

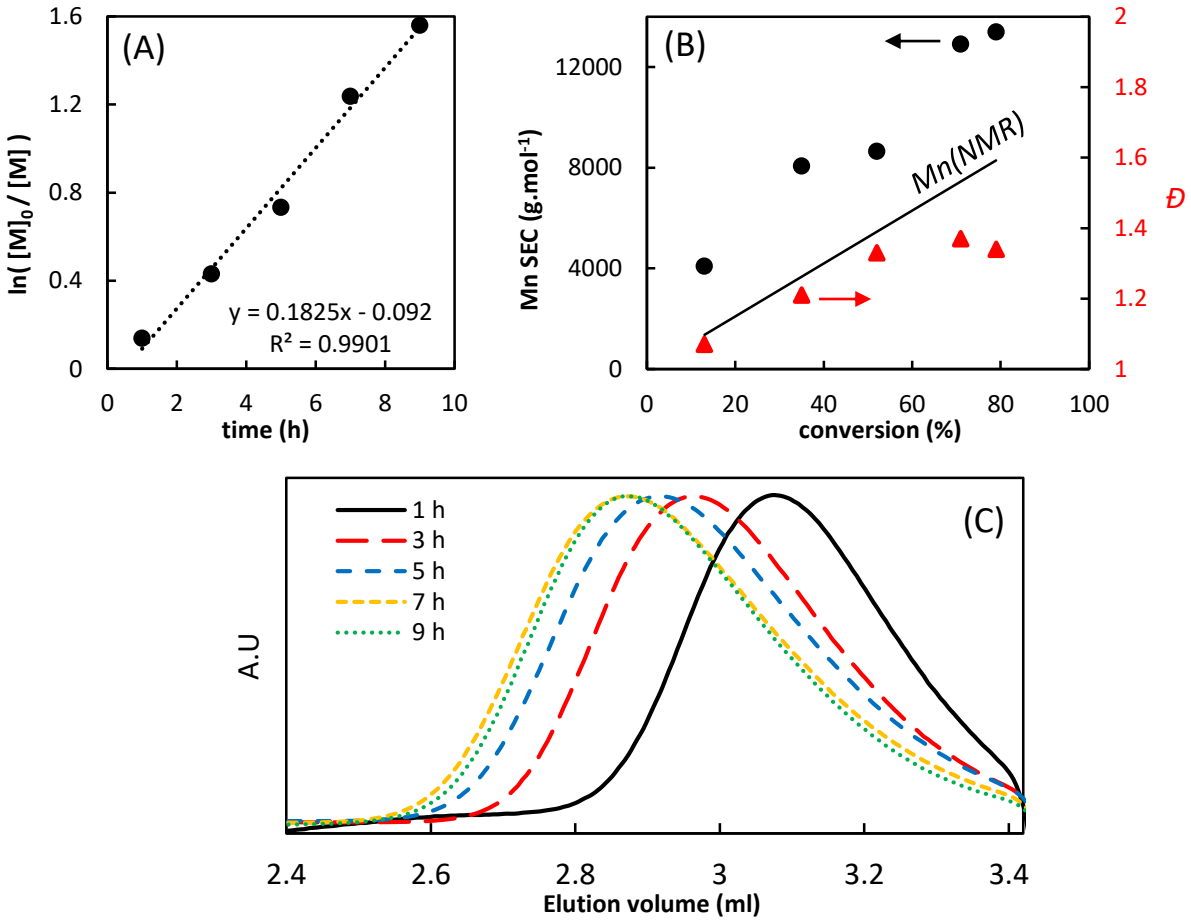

Figure II-2. 4VP polymerization kinetics. (A): ln([M]$_0$/[M]) vs time; (B): evolution of molar masses as a function of monomer conversion. (C): evolution of SEC traces.

As described earlier in chapter I, the ATRP rate law R_p should ideally exhibit a linear dependence with respect to the monomer concentration [M], due to negligible termination so that the concentration of the propagating chains [P*] is constant.

$$R_p = -\frac{d[\mathrm{M}]}{dt} = k_p[\mathrm{M}][\mathrm{P}^*] \quad \rightarrow \quad \ln\frac{[M]_0}{[M]} = k_p\,[P^*]\,t$$

The first order kinetic behavior shown in figure 2A, along with the monomodal distribution and relatively low dispersity at high monomer conversion (Đ = 1.37 at 79 % conversion) (figure 2B, 2C) suggest fast initiation, good control, and limited chain termination of the SARA ATRP of 4VP in 2-propanol under the used reaction conditions. Deviations of Mn (SEC) from predicted values Mn (NMR) are probably due to different hydrodynamic volumes of P4VP and the PMMA standards. Chain extension was also conducted to prove the livingness of the reaction and as the polymerization was successfully validated in solution, similar conditions will be used to build P4VP on different substrates in the following sections.

It should be mentioned though, that system components were carefully examined before adopting the above system. A mixed 2-propanol/water solvent caused the polymerization reaction to accelerate but compromised its control. When iron or magnesium powder were used as reducers instead of copper, we lost the control over polymer chain distribution. $CuCl_2$ ratio was also varied between 0 and 1000 ppm (with respect to 4VP) and a concentration of 500 ppm was kept as a reasonable compromise between reaction kinetics and chain length control.

II.3. P4VP on PET surfaces

Once the polymerization system optimized in solution, P4VP chains were built from PET films. The overall modification strategy is described in scheme 2 and the reactions protocols are detailed in "materials and methods". It involves the successive aminolysis with PEI, grafting of BnCl initiator and surface initiated SARA ATRP of 4VP. The aminolysis of PET was used before in our lab and the reaction was conducted in methanol [9]. However, DMSO was reported in the literature to allow a denser network of amines [10]. In our work, methanol and DMSO were assessed and indeed DMSO was found to nearly double the amount of amines grafted on the PET surface and became the solvent of choice for the PET aminolysis reaction.

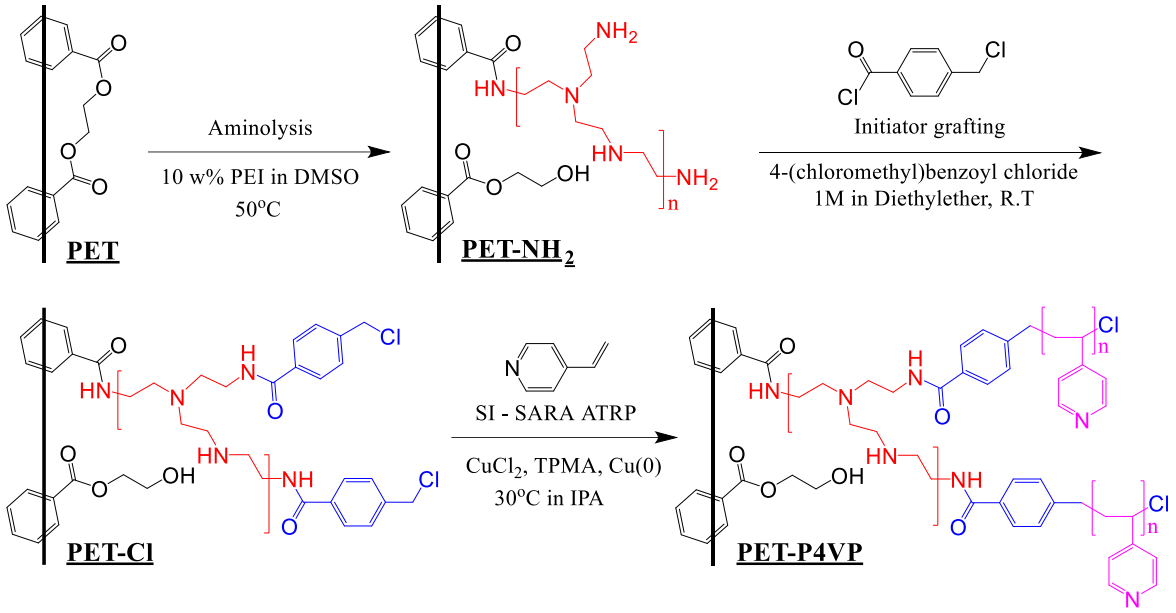

Scheme II-2. SI-SARA ATRP of 4VP on PET surface

To ensure a successful modification after each step, PET films were characterized by means of different techniques starting with water contact angle (WCA).

Water contact angle (WCA):

As shown in figure 3, WCA clearly changes after following each modification step. After aminolysis, it drops from a hydrophobic 80.0 ± 1.0° for non-modified PET surface to a hydrophilic 29.0 ± 0.5° for PEI covered substrate (PET-NH_2) due to amine functions. Colorimetric analysis showed a surface density of 0.71 ± 0.05 NH_2/nm^2 after aminolysis. WCA then increases to 52.0 ± 1.0° after grafting the less water soluble BnCl initiator (PET-Cl). This increase in hydrophobicity

is correlated with a drop of surface amine density to 0.22 ± 0.03 NH_2/nm^2. After the surface initiated polymerization of 4VP for at least one day, WCA drops to 35.0 ± 1.2°. In order to examine the nature of the outer layer, modified films were washed with HCl (0.1 M) to protonate the pyridine units. As a result, The WCA further dropped to a very hydrophilic 16.0 ± 0.6° as expected, then increased back to 35° after a NaOH (0.1 M) wash. This WCA behavior gives a first hint of a potential pH-sensitive P4VP outer layer on the PET film surface.

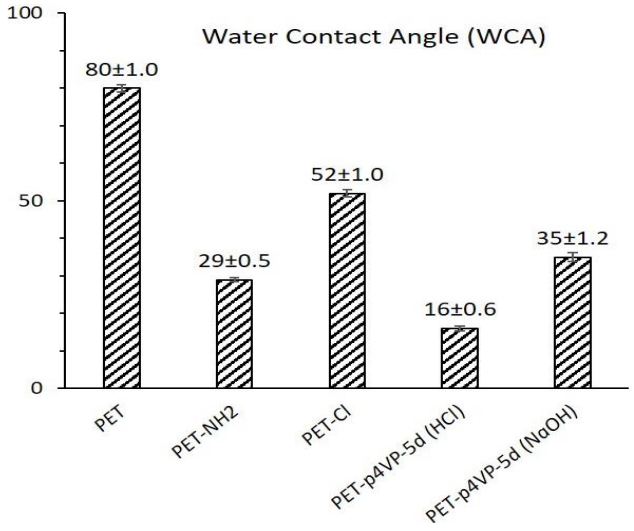

Figure II-3. Water Contact Angle (WCA) measurements of modified PET substrate

The promising WCA behavior encouraged us to look further into the chemical nature of the P4VP-modified surfaces, starting with infrared spectroscopy.

Attenuated total reflection (ATR):

ATR spectrum of PET surface was compared to the PET-P4VP surface as shown in figure 4.

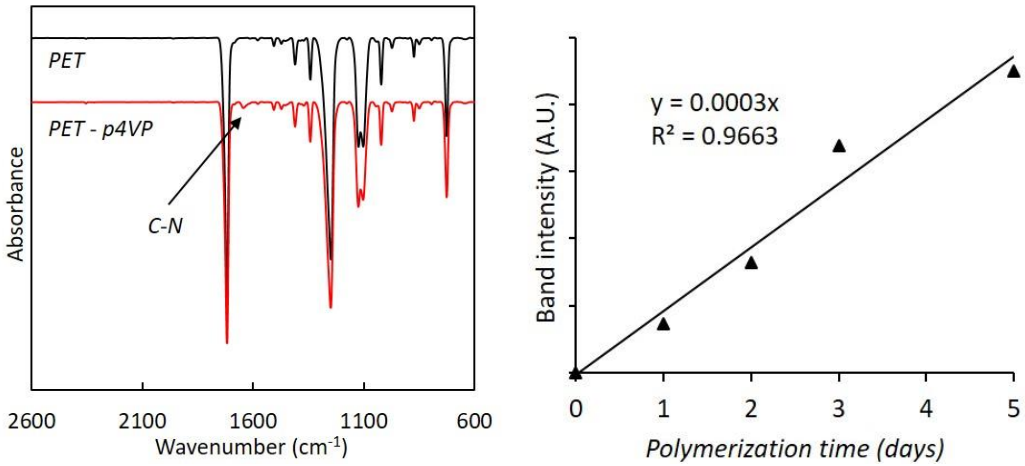

Figure II-4. ATR spectra of PET and PET-P4VP surfaces (left) and pyridinic C-N stretching band intensity at 1640 cm^{-1} as a function of polymerization time (right)

Looking at the spectra in Figure 4, one can see the single peak at 1640 cm^{-1} that corresponds to the pyridinic C-N stretching band on the PET-P4VP film spectrum (after 5 days of polymerization). Even after an extensive soxhlet wash in ethanol, this pyridinic peak could still be seen, proving the strong covalent nature of the bond linking the P4VP layer to the PET substrate.

Reaction kinetics were also examined. Figure 4 shows the evolution of the pyridinic stretching band intensity at 1640 cm^{-1} as a function of polymerization time. The linear increase in signal intensity reflects a living polymerization of P4VP within the studied time frame, giving a thicker and/or denser layer of P4VP.

After ATR, modified surfaces will be analyzed by the more surface sensitive x-ray photoelectron spectroscopy (XPS).

X-ray photoelectron spectroscopy (XPS):

XPS analysis was conducted to examine the surface chemical composition after each modification step shown in scheme 2. Figures 5 and 6 show high resolution C1s and N1s spectra giving a more surface sensitive insight into the chemical nature of the modified substrate. Specific peak components are shown in tables 2 and 3, and elements contributions are shown in table 4.

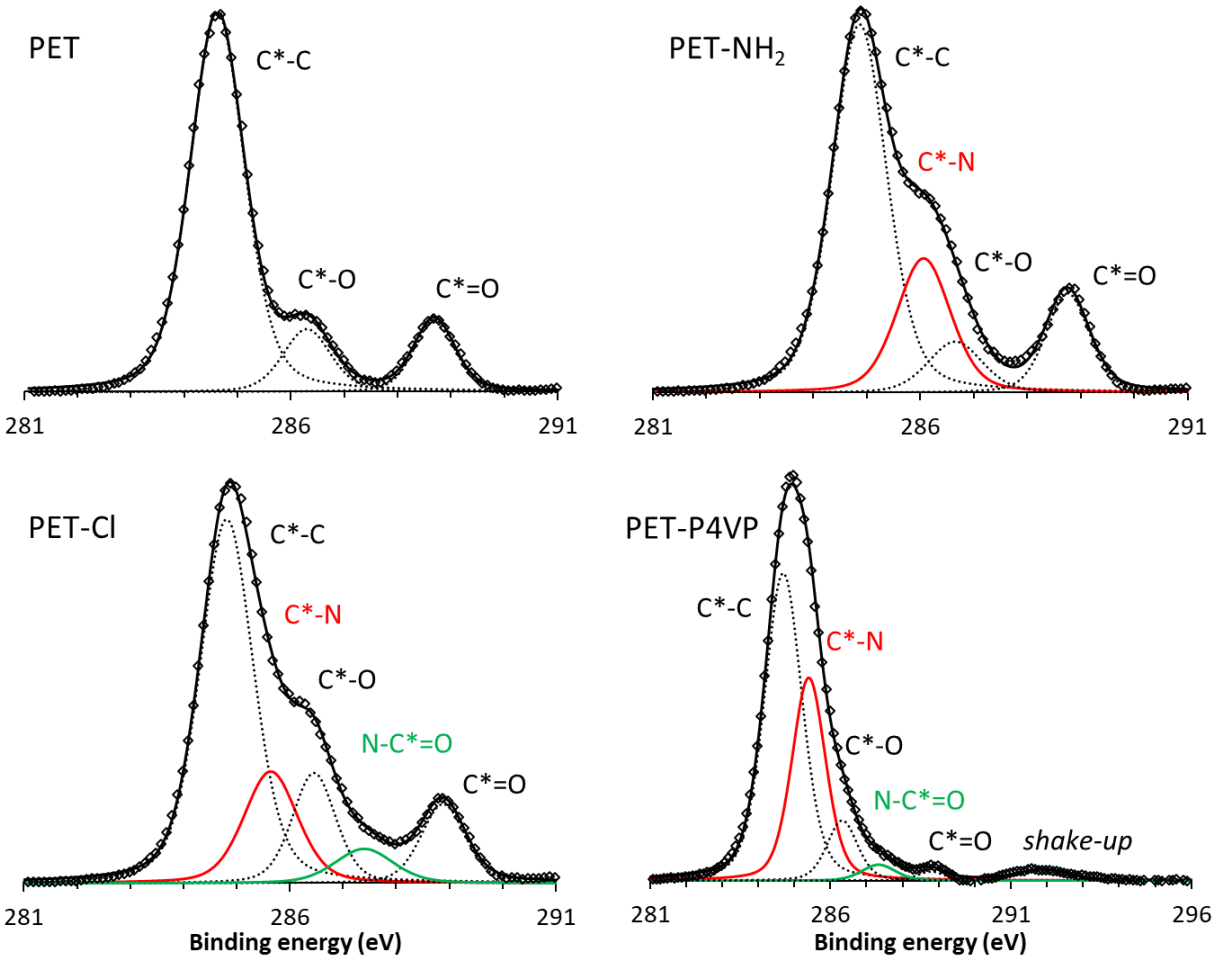

Figure II-5. XPS C1s spectra of native PET, after aminolysis (PET-NH_2), initiator grafting (PET-Cl) and 5 days of polymerization (PET-P4VP)

C1s peak of native PET (figure 5) shows three components that correspond to aromatic C*-C (284.8 eV), alongside C*-O (286.5) and C*=O (288.9 eV). The aminolysis is evidenced by the C*-N peak that appears at 285.6 eV (Red) and the grafting of the BnCl initiator is then shown by the appearance of the N-C*=O peak at 287.5 eV (Green). After polymerization of 4VP, the C1s spectrum of PET-P4VP surfaces shows an increased contribution for both C*-C (284.8 eV) and C*-N (285.6 eV) components versus an ever decreasing contribution for C*-O (286.5 eV), C*=O (288.9 eV) and N-C*=O (287.5 eV) (table 2).

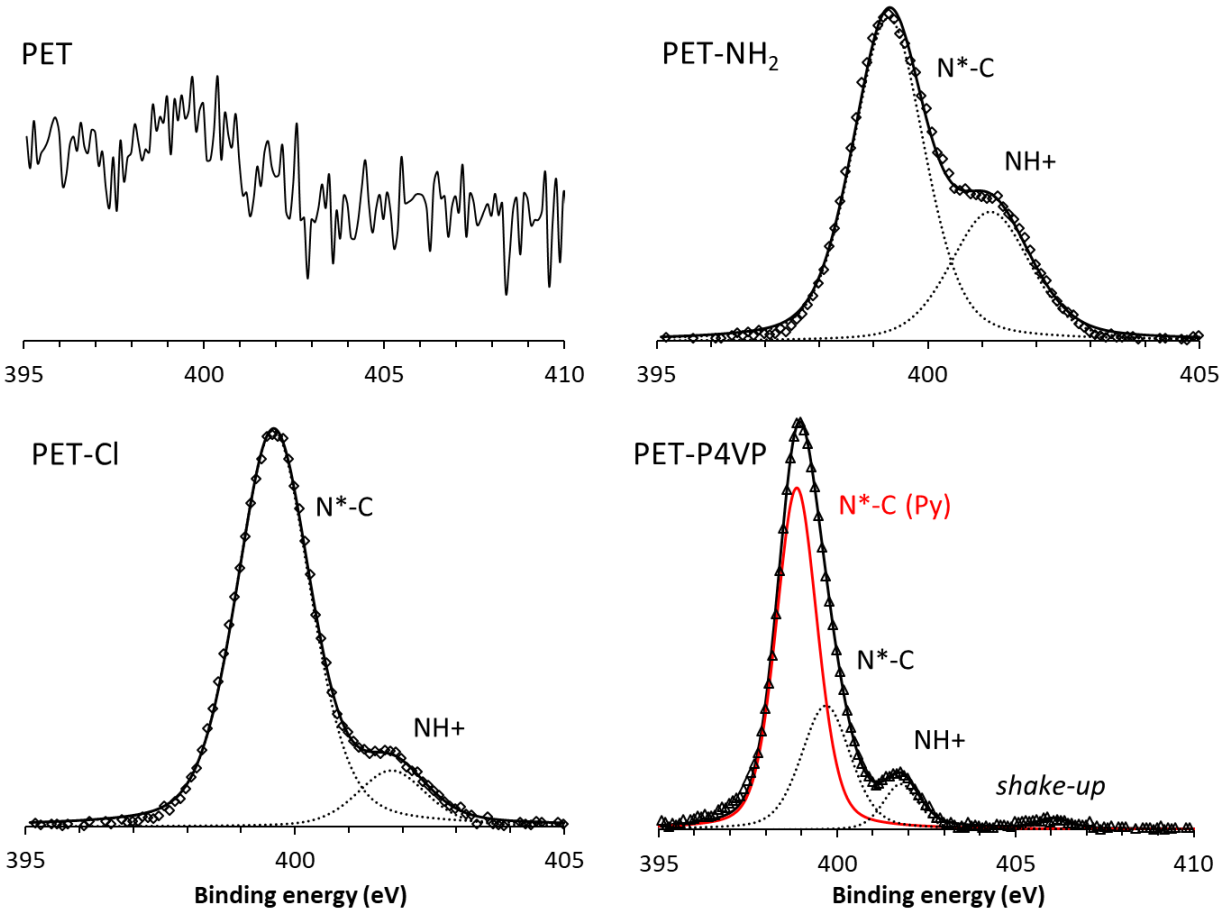

Figure II-6. XPS N1s spectra of native PET, after aminolysis (PET-NH_2), initiator grafting (PET-Cl) and 5 days of polymerization (PET-P4VP)

N1s spectra in figure 6 show no signal detected on PET substrate. The appearance of N*-C peak at 399.3 eV after aminolysis shows a successful grafting of PEI. Another peak at 401.2 eV is associated with protonated amines NH^+. The later reduction of this peak after initiator grafting is due to the much weaker basicity of formed amides (scheme 2). Although weaker, this peak still exists as the initiator grafting has a yield of 60-70% as shown by the colorimetric analysis. Finally, the introduction of P4VP by SI-SARA ATRP is proven by the pyridinic N*-C peak that appears at 398.8 eV, and the noticeable decrease of all other peaks (table 3).

Table II-2. Peak characteristics and relative contribution in C1s spectra

			Atomic %			
	Peak BE	FWHM (eV)	*PET*	*PET-NH_2*	*PET-Cl*	*PET-P4VP (5 days)*
C* - C	284.8	1.21	77.6	58.4	54.3	65
C* - O	286.5	0.95	11.3	8.1	13.4	6.2
C* = O	288.9	0.94	11.1	12.6	9.9	1.3
C*-N	285.6	1.19	-	20.9	16.8	25
N-C*=O	287.5	1.2	-	-	5.6	2.5

Table II-3. Peak characteristics and relative contribution in N1s spectra

			Atomic %			
	Peak BE	FWHM (eV)	*PET*	*PET-NH_2*	*PET-Cl*	*PET-P4VP (5 days)*
N* - C	399.3	1.56	-	69.1	88.3	26.9
NH^+	401.2	1.75	-	30.9	11.7	7.5
N* - C (Py)	398.8	1.2	-	-	-	64.3
shake up	406.1	1.01	-	-	-	1.4

Table 4 shows the evolution of elements contributions after each modification step and most importantly as a function of polymerization time. Going from PET-Cl to different PET-P4VP surfaces, carbon and nitrogen contributions increased while oxygen contribution decreased. Furthermore, a C/N ratio of 14.0 was observed on PET-Cl surface. This ratio decreases to 9.6 after one day of polymerization then goes down to 9.1 then 8.1 after three and five days of polymerization, respectively, approaching the theoretical C/N ratio of 7.0 for pure P4VP.

Table II-4. Total element contribution determined by XPS

	Atomic %					
	PET	*PET-NH_2*	*PET-Cl*	*PET-P4VP (1 day)*	*PET-P4VP (3 days)*	*PET-P4VP (5 days)*
C	77	68	70	77	78	81
N	-	7	5	8	9	10
O	23	25	17	13	12	8
Cl	-	-	4	2	1	1

XPS analysis proved the covalent bonding between the substrate and the P4VP layer, and an increasing thickness of P4VP with polymerization time, though the absolute thickness was not obtained.

ToF-SIMS:

In order to provide more chemical and dimensional specificity of the surface, high-resolution time-of-flight secondary ion mass spectrometry (ToF-SIMS) analysis was performed. Secondary ion fragments from each layer were identified as follows: the fragment at m/z = 104 ($C_6H_4CO^+$) was chosen for PET [11] and the fragment at m/z = 42 ($C_2H_4N^+$) was chosen for PEI [12] in addition to the easily attributed 4VP fragment of m/z = 106 ($C_7H_8N^+$) [13]. An additional fragment at m/z = 153 ($C_8H_6ClO^+$) was attributed to the BnCl initiator and mass spectra were overlaid in figure 7, with zoom into m/z of interest.

No signal was detected at m/z = 42 before PET modification, it first appears after aminolysis and the fragment identified as $C_2H_4N^+$ is emitted. BnCl initiator specific fragment $C_8H_6ClO^+$ appears at m/z = 153 only after initiator grafting. At m/z = 106, P4VP was detected after polymerization and identified through the $C_7H_8N^+$ fragment.

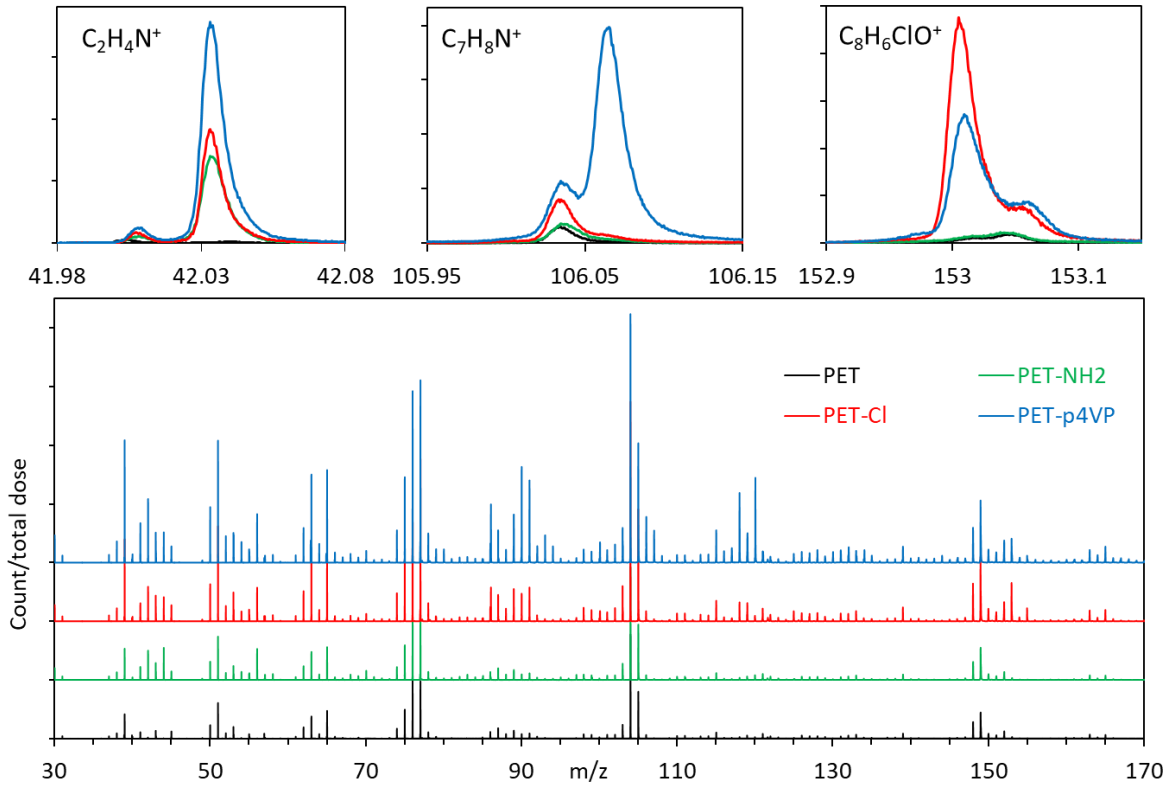

Figure II-7. TOF-SIMS positive spectra of native PET, after aminolysis (PET-NH_2), initiator grafting (PET-Cl) and 5 days of polymerization (PET-P4VP) with, from bottom up, zoom in to m/z: 42, 106 and 153

Afterwards, and on the final PET-P4VP surface, the intensity of the secondary ions specific to each layer was followed along the z-axis, i.e. as a function of sputtering time as shown in figure 8. Fragments with m/z = 42, 104 and 106 were used to follow the PEI, PET and P4VP signals, respectively.

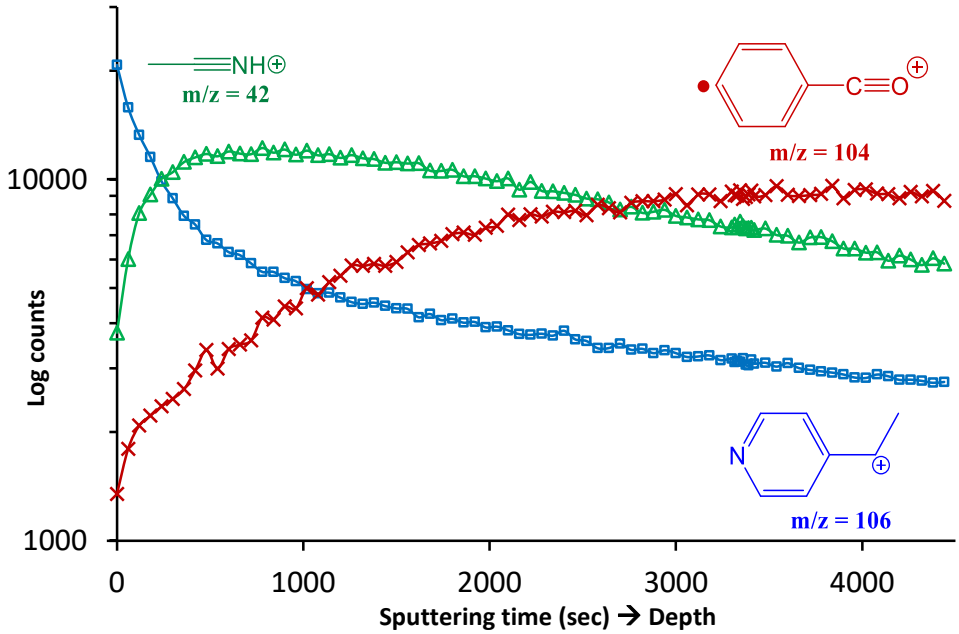

Figure II-8. Secondary ions intensity (logarithmic) as a function of sputtering time of the PET-P4VP-5d surface

At the outer surface (t = 0 s), P4VP is predominately present with negligible intensity from the PEI and PET substrate. As we go down the Z axis, P4VP signal intensity gradually decreases as both PEI and PET signals increase. Around t = 500 s, PEI signal reaches its maximum intensity then decreases along with P4VP, while PET signal continues to increase up to t = 4500 s where only traces of P4VP and PEI are detected. This depth profile shows no clear interfaces between layers as no sudden shifts in signal intensities were detected. This reveals an important aspect of these surfaces. The absence of sharp interfaces reflects an interpenetrating "interphases" of successive layers. In fact, this aspect can be attributed to the use of the branched PEI that offers a dense network of amines that allows multiple attachment sites between the PEI layer and the PET substrate and multiple initiating sites for the later polymerization of 4VP. As a result, PET substrate was indeed functionalized with a covalently attached, dense and uniform layer of P4VP, but

initiated from different sites that are geometrically localized at various depths. Consequently, interphases are observed rather than sharp interfaces between the consecutive components as shown in the 3D reconstruction of figure 9.

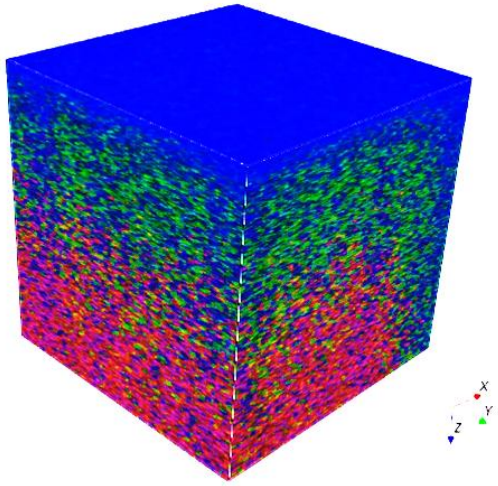

Figure II-9. 3D reconstruction of PET-P4VP-5d surface, m/z = 106 (Blue), 42 (green) and 104 (red)

Once the modification of PET with P4VP proven successful, we wanted to have a look at the surface morphology after each step. In the next section, PET film are examined under an atomic force microscope (AFM) and PET fibers are viewed under a scanning electron miscroscope (SEM).

Surface morphology:

The surface topography of the modified PET film was studied using tapping mode AFM after each treatment as shown in figure 10.

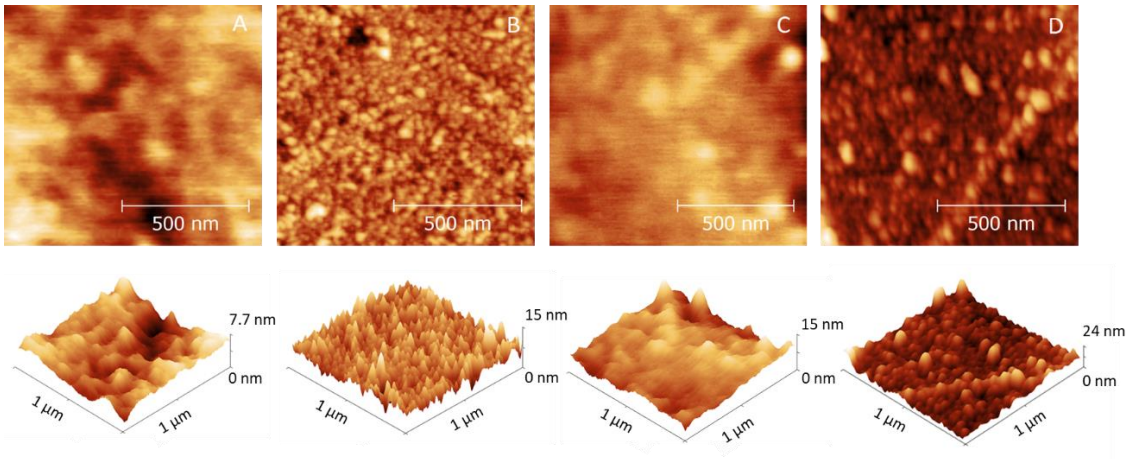

Figure II-10. AFM topography images (up) and 3D reconstruction (down) of PET surfaces after each modification. (A): non-modified PET, (B): after aminolysis, (C): grafted initiator, (D): PET-P4VP-5d

A measured root-mean-square (RMS) roughness of 1.21 nm/µm^2 was observed for the bare clean PET surface (figure 10A). After aminolysis (figure 10B), RMS roughness increases to 1.66 nm/µm^2, and further up to 1.97 nm/µm^2 after the incorporation of the initiator (figure 10C). Figure 10D shows the final aspect of the surface after the surface initiated SARA ATRP of 4VP, with a dry RMS roughness ranging between 2.60 and 3.30 nm/µm^2 after different polymerization times. This increase in surface roughness can be attributed first to the use of the amorphous PEI and then to the polymerization reaction, even though the surface can still be considered smooth.

PET fibers, modified according to the same strategy (scheme 2), were observed under a scanning electron microscope (SEM) as shown in figure 11.

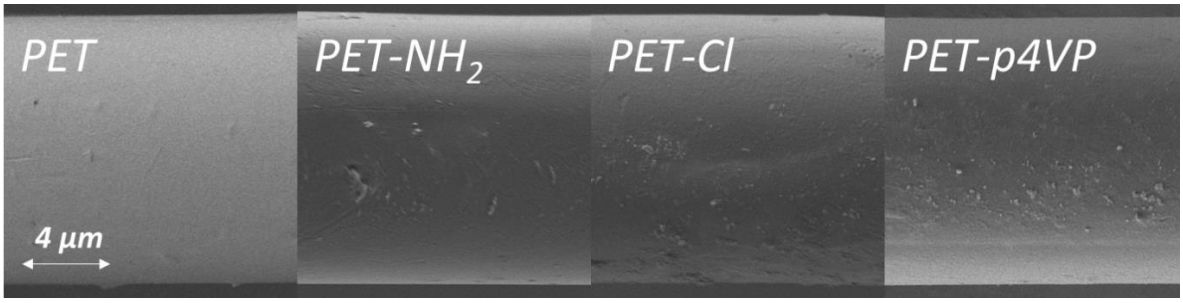

Figure II-11. SEM images of modified PET fibers

Even though SEM images supports the fact that a smooth homogenous layer of P4VP was successfully grafted on the PET surface, it reveals an important drawback of this strategy. The average diameter of those fibers stayed within the average diameter of bare non-modified fibers of 12 ± 1 µm. This means that at best, only few nanometers of P4VP were built on the PET surface. This drawback needs to be dealt with in the next chapter if we want to build a thick layer of the highly metal chelating dipicolinic acid-based polymer on fiber materials.

Meanwhile, and after a successful grafting of P4VP on the organic PET surface, the surface initiated polymerization of 4VP was extended to a different substrate. In the next section, SI-SARA ATRP will be applied to an inorganic silica substrate.

II.4. P4VP on silica surfaces

Before applying the same polymerization system on silica, a different approach has to be used to fix the BnCl initiator on the silica (SiO_2) surface. APTES-based molecules are extensively studied as preferred candidates to tailor silicon surfaces and represent an initial step towards the covalent attachment of a variety of functional molecules on mineral surfaces [14-16], including radical initiator for subsequent polymerization [17-19]. Herein, the silica surface was first silanized with the new APTES-BnCl initiator synthesized as shown in scheme 3.

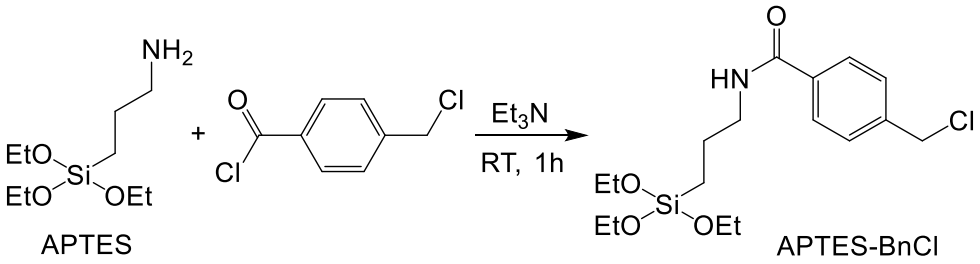

Scheme II-3. Synthesis of APTES-BnCl

SI-SARA ATRP of 4VP was then conducted on the silanized surface. The overall modification strategy is described in scheme 4. Protocols for APTES-BnCl synthesis, the silanization of silica surface and the surface initiated polymerization are detailed in "materials and methods".

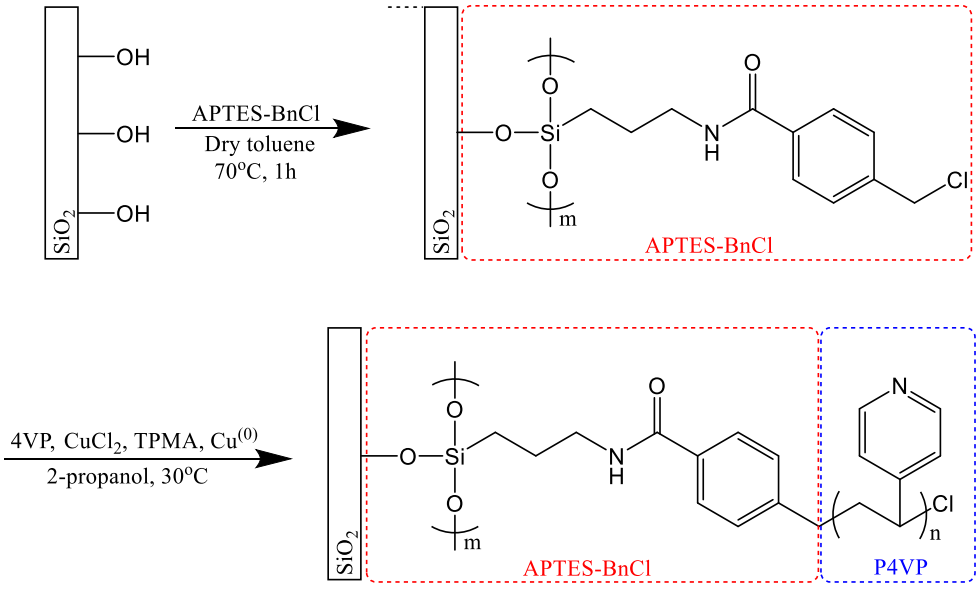

Scheme II-4. SI-SARA ATRP of 4VP on silica

This strategy was applied on a flat silica surface, then on silica microparticles to be used as a pH-switchable barrier for oil/water separation.

II.4.1. P4VP on flat silica

A silicon wafer was treated with a highly oxidizing piranha solution to bare a clean silanol-terminated silica surface, as detailed in "materials and methods". The strategy described in scheme 4 was then applied and the modified surface was examined by different techniques, starting with WCA.

Water contact angle (WCA):

To ensure a successful modification, Water Contact Angle (WCA) was measured (figure 12) on bare silanol-terminated silica (*Si-OH*), initiator-grafted (*APTES-BnCl*) surface and P4VP-grafted surface. WCA analysis show that a hydrophilic surface (Θ = 24.0° ± 2.0) is seen on silanol-terminated silica surface (Si-OH). The APTES-BnCl grafted surface gave a higher angle of 61.0° ± 1.0, demonstrating the hydrophobic character of BnCl initiator. The successful grafting of the pH-sensitive P4VP layer was demonstrated by a switchable WCA between 73.0° ± 2.0 for the water washed surface (hydrophobic P4VP), and a WCA of 18.0° ± 1.0 for the HCl rinsed substrates (protonated hydrophilic P4VP). These results gave a first hint of a pH-sensitive surface and encouraged further detailed analysis of the modified substrates.

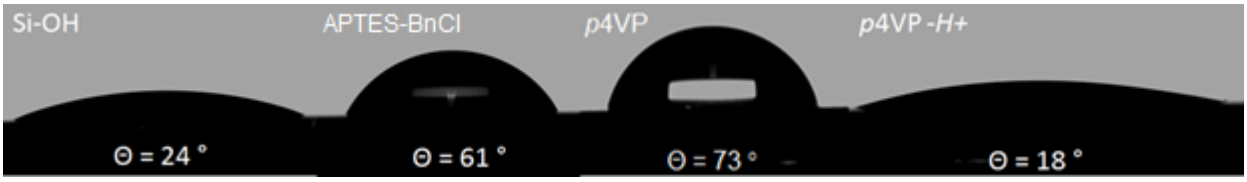

Figure II-12. Water Contact Angle (WCA) measurements of modified silica surface

X-ray photoelectron spectroscopy (XPS):

Figure 13 shows the complete survey of the XPS spectra across modification steps. Silica surface shows only Si and O peaks around 100 eV (Si2p), 150 eV (Si2s) and 530 eV (O1s), with minor C1s contaminants at around 285 eV. High resolution spectra (figure 14) later showed a 76.6 % contribution for bulk Si-Si compared to 23.4 % for surface Si-O (table 6), as the ellipsometric measurement showed only a 2 nm thick layer of SiO_2 on top of the bulk silicon, a thickness lower than the ~10 nm probing depth of XPS.

APTES-BnCl modified surface show the same peak positions as bare SiO_2, with an additional peak of Cl2p at around 200 eV and a small N1s peak at around 400 eV (figure 13). An increase in atomic % (table 5) of carbon from 5.7 % to 31.7 % is expected for a homogenous top layer of APTES-BnCl. However, ellipsometry measurement showed a thin monolayer (~1 nm) of APTES-BnCl, too thin to mask signals from the SiO_2 sublayer.

After the 4VP polymerization, the XPS spectrum shows trace levels of both oxygen and silicon signals with the enhancement of carbon and nitrogen peaks (figure 13). The minimal signal of SiO_2 sublayer is supported by the ellipsometric measurements where a layer of 10-12 nm is present at the surface. Atomic % data (table 5) gives a carbon/nitrogen ratio of 7.9/1.0, close to the theoretical ratio of 7/1 for pure P4VP.

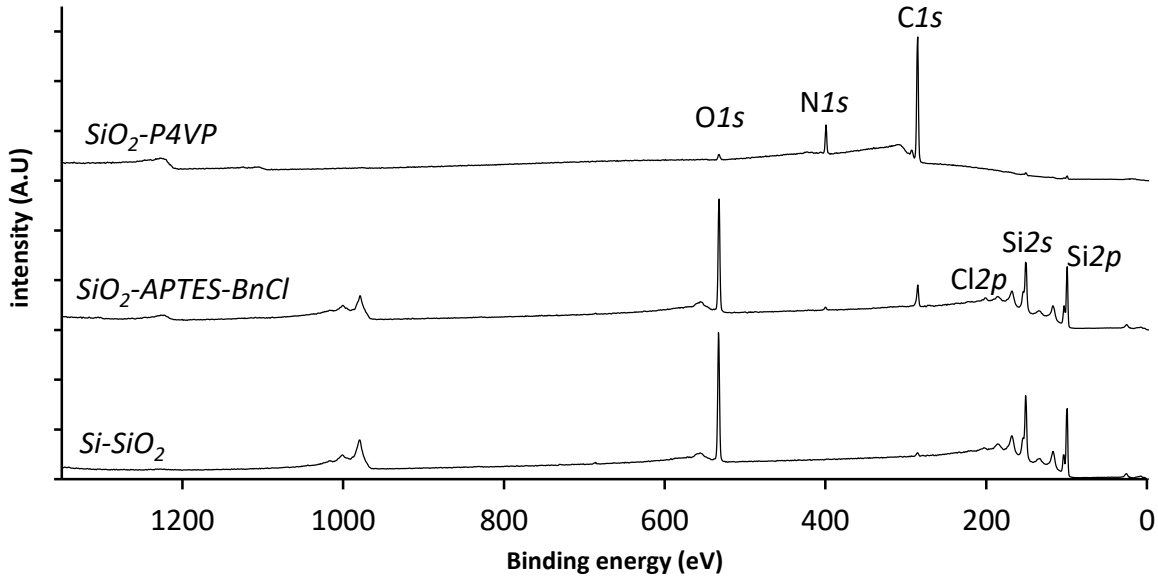

Figure II-13. XPS survey of bare and modified silicon wafer

Table II-5. Total elements contributions determined by XPS

Surface	C	O	N	Si	Cl
Si-SiO_2	5.7	34.3	-	60	-
SiO_2-APTES-BnCl	16.2	31	1.5	49.9	1.4
SiO_2-P4VP	82	2.5	10.3	5.2	-

High resolution XPS analysis was also conducted to examine each step.

Si-SiO_2 surface:

Figure 14 shows the high-resolution spectrum of the silanol-terminated silicon wafer. Two distinct doublets were observed in the *Si2p*, corresponding to bulk silicon Si*-Si (99.2 eV) and silicon bonded to oxygen Si*-O (103.3 eV), their relative contributions are presented in Table 6.

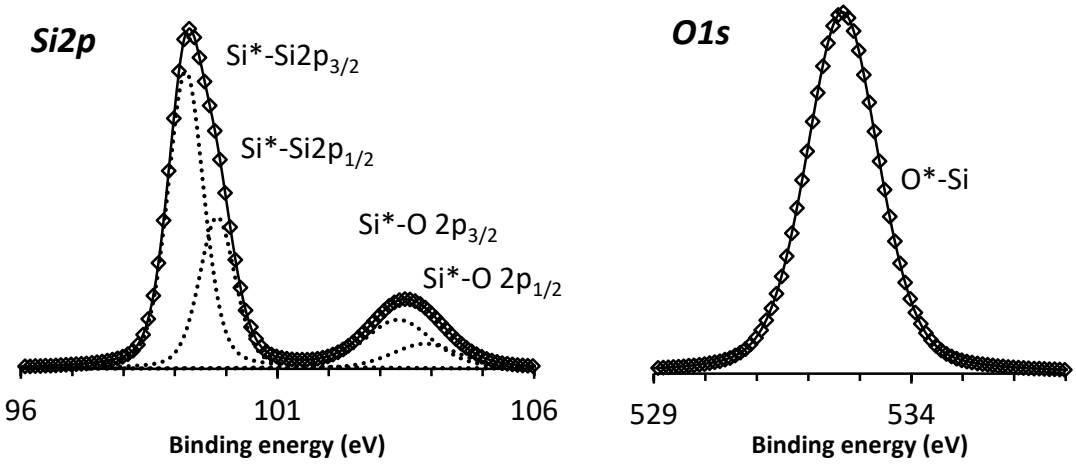

Figure II-14. High resolution XPS spectra of silica surface

Table II-6. Peak characteristics and relative contributions of Si2p spectrum of silanol-terminated silica

	Position (eV)	FWHM (eV)	Contribution (%)
Si* - Si	99.2	0.83	76.6
Si* - O	103.3	1.56	23.4

SiO_2-APTES-BnCl surface:

High-resolution XPS spectra of APTES-BnCl modified silica surface are presented in Figure 15. The C1s spectrum shows all peaks expected from APTES-BnCl grafted surface, namely, C*–Csp^3 at 285 eV, C*–Csp^2 at 284.6 eV, C*–N at 286.3 eV, and N-C*=O at 288.1 eV. The N1s peaks (hydrogen bonded NH^+ at 401.6 eV5 and N*-C at 399.8 eV), along with Cl2p peaks (C–Cl* at 200.3 and 201.9 eV), further confirmed a successfully modified surface. Table 7 provides the peaks contributions in each high-resolution spectrum of Figure 15.

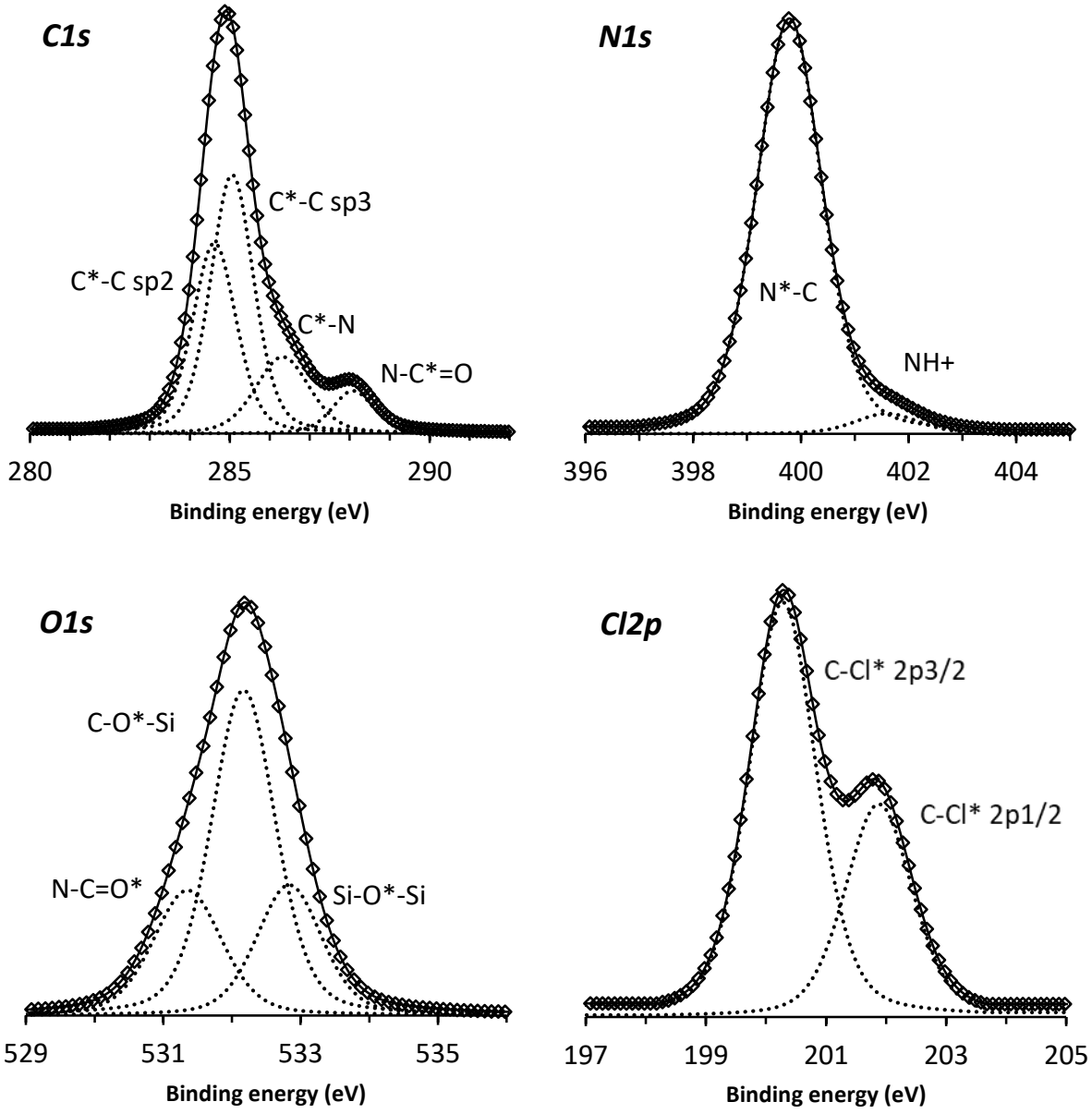

Figure II-15.XPS high resolution spectra of APTES-BnCl modified silica

Table II-7. Peak characteristics and relative contributions of APTES-BnCl modified silica

	Position (eV)	FWHM (eV)	Contribution (%)
C* - C sp3	285	1.27	43.9
C* - C sp2	284.6	1.29	32.7
N - C* = O	288.1	1.24	7.1
C* - N	286.3	1.61	16.3
N* - C	399.8	1.44	95.4
NH+	401.6	1.40	4.6
N - C = O*	531.4	1.19	22.6
C - O* - Si	532.2	1.11	54.9
Si - O* - Si	532.8	1.13	22.5
C-Cl* $2p_{3/2}$	200.3	1.33	50
C-Cl* $2p_{1/2}$	201.9	1.33	50

It is interesting to attempt to figure out the way APTES-BnCl molecules can be attached to the surface. This can be shown by the C/N atomic ratio in the XPS spectrum. Possible structures are depicted in Figure 16 where the molecules can be attached as a monopod (C/N = 15), dipod (C/N = 13), tripod or crosslinked (C/N = 11). An atomic ratio of C/N = 10.8 found for APTES-BnCl modified surface (table 5) shows a dominant contribution of the tripodic or crosslinked structures. Differentiating between those two structures needs further analysis.

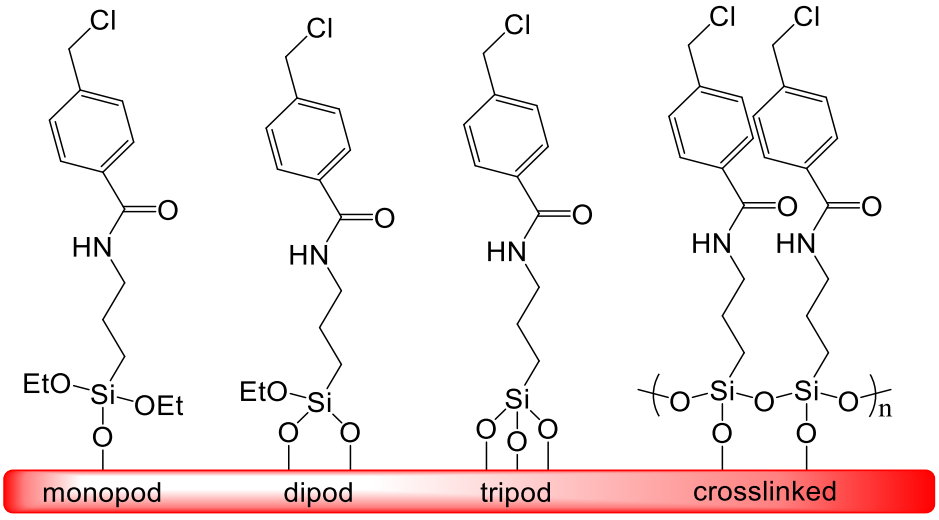

Figure II-16. Different possible forms of the attachment of APTES-BnCl to silica surface

SiO_2-P4VP surface:

The high resolution spectra of the P4VP modified silica, after 22 hours of polymerization, is shown in figure 17. The C1s spectrum confirms the polymer backbone's C*-C peak at 284.7 eV, the aromatic C*-C peak at 285.3 eV and the aromatic C*-N peak at 285.9 eV. The atomic contribution of these peaks is shown in table 8, where a ratio of 2.5/3/2.2 for C-C/*Ar*C-C/*Ar*C-N further proves the presence of 4VP units when compared to the theoretical ratio of 2/3/2 for pure P4VP. No peaks for C*=O or aliphatic C*-N from the previous spectrum (figure 15) are present, hypothesizing that the APTES-BnCl layer was completely covered with the polymer. N1s spectrum in Figure 17 shows a unique pyridinic N*-C peak at 400.7 eV, with shake-up peaks at higher energy, as expected from a quasi-pure P4VP outer layer.

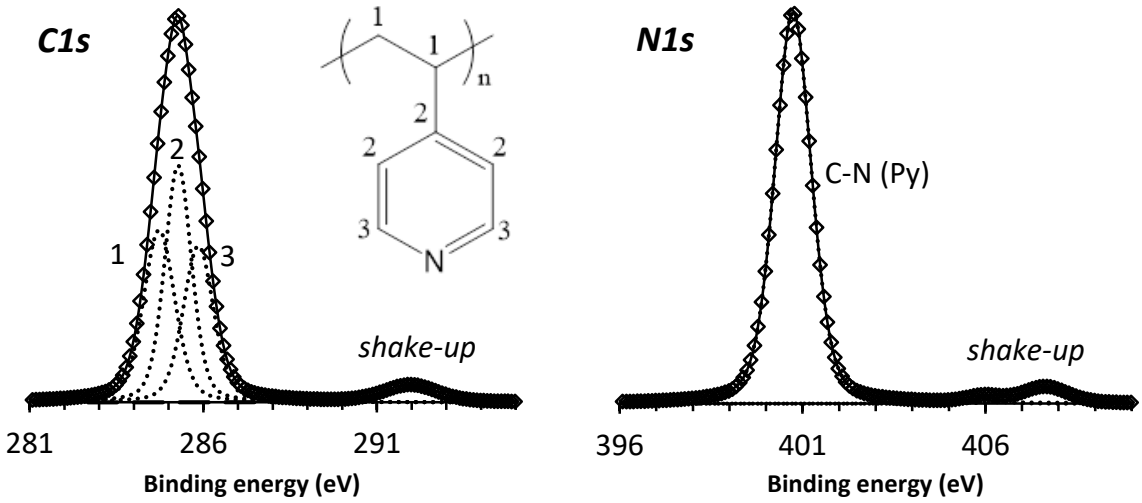

Figure II-17. High resolution spectra of P4VP-modified silica

Table II-8. Peak characteristics and relative contributions in the C1s spectrum of P4VP-modified silica

	Position (eV)	FWHM (eV)	Contribution %
Backbone C*-C	284.7	1.07	31.1
Aromatic C*-C	285.3	0.92	36.6
Aromatic C*-N	285.9	1.03	27.2
shake-up	291.9	1.84	5.1

ToF-SIMS:

TOF-SIMS depth profiles are shown in figure 18. $C_7H_8N^+$ Fragment at m/z = 106 is the main fingerprint of P4VP, the fragments at m/z = 28 (Si^+), 60 (SiO_2^-) and 77 (SiO_3H^-) were chosen to follow the silica-APTES-BnCl layer. Due to the Si-O function of the APTES-BnCl, it was difficult to separate its fragments from the silica ones.

The P4VP intensity exhibits an initial linear decrease for the first 30 seconds of sputtering time followed by an exponential decrease to reach after 100 s a steady state of few counts. The interface between p4VP and the Si sublayer is clearly visible due to the decay of the P 4VP signal by 2 to 3 orders of magnitude simultaneously with the rise of the Si^+, SiO_2^- signals. It is important to note that at the interface the intensity of SiO_3H^- signal gets a boost when it is compared to the other characteristic peaks of the Silica-APTES-BnCl layer. This could be attributed to the high probability of extracting this ion at the interface both from the APTES-BnCl monolayer and the substrate. However, it can also be attributed to the SIMS matrix effect where the yield of some ions appear to be enhanced at an oxide interface [20].

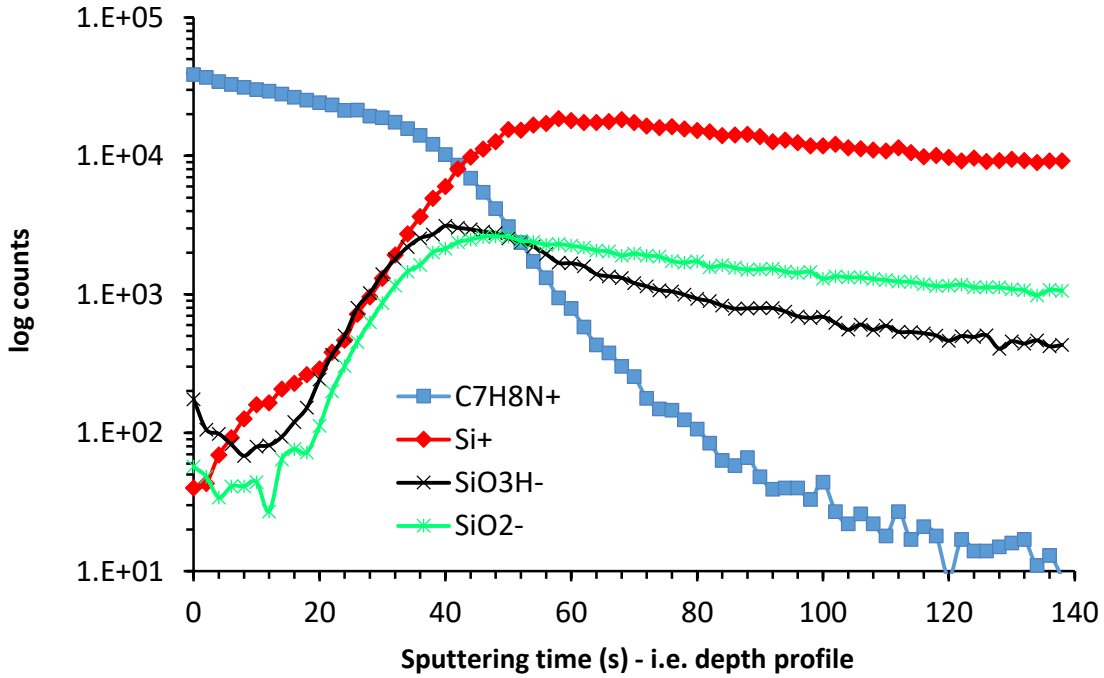

Figure II-18. Evolution of the intensity of the emitted fragments ($C_7H_8N^+$, Si^+, SiO_3H^-, SiO_2^-) as a function of sputtering time of the P4VP-modified silica surface on a logarithmic scale.

Figure 19 shows the 3D rendering of the positively charged ions of m/z = 28 and 106 collected at every depth (2 sec) of the performed depth profile measurement. This 3D image confirms that the P4VP is uniformly distributed across the region being analyzed and not concentrated in selected voxels (air-P4VP interface or P4VP-Silica interface).

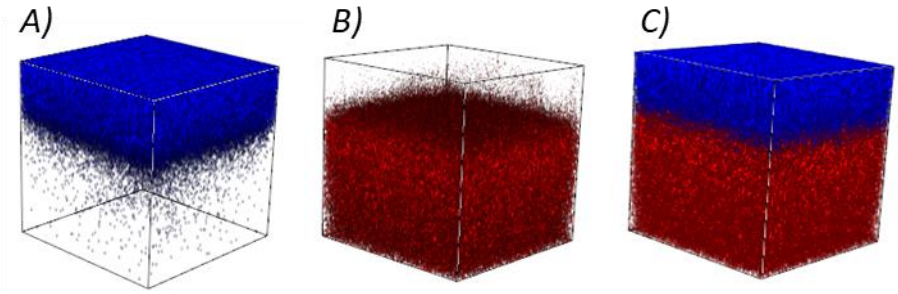

Figure II-19. 3D reconstruction of the modified surface, A) P4VP (blue), B) Si (red), C) Total overlay

These results become significant when compared to the earlier PET-P4VP surface (figure 9). When polyethyleneimine (PEI) was used to link P4VP to a polyethylene terephthalate (PET) substrate, no sharp interface was detected between the layers, and a rather interpenetrating layers (interphases) were obtained due to the branched nature of PEI and that of the "soft" organic PET substrate. On silica, more sharp interfaces were detected where P4VP is polymerized using a monolayer of initiator attached to the "harder and polished" silica surface.

Atomic force microscopy (AFM):

Figure 20 shows the topography and 3D AFM images obtained for (a) bare silica surface, (b) APTES-BnCl-silanized surface and (c) Silanized substrate after surface initiated polymerization of 4VP.

A measured RMS roughness of 0.48 nm/µm^2 was observed for clean silica substrate (Fig. 20A). A slight increase in the surface roughness to 0.53 nm/µm^2 is observed after the APTES-BnCl treatment (Fig. 20B). This increase in roughness can be attributed to the formation of a few number of a 4-6 nm thick island-like aggregates coming from the APTES-BnCl oligomers formed inevitably in the APTES-BnCl solution in toluene. Fig. 20C shows the topography of the P4VP layer built from the APTES-BnCl initiator by SI-SARA ATRP where RMS increased to 0.67 nm/µm^2 after almost one day of polymerization.

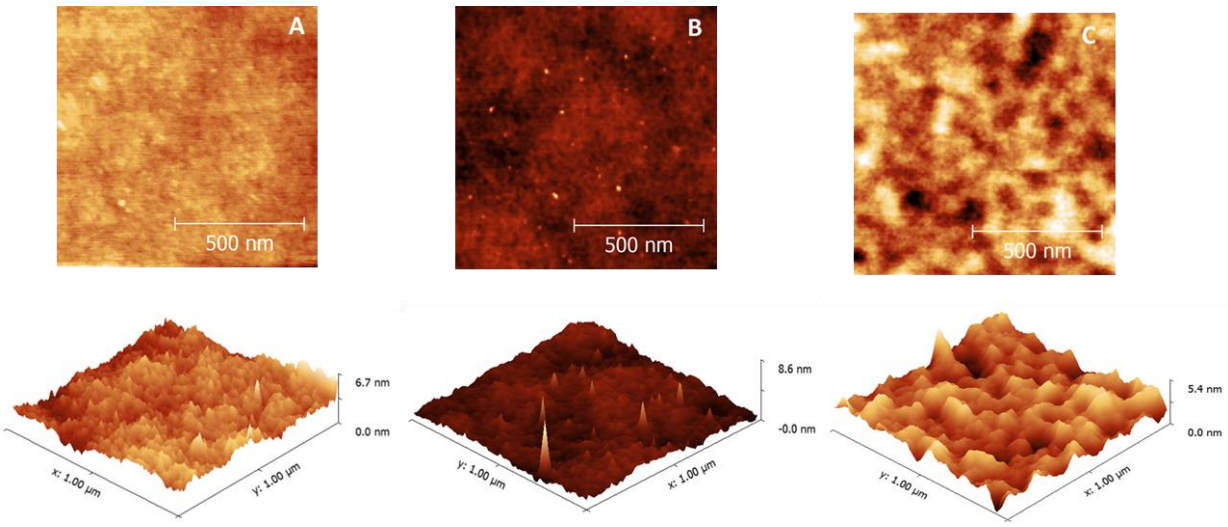

Figure II-20. AFM topography images (up) and 3D reconstruction (down) of (A): SiO_2 surface, (B): APTES-BnCl modified surface, (C): P4VP top layer

These observations proves that smooth, uniform and homogenous surfaces were obtained after each step. P4VP outer layer is also expected to be smoother when built on silica than on the PET substrate (figure 10)

Stability of modified surfaces:

As reported in the literature, silica surfaces modified with an APTES-based molecule show a low stability of just few hours [21] as these films are highly sensitive to hydrolysis. Therefore, the stability of APTES-BnCl and P4VP surfaces was examined. After 5 days exposed to room temperature and humidity, the XPS measurements show a complete degradation of the APTES-BnCl layer, whereas samples bearing P4VP show no alteration. Moreover, ToF-SIMS analysis later showed high stability of P4VP-modified surfaces left for one year under room conditions. These measurements proved that the P4VP layer is thick and homogenous enough to prevent hydrolysis of the APTES-BnCl sublayer, and therefore proved a high stability of the final P4VP-modified silica surfaces.

II.4.2. P4VP on silica particles

Even though the 4VP is used in this project as a model monomer that allows the development of grafting techniques for the dipicolinic acid-based chelating monomer later discussed in chapters III and IV, we wanted to give the P4VP-modified surfaces a meaningful application.

Taking advantage of the pH-switchable hydrophilicity/hydrophobicity of pyridine units by protonation/deprotonation (scheme 5), silica microparticules were modified according to the same strategy described earlier in scheme 4.

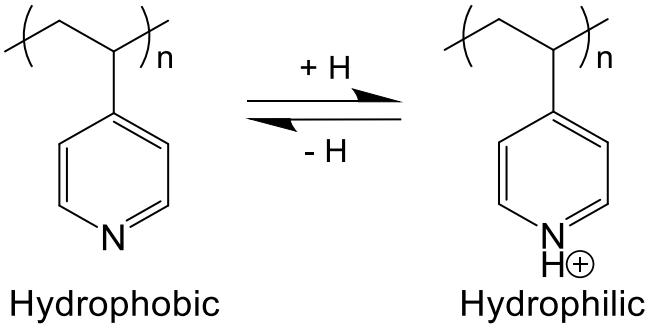

Scheme II-5. pH sensitivity of P4VP

The preparation of a pH-sensitive membrane based on 4VP, copolymerized with methyl methacrylate (MMA) using SARA ATRP, was reported before [22]. The PMMA-b-P4VP block copolymer was cast into a membrane and used for an efficient pH-induced oil/water separation. Herein, silica microparticles (70-200 µm) were modified with an outer layer of P4VP and used for an efficient pH-switchable oil/water separation process. The successful modification was verified by XPS, giving results similar to those seen on flat silica (figures 13-17).

Furthermore, ATR spectra of the silica-P4VP microparticles are shown in figure 21. The appearance of the *Si-C* peak at 1261 cm^{-1} proved the covalent attachment between the APTES-BnCl molecule and the silica surface and the P4VP outer layer can be detected through the pyridinic C-N vibration at 1635 cm^{-1}.

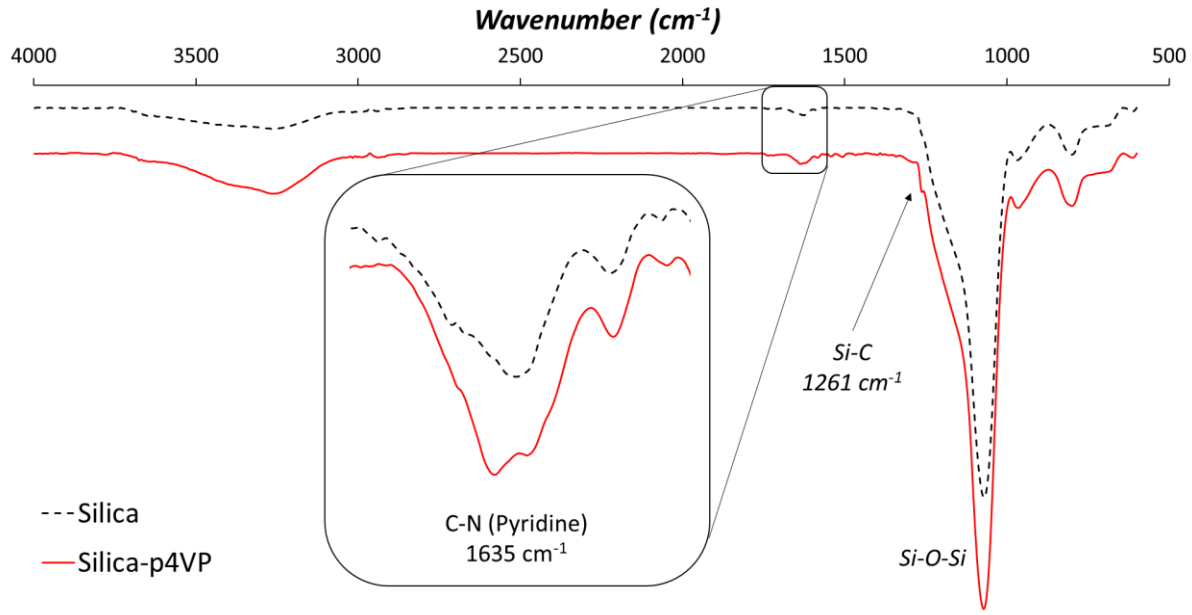

Figure II-21. ATR spectra of bare silica particles (black dashed line) and silica-P4VP particles (red line)

The P4VP-coated silica powder was then used as a pH-switchable barrier for oil/water separation.

pH-switchable oil/water separation:

The wettability of P4VP (pKa = 4.5) surface can be switched at different pH by the protonation/deprotonation of pyridyl groups (scheme 5). This property was shown earlier on a flat surface by the WCA measurements (figure 12) where the P4VP surface switched between hydrophobicity and hydrophilicity by alternating neutral water/diluted HCl washes. Silica powder modified with P4VP was used as a pH-controlled barrier for oil/water separation. The experimental set-up is shown in figure 22.

In a blank experiment, non-modified silica was put into a separatory funnel to a height of ~3 cm. A layered mixture of 10 mL dichloromethane (DCM) (bottom layer), 30 mL water (middle layer) and 10 mL n-hexane (top layer) were added on top of the silica (figure 22A), both organic solvents were colored with iodine [22] for better visualization. When the tap was opened (figure 22B), all solvents passed through within few minutes and no retention behavior was observed for the non-modified silica.

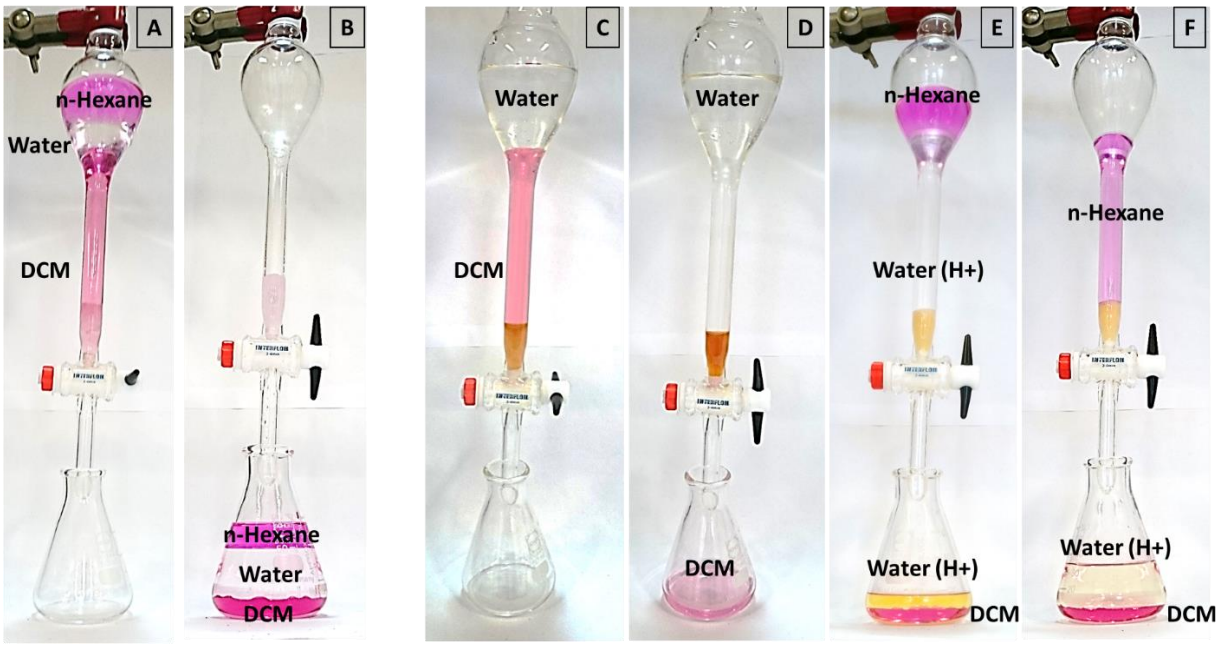

Figure II-22. Oil/Water separation on non-modified/blank silica (A,B) vs P4VP-modified (C, D, E, F) silica

In figure 22C, P4VP-modified silica was put to a height of ~3 cm followed by a layered mixture of DCM and water. When the tap was opened (figure 22D), DCM slowly passed through within a couple of minutes and the water was retained by the hydrophobic P4VP-modified silica. No water passed through the P4VP-modified silica even when left for several hours. Afterwards, few milliliters of concentrated HCl were added and the water was topped with a layer of n-hexane (figure 22E). Within a minute, water started to pass through, which can be explained by the protonation of the P4VP-modified silica, now turned hydrophilic (scheme 5). After all the water passed through, n-hexane was retained (figure 22F), proving the hydrophilic behavior of the protonated P4VP-modified silica, again with no change when the set-up was left for several hours.

II.5. Conclusion

In this chapter, the Cu^0-mediated CRP of 4VP was investigated. The polymerization system was optimized in solution as to obtain fairly controlled polymer chains. This reaction was then applied on PET then silica surfaces, with the initiator grafted in accordance to each substrate's chemistry. All modified surfaces were examined by several characterization techniques that gave access to surface chemistry and morphology. Finally, P4VP-modified silica powder was used for oil/water separation by switching its hydrophilicity/hydrophobicity.

The 4VP mainly served as model monomer for subsequent studies. In chapter III, a new monomer derived from chelidamic (4-hydroxy dipicolinic acid) will be discussed. The new monomer called 4-vinyl dimethyl dipicolinate (VDPM) will be synthesized and then used to obtain a highly chelating poly(4-vinyl dipicolinic acid) polymer (PVDPA). This polymer will later prove in chapter IV to be highly performing, either in its free (in solution) form or when grafted on solid substrates.

II.6. References

1. Yang, R., et al., *Synthesis of poly (4-vinylpyridine) and block copoly (4-vinylpyridine–b-styrene) by atom transfer radical polymerization using 5, 5, 7, 12, 12, 14-hexamethyl-1, 4, 8, 11-tetraazamacrocyclotetradecane as ligand.* European polymer journal, 2003. **39**(10): p. 2029-2033.
2. Tsarevsky, N.V., et al., *Rational selection of initiating/catalytic systems for the copper-mediated atom transfer radical polymerization of basic monomers in protic media: ATRP of 4-vinylpyridine.* Macromolecules, 2006. **39**(20): p. 6817-6824.
3. Lewis, G.T., V. Nguyen, and Y. Cohen, *Synthesis of poly (4-vinylpyridine) by reverse atom transfer radical polymerization.* Journal of Polymer Science Part A: Polymer Chemistry, 2007. **45**(24): p. 5748-5758.
4. Chen, H., et al., *Reverse ATRP of 4-vinylpyridine with Diethyl 2, 3-Dicyano-2, 3-Diphenylsuccinate/CuCl 2/5, 5, 7, 12, 12, 14-hexamethyl-1, 4, 8, 11-tetraazamacrocyclotetradecane.* Materials Science and Engineering: C, 2009. **29**(5): p. 1604-1608.
5. Xia, J., X. Zhang, and K. Matyjaszewski, *Atom transfer radical polymerization of 4-vinylpyridine.* Macromolecules, 1999. **32**(10): p. 3531-3533.
6. Wang, W., et al., *Favorable hydrogen bonding in room-temperature Cu (0)-mediated controlled radical polymerization of 4-vinylpyridine.* Polymer Chemistry, 2012. **3**(10): p. 2731-2734.
7. Qiu, J.-H., et al., *Synthesis and antibacterial activity of copper-immobilized membrane comprising grafted poly (4-vinylpyridine) chains.* Journal of colloid and interface science, 2011. **354**(1): p. 152-159.
8. Zhang, T., et al., *Surface-initiated Cu (0) mediated controlled radical polymerization (SI-CuCRP) using a copper plate.* Polymer Chemistry, 2015. **6**(14): p. 2726-2733.
9. Lepoittevin, B., et al., *Hydrophilic PET surfaces by aminolysis and glycopolymer brushes chemistry.* Journal of Polymer Science Part A: Polymer Chemistry, 2016. **54**(17): p. 2689-2697.
10. Jiang, L., Y. Jin, and R.K. Marcus, *Polyethylenimine modified poly (ethylene terephthalate) capillary channeled-polymer fibers for anion exchange chromatography of proteins.* Journal of Chromatography A, 2015. **1410**: p. 200-209.
11. Lang, F.-R., et al., *Surface analysis of polyethyleneterephthalate by ESCA and TOF-SIMS.* Fresenius' journal of analytical chemistry, 1997. **358**(1-2): p. 251-254.
12. Ademovic, Z., et al., *Surface modification of PET films using pulsed AC plasma polymerisation aimed at preventing protein adsorption.* Plasma Processes and Polymers, 2005. **2**(1): p. 53-63.
13. Mouhib, T., et al., *C60 molecular depth profiling of bilayered polymer films using ToF-SIMS.* Surface and Interface Analysis, 2011. **43**(1-2): p. 175-178.
14. Haller, I., *Covalently attached organic monolayers on semiconductor surfaces.* Journal of the American Chemical Society, 1978. **100**(26): p. 8050-8055.
15. Falsey, J.R., et al., *Peptide and small molecule microarray for high throughput cell adhesion and functional assays.* Bioconjugate chemistry, 2001. **12**(3): p. 346-353.
16. Gunda, N.S.K., et al., *Optimization and characterization of biomolecule immobilization on silicon substrates using (3-aminopropyl) triethoxysilane (APTES) and glutaraldehyde linker.* Applied Surface Science, 2014. **305**: p. 522-530.
17. Zhou, Z., S. Zhu, and D. Zhang, *Grafting of thermo-responsive polymer inside mesoporous silica with large pore size using ATRP and investigation of its use in drug release.* Journal of Materials Chemistry, 2007. **17**(23): p. 2428-2433.
18. Vasani, R.B., et al., *Stimulus-responsiveness and drug release from porous silicon films ATRP-grafted with poly (N-isopropylacrylamide).* Langmuir, 2011. **27**(12): p. 7843-7853.
19. Pasetto, P., et al., *Mechanistic insight into surface-initiated polymerization of methyl methacrylate and styrene via ATRP from ordered mesoporous silica particles.* Macromolecules, 2009. **42**(16): p. 5983-5995.
20. Deline, V., et al., *Mechanism of the SIMS matrix effect.* Applied Physics Letters, 1978. **33**(9): p. 832-835.
21. Zhang, F., et al., *Chemical vapor deposition of three aminosilanes on silicon dioxide: surface characterization, stability, effects of silane concentration, and cyanine dye adsorption.* Langmuir, 2010. **26**(18): p. 14648-14654.
22. Li, J.-J., Y.-N. Zhou, and Z.-H. Luo, *Smart fiber membrane for pH-induced oil/water separation.* ACS applied materials & interfaces, 2015. **7**(35): p. 19643-19650.

III. Poly(4-vinyldipicolinic acid)

An innovative functional polymer

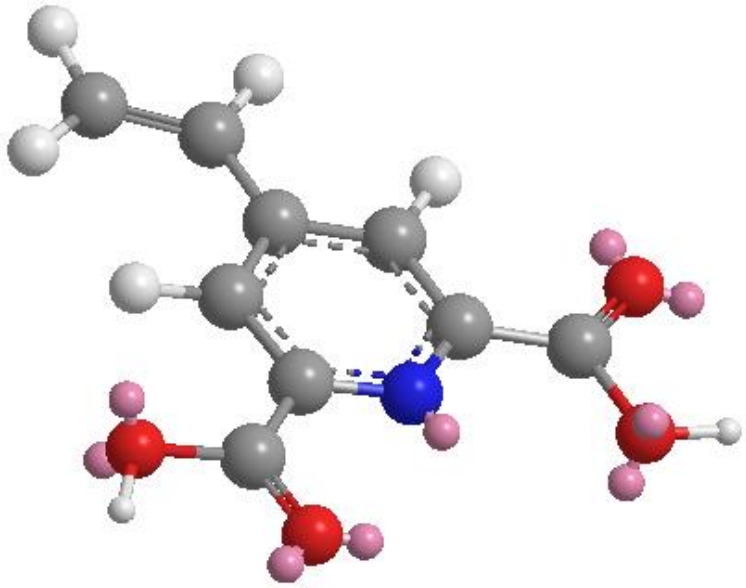

III.1. Introduction

Following the studies conducted on 4VP in chapter II, we move on in this chapter to our new highly chelating polymer that is at the heart of this project. This polymer called poly(4-vinyl dipicolinic acid) (PVDPA) is derived from chelidamic acid which is derived from chelidonic acid (figure 1), a constituent of a plant called *chelidonium majus*. Chelidonic acid is known to have many pharmacological effects, including analgesic, antimicrobial, anti-inflammatory and anti-depressant effects [1-3]. Chelidamic and dipicolinic acids, on the other side, are known to strongly bind to a lot of metals including transition metals, lanthanides and the most important uranium [4-10]. Earlier attempts were made in our lab to attach a polymerizable function on chelidamic acid but strategies were time consuming and the resulting polymers weren't water soluble, nor had the right physicochemical properties to be considered interesting with respect to the application of aqueous radiodecontamination. To the best of our knowledge, PVDPA is indeed a new polymer that has very interesting chelating capacity and physicochemical properties as we will later discuss in chapter IV.

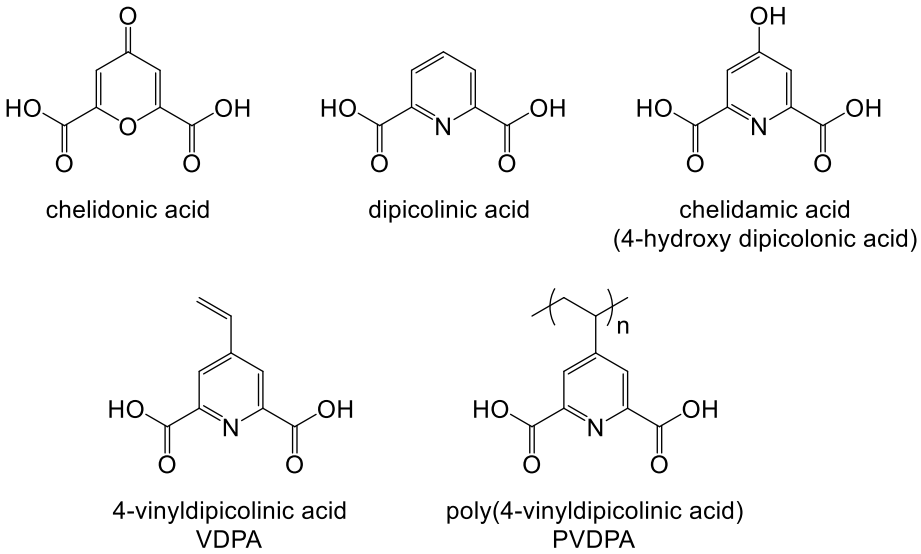

Figure III-1. Chelidonic acid and its derivatives

Chelidonic acid can be obtained synthetically by a simple reaction of acetone with diethyloxalate, and then turned to chelidamic acid (4-hydroxydipicolinic acid) when reacting with aqueous ammonia [11] as shown in scheme 1.

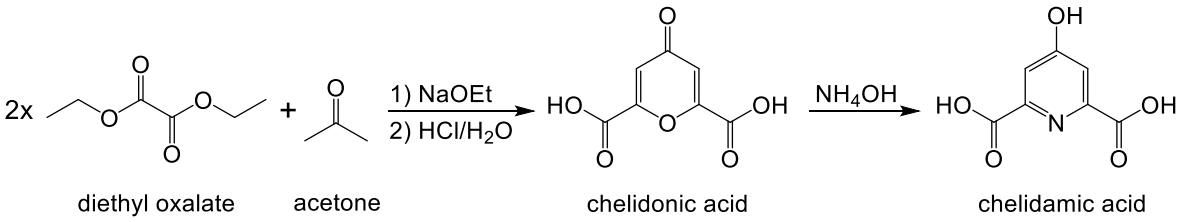

Scheme III-1. Synthetis of chelidamic acid

To synthesize the VDPA monomer from chelidamic acid, one should pass by its 4-vinyl dimethyl dipicolinate (VDPM) ester form as shown in scheme 2. VDPM is then hydrolyzed and the resulting VDPA could be polymerized in water to get the PVDPA polymer. However, aqueous polymerization was found to be a bit too complicated to tame. Furthermore, co-polymerization with hydrophobic co-monomers like styrene will also be challenging (nanoparticles being an exception). An easier strategy would be to polymerize the VDPM ester monomer in an organic medium and the obtained PVDPM could be then easily hydrolyzed to get the water soluble PVDPA polymer (scheme 2).

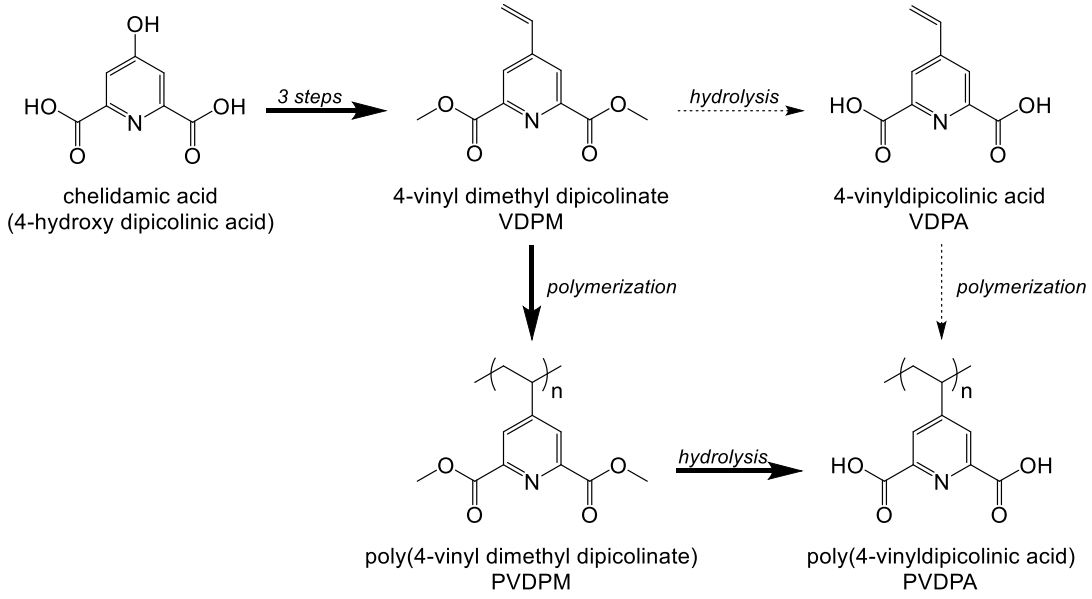

Scheme III-2. Synthesis of PVDPA

In the following sections, the synthesis of the VDPM monomer is detailed. Its polymerization is then discussed in solution and from PET surfaces. Later on, we will describe how we went from PET to poly(vinyl chloride) (PVC) as a more efficient, easier to use substrate for surface-initiated polymerization of the VDPM monomer.

III.2. Synthesis of VDPM monomer

Several strategies were evaluated for the synthesis of the VDPM monomer. Cross coupling reactions between halogenated chelidamic acid and triethoxyvinylsilane were tried either in PEG/water mixture or dioxane as solvents [12]. The coupling reaction was also tried with a vinylboronic acid pinacol ester [13]. The monomer was obtained either in poor yield and/or was too difficult to extract from the reaction medium and purified.

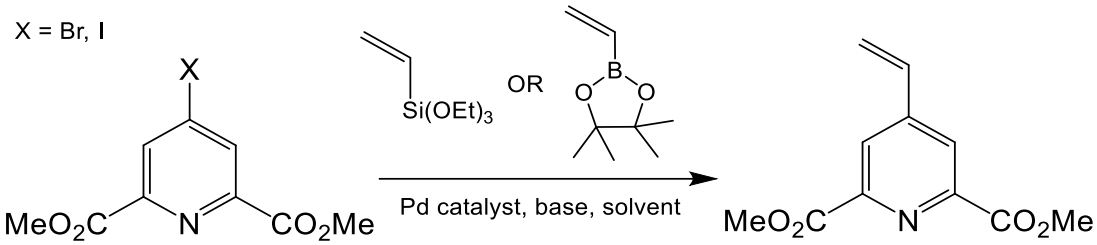

Scheme III-3. VDPM synthesis using triethoxyvinylsilane or a vinylboronic acid pinacol ester

The solution was offered by potassium vinyltrifluoroborate [14-16], which has the advantage of being a potassium salt, much more stable than silanes and boronic esters, in addition to the fact that it affords a product that is easier to isolate and purify with a much higher yield. The overall synthesis was done as follows:

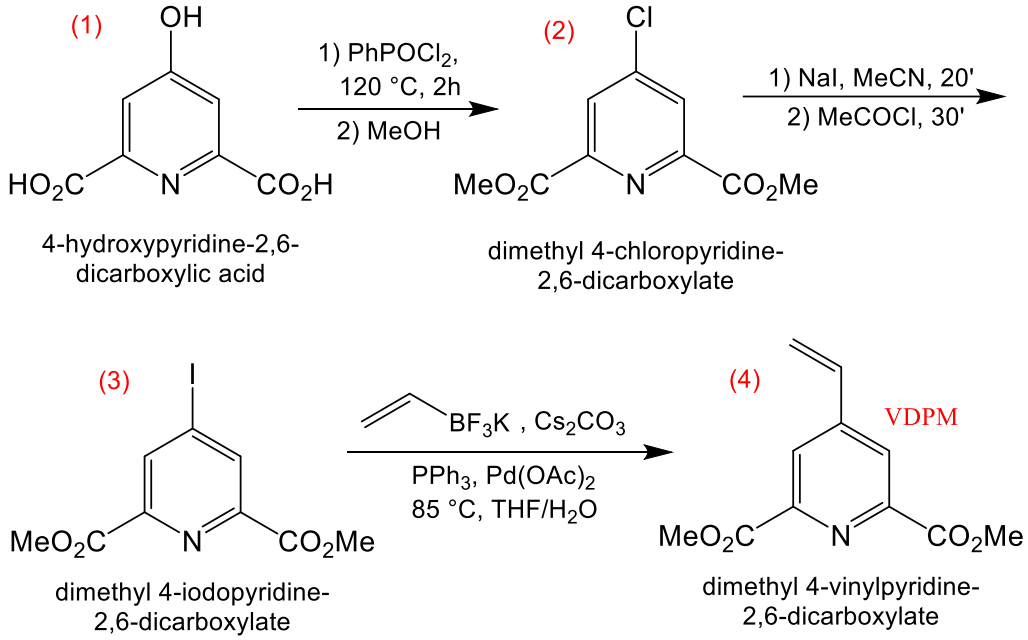

Scheme III-4. VDPM synthesis using potassium vinyltrifluoroborate

Dimethyl 4-chloropyridine-2,6-dicarboxylate (2) was first obtained in good yield according to a literature described two-step procedure involving the reaction of the 4-hydroxypyridine-2,6-dicarboxylic acid (chelidamic acid) hydrate (1) with phenylphosphonic dichloride ($PhPOCl_2$) then treated with methanol in a one pot reaction (yield = 87%).

Dimethyl 4-iodopyridine-2,6-dicarboxylate (3) was then synthesized by the reaction of (2) with sodium iodide (NaI) with acetyl chloride (MeCOCl) to substitute the chloride with an iodide function as a better leaving group for the later Suzuki coupling reaction (yield = 90%).

The VDPM monomer (4) was finally obtained following a palladium catalyzed Suzuki coupling with potassium vinyltrifluoroborate (CH_2=CH-BF_3K). The structure was verified by ^{1}H NMR, especially the vinylic protons at 5.63 (d, 1H, J = 11.1 Hz, C=C$\boldsymbol{H}_{trans}$), 6.14 (d, 1H, J = 17.4 Hz, C=C$\boldsymbol{H}_{cis}$) and 6.75 (dd, 1H, J = 17.4 Hz, J = 11.1 Hz, C$\boldsymbol{H}$=CH_2). ^{13}C NMR and ESI mass spectrometry further proved the monomer structure (yield = 70-80%).

All protocols are detailed in “materials and methods”.

III.3. Polymerization of VDPM in solution

Inspired by the SARA ATRP polymerization of 4VP (chapter II), the polymerization of the new VDPM monomer was conducted. Reaction conditions were optimized and the obtained polymers were characterized. Benzyl chloride (BnCl), $CuCl_2$, TPMA and Cu^0 were kept as initiator, catalyst, ligand and reducer, respectively, in the polymerization system. DMSO, and later acetonitrile, were used as solvents. The reaction was conducted both at 30° and 50 °C.

III.3.1. PVDPM homopolymer

SARA ATRP was first used for the homopolymerization of the new VDPM monomer as follows:

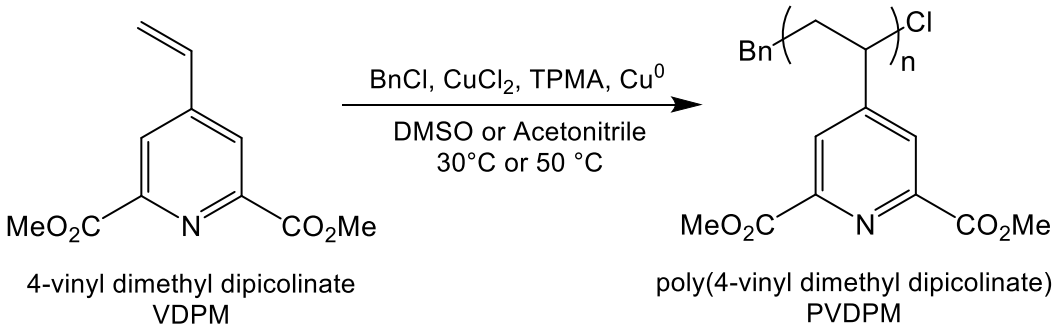

Scheme III-5. SARA ATRP polymerization of VDPM

The monomer concentration was kept at 0.5 M in DMSO or acetonitrile (T= 30 or 50 °C), metallic copper wire was fixed at 1 cm/mL and initial molar ratios for the polymerization system components were as follows:

$$VDPM / BnCl / CuCl_2 / TPMA = 100 / 1 / 0.01 / 0.4$$

A successful polymerization was verified by ^1H NMR ($CDCl_3$) and the reaction kinetics were studied by following the disappearance of the vinyl proton peaks at 5.32 ppm, 5.83 ppm and 6.45 ppm as references for 1 proton each (figure 2).

To note that concentrations and molar ratios in the polymerization reaction were modified with respect to those used for 4VP (chapter II) in order to obtain a first order kinetics.

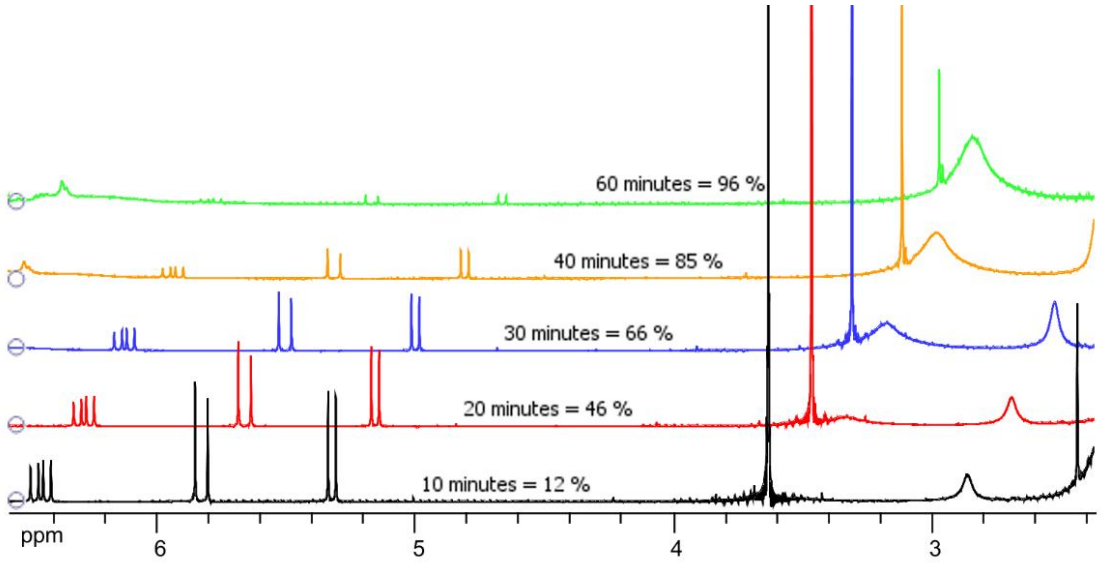

Figure III-2. VDPM homopolymerization monitored by ^{1}H NMR ($CDCl_3$)

The monomer conversion was then calculated using the methyl protons peak (6 protons) at 3.63 ppm that turns from a high singlet in the monomer form to a larger peak at 3.49 ppm in the polymer form. The monomer conversion is then calculated using the peak area $\mathcal{A}$ in the region between 3.10 ppm and 3.95 ppm as follows:

$$VDPM\ monomer\ conversion\ (\%) = \frac{\mathcal{A}_{3.10-3.95\ ppm} - 6}{\mathcal{A}_{3.10-3.95\ ppm}} \times 100$$

Reaction kinetics and polymer characteristics are summarized in table 1 and figure 3.

Table III-1. VDPM polymerization kinetics

Time (min)	Conversion (%)	Mn (NMR) 10^3 gmol^{-1}	Mn (RI) 10^3 gmol^{-1}	Mn (LS)** 10^3 gmol^{-1}	Đ (RI)
10	10	2.2	70 (19)*	58 (21.8)*	1.2 (2.7)*
20	45	9.9	63	64.5	1.7
30	65	14.4	50	47.8	1.7
40	85	18.8	43	45.2	2
60	96	21.2	34	34.4	2.5

VDPM / BnCl / CuCl2 / TPMA = 100 / 1 / 0.01 / 0.4

* At 10% conversion, calculations were made without and (with) the shoulder peak at higher elution volume

** with dn/dc in DMF estimated at 0.16 mL/g similar to that of P4VP

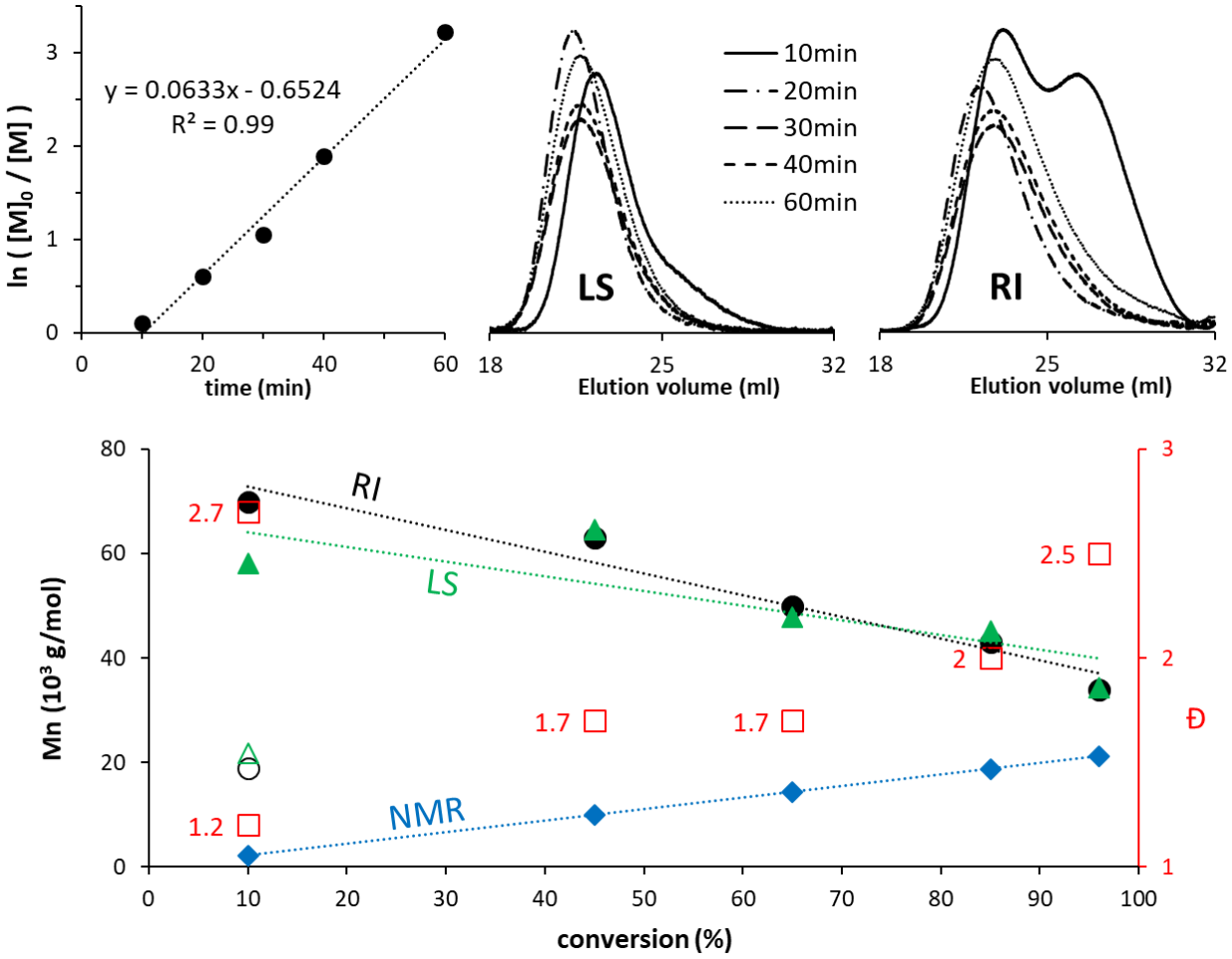

Figure III-3. VDPM polymerization kinetics. ln ($[M]_0/[M]$) vs time (up left); LS (up middle) and RI (up right) SEC traces and obtained molar masses as a function of monomer conversion (down)

The first order kinetic behavior shown in figure 3 (up left) by the linear increase of $\ln([M]_0/[M])$ as a function of reaction time suggests fast initiation and limited chain termination under the used reaction conditions, a sign of a good reaction livingness.

SEC results, however, are a whole different story. First of all, the SEC traces show a double population at 10% conversion and important tailing at higher conversions. Going from 1 to 9 hours of reaction time and monomer conversions from 10 to 96%, the calculated Mn (NMR) values go from 2.2 up to 21.1 $kg.mol^{-1}$, correspondingly. However, Mn (RI) values decrease from 70 down to 34 $kg.mol^{-1}$ (with respect to PMMA standards) and Mn (LS) values from 58 down to 34.4 $kg.mol^{-1}$ as shown in table 1 and figure 3.

Surprisingly, calculated Mn (RI) and Mn (LS) are inversely proportional to monomer conversion. Polymer samples are eluted in a wrong order and longer chains seem to be more delayed than short ones, an unusual behavior for a size-dependent SEC analysis.

We suspected an adsorption phenomenon induced by an interaction between the ester functions of PVDPM and the column's polyester stationary phase. The fact that our PVDPM polymer has two ester functions on each repeating unit means that an adsorption phenomenon may give flawed results. Longer chains have more ester functions and therefore adsorb more to the stationary phase and are retained more than short chains.

Fortunately, the system was equipped with a light scattering (LS) detector which should be able to estimate molar masses independently of elution order. However, Mn (LS) values and behavior were similar to Mn (RI) as shown in table 1 and figure 3 (down). This observation may be the result of polymer aggregation or self-assembly in DMF. Interestingly, this aggregation phenomenon seems to be inversely proportional to polymer chain length and is most pronounced for small chains as seen in figure 3.

To conclude, the SEC analysis remains a challenge and the control over PVDPM chain length distribution remains unknown, which should be a priority in future studies. For now, only the livingness of the polymerization reaction was proven. In the next section, MALDI-ToF will be used to see whether or not the chlorine chain ends are preserved.

MALDI-ToF:

A PVDPM sample of an estimated molar mass of 17 $kgmol^{-1}$ (77 repeating unit) was analyzed by MALDI-ToF in an AcN-DCTB matrix. In the obtained spectrum (figure 4), the signals are separated by ~221.1 units, which corresponds to molar mass of VDPM repeating unit. The molar masses of individual species correspond to the expected structure as can be seen in the zoomed views in figure 4, with the chlorine atom always present.

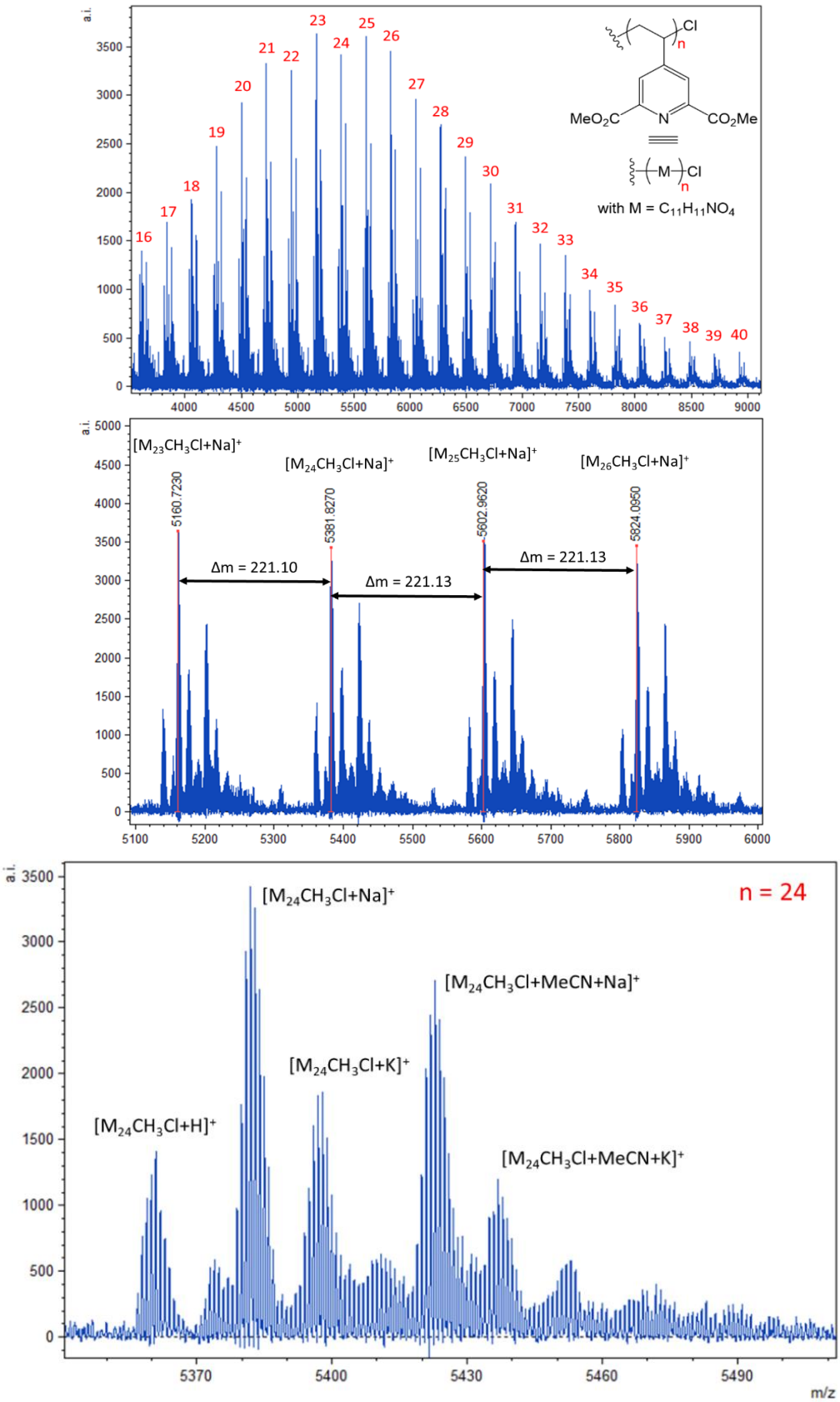

Figure III-4. MALDI-ToF analysis of PVDPM

The most important information drawn from this MALDI-ToF analysis was that the chain-end's chlorine atom was preserved, a proof of the livingness of the polymerization reaction, which will later allow us to reach high chain lengths, an important feature which will be proven essential to synthesize highly absorbing surfaces, later discussed in the chapter IV. It should be noted that the spectrum in figure 4 doesn't reflect the real molar mass nor the chain lengths distribution of the analyzed sample due the high dependence of the signal intensities on the polymer structure and experimental conditions like the solvent, the matrix and the ionization energy, making it difficult to extract heavier chains without optimizing each parameter.

In the following section, the copolymerization of VDPM monomer with styrene will be discussed.

III.3.2. Poly(VDPM/styrene) copolymers

Even if the radiodecontamination in aqueous environments is the main application targeted in our work, it should be interesting to explore different strategies that allow the tuning of the physicochemical properties of PVDPA if the polymer is to be used in different environments like in organic media, or where a specific set of properties is needed to build certain surface architectures (ex: honeycomb architecture). Herein, the copolymerization of VDPM with styrene is examined.

III.3.2.1. Styrene homopolymerization

The SARA ATRP of styrene is described in the literature [17]. We began by adapting it to our system and the modified reaction is described as follows:

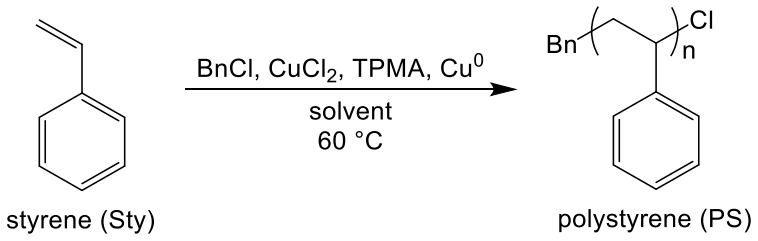

Scheme III-6. SARA ATRP polymerization of styrene

The reaction kinetics were investigated and the ln ($[M]_0$ / [M]) = f (polymerization time) plots of the styrene polymerization in different solvents are shown in figure 5.

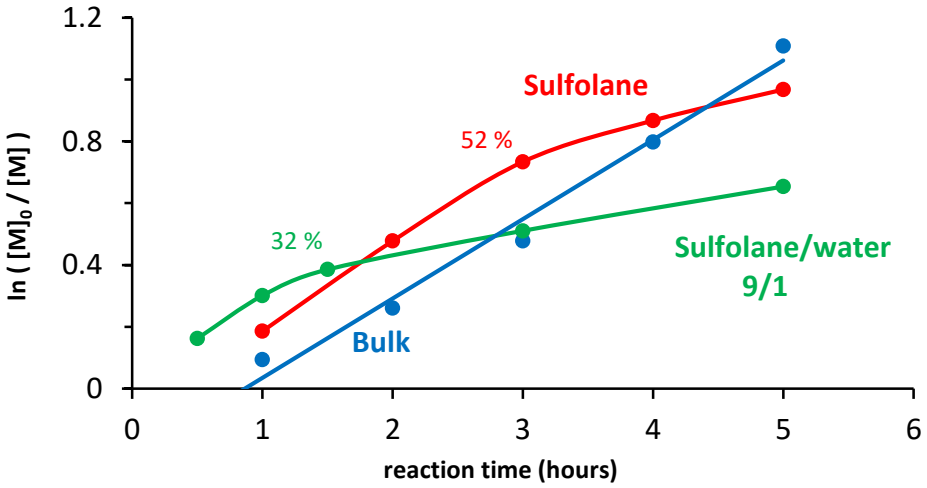

Figure III-5. Styrene homopolymerization kinetics

The above plot shows that initiation was fastest in sulfolane/water, followed by sulfolane then by the bulk polymerization. However, in sulfolane/water, the propagation slowed down dramatically after ~30 % monomer conversion, probably due to decreasing solubility of polystyrene chains at higher conversion in the sulfolane/water mixture. In sulfolane alone, the propagation slowed down after ~52 % but stayed efficient. The bulk polymerization showed an efficient and consistent propagation throughout the reaction.

It's worth mentioning also that in an attempt to further reduce that copper load in the reaction, metallic copper reducer was replaced with sodium dithionite ($Na_2S_2O_4$) according to [18] and the reaction was doped with 2%v water to slowly solubilize the sodium salt into the system. Perfectly controlled polystyrene was obtained (Đ = 1.09).

The synthesized polystyrene was analyzed by NMR and SEC and excellent control was achieved. Main results are shown in table 2.

Table III-2. Polystyrene obtained in different polymerization conditions

$CuCl_2$ / BnCl	solvent	reducer	time	conversion (%)	Mn (NMR) 10^3 gmol^{-1}	Mn (SEC) 10^3 gmol^{-1}	Đ (SEC)
0.02	bulk	Cu (0)	5 h	67	6.98	7.87	1.12
0.02	sulfolane	Cu (0)	5 h	62	6.46	6.76	1.18
0.02	sulfolane/water (9/1)	Cu (0)	5 h	49	5.1	5.11	1.16
0.1	sulfolane/water (98/2)	$Na_2S_2O_4$	> 24 h	34	3.54	3.35	1.09

T = 60 °C and styrene / BnCl / TPMA = 100 / 1 / 0.2

The styrene homopolymerization was successful. Nevertheless, when compared with VDPM polymerization, higher temperature (60 °C) was needed, and another solvent (sulfolane) was used. The non-solubility of polystyrene in acetonitrile and DMSO caused the polymerization reaction to be terminated too early due to the precipitation of polystyrene. These results made the VDPM/styrene copolymerization more challenging.

It should be mentioned also that even though excellent control of polystyrene chain lengths was achieved using $Na_2S_2O_4$ as a reducer, applying this technique to VDPM polymerization was not straightforward and further studies would be needed. We maintain then Cu^0 as a reducer for subsequent studies.

III.3.2.2. VDPM/styrene copolymerization

Several attempts were made to have a successful copolymerization between VDPM and styrene, the overall reaction is described as follows:

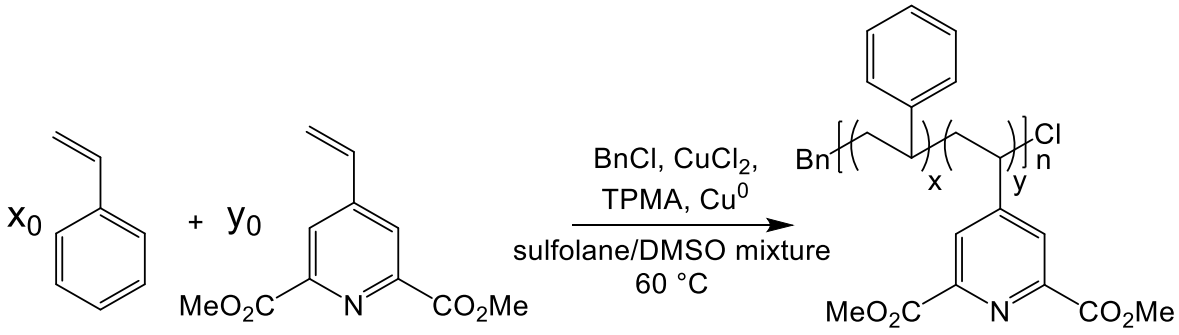

Scheme III-7. SARA ATRP copolymerization of VDPM/styrene

Different types of copolymers can be obtained depending on the polymerization system components and reaction conditions (choice of solvents, delayed comonomer injection…). SARA ATRP polymerization allowed us to synthesize linear copolymers (statistical, gradient and block copolymers) and classical radical polymerization in aqueous solution using VDPA (hydrolyzed VDPM) comonomer allowed the synthesis of monodisperse latex nanoparticles with polystyrene core and PVDPA shell. These different copolymers are described in scheme 8.

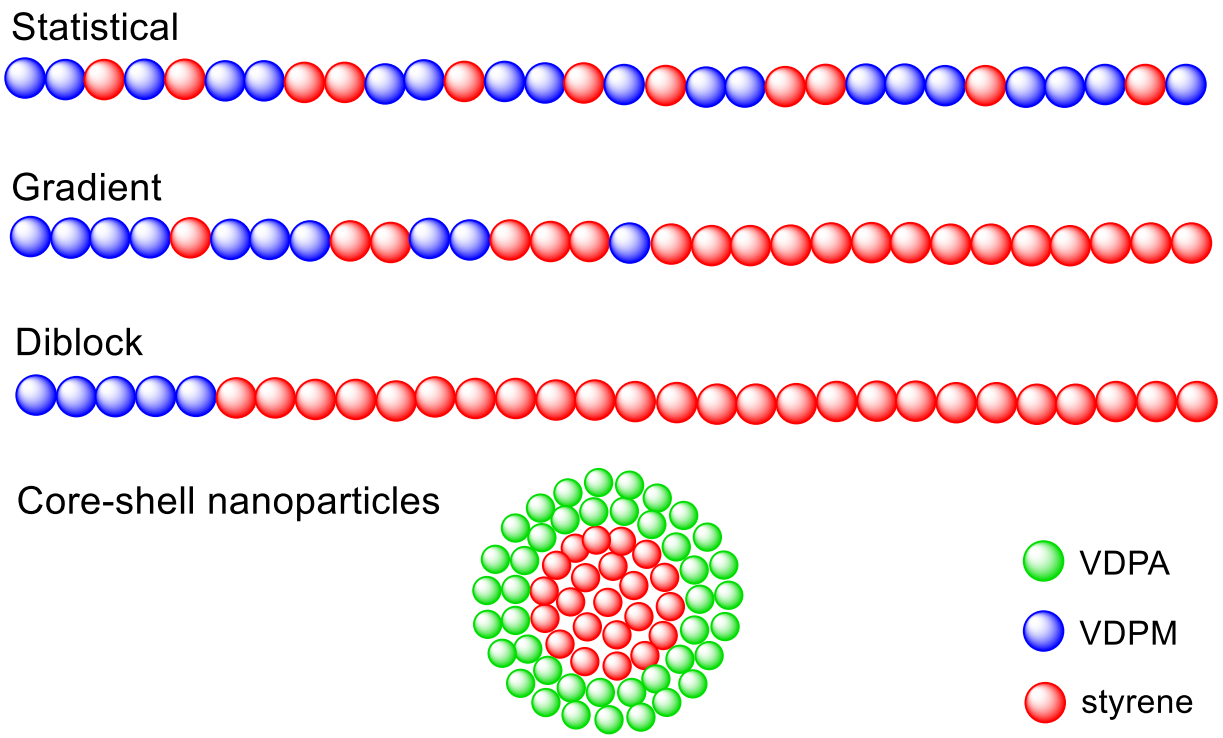

Scheme III-8. Different styrene/VDPM copolymers

III.3.2.2.1. Statistical copolymer

The statistical copolymer was obtained by the simultaneous copolymerization of a 1/1 ratio of the two comonomers ($x_0 = y_0$) in a sulfolane/DMSO mixed solvent at 60 °C. Initial molar ratios of the polymerization system components were as follows:

Styrene / VDPM / BnCl / $CuCl_2$ / TPMA = 50 / 50 / 1 / 0.2 / 4

The ^1H NMR ($CDCl_3$) spectrum (figure 6) of the purified polymer showed that indeed a statistical copolymer was obtained, with methyl protons from VDPM appearing at 3.91 ppm, and the aromatic protons from both comonomers visible between 5.8 and 7.8 ppm. Nevertheless, peaks integrations shown that the VDPM comonomer was more incorporated into the copolymer with 65 % contribution, against 35 % for styrene comonomer as shown in figure 6.

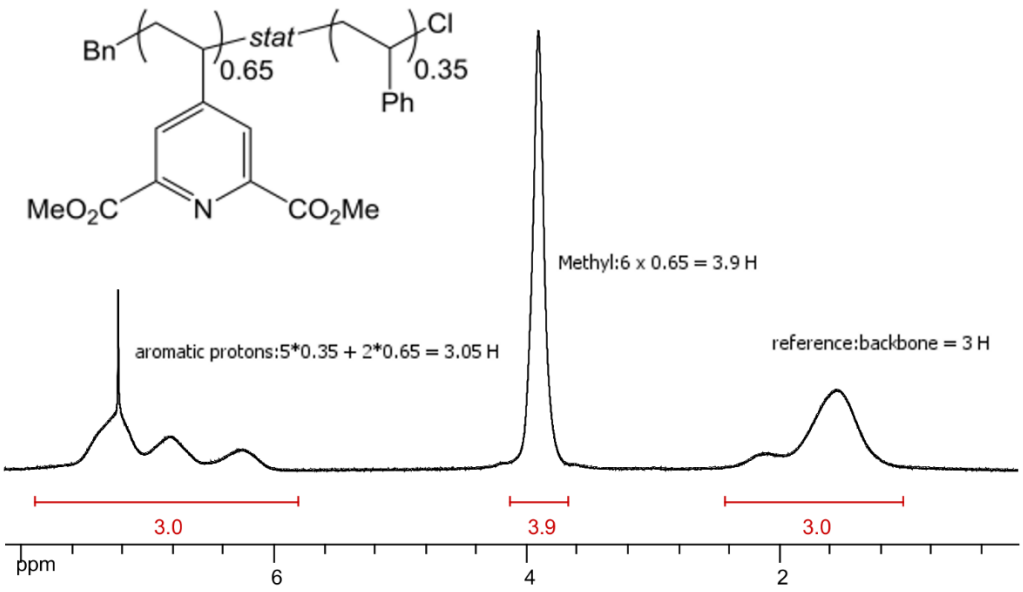

Figure III-6. ^{1}H NMR spectrum of VDPM/styrene statistical copolymer

We saw earlier that the two separate homopolymerizations have different kinetics, where the VDPM reaches total conversion within one hour (figure 3) while the styrene takes several hours to reach similar conversions (figure 5). This can explain the fact that, in the statistical copolymer, the VDPM comonomer is more present as it is more reactive than styrene, which will later help us synthesize the gradient then the diblock copolymer.

III.3.2.2.2. Gradient copolymer

This time, an initial VDPM comonomer ratio of 5 % (i.e. x_0/y_0 = 95/5) was used in the following system: Styrene / VDPM / BnCl / $CuCl_2$ / TPMA = 95 / 5 / 1 / 0.01 / 0.44

As expected, the more reactive VDPM comonomer was incorporated faster than styrene. The result was a gradient copolymer where the VDPM units are relatively dense at the beginning of the polymerization and become diluted with increasing chain lengths.

The ln ($[M]_0$ / [M]) = f (polymerization time) plot (figure 7) shows how VDPM has both higher initiation and propagation rates when compared to the styrene comonomer.

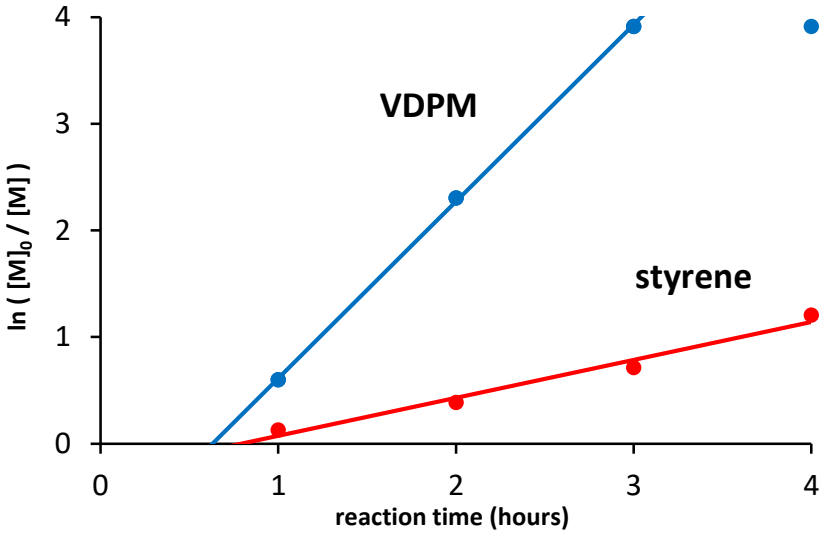

Figure III-7. Gradient copolymerization kinetics

Once the copolymers was precipitated in methanol and purified, its ^{1}H NMR spectra (figure 8) allowed us to determine the VDPM incorporation in the final copolymer. Taking the VDPM's methyl peak at ~4 ppm as a reference for 6 protons, VDPM incorporation was calculated as follows:

$$VDPM\ comonomer\ incorporation\ (\%) = \frac{1}{(\mathcal{A}_{6-8\ ppm} - 1)/5} \times 100$$

where aromatic protons from both comonomers are gathered under the peak between 6 and 8 ppm.

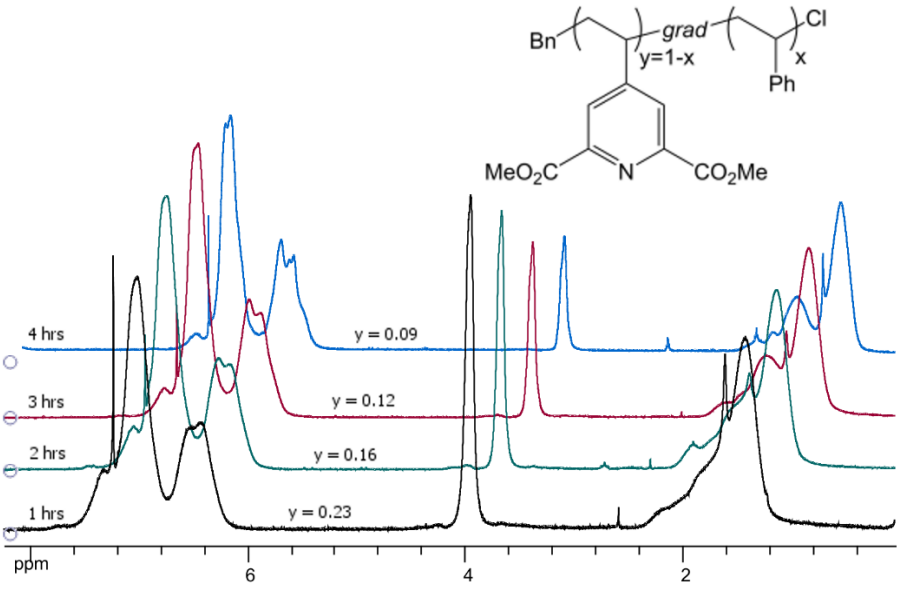

Figure III-8. ^{1}H NMR spectra of gradient copolymers after different reaction times (hours), y = VDPM comonomer incorporation

The molar masses calculated from NMR were compared with those determined by SEC analysis. Results are shown in table 3 and plotted as a function of styrene comonomer conversion in figure 9.

Table III-3. Gradient copolymer kinetics

time (hours)	Styrene conversion %	VDPM conversion %	VDPM incorporation %	Mn (NMR) 10^3 g.mol^{-1}	Mn (SEC) 10^3 g.mol^{-1}	Đ (SEC)
1	12	45	9	1.8	4.6	1.5
2	32	90	12	4.3	5.4	1.42
3	51	> 98	16	6.3	6.6	1.33
4	70	> 98	23	8.1	8.9	1.26

Styrene / VDPM / BnCl / $CuCl_2$ / TPMA = 95 / 5 / 1 / 0.01 / 0.44
Solvent: sulfolane, T = 60 °C

As shown in table 3, between 1 and 4 hours of polymerization, styrene conversion went from 12 to 70% and VDPM conversion from 45 to 98%, giving a theoretical Mn (NMR) between 1.8 and 8.1 10^3 g.mol^{-1} and a measured Mn (SEC) between 4.6 and 8.9 10^3 g.mol^{-1}, correspondingly.

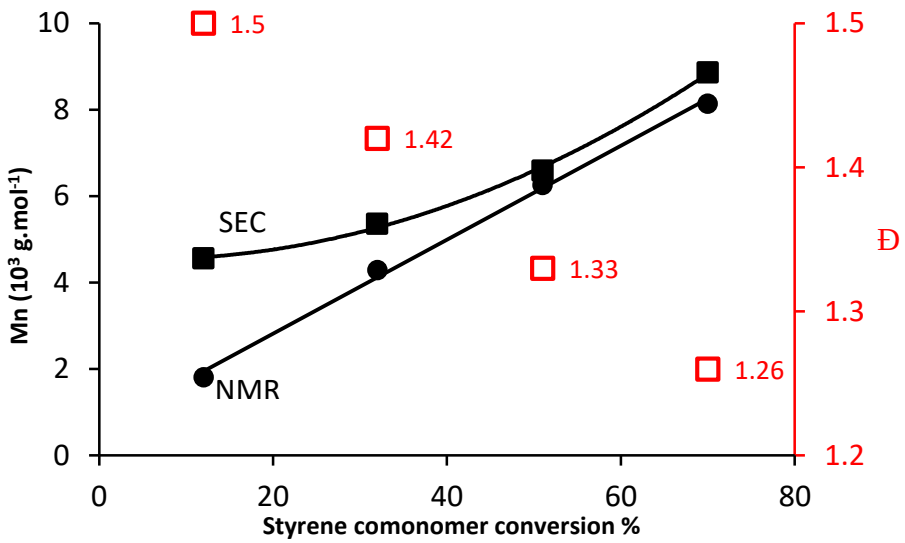

Figure III-9. Mn (SEC), Mn (NMR) and dispersity (Đ) as a function of styrene comonomer conversion (%)

When plotted in figure 9, a non-classical behavior is observed. First of all, the Mn (SEC) began far from Mn (NMR) and the two values became closer at higher styrene conversion. Đ was also much higher at first, and linearly decreased as a function of styrene conversion. In order to explain this phenomenon, we have to keep in mind that the VDPM component is not soluble in the THF eluent, causing an important change in the hydrodynamic volume of the resulting copolymer in THF, when compared with the polystyrene standard. This change is more important with high VDPM incorporation in the final copolymer. Knowing that in our case, VDPM incorporation ratio decreased in longer copolymers (and styrene component became more dominant), we can reasonably predict that longer copolymers behaved more like pure polystyrene than shorter ones. This hypothesis can explain the closer results at higher styrene conversion between the two Mn (NMR and SEC), and the apparent decrease in dispersity Đ.

III.3.2.2.3. Block copolymer

Finally, we took advantage of the higher reactivity of VDPM to synthesize a PVDPM-*block*-PS copolymer in a one pot reaction. We began by polymerizing the VDPM comonomer to a 10 units long oligomer (VDPM/BnCl = 10) in DMSO at 60 °C. After ~30 minutes, NMR showed complete VDPM conversion. At this point, styrene comonomer (St/BnCl = 400) was injected followed with sulfolane. The overall molar ratios are:

$$\text{Styrene / VDPM / BnCl / } CuCl_2 \text{ / TPMA = 400 / 10 / 1 / 0.02 / 0.4}$$

Styrene conversion was monitored by NMR and block copolymers with variable polystyrene block lengths were obtained depending on reaction time. Below is the ^{1}H NMR ($CDCl_3$) spectrum of a PVDPM$_{10}$-*block*-PS$_{165}$ copolymer:

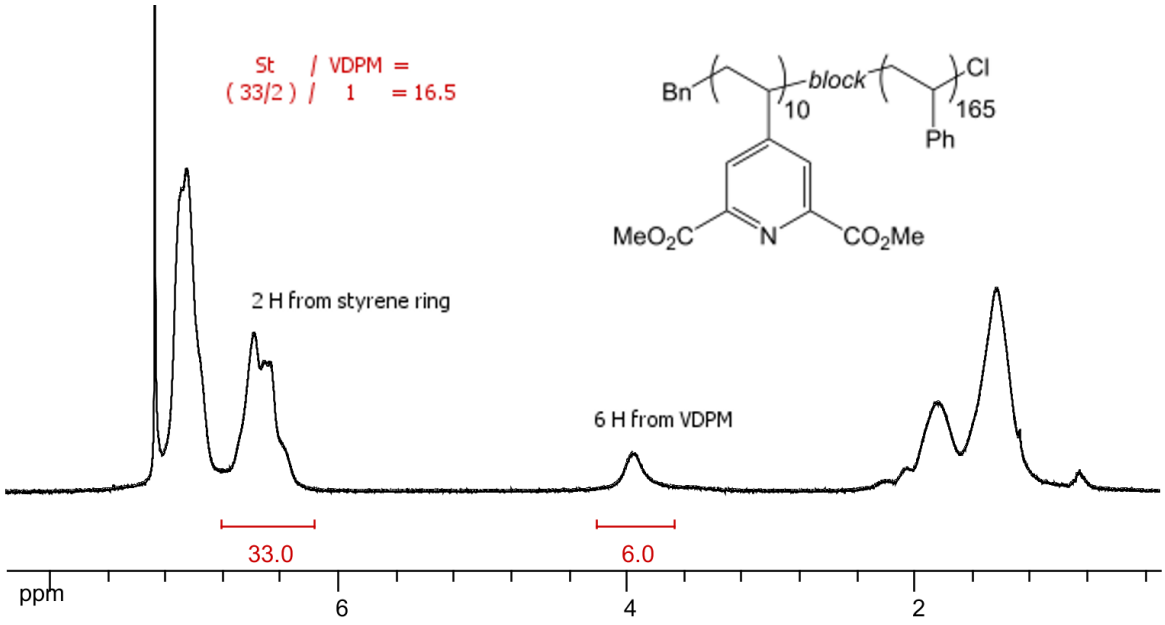

Figure III-10. ^{1}H NMR spectrum of the PVDPM$_{10}$-block-PS$_{165}$ copolymer

III.3.2.2.4. Core-shell nanoparticles

VDPA was obtained by hydrolyzing the VDPM monomer in NaOH 1 M. Afterwards, concentrated HCl allowed the protonation of VDPA which precipitates in water and can be then recovered by filtration. VDPA was then dissolved back in water and used to synthesize core-shell nanoparticles when copolymerized with styrene.

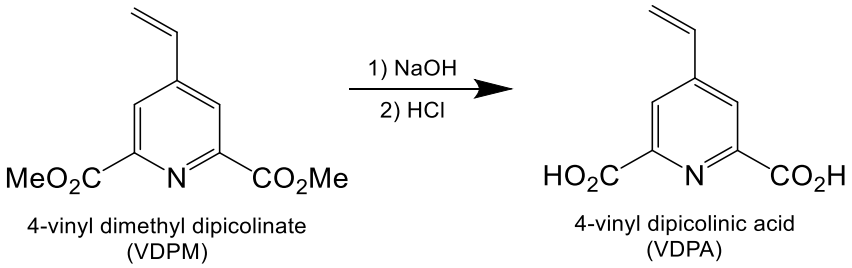

Scheme III-9. VDPM hydrolysis to VDPA

Briefly, styrene was injected in an aqueous solution of deprotonated VDPA (pH = 8 adjusted with NaOH) under inert atmosphere and constant stirring, the solution was heated gradually to 70 °C before injecting the potassium persulfate ($K_2S_2O_8$, KPS) initiator. Nanoparticle average diameter was monitored by DLS and the reaction was stopped at 2 hours. The nanoparticles suspension was dialyzed to remove excess comonomers and analyzed. Stable monodisperse nanoparticles were obtained, having a polystyrene core and PVDPA shell. DLS analysis (figure 11) shows the monodispersity of the nanoparticles and that an average diameter of 70 nm (PdI = 0.04) was obtained after 30 minutes of polymerization and reached 82 nm (PdI = 0.08) after 2 hours.

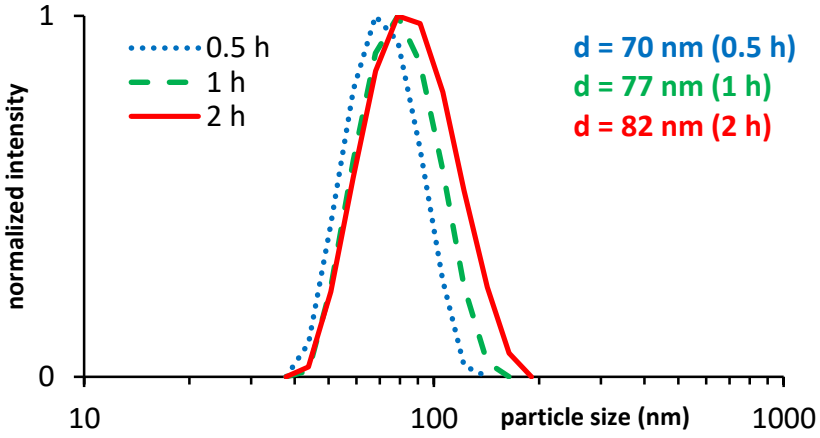

Figure III-11. DLS analysis of the latex core-shell nanoparticles

To prove that a PVDPA shell is successfully obtained, the pH of the nanoparticles aqueous suspension was modified (figure 12). At high pH, the nanoparticle average diameter increased from 82 nm (neutral) to 92 nm (alkaline), probably due to the swelling of the negatively charged PVDPA shell. At low pH, the monodispersity is lost due to a visible aggregation. The higher population at around 270 nm corresponds to an expected behavior of a protonated PVDPA shell, which is no more stable in aqueous media and tend to precipitate.

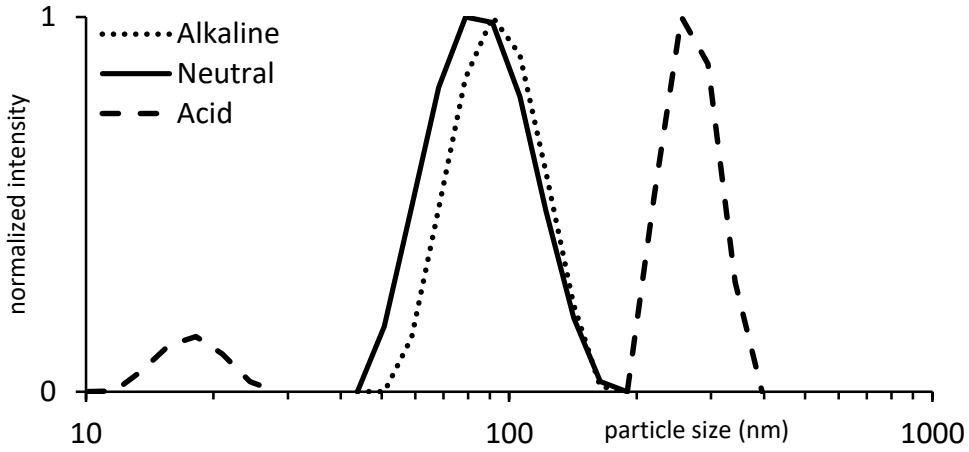

Figure III-12. DLS analysis of the latex suspension at different pH

Furthermore, when seen under a scanning electron microscope (figure 13), nanoparticles (neutral pH) had an average diameter of 65 nm. The downshift from DLS diameter (82 nm) is probably due to SEM conditions where the nanoparticles are dried, causing them to shrink, proving once more that PVDPA is actually present at the nanoparticles shell.

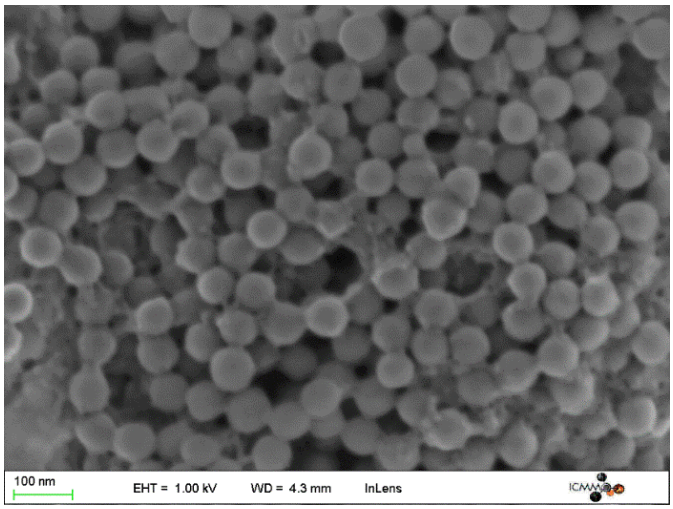

Figure III-13. SEM image of the latex nanoparticles

III.4. PVDPM functional surfaces

Once the VDPM successfully polymerized in solution, we proceeded to the surface-initiated polymerization on different substrates. Obviously, we began with modifying a PET substrate after this strategy was successfully used for 4VP (chapter II), we later dropped out PET as a substrate in favor of PVC-based substrates. In this section, we will explain how this transition from PET to PVC allowed us to reach higher degrees of surface functionalization, all with an even more simplified and efficient procedure.

III.4.1. PVDPM on PET surfaces

PET surface was modified according to a strategy similar to the one used with 4VP (chapter II). Under the proper reaction conditions, PVDPM chains were built on PET surface according to scheme 10.

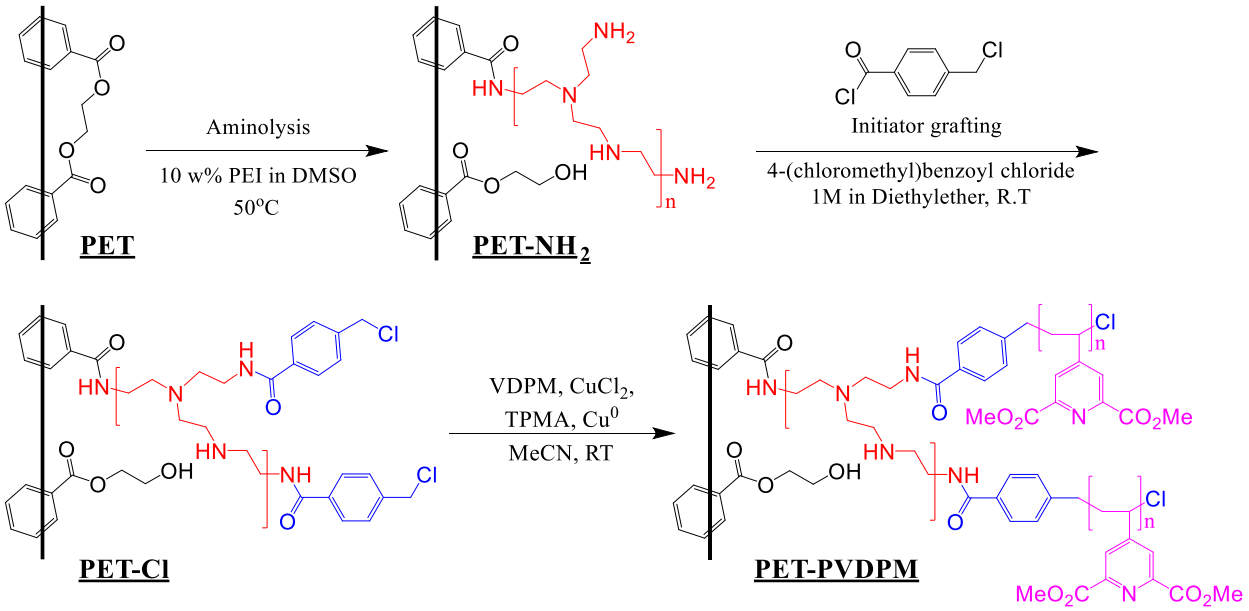

Scheme III-10. PET-initiated VDPM polymerization

The modification protocols are detailed in "materials and methods". Similarly, the obtained surfaces were examined using different surface characterization techniques.

ATR:

Infrared ATR spectroscopy gave the first evidence of a successful PET surface modification. The Spectrum of the modified surface (24 hours polymerization time) was compared to both non-modified PET surface and pure PVDPM spectra as shown in figure 14.

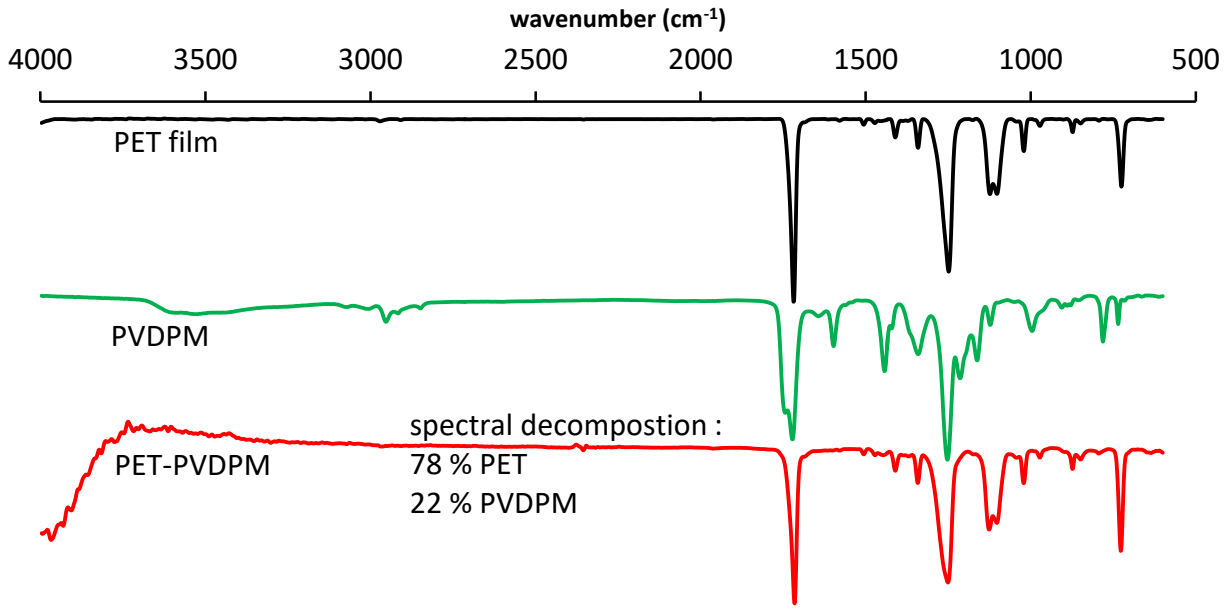

Figure III-14. ATR spectra of PET-PVDPM surface

Knowing that ATR can detect molecular vibrations from down to a 2 µm depth, it was too difficult for the naked eye to clearly see peaks coming from the few nanometer thick PVDPM layer. This obstacle was overcome with a spectral decomposition using Fluortools™ software that showed 22% spectral contribution for PVDPM on the final surface, proving a successful grafting of a PVDPM layer. Spectral decomposition is a mathematical operation that determines the contribution of different components, PET and PVDPM in this case, in the mixed ATR spectrum. It's worth mentioning that when PET fibers (not films) were similarly modified, only 6% spectral contribution was detected.

ATR is then followed by the more surface sensitive x-ray photoelectron spectroscopy (XPS).

XPS:

PET surfaces were analyzed by XPS after each step of modification in the strategy described in scheme 10. XPS surveys are shown in figure 15 and elements contribution can be seen in table 4.

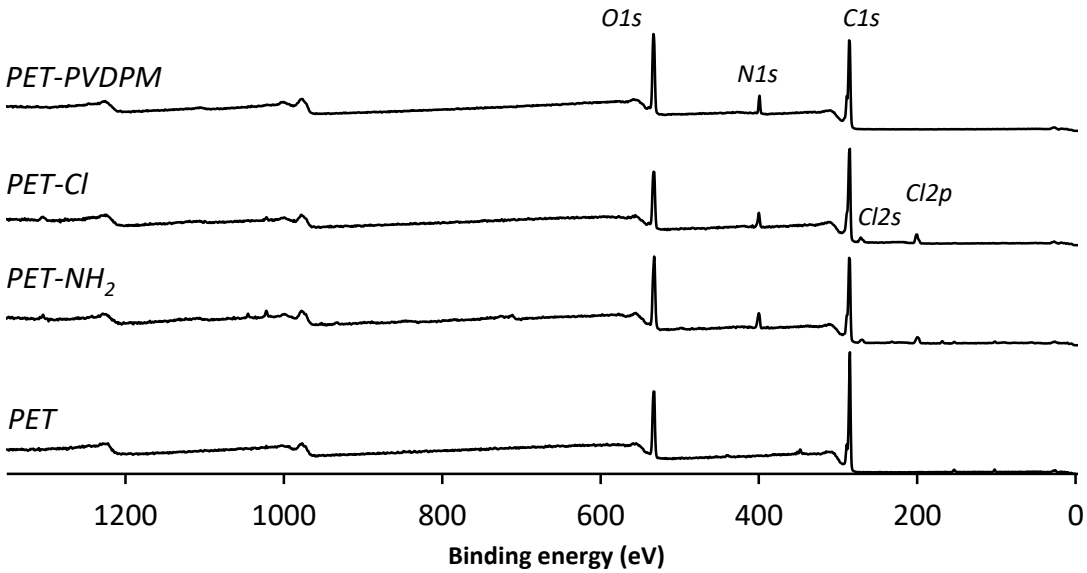

Figure III-15. XPS survey of modified PET surfaces

Table III-4. Elements contribution on the modified PET surfaces

Atomic %	*PET*	*PET-NH$_2$*	*PET-Cl*	*PET-PVDPM*
C	77	68	70	72
N	-	7	5	4
O	23	25	17	24
Cl	-	-	4	-

The analysis of spectra and elements contributions clearly show the successful modification of the PET substrate. Detailed analysis of PET, PET-NH_2 and PET-Cl surfaces was discussed earlier in chapter II. The high resolution XPS analysis of the final PET-PVDPM surface is shown in figure 16.

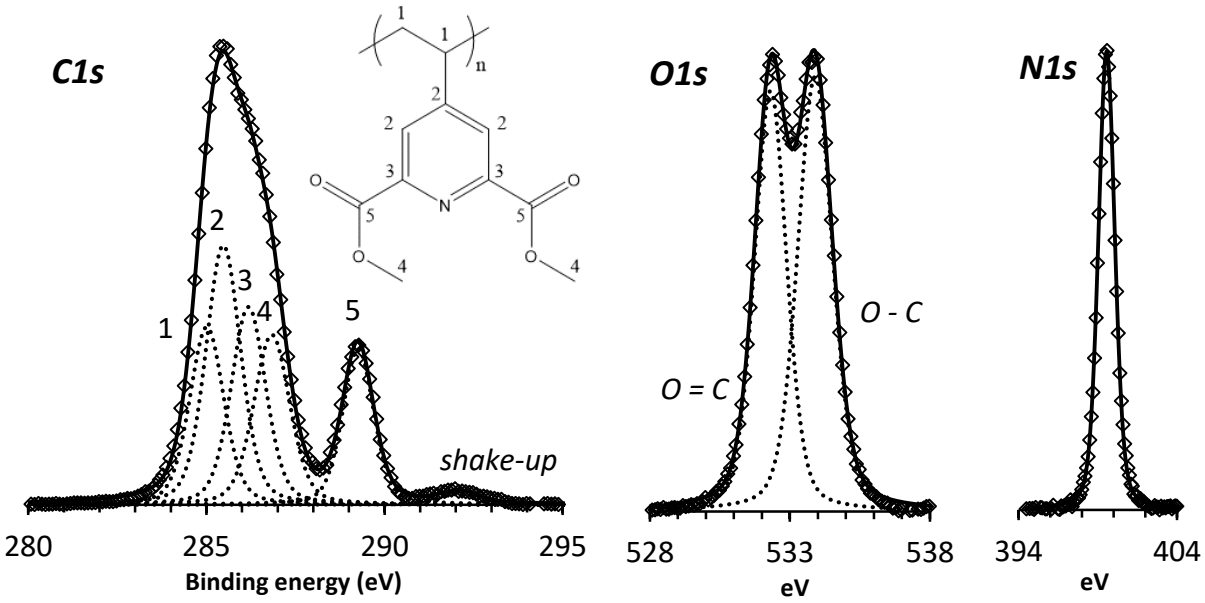

Figure III-16. High resolution XPS spectra of the PET-PVDPM surface

Table III-5. Total elemental contribution and atomic ratios on the PET-PVDPM surface

	Peak BE	Exp %	Calc %
C	285.12	72	69
O	532.79	24	25
N	399.19	4	6

	Experimental	Calculated
C/N	12.1	11.5
C/O	2.99	2.76
O/N	4.05	4.17

Looking at the elemental ratios (table 5), experimental results agree perfectly with the theoretical (calculated) ratios expected from a pure PVDPM layer. XPS here proves a successful PET modification with a homogenous PVDPM outer layer of a minimal thickness greater that XPS's probing depth of 10 nm.

We concluded that, just like in the case of 4VP (chapter II), VDPM was successfully polymerized from a PET surface. In the next section, we will discuss how and why PET was later replaced by PVC as more convenient substrate to synthesize the desired functional surfaces.

III.4.2. PVDPM on PVC surfaces

Throughout this project, we always looked to simplify our strategies to obtain the final functional surfaces. We considered that the PET modification process, even if proved to be successful, still had the inconvenience of being a multiple step strategy with the need for prior aminolysis and grafting of the BnCl radical initiator, which limited the economic viability of this strategy. In addition to that, we saw that only a few dozen nanometers of PVDPM were grafted on the PET surface, probably limiting the absorbing capacity of these surfaces. Therefore, we looked for an alternative substrate which can fulfil the following conditions:

- The substrate should be commercially available in the form of fibers just like PET and at a low cost.
- The substrate should offer chemical and physical resistance that at least matches PET and should be usable in an aqueous environment.
- The substrate should have additional advantages to explain the transition from PET. Most importantly, it should be easier to modify, and should allow the grafting of a much thicker layer of PVDPM.

The solution was brought by PVC, a widely available substrate, especially in the form of fiber, which offers high chemical and mechanical resistance, especially in aqueous environment. This simplified strategy for VDPM polymerization on PVC substrate is described as follows:

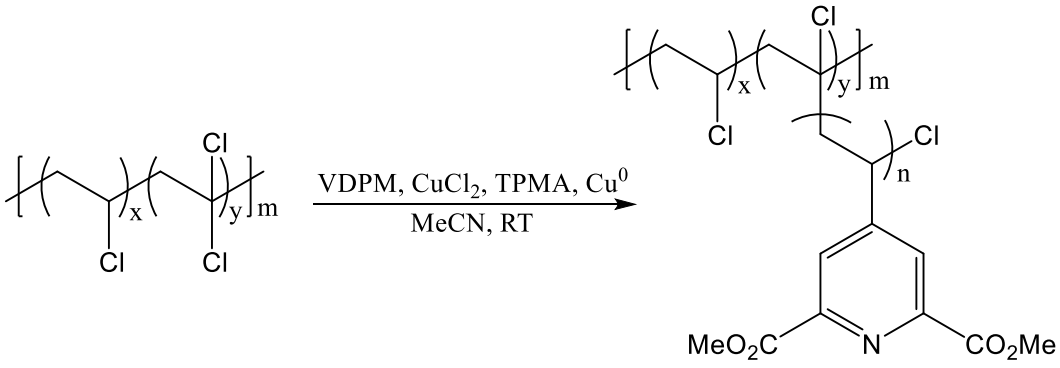

PVC - co - CPVC (PVC-co-CPVC) - *graft* - PVDPM

Scheme III-11. PVC-initiated VDPM polymerization

PVC has the advantage of having a chlorine atom in its polymer's repeating unit (**x**) with variable levels of doubly chlorinated units (**y**) called labile chlorines (scheme 11), a ready to use radical initiator for subsequent polymerization. This very important property would reduce the modification process to only one functionalization step. This strategy was first applied on pure PVC powder (x >>> y), then on CPVC-coated polypropelene (PP) films (x <<< y) before applying it on the final substrate in the form of PVC-co-CPVC fibers (x/y = 7/3).

III.4.2.1. Polystyrene graft polymerization on PVC (x >>> y)

Before grafting VDPM, we wanted to see if PVC is a good initiator for radical polymerization of a classical monomer like styrene. This was done by applying the same styrene homopolymerization described earlier in sulfolane, while replacing the BnCl radical initiator with the PVC macroinitiator, this reaction is described in scheme 12.

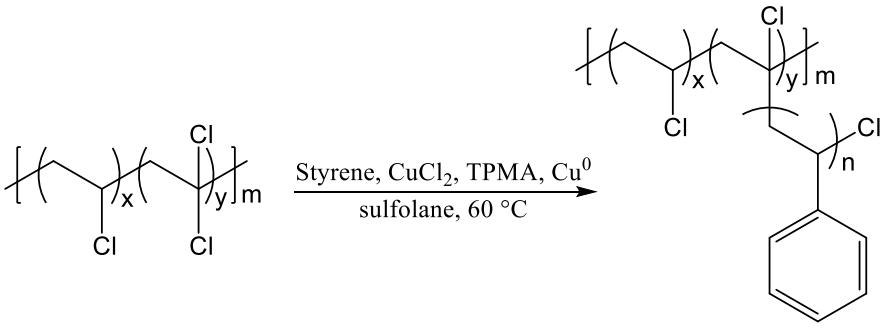

PVC - co - CPVC PVC - *graft* - PS

Scheme III-12. PVC initiated styrene polymerization

Below is the ^{1}H NMR ($CDCl_3$) spectrum of the obtained graft copolymer.

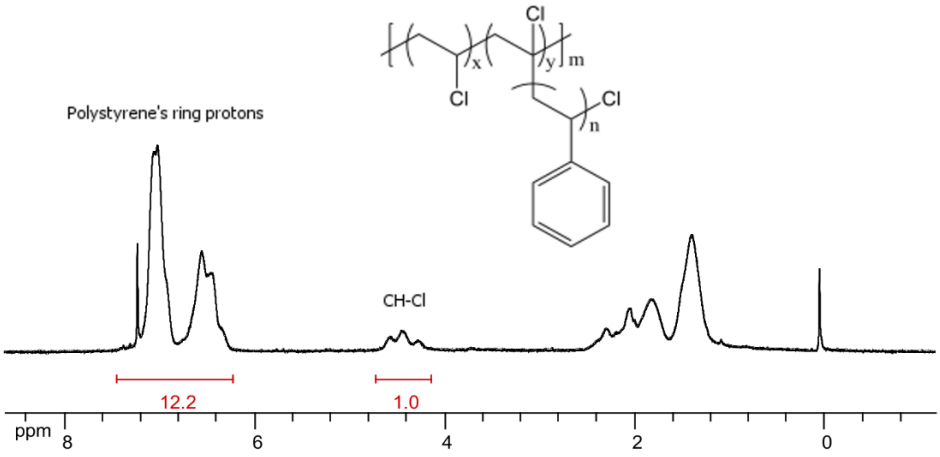

Figure III-17. ^{1}H NMR spectrum of PVC-g-PS

Figure 17 shows that PVC was successfully used as an initiator for styrene polymerization. Using the CH-Cl peak as a 1 proton reference (around 4.4 ppm), the polystyrene's ring protons between 6.2 and 7.4 ppm allowed us to calculate a 70 % molar contribution for polystyrene against 30 % for the PVC macroinitiator (i.e. m/n = 3/7).

To estimate the polystyrene chain lengths, the doubly chlorinated units (y) have to be of known quantity. The technique known as the phenolysis of PVC [19] allowed us to estimate that ~0.2 % of PVC units are capable of initiating the radical polymerization, known as labile chlorine, the phenolysis protocol is detailed in "materials and methods". Using the PVC-g-PS NMR spectrum (figure 17), we were able to estimate that a degree of polymerization as high as 1220 was reached. This was the first evidence of the very high efficiency of PVC as macroinitiator, and later on as a substrate to build PVDPM chains from.

III.4.2.2. PVDPM on PVC powder surface (x >>> y)

Once the efficiency of PVC as macroinitiator was proved with styrene, we directly applied it to the VDPM polymerization (scheme 11). However, because our goal was to modify the surface of PVC, we had no interest of solubilizing it. The VDPM was polymerized on the PVC powder suspended in acetonitrile and acting as a surface. Protocols are detailed in "materials and methods". The first observation was a 25 % mass gain for the modified PVC powder, giving the first evidence of a grafted layer of PVDPM. Furthermore, the modified PVC powder was no longer soluble in THF, a very good PVC solvent and a non-solvent for PVDPM, which supports the suggestion that PVC particles could be now protected with a thick enough PVDPM outer layer.

To test this hypothesis, we performed an NMR analysis on the modified PVC powder in deuterated DMSO. The methyl protons around 3.7 ppm in the ^{1}H NMR spectrum in figure 18 shows that PVDPM chains were successfully grafted on PVC. Using NMR, we also calculated that PVDPM represents ~6 % of the final product. However it wasn't possible to estimate the PVDPM chain lengths as only the labile chlorine on the PVC powder surface were used to initiate the polymerization, and a big majority of those sites were inaccessible inside the PVC particles suspended in acetonitrile during the polymerization reaction.

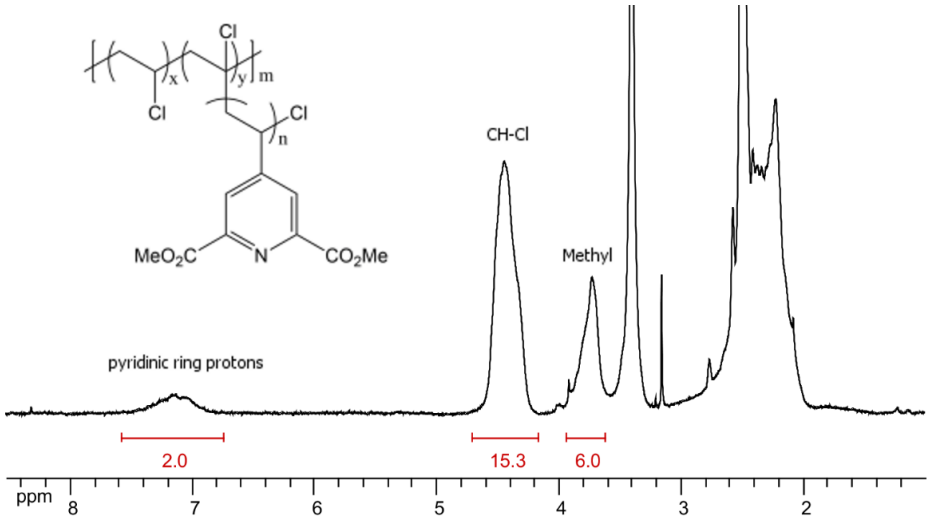

Figure III-18. ^{1}H NMR spectrum of PVC-g-PVDPM modified powder

We then used ATR and XPS to further prove the presence of the PVDPM layer on PVC particles.

ATR:

ATR spectrum (figure 19) of the modified PVC-g-PVDPM powder showed peaks from PVDPM chains and an overall 11% spectral contribution for PVDPM, which is most visible by the C=O vibration at around 1722 cm^{-1}, a further evidence of a PVDPM layer surrounding the PVC particles.

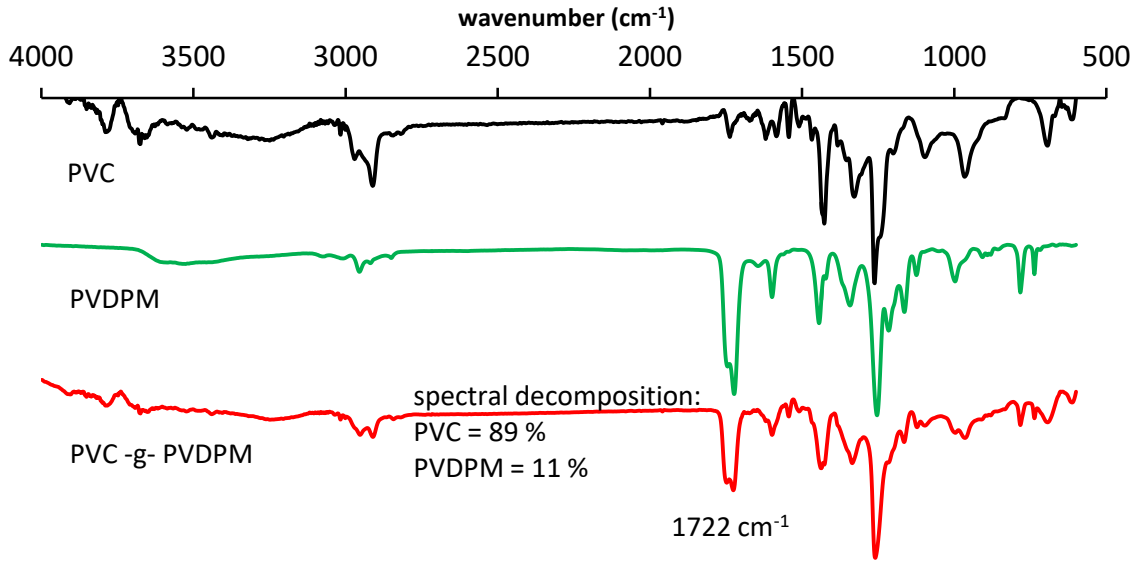

Figure III-19. ATR spectrum of PVC-g-PVDPM modified powder

XPS:

The successful grafting of PVDPM on PVC was also proved by XPS. Surveys are shown in figure 20 and elemental contributions in table 6.

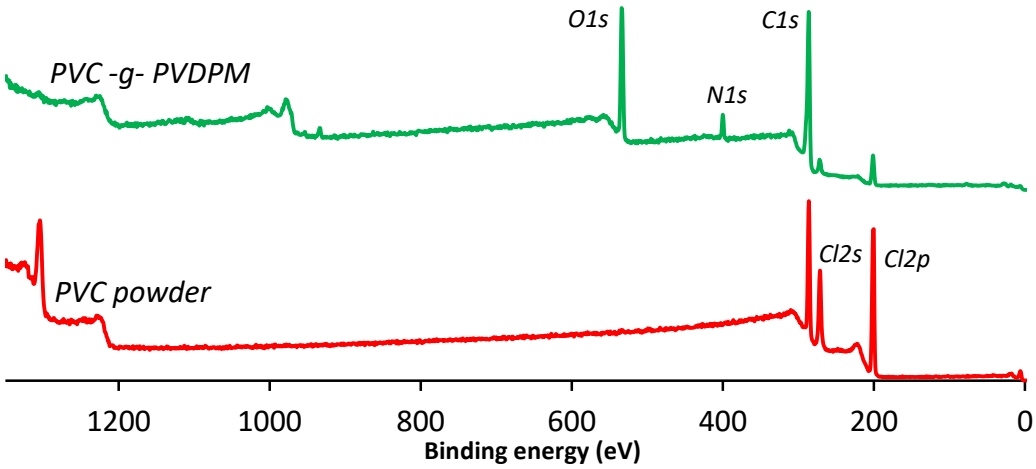

Figure III-20. XPS survey of pure PVC powder and PVC-g-PVDPM

As expected, looking at the pure PVC surface (figure 20), one can see three main peaks, C1s (286 eV), Cl2s (271 eV) and Cl2p (201 eV) with a C/Cl ratio of 65/35 (table 6). When PVC powder surface was modified with a layer of PVDPM, N1s and O1s peaks appeared at around 286 and 533 eV, respectively, while the Cl peaks decreased dramatically. Cl elemental contribution dropped from 35% on bare PVC to 5% on PVC-*g*-PVDPM, proving that PVC particles were indeed covalently covered with a layer of PVDPM.

Table III-6. Total elemental contribution and atomic ratios of PVC vs PVC-g-PVDPM surface

	PVC powder	PVC-g-PVDPM	PVDPM (Calculated)
C	65	86	69
O	-	22	25
N	-	5	6
Cl	35	5	-
C/N	-	17.2	11.5
C/O	-	3.9	2.7
O/N	-	4.4	4.2

However, the atomic ratios in table 6 show that the experimental C/N and C/O ratios of 17.2 and 3.9, respectively, on PVC-*g*-PVDPM don't fit perfectly with the theoretical values of 11.5 and 2.7 even if elemental contribution are reasonably close. On the other hand, O/N experimental ratio of 4.4 is closest to its theoretical ratio of 4.2 (table 6). This means that a carbon excess is present within the probing depth of XPS (~10 nm). To figure that out, we turn to the C1s high resolution spectra of bare PVC and PVC-*g*-PVDPM shown in figure 21. Peaks components are listed in table 7. For a better comparison, peak components from PVDPM's C1s spectrum drawn from figure 16 are also put in table 7.

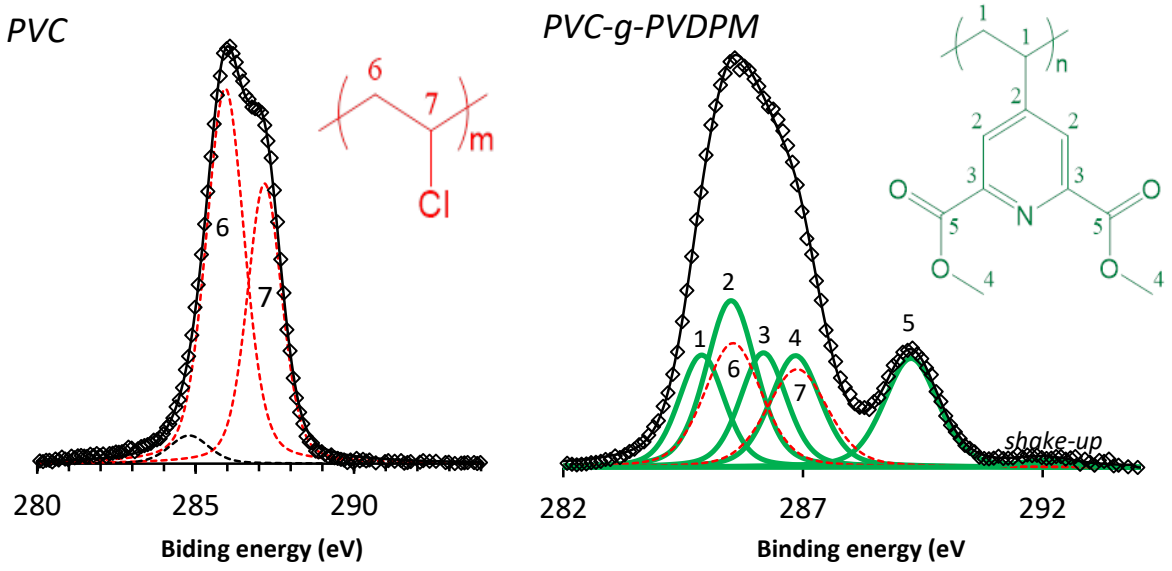

Figure III-21. High resolution C1s spectra of bare PVC and PVC-g-PVDPM

Bare PVC's spectrum (figure 21 left) shows two main components at 285.9 and 287.2 eV that correspond to C(6) and C(7), respectively, with a small impurity peak at 284.8 eV that is excluded. In the PVC-*g*-PVDPM spectrum (figure 21 right), these two components can still be seen (red dashed line), even if they are now dominated by PVDPM components C(1) to C(5) and shake-up (green solid line). The PVC-g-PVDPM spectrum fit was optimized using PVDPM's components drawn from figure 16.

The fact that PVC substrate is still visible now explains the excess carbon seen on PVC-g-PVDPM surface with probably only a few nanometers thick outer layer of PVDPM surrounding the PVC powder particles. The remarkable mass gain of 25%, not seen in the case of PET films or fibers, can be here explained by the high surface area of PVC powder, offering a lot more initiation site than flat PET surfaces.

Table III-7. High resolution C1s components of bare PVC, PVDPM and PVC-g-PVDPM

C1s		Peak BE	FWHM eV		Peak BE	FWHM eV	Atomic %
1	PVDPM (figure 16)	285.03	1.23	PVC-g-PVDPM	284.9	1.14	11.9
2		285.47	1.25		285.47	1.25	19.48
3		286.13	1.15		286.08	1.15	12.34
4		286.83	1.25		286.77	1.25	12.43
5		289.25	1.12		289.25	1.34	13.6
shake-up		292.16	1.47		292.05	1.31	0.84
6	PVC	285.93	1.43		285.53	1.41	12.53
7		287.17	1.29		286.87	1.51	16.89

Herein, we saw that a PVC surface was successfully used to build a PVDPM layer, reducing the surface modification strategy to a unique step when PVC is used as a substrate instead of PET. However, it's obvious that the PVDPM layer is still limited to a few nanometers thickness, limiting the attractiveness of PVC as a substrate. To solve this problem, we need to look back at scheme 11 to be reminded that only the doubly chlorinated CPVC units (y) are capable of initiating the radical polymerization and not the PVC units with a single chlorine atom (x). Or the PVC powder has not more than 0.2% of CPVC units as the phenolysis technique showed earlier, we concluded that the initiating sites on the PVC powder surface are rare. In the following section we will apply the same modification strategy on a pure CPVC surface to see if a thicker layer of PVDPM can be built.

III.4.2.3. PVDPM on CPVC films (x <<< y)

Commercial packaging polypropylene (PP) films coated with CPVC from Innovia™ where all the repeating units are doubly chlorinated (x=0, y=1) were modified with PVDPM (scheme 11) and examined. It's important to note that the CPVC-coated PP film is an ordinary commercial film used for food packaging and that surface analysis of such substrate posed several challenges. Chemical additives and the manufacturing process used to produce these films usually give surfaces with low purity, high surface roughness and less than perfect homogeneity of the outer CPVC coating. Still, the modified CPVC-g-PVDPM surface were studied using ATR and ToF-SIMS to ensure a successful grafting of a PVDPM layer.

ATR:

ATR spectra of commercial CPVC substrate modified with a PVDPM layer (figure 22) showed that a PVDPM layer of variable thickness was built. After 1 day of polymerization, PVDPM has a 29 % spectral contribution on the modified surface, and when the reaction time was extended to 3 days, PVDPM spectral contribution reached up to 83%.

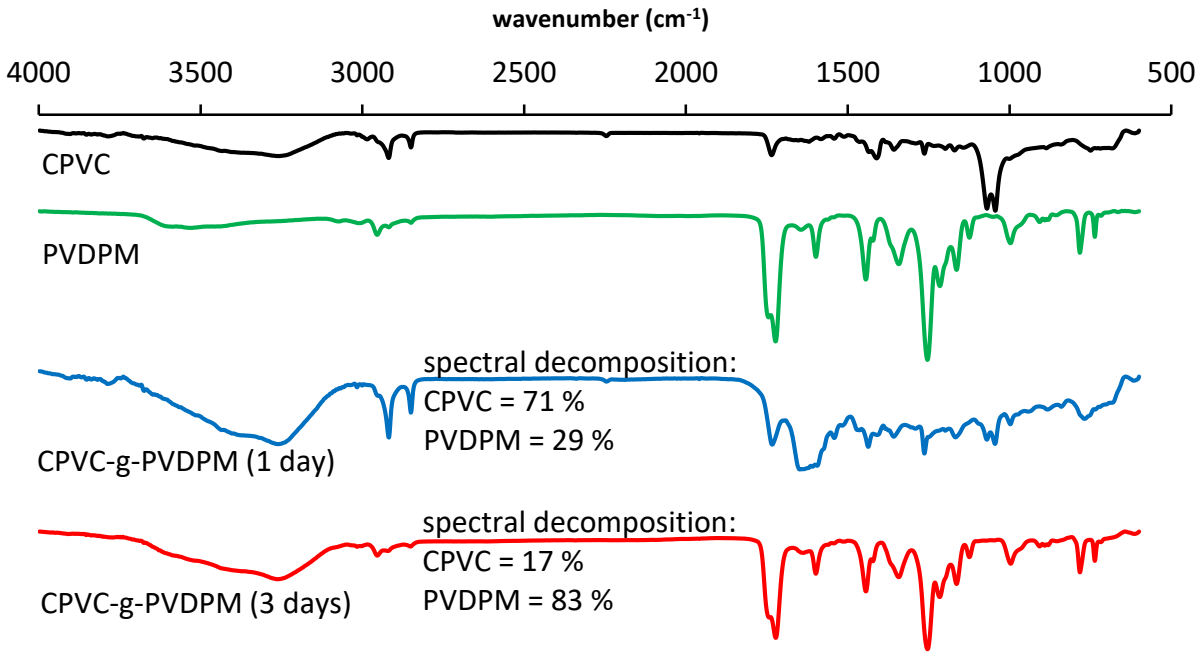

Figure III-22. ATR analysis of CPVC-g-PVDPM surfaces

Having 83% spectral contribution in the 2 µm ATR probing depth here gives the first evidence of a potential micrometer scale layer of PVDPM thanks to abundance of the doubly chlorinated CPVC units (y) (scheme 11) capable of initiating the radical polymerization. A pure CPVC surface seems to be more reactive than pure PVC. In the next section, ToF-SIMS, this time possible on a flat film surface, is used to further prove that longer polymerization time gave a thicker PVDPM outer layer.

ToF-SIMS:

ToF-SIMS analysis was performed on CPVC-*g*-PVDPM films. A series of secondary ion fragments was identified and followed along the z-axis (i.e. surface sputtering time) as shown in figure 23 in which we compare CPVC-*g*-PVDPM surfaces after 1 and 3 days of reaction time. Three secondary ions fragments were followed, each representing a sublayer. The $C_{11}H_{12}NO_4^+$ fragment (m/z = 222 u) was assigned to the protonated PVDPM's repeating unit ($M\text{-}H^+$), the Cl^+ (m/z = 35 u) ion coming either from CPVC or the PVDPM chain ends and the $C_5H_9^+$ (m/z = 69 u) coming most probably from the PP sublayer.

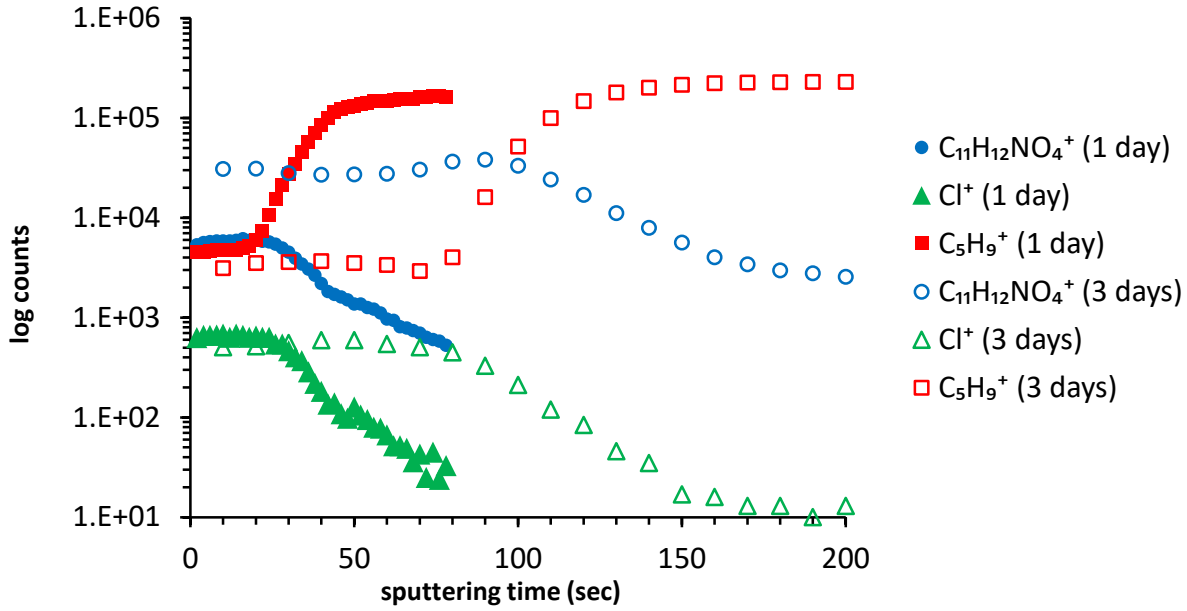

Figure III-23. ToF-SIMS depth profiling of CPVC-g-PVDPM surfaces

Looking at the depth profile (figure 23), the first observation was that the ion intensity levels took longer time to change (either up or down) when the surface was modified for 3 days (hollow points), indicating a thicker PVDPM layer, consistently with ATR's conclusion (figure 22). In fact, when analyzing the 1 day-modified surface under the same conditions (solid point), we had to acquire faster mass spectra (every 2 sec) than for the 3 days-modified surface (every 10 seconds), to get a better resolved profile with enough data points.

Looking again at the above depth profiles, the PVDPM/substrate interface was encountered at around 30 sec for the 1 day-modified films where the $C_{11}H_{12}NO_4^+$ fragment intensity drop of ~2 orders of magnitude is seen against a ~2 order of magnitude increase for the $C_5H_9^+$ fragment

intensity. The same relative behavior was seen for the 3 days-modified films, only that the interface was encountered this time at around 100 sec of sputtering. A thicker layer of PVDPM was clearly built when film were modified for longer time, proving an effective polymer chain propagation and limited termination.

In the next section, the modification of PVC-based fibers is discussed.

III.4.2.4. PVDPM on PVC-co-CPVC fibers (x/y = 7/3)

We move on to the surface-initiated polymerization of VDPM on PVC-co-CPVC Rhovyl™ fibers having 30 % doubly chlorinated units (x/y = 7/3). These fibers were modified with PVDPM (1 to 3 days of polymerization time), again as shown in scheme 11, and examined. The first observation was an impressive mass gain of the modified fibers. Up to ~250 % mass gain was reached, meaning for example that a 100 mg of fibers, weighted ~350 mg after the modification reaction. This mass gain exceeds by far both pure PVC and pure CPVC substrates. (PVC-co-CPVC)-*g*-PVDPM fiber were then analyzed.

ATR:

The ATR spectrum of (PVC-co-CPVC)-*g*-PVDPM fibers was compared to those of bare PVC-co-CPVC fibers and pure PVDPM in figure 24.

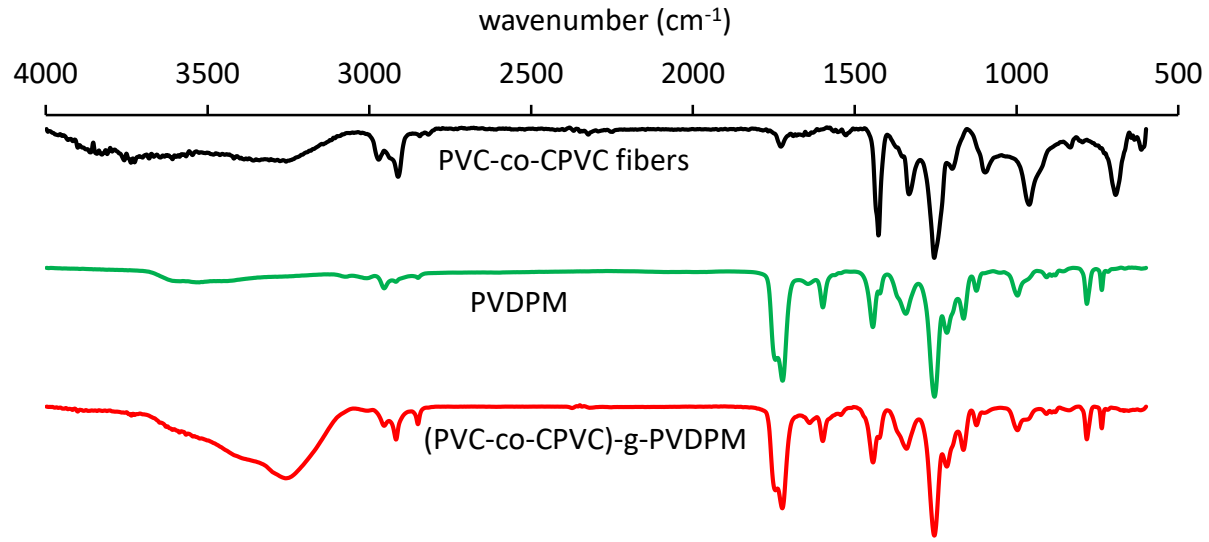

Figure III-24. ATR spectra of (PVC-co-CPVC)-g-PVDPM fibers

Indeed, no signs of the PVC-co-CPVC substrate were detected. As mentioned earlier, this technique can penetrate down to 2 µm. The fact that no peak from the PVC-co-CPVC substrate was detected, proves that the PVDPM layer has possibly a thickness greater than 2 µm. when compared with the PET-PVDPM surface (figure 14) where only few dozen nanometers of PVDPM layer were probably reached (and no mass gain was seen), one can see that PVC-based surfaces are way more efficient. Using a PVC-based substrate is not only much easier compared to PET with a unique modification step, but also much more efficient, a PVDPM layer of several micrometers thickness can be built. To further prove it, PVDPM-modified fibers, both PET and PVC-co-CPVC were seen under an electron microscope in the following section.

SEM:

Herein, (PVC-co-CPVC)-*g*-PVDPM fibers are seen by SEM and compared to PET-PVDPM fibers modified according to the strategy described earlier in scheme 10. Both fibers are shown before and after building the PVDPM layer in figure 25.

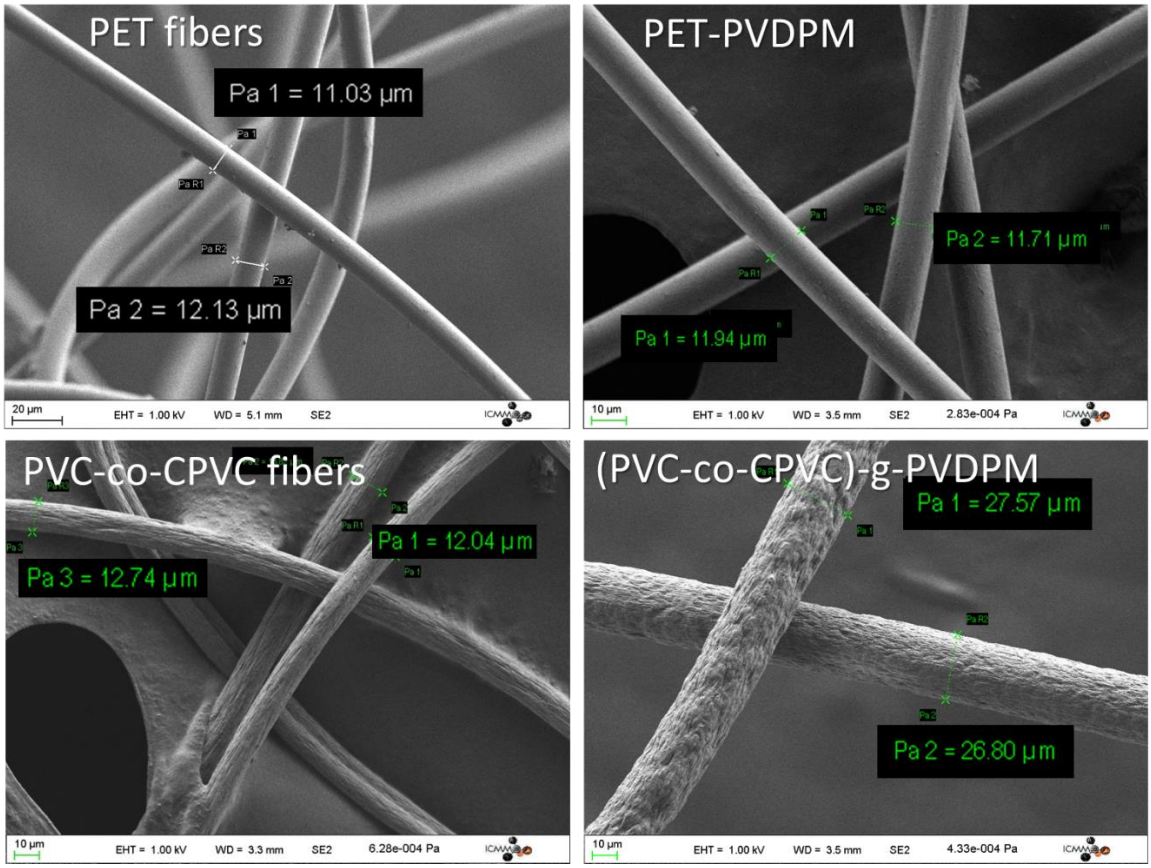

Figure III-25. SEM images of PVDPM-modified PET and PVC-co-CPVC fibers

Both non-modified PET and PVC-co-CPVC fibers had a similar diameter of 12 ± 1 µm. PET-PVDPM fibers (figure 25 up right) had an average diameter of 11.8 µm. (PVC-co-CPVC)-*g*-PVDPM fibers (figure 25 down right), however, reached an average diameter of 27.2 µm in the shown example. As a result, PET-PVDPM fibers diameter showed no remarkable increase, in agreement with a limited nanometer scale layer of PVDPM and no mass gain of fibers after modification. On the other hand, (PVC-co-CPVC)-*g*-PVDPM fibers diameters ranged between 24 and 30 µm, meaning that an enormous 6 to 9 µm thick layer of PVDPM was built around the PVC-co-CPVC fibers, in agreement with a mass gain of up to 250 %.

III.5. Conclusion

In this chapter, PVDPM was successfully synthesized in solution then built on both PET and PVC-based surfaces of different forms (powder, films, and fibers). All surfaces were examined by means of different advanced techniques. PVC-based surfaces showed superior performance as a substrate for surface initiated polymerization of VDPM, especially the PVC-co-CPVC fibers, justifying the transition we made from PET to PVC as a preferred substrate to prepare highly absorbing materials for radiodecontamination application. Major advantages of PVC over PET are summarized in the following table.

Table III-8. PET vs PVC for surface initiated polymerization of VDPM

criteria	**PET**	**PVC**
Chemical/physical resistance	highly resistant	highly resistant
Commercial availability	available at low cost	available at low cost
VDPM polymerization strategy	multiple step (scheme 10)	one step (scheme 11)
Mass gain after modification	negligible	up to 250 % mass gain
PVDPM layer thickness	few nanometers	several micrometers

Later on, PVDPM will be hydrolyzed to PVDPA (scheme 2) both in its free form as water soluble polymer and its grafted form as a (PVC-co-CPVC)-g-PVDPA fibers. The interaction of these functional materials with different metals, especially lanthanides and uranium, will be examined in the next chapter, and their performance vis-à-vis different applications will be discussed.

III.6. References

1. Gilca, M., et al., *Chelidonium majus–an integrative review: traditional knowledge versus modern findings.* Complementary Medicine Research, 2010. **17**(5): p. 241-248.
2. Kim, D.-S., et al., *The therapeutic effect of chelidonic acid on ulcerative colitis.* Biological and Pharmaceutical Bulletin, 2012. **35**(5): p. 666-671.
3. Jeong, H.-J., et al., *Chelidonic acid evokes antidepressant-like effect through the up-regulation of BDNF in forced swimming test.* Experimental Biology and Medicine, 2016. **241**(14): p. 1559-1567.
4. Zhou, G.-W., et al., *3-D hydrogen-bonded frameworks of two metal complexes with chelidamic acid: Syntheses, structures and magnetism.* Bulletin of the Korean Chemical Society, 2004. **25**(5): p. 676-680.
5. Su, X.-C., et al., *A dipicolinic acid tag for rigid lanthanide tagging of proteins and paramagnetic NMR spectroscopy.* Journal of the American Chemical Society, 2008. **130**(32): p. 10486-10487.
6. Kondo, M., et al., *Self-assembling construction of a novel nanoscale heptacobalt complex with an S-shaped folding.* CrystEngComm, 2008. **10**(11): p. 1516-1519.
7. Cantos, P.M., S.J. Pope, and C.L. Cahill, *An exploration of homo-and heterometallic UO 2 2+ hybrid materials containing chelidamic acid: synthesis, structure, and luminescence studies.* CrystEngComm, 2013. **15**(44): p. 9039-9051.
8. Derikvand, Z., et al., *Solution and solid state studies of three new supramolecular compounds of zinc (II), nickel (II) and uranium (VI) with chelidamic acid and 9-aminoacridine.* Inorganica Chimica Acta, 2013. **406**: p. 256-265.
9. Yang, W., et al., *Synthesis, structures, and properties of uranyl hybrids constructed by a variety of mono-and polycarboxylic acids.* Inorganic chemistry, 2013. **52**(21): p. 12394-12402.
10. Aspinall, H.C., *Chiral lanthanide complexes: coordination chemistry and applications.* Chemical reviews, 2002. **102**(6): p. 1807-1850.
11. Howáth, G., et al., *A new Efficient Method for the Preparation of 2, 6-Pyridinedihiethyl Ditosylates from Dimethyl 2, 60-Pyridinedicarboxylates.* Synthetic communications, 1999. **29**(21): p. 3719-3731.
12. Shi, S. and Y. Zhang, *Pd (OAc) 2-catalyzed fluoride-free cross-coupling reactions of arylsiloxanes with aryl bromides in aqueous medium.* The Journal of organic chemistry, 2007. **72**(15): p. 5927-5930.
13. Nakamura, T., et al., *Efficient Formation of Luminescent Lanthanide (III) Complexes by Solid-Phase Synthesis and On-Resin Screening.* Chemistry–An Asian Journal, 2013. **8**(11): p. 2685-2690.
14. Iglesias, C.P., et al., *Effect of a halogenide substituent on the stability and photophysical properties of lanthanide triple-stranded helicates with ditopic ligands derived from bis (benzimidazolyl) pyridine.* Journal of the Chemical Society, Dalton Transactions, 2000(13): p. 2031-2043.
15. Molander, G.A. and A.R. Brown, *Suzuki− Miyaura Cross-Coupling Reactions of Potassium Vinyltrifluoroborate with Aryl and Heteroaryl Electrophiles.* The Journal of organic chemistry, 2006. **71**(26): p. 9681-9686.
16. Picot, A., et al., *Synthesis, structures, optical properties, and TD-DFT studies of donor-π-conjugated dipicolinic acid/ester/amide ligands.* Tetrahedron, 2008. **64**(2): p. 399-411.
17. Mendes, J.P., et al., *Sulfolane: An efficient and universal solvent for copper-mediated atom transfer radical (co) polymerization of acrylates, methacrylates, styrene, and vinyl chloride.* ACS Macro Letters, 2014. **3**(9): p. 858-861.
18. Góis, J.R., et al., *Improvement of the control over SARA ATRP of 2-(diisopropylamino) ethyl methacrylate by slow and continuous addition of sodium dithionite.* Polymer Chemistry, 2014. **5**(16): p. 4617-4626.
19. Robilă, G., E. Buruiană, and A. Caraculacu, *Determination of labile chlorine in PVC with the aid of phenolysis reaction.* European Polymer Journal, 1977. **13**(1): p. 21-24.

IV. PVDPA – Metal complexes

A promising performance

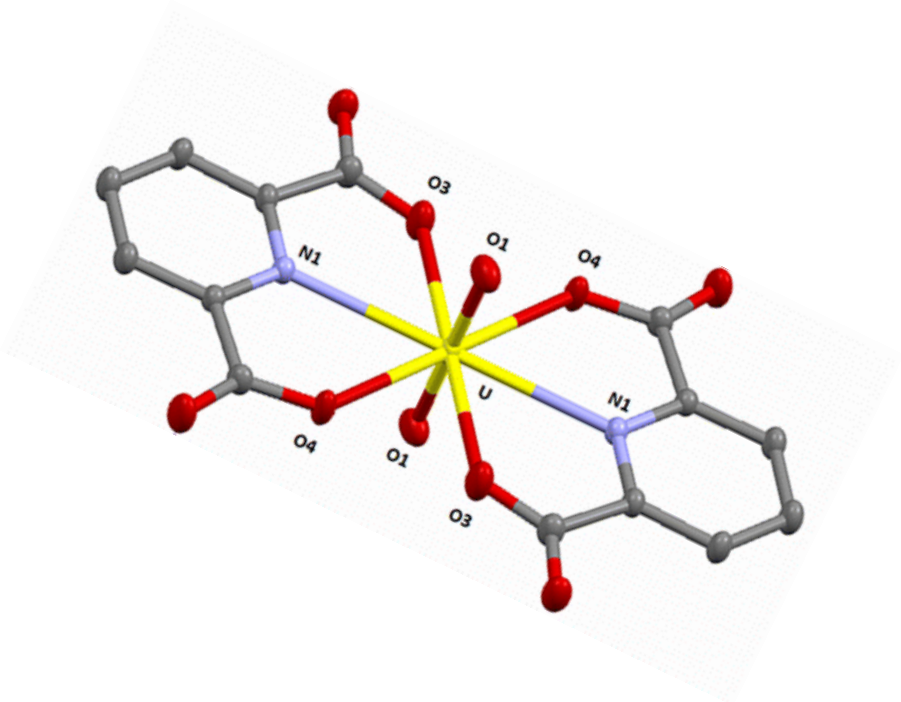

IV.1. Introduction

After polymerization, either in solution or from a solid substrate, it was important to evaluate the performance of the new polymer as a lanthanides/actinides scavenger in an aqueous environment. The first step was the hydrolysis of PVDPM (free or grafted) to get the water soluble PVDPA. In the case of a free polymer, a PVDPM sample of an estimated molar mass of around 17 $kg.mol^{-1}$ (77 repeating units) was treated in a NaOH 1 M solution and then concentrated HCl was added to precipitate PVDPA which was isolated by filtration. The reaction is shown is scheme 1.

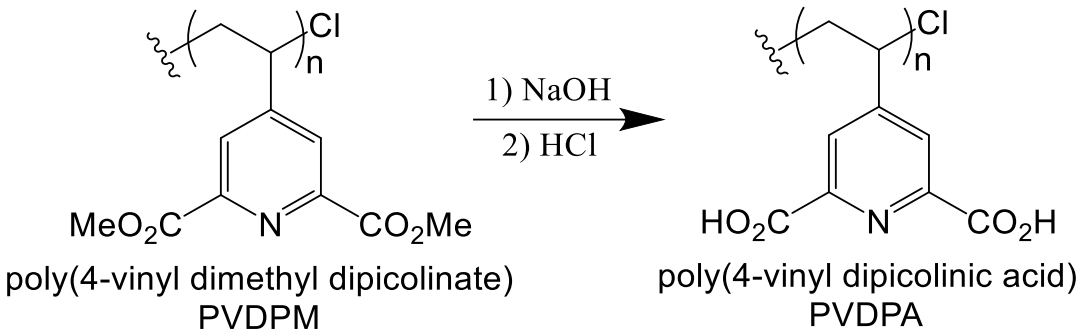

Scheme IV-1. PVDPM hydrolysis to PVDPA

PVDPA's spontaneous complexation with lanthanides/actinides in aqueous solution at pH~7 was conducted by mixing a PVDPA solution with a lanthanide/actinide solution at different PVDPA / metal ratios at room temperature. The same polymer was used in all complexation studies.

Due to the special precautions needed to handle uranium solutions even in its depleted form, studies were conducted first with lanthanides (especially europium) and when proven successful, the PVDPA-uranium complexes were studied.

Both in its free and grafted forms, PVDPA will show high scavenging performance towards several lanthanide (III) ions and uranium (VI).

IV.2. PVDPA - Lanthanides (III) complexes

The first evidence of a spontaneous interaction between PVDPA and a lanthanide was observed upon mixing a PVDPA solution with an equimolar Eu(III) nitrate solution. Within seconds, an unknown white precipitate was observed. When this precipitate was isolated by filtration, it exhibited a strong reddish fluorescence under a UV light as shown in figure 1.

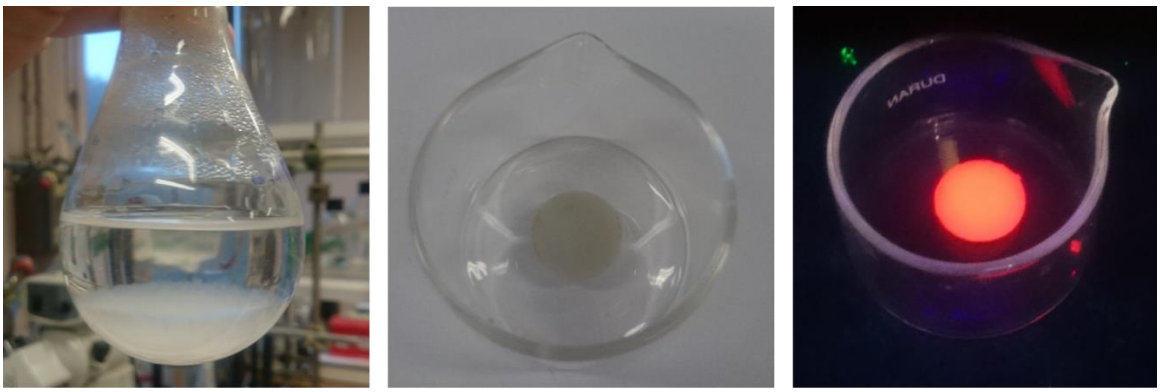

Figure IV-1. PVDPA – Eu(III) precipitation from aqueous mixture

We hypothesized that the white fluorescent solid is actually a PVDPA - Eu(III) complex and we tried to prove this hypothesis plausible. Due to the non-solubility of this complex in common solvents, the most suitable way was to perform ATR on the solid precipitate and compare its spectrum to the pure PVDPA's.

ATR:

In figure 2, the ATR spectrum of pure PVDPA and the presumed PVDPA – Eu(III) complex are overlaid.

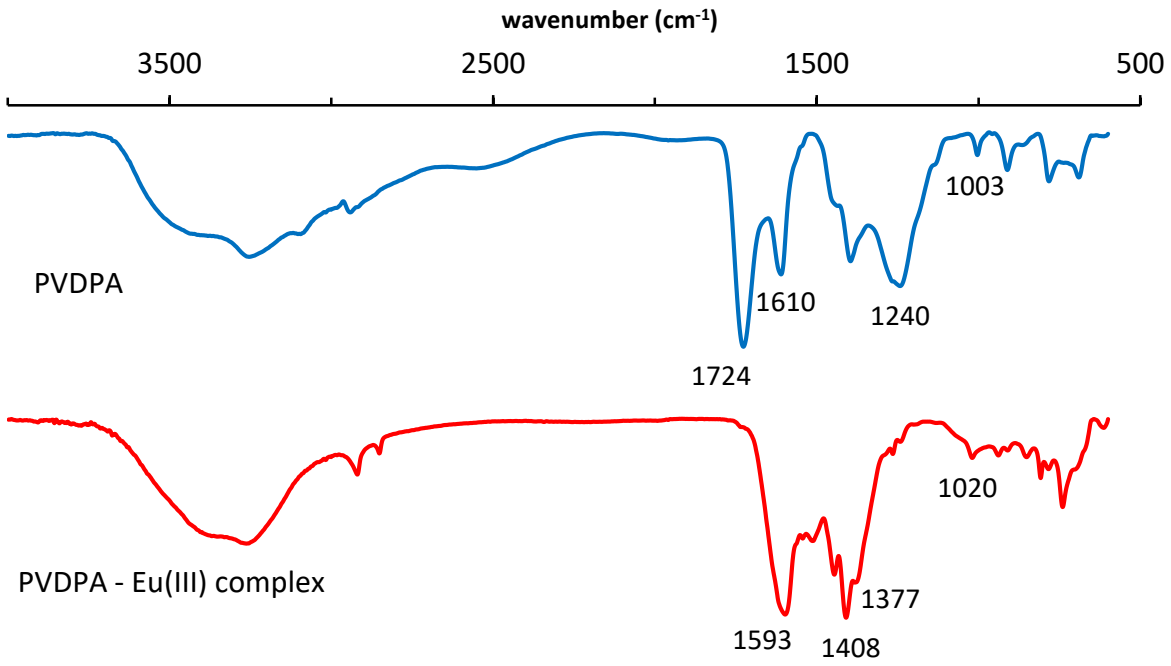

Figure IV-2. ATR spectrum of PVDPA - Eu(III) complex

Looking at the PVDPA spectrum, main peak at 1724, 1240 and 1610 cm^{-1} were assigned to C=O, C-O and pyridinic C=N stretching vibrations. In the PVDPA – Eu(III) complex spectrum, those peaks were replaced by peaks at 1593 cm^{-1} (COO^- symmetrical stretching) and 1408 cm^{-1} (COO^- asymmetrical stretching) proving that PVDPA matched the Eu(III) through its carboxyl functions. The C=N peak shifting down to 1377 cm^{-1} indicated the nitrogen's contribution to the chelation ring in agreement with literature data [1]. Pyridine ring breathing peak shifting up from 1003 to 1020 cm^{-1} is a further evidence of complexation.

In the following sections we will further examine the interaction between PVDPA and Eu(III) in water in order to understand the complexation mechanism and why does the resulting complex precipitate.

UV spectroscopy:

We saw earlier that when the PVDPA polymer interacts with Eu(III) in water, the PVDPA – Eu(III) complex precipitate, which makes it difficult to acquire the absorption spectrum of the complex. To overcome this problem, the VDPA monomer was used instead of the PVDPA polymer. In this case, no precipitation is encountered and the absorption spectra could be acquired.

VDPA monomer:

The VDPA monomer (scheme 2) was obtained by hydrolyzing the VDPM monomer with NaOH 1 M then precipitating VDPA by adding HCl to pH < 2. VDPA is then resolubilized in water at neutral pH.

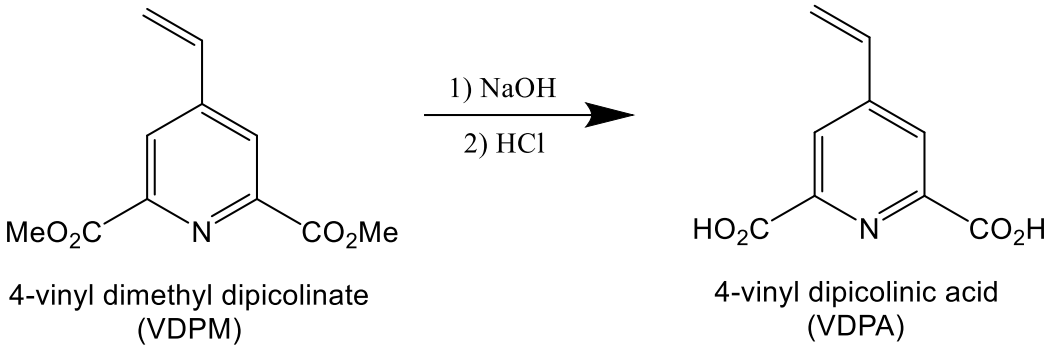

Scheme IV-2. VDPM hydrolysis to VDPA

UV absorption spectrum of a 0.1 mM VDPA solution in water is shown in figure 3. When Eu(III) was added at increasing Eu(III)/VDPA ratio, no precipitation was observed and the changes in the UV spectrum were depicted in figure 3.

Two other lanthanides, Nd(III) and Yb(III) were also examined and exhibited a similar behavior, as seen in figure 3.

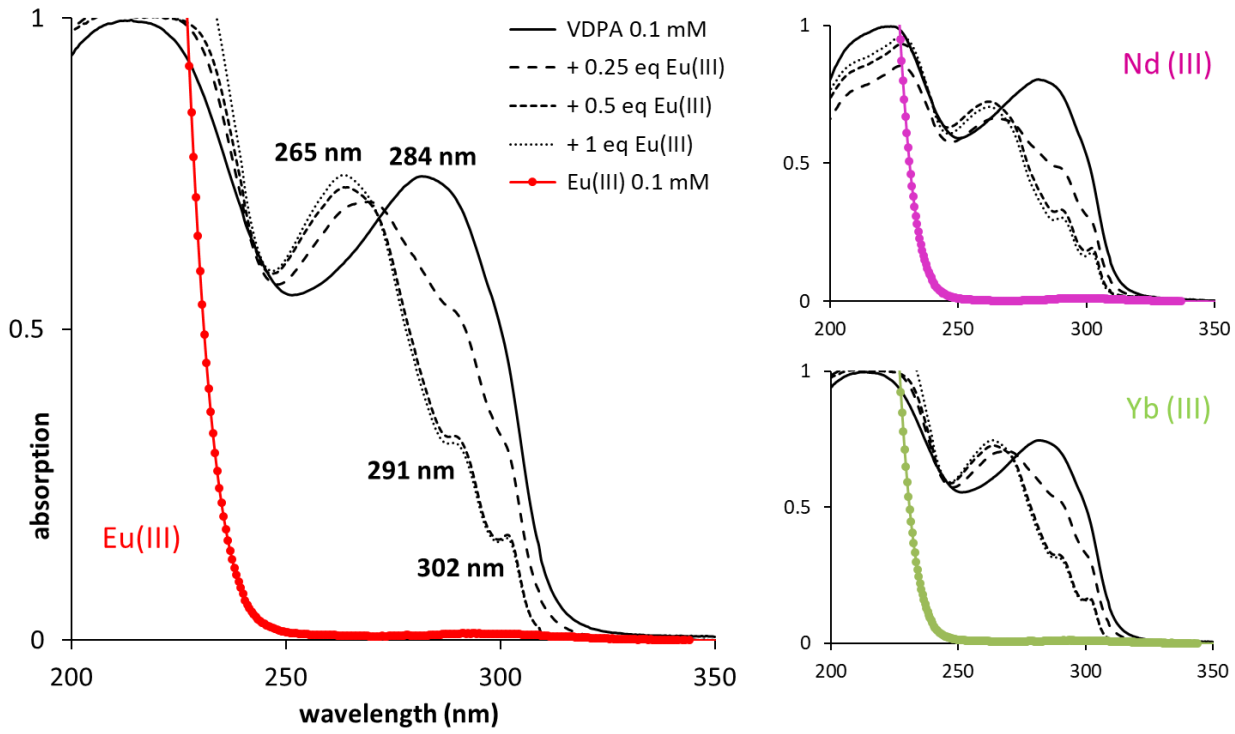

Figure IV-3. UV absorption spectra of VDPA interaction with different lanthanides (III)

As shown in figure 3, VDPA has an absorption band at around 284 nm (solid line). When Eu (III) and other lanthanides were gradually added (dashed lines), the spectrum changes and 3 peak maxima appear at 265, 291 and 302 nm. No change is seen at Eu (III) > 0.5 equivalent.

Two main conclusions were drawn:

1. The change in peaks positions and number shows that an interaction is taken place between VDPA and the added lanthanide ions Ln(III).
2. The interaction is present up to a Ln(III) / VDPA ratio of ~0.5 which may be explained by the possible formation of $Ln(VDPA)_2^-$ complex

$$Ln(III) + 2\ VDPA^{2-} \rightarrow Ln(VDPA)_2^-$$

PVDPA polymer:

Once the interaction between the VDPA monomer and trivalent lanthanides Ln(III) ions was proven, we went back to study the PVDPA polymer interaction with Ln(III) in aqueous solution.

We hypothesized earlier that the white fluorescent precipitate seen when Eu(III) was added to a PVDPA solution is probably a PVDPA – Eu(III) complex and we gave a first evidence by comparing the infrared spectrum of this precipitate with the pure PVDPA spectrum (figure 2).

The precipitation phenomenon is particularly interesting if our polymer is to be used for lanthanides scavenging in water. If true, we should be able to decontaminate a lanthanide solution by simply adding PVDPA then passing the solution through a filter to isolate the precipitated complex.

To put this idea to test, we used UV absorption spectroscopy to study the decontamination of lanthanide solutions with PVDPA. However, preliminary scans showed that lanthanide solutions don't have useable absorption peaks in the available wavelength range of 200-800 nm. To solve this problem, a reverse titration was conducted where different lanthanides were added to a PVDPA solution of a known initial concentration of 0.25 mM. The solution was then filtrated and the absorption spectra registered (figure 4).

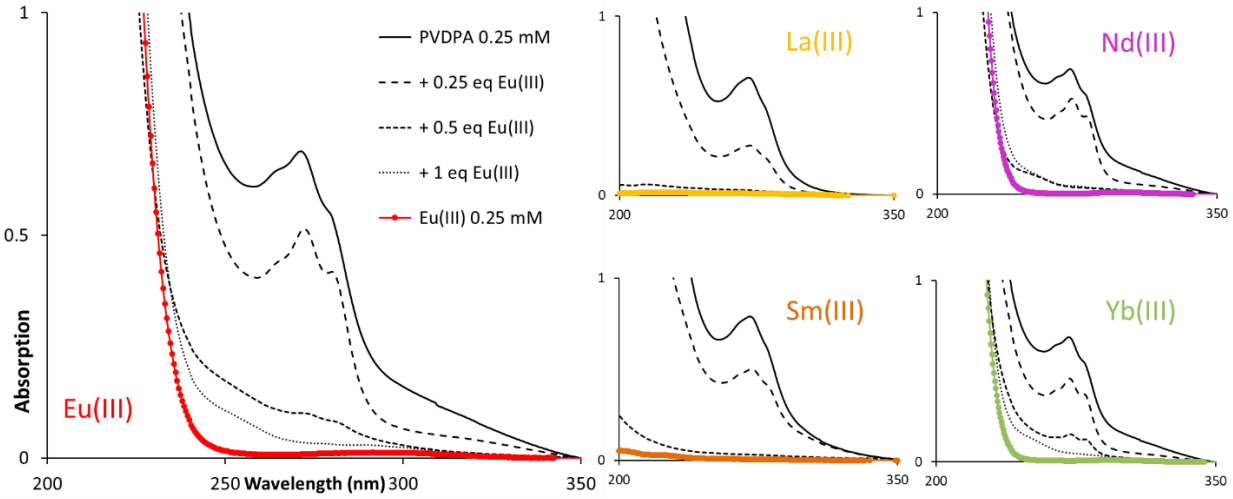

Figure IV-4. UV absorption spectra of remaining PVDPA after addition of different lanthanides (III)

As shown in figure 4, the PVDPA absorption spectrum went down when lanthanides were added in increasing ratios, proving again that the precipitate is most probably a PVDPA - Ln(III) complex. The same experiment was then repeated while looking closely at the PVDPA absorption intensity at 272 nm and with more intermediate steps of added Eu(III). The results are shown in figure 5.

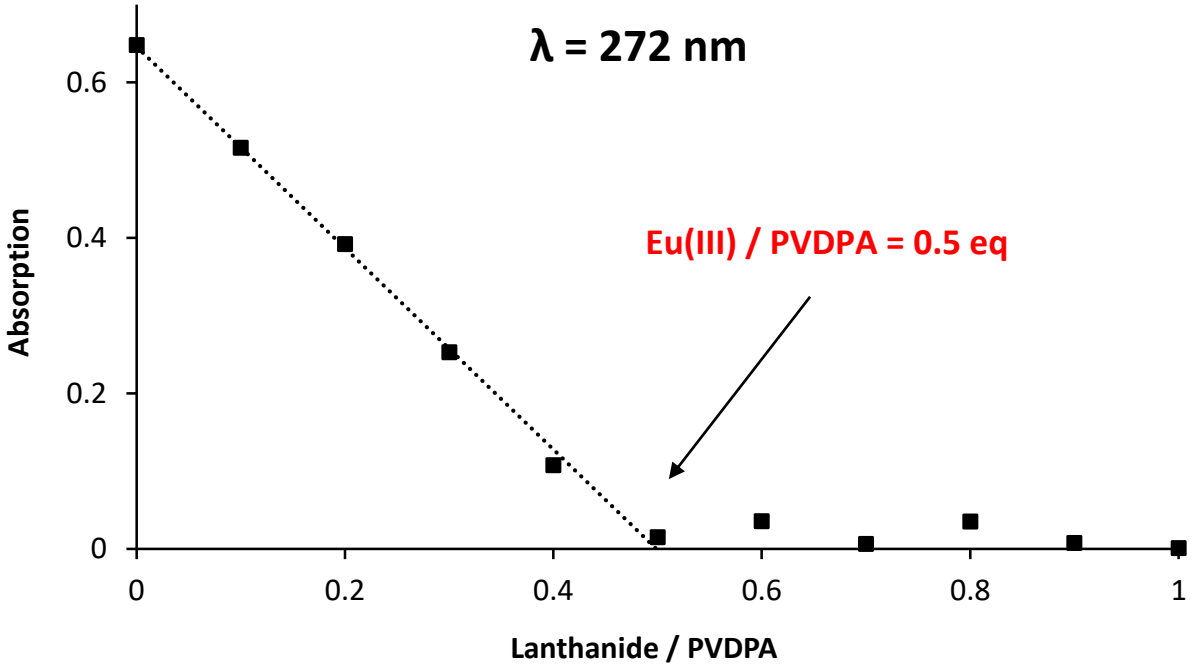

Figure IV-5. Absorption at 272 nm at variable Eu(III) / PVDPA ratios

Two main conclusions were drawn from this study:

1. All the examined lanthanides showed the exact same behavior, meaning that PVDPA is interacting similarly with these lanthanide (III) ions.
2. PVDPA was completely precipitated at 0.5 equivalent of lanthanide (III), meaning that reciprocally, 2 equivalents of PVDPA would be needed to decontaminate a given lanthanide (III) solution by the probable formation of $Ln(PVDPA)_2^-$ complex as follows:

$$Ln(III) + 2\ PVDPA^{2-} \rightarrow Ln(PVDPA)_2^-$$

How to explain the precipitation?

The fact that the PVDPA – Ln(III) complexes precipitate is a major advantage for lanthanides scavenging. A simple filtration would be sufficient to decontaminate a lanthanide aqueous solution. But the question is why does the polymer complex precipitate?

The answer can be found in the above UV absorption study. We saw that the interaction between lanthanides and the VDPA monomer is limited to a Ln(III) / VDPA ratio of 0.5 (figure 3). Similarly, the PVDPA polymer precipitate entirely when the Ln(III) / PVDPA ratio reaches 0.5 (figures 4 and 5). It seems that the lanthanide center is indeed linked to 2 PVDPA ligand units. This conclusion being in perfect agreement with literature data for the lanthanides - dipicolinic acid coordination modes [2].

Knowing that crosslinked polymers tend to have very low solubility in most common solvents, we believe that the precipitation in probably due to an intrachain and/or interchain crosslinking phenomenon, as described in scheme 3.

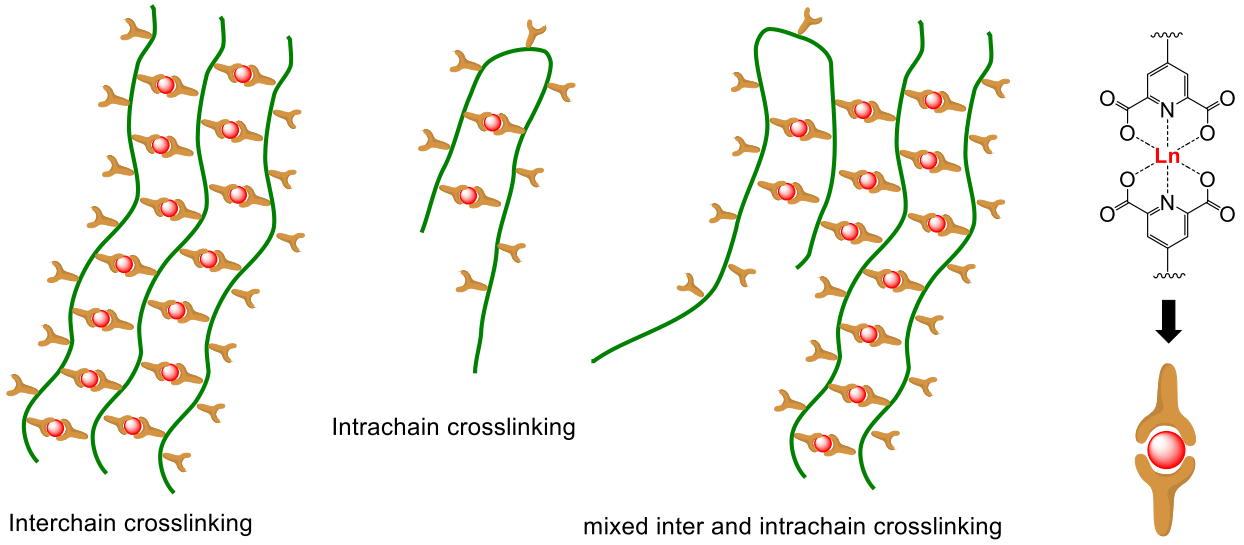

Scheme IV-3. Proposed PVDPA crosslinking by lanthanides(III) ions

To further prove the formation of the $Ln(PVDPA)_2^-$ complexes, time-resolved laser-induced fluorescence spectroscopy (TRLFS) is used in the following section to examine the Eu(III) coordination environment.

TRLFS:

Time-resolved laser-induced fluorescence spectroscopy (TRLFS) had the final word in proving the complexation mode between PVDPA and Eu(III). The above UV absorption study favored the $Eu(PVDPA)_2^-$ configuration. If so, the TRLFS results should give further evidence.

After laser excitation, Eu(III) exhibits radiative relaxation (fluorescence) emitting light in the visible spectrum. The emission bands of Eu(III) originate from electronic transitions from the lowest excited state $^5D_0$, to the ground state ^7F_J (J=0-6) [3]. The intensity, splitting and energy of the luminescence bands as well as the relative intensities of the different bands are very sensitive to the symmetry and the detailed nature of the ligand environment [4]. The simplified energy diagram of Eu(III) is shown in scheme 4, with only two transitions of interest shown for clarity.

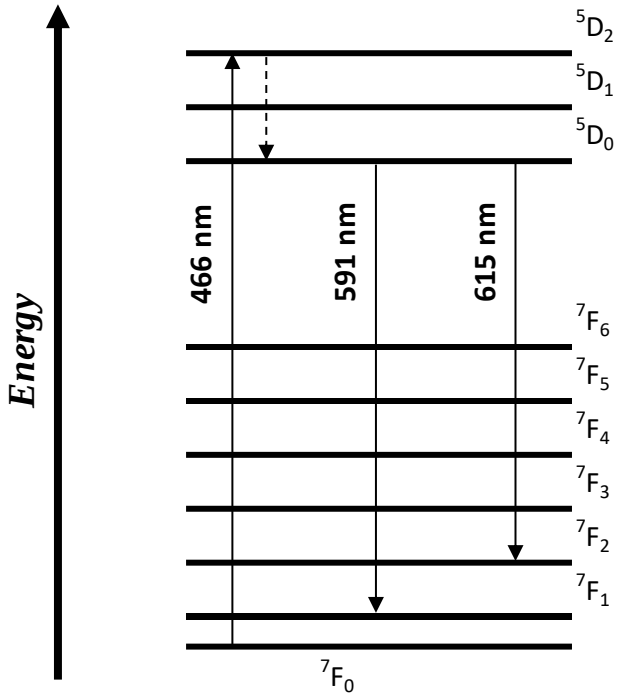

Scheme IV-4. Energy diagram of Eu(III)

The excitation wavelength of the laser source was set at 466 nm ($^7F_0 \rightarrow {}^5D_2$) with pulse energies of 7.5 mJ. Emission spectra were recorded between 470 and 720 nm. Static luminescence spectra of Eu(III) have been normalized to the peak area of the $^5D_0 \rightarrow {}^7F_1$ transition at 591 nm, which is a magnetic dipole and therefore not influenced by complexation [5].

The luminescence spectra of Eu(III) 1 mM before and after adding 1 then 2 equivalents of PVDPA are shown in figure 6. (NB: PVDPA concentration refers to the concentration of dipicolinic acid repeating units).

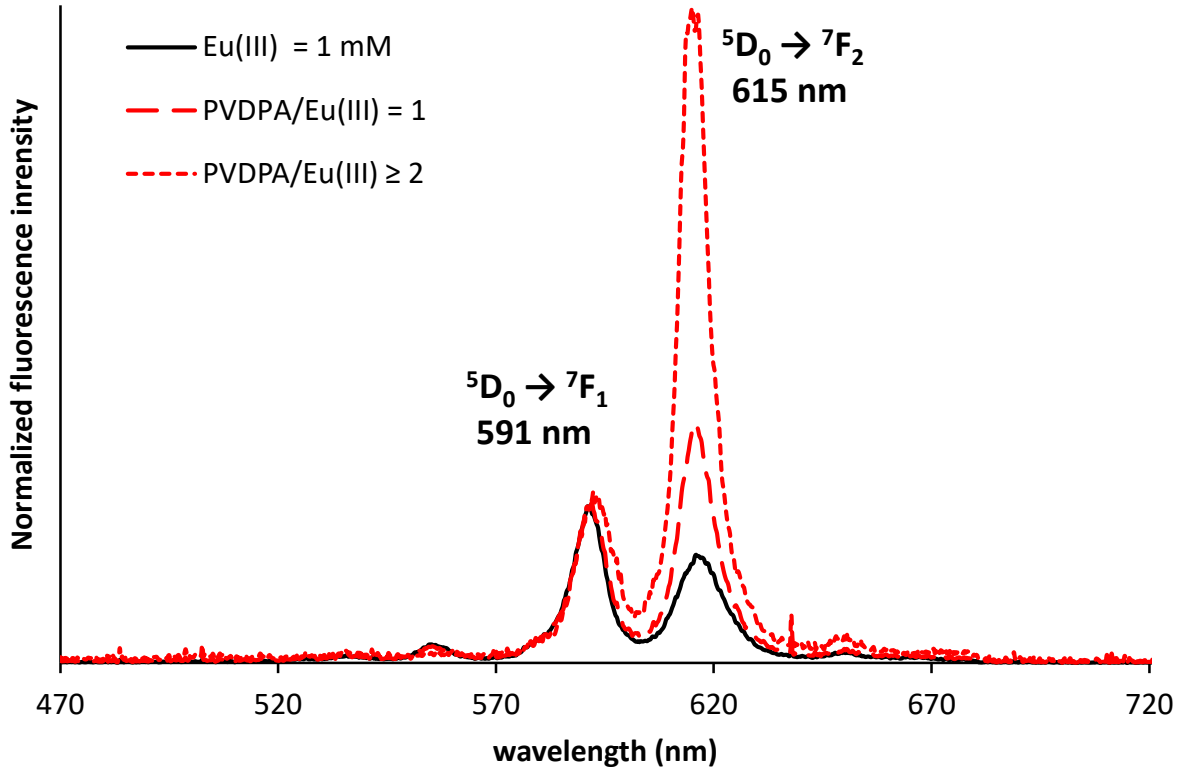

Figure IV-6. Emission spectra of 1 mM Eu(III) solution before and after adding 1 and 2 equivalents of PVDPA

During ligand addition, the characteristic changes in Eu(III) luminescence spectrum caused by complex formation can be seen by the strong increase of the $^5D_0 \rightarrow {}^7F_2$ transition at 615 nm.

To determine the complex configuration, the fluorescence was time-resolved and the decay lifetimes were calculated by fitting the integrated luminescence signal to a sum of exponential decay functions:

$$I\,(t) = \sum_i Ii_0 \exp(-t/\tau_i)$$

I* (t)** being the total luminescence intensity at time **t**, ***Ii*₀** the luminescence intensity of the species ***i at the time t = 0, and **τ_i** the corresponding lifetime.

The number of water molecules (hydration number) in the first coordination shell was determined from the luminescence lifetimes, using the following empirical formula [6]:

$$n\ H_2O(\pm 0.5) = \frac{1.07}{\tau} - 0.62$$

Lifetime measurements and resulting hydration numbers are given in the following table:

Table IV-1. Lifetimes and hydration numbers at different PVDPA / Eu(III) ratios

	τ_1 (µs)	n(H_2O) ± 0.5	τ_2 (µs)	n(H_2O) ± 0.5
Eu(III) = 1 mM	110	8.6	-	-
PVDPA / Eu(III) = 1	110	8.6	300	2.7
PVDPA / Eu(III) ≥ 2	-	-	300	2.7

As seen in table 1, the addition of 2 PVDPA equivalents to the Eu(III) solution prolonged the lifetime from 110 µs for the Eu(III) aqua ion to 300 µs for PVDPA / Eu(III) ≥ 2. $\boldsymbol{\tau_1}$ (110 µs) allowed us to estimate a 8.6 ± 0.5 (rounded to 9) hydration number for the aqua Eu(III) in perfect agreement with literature data [7].

In the case where PVDPA / Eu(III) ≥ 2, $\boldsymbol{\tau_2}$ (300 µs) indicated a hydration number of 2.7 ± 0.5 (rounded to 3), meaning that PVDPA, kicked out 6 water molecule from the Eu(III) hydration shell, in perfect coherence with a two trivalent ligands linked to a Eu(III) center, herein the formation of the $Eu(PVDPA)_2^-$ complex.

In the intermediate case where PVDPA / Eu(III) = 1, both $\boldsymbol{\tau_1}$ (110 µs) and $\boldsymbol{\tau_2}$ (300 µs) were needed for the best fit of luminescence decay, indicating the presence of both the free Eu(III) aqua ion and the $Eu(PVDPA)_2^-$ complex.

Where is Eu(PVDPA)$^{+}$?

When we think of the interaction between Eu(III) and the deprotonated PVDPA^{2-}, we imagine a mono-complex Eu(PVDPA)$^{+}$ being formed before the Eu(PVDPA)$_2^{-}$ bi-complex according to the following reaction:

$$Eu\ (III)_{\ liq} \xrightarrow{PVDPA^{2-}} Eu(PVDPA)^{+}_{\ liq} \xrightarrow{PVDPA^{2-}} Eu(PVDPA)_2^{-}{}_{\ solid}$$

However, the TRLFS study showed that at PVDPA / Eu(III) = 1, instead of Eu(PVDPA)$^{+}$, a mixture of free Eu(III) and the Eu(PVDPA)$_2^{-}$ complex is present. This can be explained by the fact that Eu(PVDPA)$_2^{-}$ precipitate and push the equilibrium forward. Future studies should be conducted in order to elucidate this phenomenon.

After studying the PVDPA complexation with lanthanides, we could proceed to examine the formation of PVDPA – uranium (VI) complexes.

IV.3. PVDPA - Uranium (VI) complexes

Herein, upon mixing a uranyl nitrate aqueous solution with a PVDPA solution, a white precipitate is seen. This precipitate exhibits this time a greenish fluorescence under a UV lamp (figure 7).

In the case of VDPA monomer – U(VI) mixture, no precipitate was formed allowing the UV-Vis study of the complex. Interestingly though, the U(VI) solution, originally fluorescent under an ordinary UV lamp, was no longer luminescent when VDPA was added (figure 7). In other words, the uranyl fluorescence was quenched upon VDPA monomer addition. This additional phenomenon will be later investigated by TRLFS.

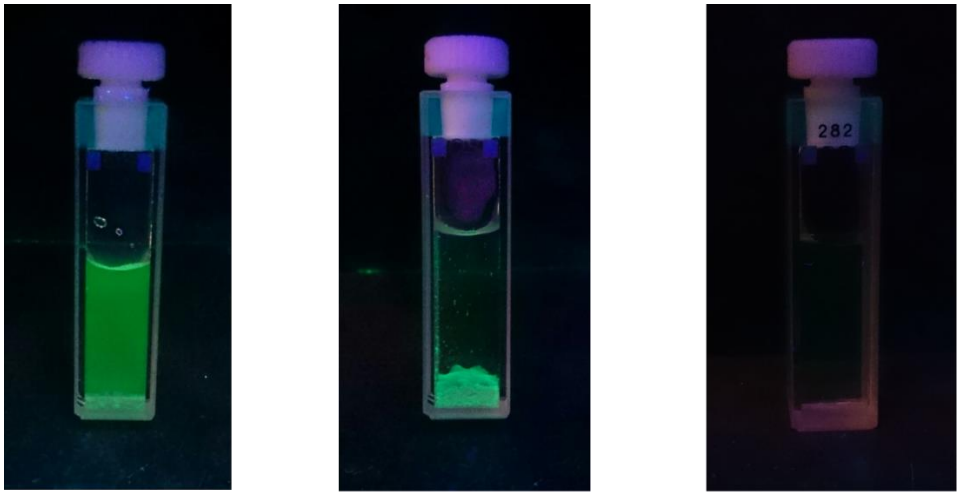

Figure IV-7. Uranium (VI) solution before and after adding PVDPA (polymer) and VDPA (monomer)

UV spectroscopy

VDPA monomer:

UV absorption spectroscopy is used here to put in evidence the interaction between the VDPA ligand and U(VI) ions in aqueous solution. Into a 0.1 mM solution of VDPA monomer, U(VI) was gradually added and the absorption spectra analyzed. The results are shown in figure 8.

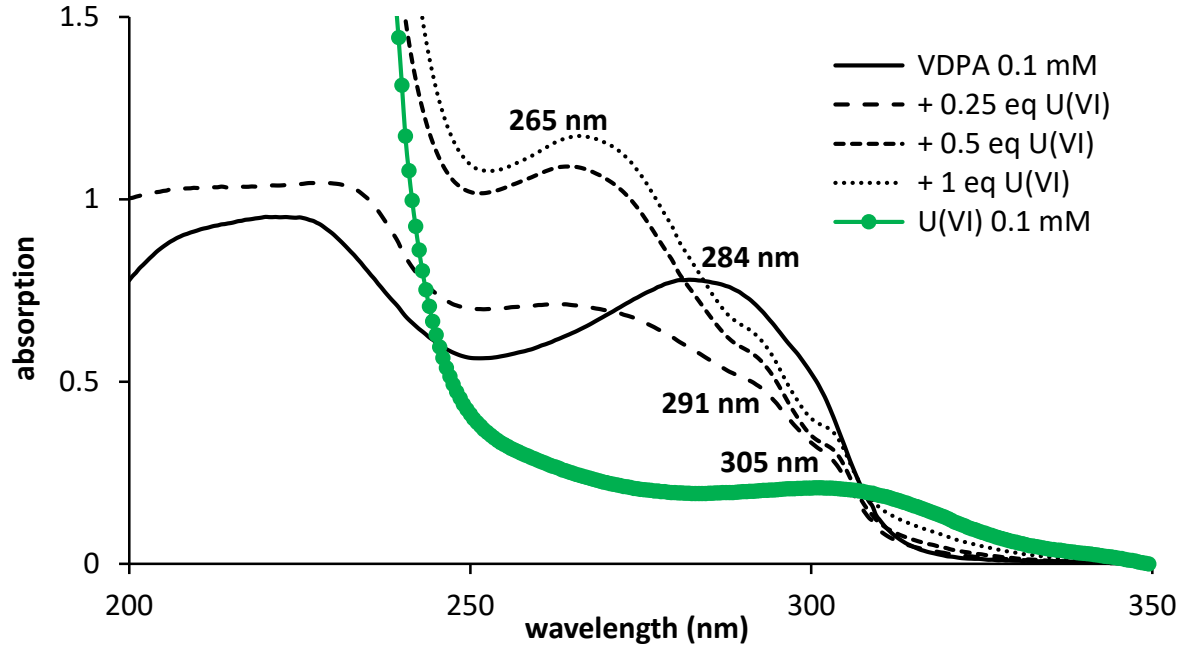

Figure IV-8. UV absorption spectra of VDPA – U(VI) complexes

Similarly to VDPA - Ln(III) seen before in figure 3, when U(VI) was added, the single VDPA peak at 284 nm was replaced by 3 maxima, a main peak at 265 nm and two shoulder peaks at 291 and 305 nm. Again, no further changes were seen at U(VI) > 0.5 equivalent and the same 2 conclusions were drawn:

1. The change in peaks positions and number shows that an interaction is taking place between the VDPA and the added uranyl ion.
2. The interaction is present up to a U(VI) / VDPA ratio of 0.5 which may be explained by the formation of $UO_2(VDPA)_2$ complex

$$UO_2^{2+} + 2\ VDPA^{2-} \rightarrow UO_2(VDPA)_2$$

To note that TRLFS will later prove the second conclusion only partially true!

PVDPA polymer:

Into a 0.25 mM aqueous solution of PVDPA polymer, U(VI) was gradually added. The solution was filtered and the UV absorption registered and shown in figure 9.

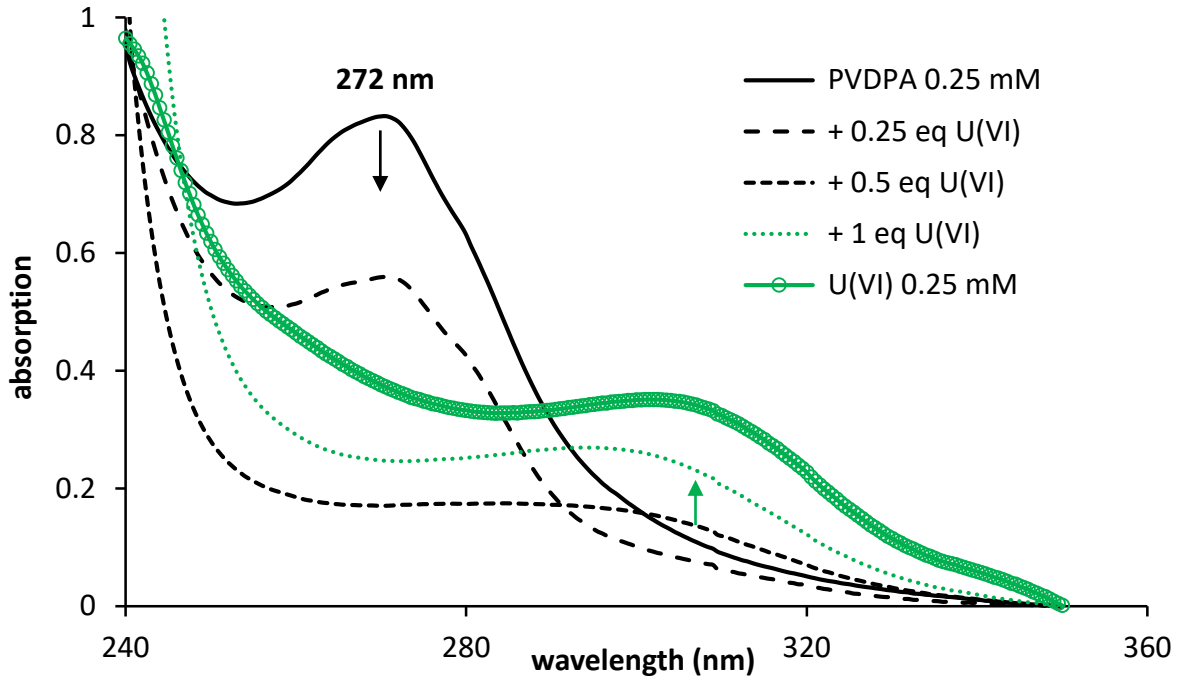

Figure IV-9. UV absorption spectra of remaining PVDPA after uranyl (VI) addition

As shown in figure 9, the PVDPA absorption spectrum went down when U(VI) was added in increasing ratios. At uranyl (VI) / PVDPA ratio higher that 0.5, no PVDPA is detected and the free U(VI) absorption increased, proving that the PVDPA – U(VI) complex was indeed precipitated and isolated when the solution filtered.

We concluded that PVDPA was completely precipitated at 0.5 equivalent of U(VI) and that reciprocally, 2 equivalents of PVDPA would be needed to decontaminate a given U(VI) solution. This results explains the observation in figure 7 where the greenish fluorescence was limited to the precipitate at the bottom of the solution.

In the following section, TRLFS will be employed to examine the coordination environment of uranyl ions when either the VDPA monomer or the PVDPA polymer were added.

TRLFS:

A 0.1 mM solution of uranyl nitrate was prepared and the pH adjusted to 7 ± 0.2 with sodium hydroxide. The fluorescence intensity of uranium species was recorded in the presence of increasing concentrations of VDPA (monomer) and PVDPA (polymer). As shown in figure 10, when either VDPA or PVDPA were added, the fluorescence intensity decreased dramatically.

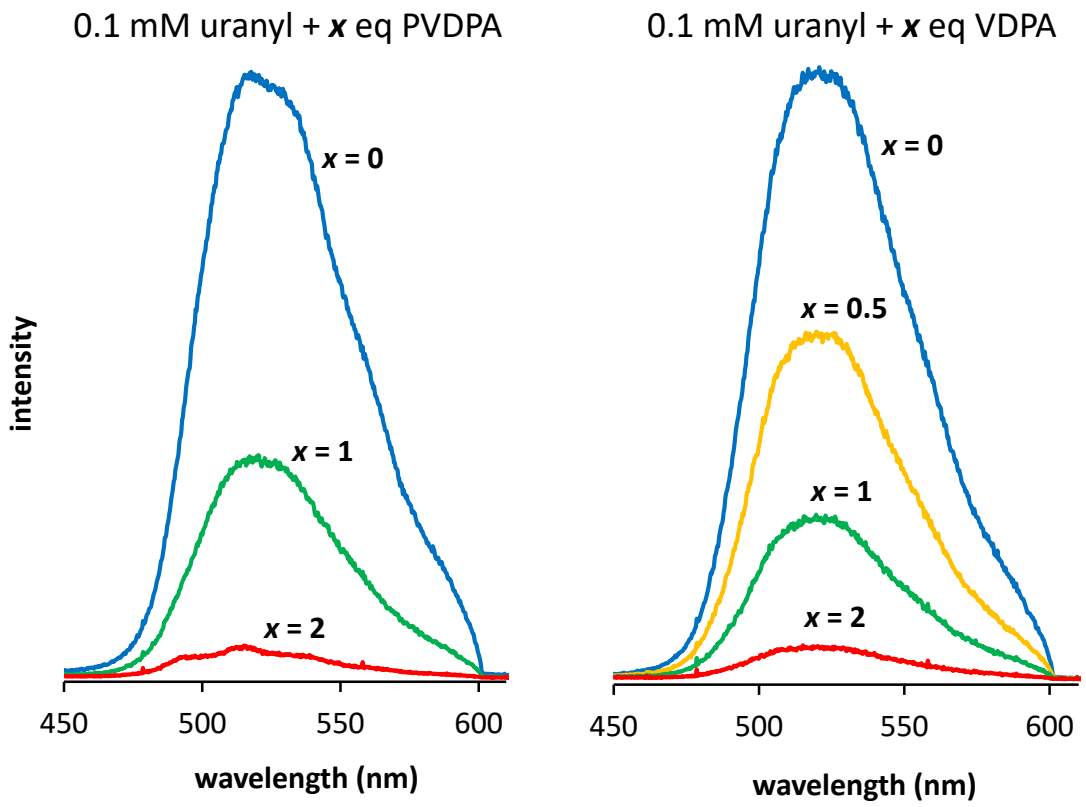

Figure IV-10. Uranyl fluorescence spectra at different PVDPA/Uranyl (left) and VDPA/Uranyl (right) ratios

The decrease of fluorescence intensity shows that an interaction is taking place between the ligand (monomer and polymer) and the uranyl ion. However, in the case of PVDPA, the peak shape changed, whether in the case of VDPA monomer no change is seen in the peak shape or position. This observation is more obvious when emission spectra were normalized, as shown in figure 11.

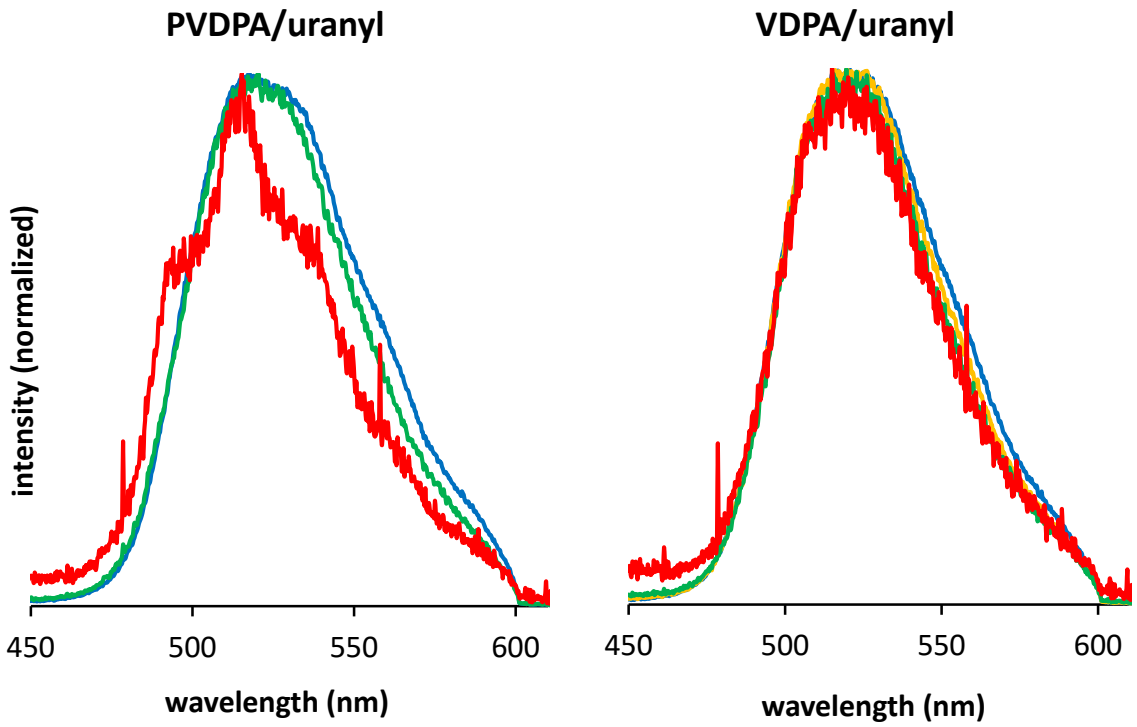

Figure IV-11. Normalized uranyl fluorescence at different PVDPA/Uranyl (left) and VDPA/Uranyl (right) ratios

Inspired by the visual observation in figure 7, we hypothesized that when PVDPA was added, the change in fluorescence spectra is due to the formation of fluorescent complexes and the fluorescence spectrum seen after adding 2 equivalents of PVDPA is actually the PVDPA - U(VI) complex fluorescence. On the other hand, when the VDPA monomer was added, the formed complex is not fluorescent and the registered fluorescence is only due to the remaining free uranyl in solution.

To test this hypothesis and further understand this phenomenon, fluorescent species in each solution had to be identified through lifetime measurements. However, contrary to the relatively simple europium (III) fluorescence studied earlier, several uranyl species are present at neutral pH, and the direct speciation at pH 7 and above (most common pH range for natural waters) is not straightforward as too many species are present due the uranyl hydrolysis [8-16].

Total peak area between 450 and 600 nm had to be used, and the fluorescence decay had to be fit to a 4th degree exponential function using origin™:

$$y = A_1*\exp(-x/t_1) + A_2*\exp(-x/t_2) + A_3*\exp(-x/t_3) + A_4*\exp(-x/t_4) + y0$$

where $\mathbf{A_i}$, the pre-exponential constant, equals the fluorescence intensity of a uranyl species of lifetime $\mathbf{t_i}$, at time zero. Normalized fluorescence decays are shown in figure 12. Decays were normalized before fitting to make it easier to compare the fits after adding the VDPA monomer or PVDPA polymer. Fitting results are shown in table 2.

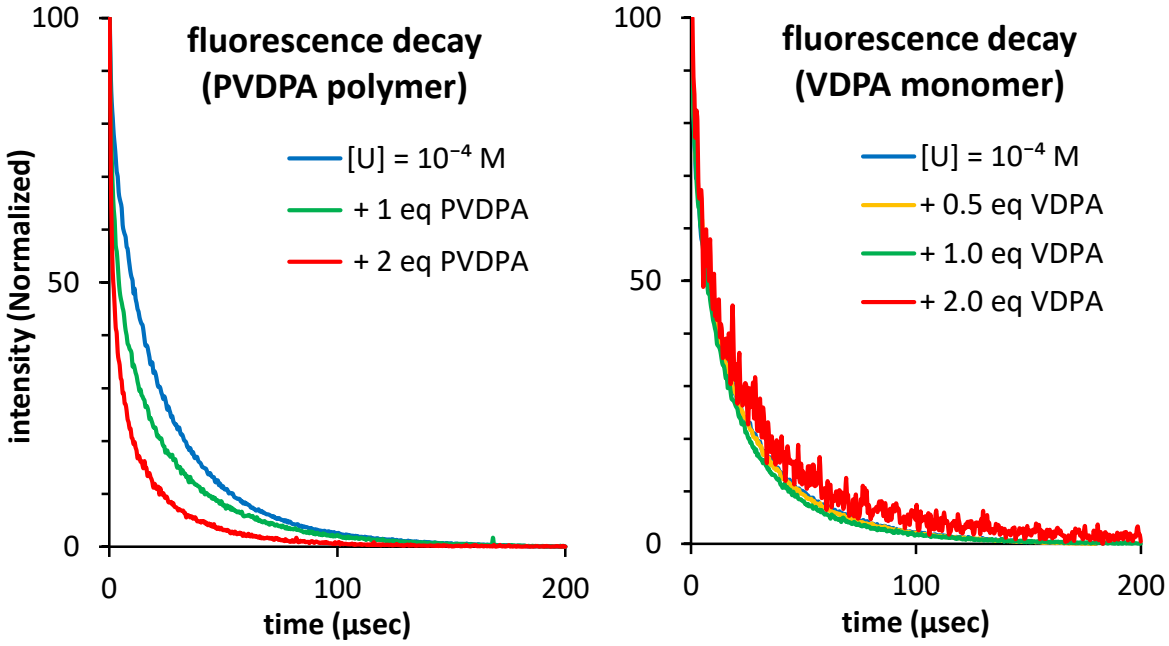

Figure IV-12. Normalized uranyl (VI) fluorescence decay at different PVDPA/Uranyl (left) and VDPA/Uranyl (right) ratios

Table IV-2. 4th exponential fitting functions

conc (10^{-4} M)		A_1	t_1	A_2	t_2	A_3	t_3	A_4	t_4
VDPA	0	27	**0.9**	27	**8.1**	46	**26.4**	6	**73.3**
	0.5	23	**0.9**	30	**8.1**	47	**26.4**	5	**73.3**
	1	25	**0.9**	33	**8.1**	44	**26.4**	3	**73.3**
	2	60	**0.9**	12	**8.1**	23	**26.4**	6	**73.3**
PVDPA	0	18	**0.9**	22	**8.1**	57	**26.4**	6	**73.3**
	1	28	**0.4**	27	**2.1**	30	**11.8**	28	**37.6**
	2	59	**0.4**	31	**3.4**	22	**14.2**	11	**33.5**

These results indicate the existence of at least 4 main uranyl species at pH~7, in agreement with literature data which concludes that several uranyl-hydroxide complexes are present. We tried to identify the uranyl species present in the original uranyl (VI) solution (before adding VDPA nor PVDPA) and we concluded that the 4 main uranyl species are:

$UO_2(OH)_3^-$	(t_1 = 0.9 µsec)	$(UO_2)_2(OH)_2^{2+}$	(t_3 = 26.4 µsec)
$(UO_2)_3(OH)_5^+$	(t_2 = 8.1 µsec)	UO_2OH^+	(t_4 = 73.3 µsec)

Discussion of polymer complexation:

The change in measured lifetimes (table 2) proves the complexation between uranyl and PVDPA. Nevertheless, elucidating the PVDPA-uranyl structure is seemingly too complicated and further studies, namely XAFS (X-ray Absorption Fine Structure), would be needed to further understand the uranyl coordination environment.

Discussion of monomer complexation:

As the chelating function is the same in both cases, it is believed that a complexation is also taking place in the case of VDPA monomer-uranyl mixture, but for some reason, fluorescence band shape and lifetimes (table 2) don't seem to change, meaning that the only florescence detected comes from the remaining free uranyl (VI) species.

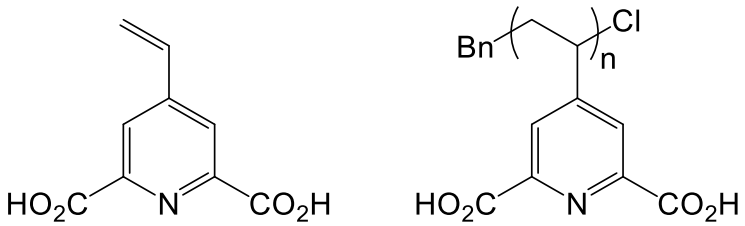

VDPA PVDPA

Scheme IV-5. Structures of VDPA monomer and PVDPA polymer

The only structural difference between the VDPA monomer and the PVDPA polymer being the vinyl function as shown in scheme 5, it seems that the vinyl function on the VDPA monomer has something to do with the fact that no fluorescence is detected from the formed complex, possible through charge transfer. Indeed, when reviewing the literature, uranyl fluorescence quenching by vinyl monomers is reported [17, 18]. However, more advanced studies should be done to elucidate this phenomenon, which is not within the scope of the present work.

IV.4. PVDPA functional surfaces

Once the complexation mechanism and efficiency of free PVDPA established, the performance of PVDPA-functionalized surfaces was examined.

Different PVDPM-functionalized surfaces described in chapter III were treated in NaOH to yield PVDPA surfaces as shown earlier in scheme 1 above. These surface were then dipped for few minutes in a Eu(III) nitrate solution, washed with distilled water and dried. Taking advantage of the europium fluorescence in the visible spectrum, these surfaces were examined under a 254 nm UV lamp as shown in figure 13.

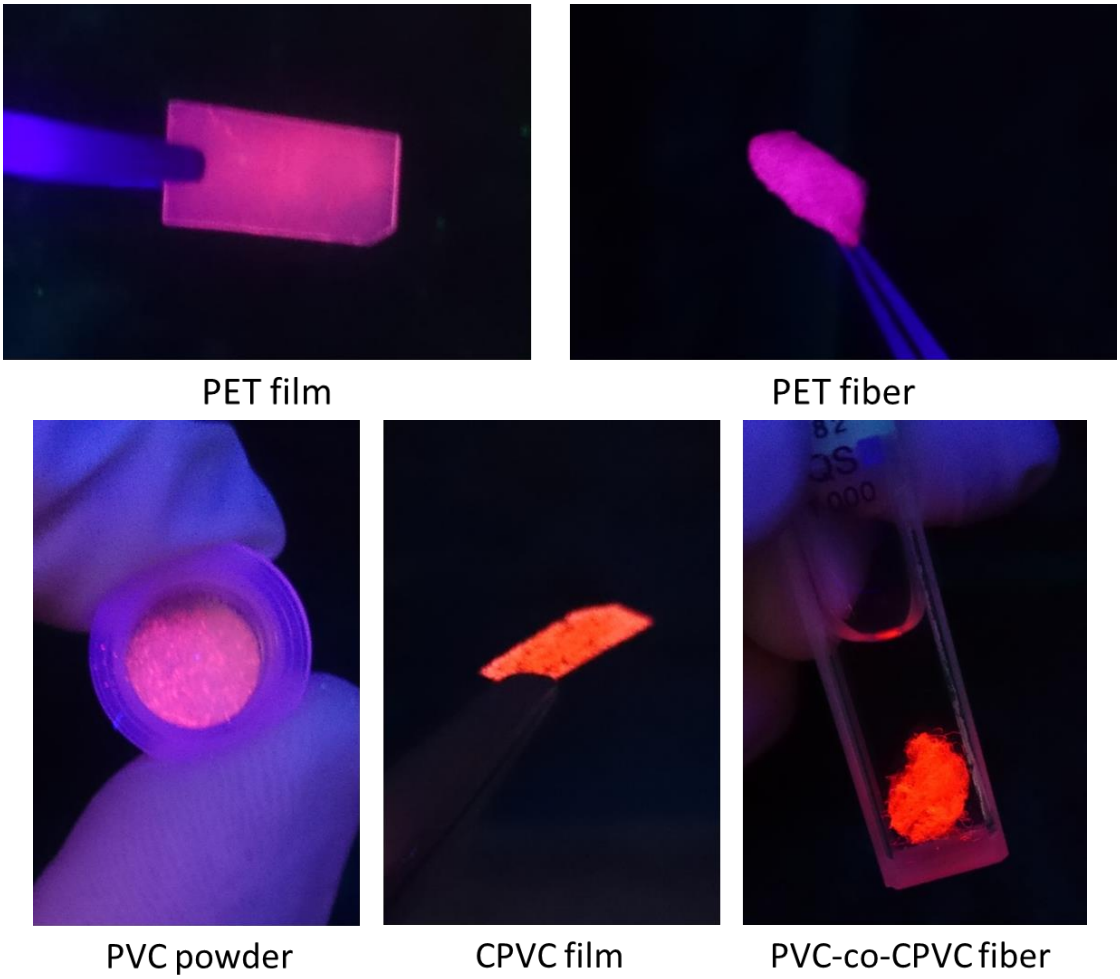

Figure IV-13. PVDPA – Eu(III) complexes on different surfaces

Looking at these different surfaces, one can see that all PVDPA-functionalized surfaces emit a reddish light under the UV lamp. However, the variation of the apparent red fluorescence intensity going from PET film and fibers to PVC powder, CPVC film and PVC-co-CPVC fibers, could indicate a variable density/thickness of the PVDPA – Eu(III) complex on the surface.

Back in chapter III, PVC-based substrates proved to be more efficient in surface initiated polymerization than PET. Most interestingly, a thicker layer of PVDPM could be built from PVC-co-CPVC fibers than from PET fibers (chapter III, figure 30). A thicker PVDPM layer means a thicker PVDPA one and accordingly a thicker PVDPA-Eu(III) complex layer, i.e. a higher trapping capacity.

To prove this hypothesis, ATR is used in the first place to show a thicker PVDPA – Eu(III) complex layer on PVC-co-CPVC fibers. The PVDPA – U(VI) complexe on the PVDPA-modified fibers was then evidenced by TRLFS. Finally, ICP-MS will prove a higher U(VI) trapping capacity of PVC-co-CPVC fibers as compared to PET fibers as substrate.

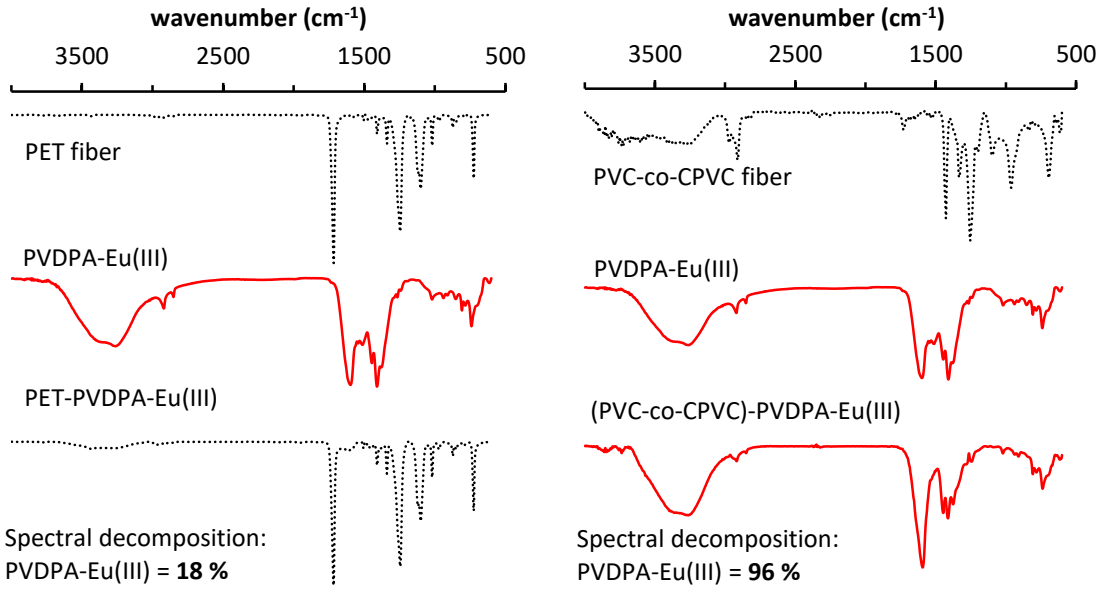

Figure IV-14. ATR of PVDPA – Eu(III) complex on PET vs PVC-co-CPVC fibers

As shown in figure 14, ATR spectral decomposition shows that the PVDPA – Eu(III) had a 18% spectral contribution on the modified PET fiber surface (figure 14 left) vs 96% on the modified PVC-co-CPVC fiber (figure 14 right). This result is in perfect agreement with a thicker PVDPM layer built on PVC-co-CPVC, as shown earlier (chapter III, figure 30).

Consequently, PVC-based fibers should also show a higher capacity in scavenging U(VI) in aqueous media. But before testing this hypothesis, the formation of the PVDPA - U(VI) complex should first be proven. This was done by dipping a piece of (PVC-co-CPVC)-g-PVPDA fiber in a U(VI) solution at pH~7 for few minutes. The fibers were then washed several time with water to remove excess U(VI) and dried. Under an ordinary UV lamp ($\lambda = 254$ nm), the green fluorescence gave the first hint of a PVDPA – U(VI) complex on the surface of the modified PVC-co-CPVC fiber (figure 15). Afterwards, the emission spectrum of this surface, excited at 430 nm, was acquired and shown in figure 15.

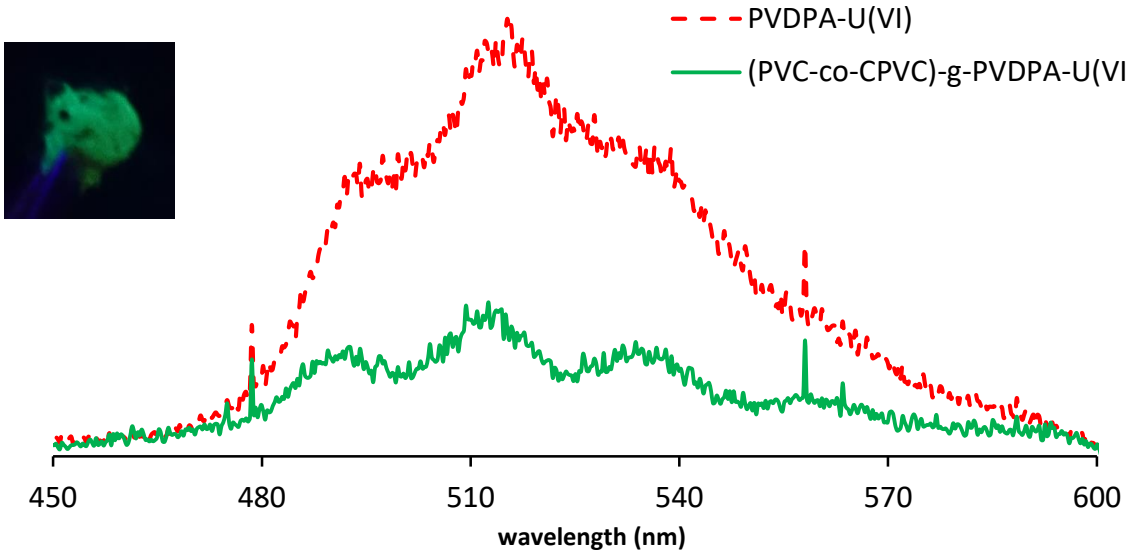

Figure IV-15. Luminescence of (PVC-co-CPVC)-g-PVDPA – U(VI)

The surface emission spectrum is compared to that of PVDPA – U(VI) complex taken from figure 10. As seen in figure 15, the spectral shape and position proves that PVDPA – U(VI) complex is indeed formed on the surface of the modified PVC-co-CPVC fiber, similar to that formed before in solution (figure 10).

The higher performance of PVC-co-CPVC as a substrate compared to PET was finally proven by ICP-MS. Two sets of fibers, PET-PVDPM and (PVC-co-CPVC)-*g*-PVDPM, the latter with a degree of grafting (d.g) of 41 % and each weighting exactly 3.1 mg, were hydrolyzed to PET-PVDPA and (PVC-co-CPVC)-*g*-PVDPA, respectively, according to scheme 1. These fibers were dipped in a 0.1 mM U(VI) solution at pH~7 overnight. The solutions were then filtered and the remaining concentration of U-238 measured with ICP-MS, as shown in figure 16.

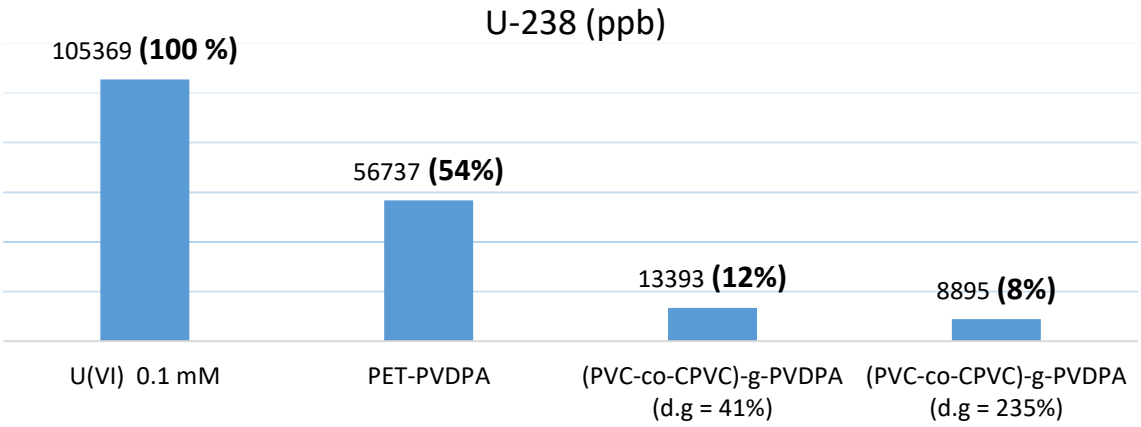

Figure IV-16. U-238 concentration (ppb) before and after treatment with modified fibers

It is very important to note that only one ICP-MS measurement was made on time on each sample to include in this manuscript and it was not repeated. Unfortunately, all ICP-MS measurements include errors and a correction factor should have been used for each measured element. For this reason, instead of discussing absolute concentrations in ppb, we will be discussing relative concentrations and compare their ratios before and after treatment with PVDPA-based materials.

Taking the initial U(VI) concentration before treatment as a 100 % reference, we can see in figure 16 that when this solution was treated with modified fiber, the relative concentration dropped to 54 % and 12 % when treated with PET-PVDPA and (PVC-co-CPVC)-g-PVDPA, respectively. This result proves that using PVC-co-CPVC as a substrate is more efficient to produce the highly absorbing materials. Unfortunately however, determining the absolute absorption capacity of these fibers could not be achieved at this stage. Greater quantities of uranium salt solutions would be needed and so we encourage future studies to explore the full capacity of our materials.

On the other hand, another question is posed here, regarding the effect of the degree of grafting (d.g), i.e. the thickness of the PVDPA layer, on the absorption capacity of the modified fibers. Does a thicker layer of PVDPA capable of absorbing more U(VI) and if so, to what extent?

Looking at figure 16, we can see that when PVC-co-CPVC fiber where modified to d.g. = 235%, the performance was slightly better with 8% remaining U(VI) than those with d.g. = 41 %. This means one of two things, the first being that the two sets of fibers have similar performances and a 235 % degree of grafting represents a negligible improvement compared to a degree of grafting of 41%, making it useless to build a thicker layer of PVDPA.

The second possibility is that a 1 mL solution of 0.1 mM U(VI), used in this experiment, is too little to show the full capacity of the d.g. = 235 % fibers. Unfortunately, once again we didn't have enough uranium, nor the time, to test this hypothesis. What we could do though, is visually comparing the instant absorbing capacity of modified fiber, without leaving the fibers overnight.

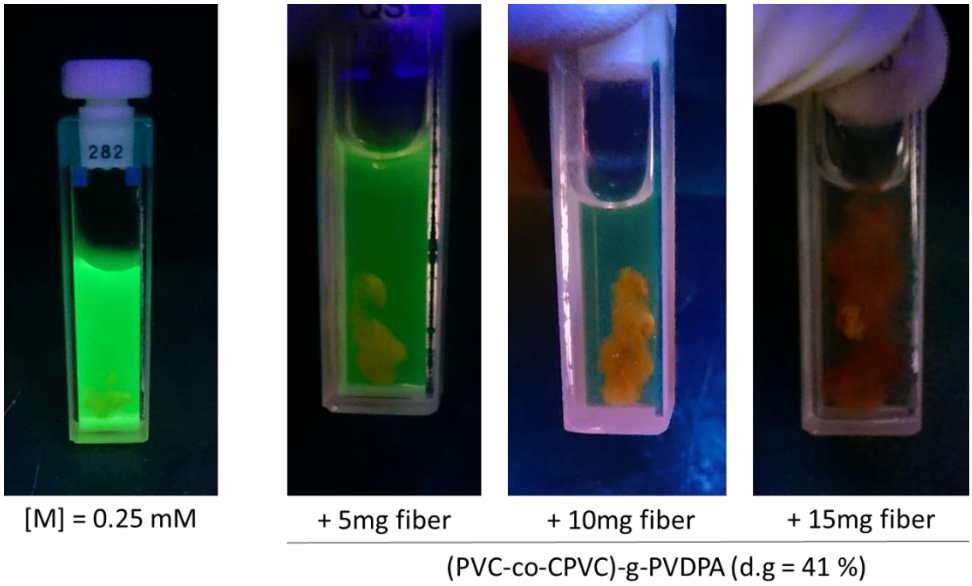

Figure IV-17. U(VI) decontamination with (PVC-co-CPVC)-g-PVDPA (d.g = 41%)

In figure 17, a 2 mL solution of 0.25 mM U(VI) was treated with an increasing quantity of (PVC-co-CPVC)-g-PVDPA fibers with a 41 % degree of grafting and observed under a 254 nm UV lamp with less than a minute separating each two steps. We saw that it was not until 15 mg of fibers were added that the green fluorescent became invisible to the naked eye. When the same experiment was done with the d.g. = 235 % fibers, only 3 mg were used to get a similar result.

To conclude, PVDPA-modified fibers were used for a successful decontamination of a U(VI) aqueous solution. PVC-co-CPVC substrate is favored over PET, because a thicker layer of PVDPA can be built on PVC surface, giving a higher absorbing capacity, in addition to an easier modification strategy discussed earlier in chapter III. A higher degree of grafting, i.e. thicker PVDPA layer, also seems to have a higher absorbing capacity, though further studies should be conducted to determine the optimal PVDPA thickness and the absolute absorbing capacity.

IV.5. Uranium harvesting from seawater

Uranium harvesting from seawater is a particularly ambitious application for our highly adsorbent PVDPA-based materials. Current state-of-the-art poly(amidoxime)-based adsorbent materials still face a major obstacle that limits its uranium adsorbing capacity, that of the very high affinity of those materials towards vanadium (V) ions. Even though V(V) exists in seawater at levels (1.9 ppb) lower than that of U(VI) (3.3 ppb), V(V) greatly outcompete uranium for binding sites [19]. Moreover, the seawater high ionic strength can affect the absorbing performance of absorbents. In this section, we will study the effect of seawater's high ionic strength on the complexation of U(VI) by PVDPA and the competition between uranium and vanadium species for PVDPA binding sites.

IV.5.1. The effect of ionic strength

The effect of seawater's ionic strength was studied by preparing a 0.1 mM U(VI) solution using distilled water and simulated seawater as solvents. Simulated seawater was prepared by dissolving the proper quantities of sodium chloride (NaCl) and sodium bicarbonate ($NaHCO_3$) in water to mimic the seawater ionic strength of 0.4 M. Two equivalents of PVDPA were added to each of the U(VI) solutions. The solutions were kept for few minutes to allow the PVDPA – U(VI) complex to precipitate then filtrated. The remaining U(VI) concentration was then measured by ICP-MS as shown in figure 18.

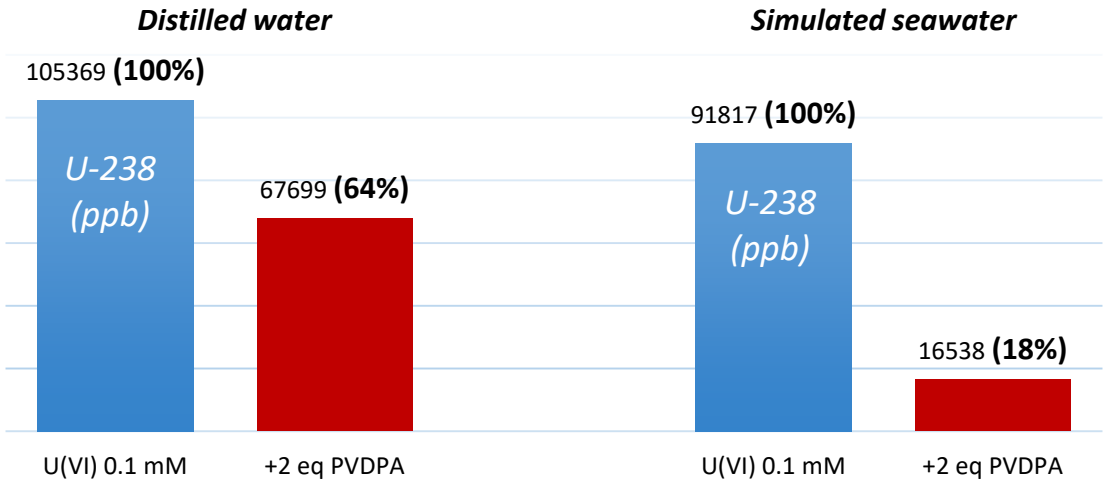

Figure IV-18. PVDPA – U(VI) complexation in simulated seawater

As seen in figure 18, when PVDPA was added and the solution filtrated, the concentration of U(VI) dropped to 64% with respect to the non-treated U(VI) solution prepared in distilled water. When simulated seawater was used, the drop in U(VI) relative concentration went down to 18% with respect to the non-treated solution. This means that PVDPA is capable of decontaminating a U(VI) solution, even at high ionic strength.

This result doesn't mean that the PVDPA complexation is not efficient in distilled water, because we saw earlier that the PVDPA complex is completely formed in a zero ionic strength solution (figures 9 and 10). Herein, our main concern was that we knew that PVDPA has a lower solubility in high ionic strength water, which we thought can decrease its performance. This experiment showed that, instead of decreasing its efficiency, the high ionic strength actually favors the precipitation of PVDPA, taking with it the U(VI) ions. Thus, the lower efficiency of PVDPA at zero ionic strength (distilled water) is probably due to slower precipitation of the complex, therefore not efficiently retained by filtration.

Back to our more important result, we conclude that the formation of the PVDPA – U(VI) complex is highly efficient at an ionic strength level similar to that of seawater. In the next section, we investigate the other obstacle that faces the uranium harvesting from seawater, that of uranium-vanadium competitive absorption.

IV.5.2. Uranium (VI) – Vanadium (V) competition

In the literature, dipicolinic acid, from which our polymer is derived, already demonstrated a higher selectivity towards U(VI) (log K = 11.6) over V(V) (log K = 9.3). Herein, we needed to examine the performance of our materials in decontaminating a U(VI) solution, even if V(V) is present. We first used UV absorption spectroscopy to see to was extent the VDPA monomer is interacting with V(V). We then put PVDPA polymer to test and tried to decontaminate a U(VI) solution after the PVDPA was saturated with V(V).

VDPA monomer:

Into a 0.1 mM VDPA solution, V(V) was added in increasing ratios using a concentrated mother solution of vanadium (V) oxide solution (V_2O_5). The resulting solutions were analyzed by UV absorption spectroscopy and the obtained spectra are shown in figure 19.

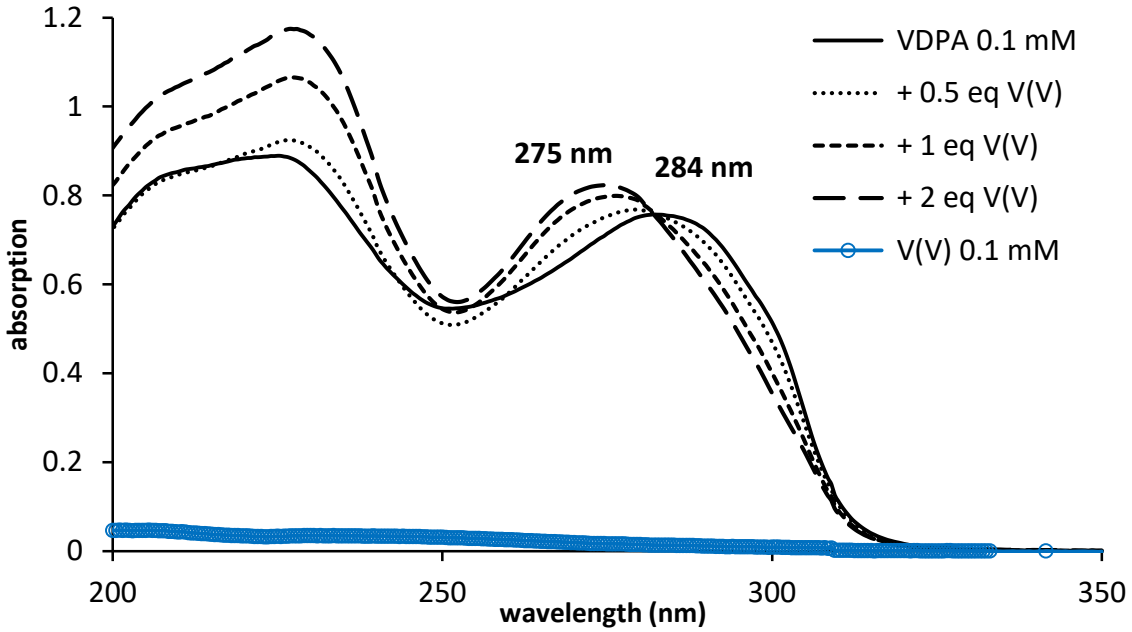

Figure IV-19. UV absorption spectra of VDPA – V(V) complexes

As seen in figure 19, the peak maximum, originally situated at 284 nm for VDPA, gradually shifted with increasing V(V) ratio to 275 nm at 2 V(V) equivalents. It should be noted that no further change was seen at V(V) ratio greater than 2 (data not shown). These results were compared with those of VDPA – Ln(III) (figure 3) and VDPA – U(VI) (figure 8) complexes and the following conclusions were drawn:

1. The change in peak maxima up to a V(V) / VDPA ratio of 2 shows an interaction is taking place between the VDPA monomer and V(V) ion. However, spectral shape is different than that of VDPA – Ln(III) and VDPA – U(VI) complexes, indicating that the binding mode is probably different.
2. The interaction is present up to a V(V)/VDPA ratio of 2, in contrast with the case of VDPA – Ln(III) and VDPA – U(VI) complexes were the interaction was limited to a ratio of 0.5, meaning that one VDPA unit could be binding 2 V(V) ions:

$$2\ VO_2^+ + VDPA^{2-} \rightarrow (VO_2)_2VDPA$$

PVDPA polymer:

A 0.25 mM solution of PVDPA polymer was prepared and saturated with 2 equivalents of V(V). No precipitation was detected. Into this solution, 0.5 equivalent of U(VI) was added and the solution filtered. The UV absorption spectra were registered at each step and plotted in figure 20.

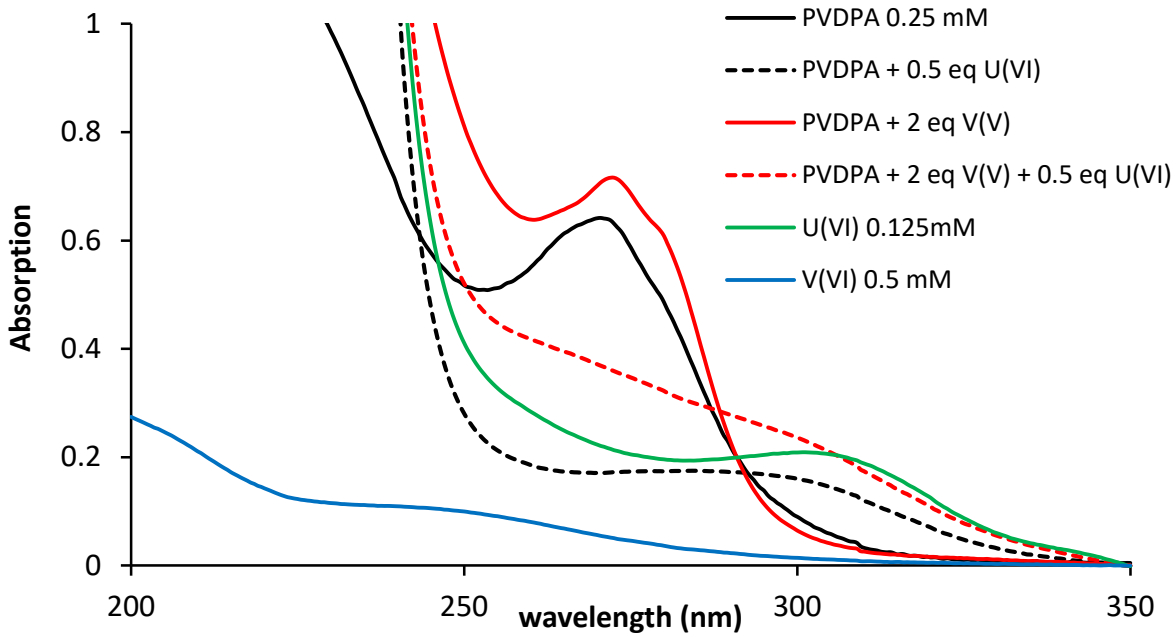

Figure IV-20. Simultaneous PVDPA interaction with U(VI) and V(V)

When 2 equivalents of V(V) were added to the 0.25 mM PVDPA solution, one can see the change in spectrum shape going from pure PVDPA (solid black line) to PVDPA+2eq V(V) (solid red line). When 0.5 equivalent of U(VI) were further added, the PVDPA was precipitated and no peak from PVDPA was detected (red dashed line). To better understand this result, the PVDPA+0.5 eq U(VI) spectrum (black dashed line) was taken from figure 9. The two dashed lines were not identical, probably due to the V(V) released when replaced by U(VI) on the PVDPA binding sites, explained by the non-zero absorption of V(V) shown in blue line.

The above result shows that even when PVDPA's binding sites were saturated with 2 equivalents of V(V), U(VI) was still able to outcompete for PVDPA's binding. This higher selectivity is probably even more enhanced thanks to precipitation, pushing the equilibrium towards U(VI) binding rather than V(V).

To further prove the affinity of PVDPA for U(VI) even if V(V) is present in the medium, we studied the emission of U(VI) when interacting with PVDPA with and without V(V). A 0.1 mM solution of U(VI) was prepared (pH~7), into which either V(V), PVDPA or both were added. All the solutions were excited at 405 nm and at least 50 emission scans were accumulated for optimal signal/noise ratio. The emission spectra are shown in figure 21.

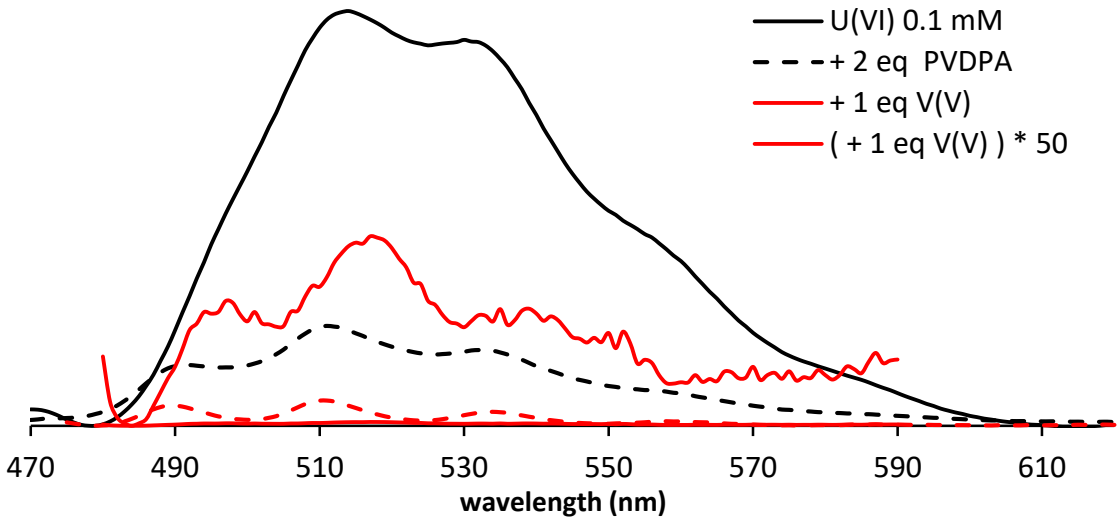

Figure IV-21. Emission spectra of different U(VI) / V(V) / PVDPA mixtures

U(VI) 0.1 mM solution emission is shown in black line. First of all, when 1 equivalent of V(V) was added (red line), the U(VI) luminescence was largely quenched. The later emission spectra was multiplied by 50 to better visualize the change in the emission spectrum. TRLFS studies in earlier sections showed that different U(VI) species are present at pH 7 due to uranium hydrolysis. Herein in figure 21, that change in peak in intensities, shape and positions show that some of the U(VI) species luminescence are quenched by V(V). Uranium quenching by transition metals was also reported in literature [20].

Later on, 2 equivalents of PVDPA polymer were added to the U(VI) solution with (red dashed line) and without (black dashed line) the presence of 1 equivalent of V(V). In both cases, the U(VI) emission spectra changed remarkably. When PVDPA was added to U(VI), the peaks intensity, number and position changed. This case was already discussed in the previous section when PVDPA-U(VI) complexation was studied by TRLFS.

When PVDPA was added to U(VI) in the presence of 1 equivalent of V(V) (red line), the U(VI) emission was more intense (red dashed line), with a change in peak position and number. We concluded that PVDPA is indeed interacting with U(VI) even when V(V) is present.

When comparing the PVDPA-U(VI) complexes in both cases, with (red dashed line) and without (black dashed line) the presence of V(V), we can see that in the two cases, the two emission spectra have the same shape in term of peaks number and position. However, the intensity of the PVDPA-U(VI) emission was lower when V(V) was present (red dashed line). This can be explained by a luminescence quenching by V(V), or by an inferior efficiency of the PVDPA-U(VI) complex formation. Having the same number of peaks at the same positions in both case favors the first explanation (i.e. V(V) is also quenching the PVDPA - U(VI) complex luminescence), but further studies would be needed to settle. This is why we later conducted an ICP-MS measurement.

A mixed solution of 0.1 mM U(VI) and 0.1 mM V(V) was prepared in simulated seawater. Two equivalents of PVDPA were then added and the remaining species measured by ICP-MS as shown in figure 22. Results were compared to the PVDPA - U(VI) complex formation in seawater taken from figure 18.

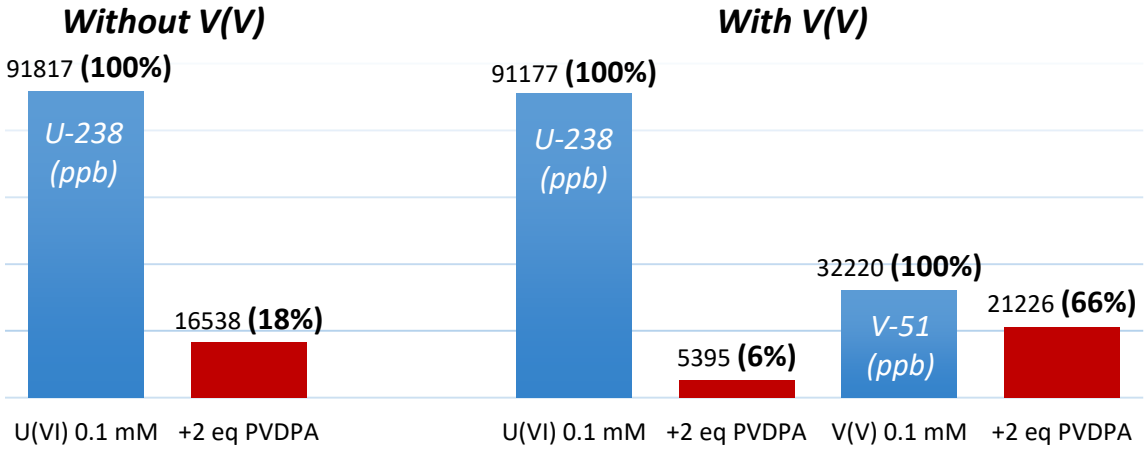

Figure IV-22. PVDPA-U(VI) complexation with and without V(V)

As discussed earlier, the U(VI) relative concentration dropped down to 18% when the solution treated with 2 equivalents of PVDPA. Herein, when V(V) was introduced into the system, the relative concentration of U(VI) went further down to 6% (figure 22). V(V) on the other hand, went down to 66% with respect to the non-treated solution. We conclude that the U(VI) complexation is indeed enhanced in the presence of V(V), making our PVDPA-based absorbent materials very promising vis-à-vis the application of uranium harvesting from seawater.

IV.6. Polymer assisted Actinide Lanthanide EXtraction (PALEX)

Back in chapter I, we discussed the potential application of PVDPA in spent nuclear fuel recycling and we proposed a recycling process we called PALEX (**P**olymer assisted **A**ctinide **L**anthanide **EX**traction). In the PALEX process (scheme 6), lanthanides and actinides are simultaneously trapped in an aqueous solution and separated from other fission products. Lanthanides are then separated from actinides by pH tuning.

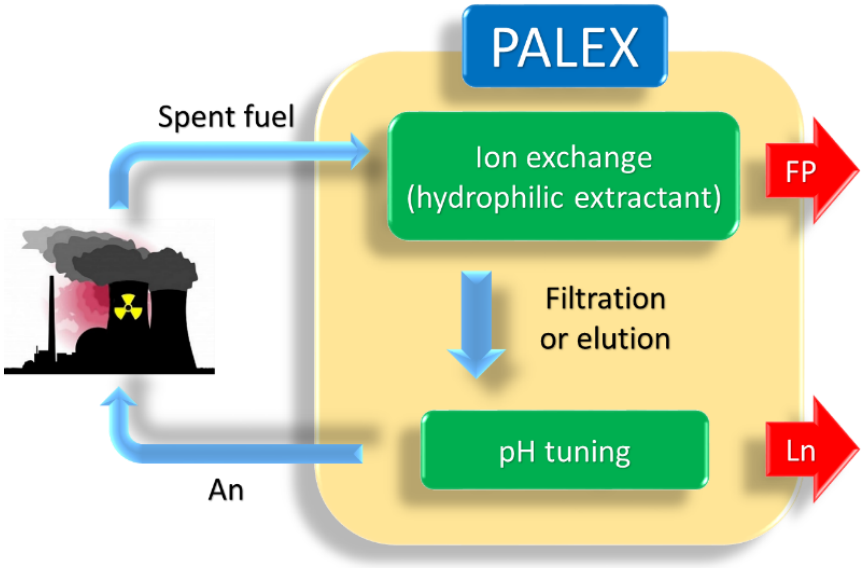

Scheme IV-6. Proposed PALEX process

Despite our limited resources vis-à-vis this application and the extreme difficulty of establishing such a process, we tried to obtain preliminary experimental results to encourage future developments and serious consideration of the PALEX process.

In order to do that, the simultaneous complexation of lanthanides and uranium with PVDPA was first examined. For practical reasons, Eu(III) was used as lanthanide for fluorescence studies and Nd(III) for ICP-MS measurements. The interaction of PVDPA was then examined with two major fission products, cesium (Cs) and strontium (Sr). Finally, the PALEX process was mimicked using free PVDPA and (PVC-co-CPVC)-*g*-PVDPA fibers.

IV.6.1. Lanthanides (III) / Uranium (VI) simultaneous complexation

In order to prove the simultaneous complexation between PVDPA and both lanthanides and actinides, PVDPA was added to a mixed aqueous solution of Eu(III) and U(VI). The first hint of a simultaneous complexation was given visually as shown in figure 23.

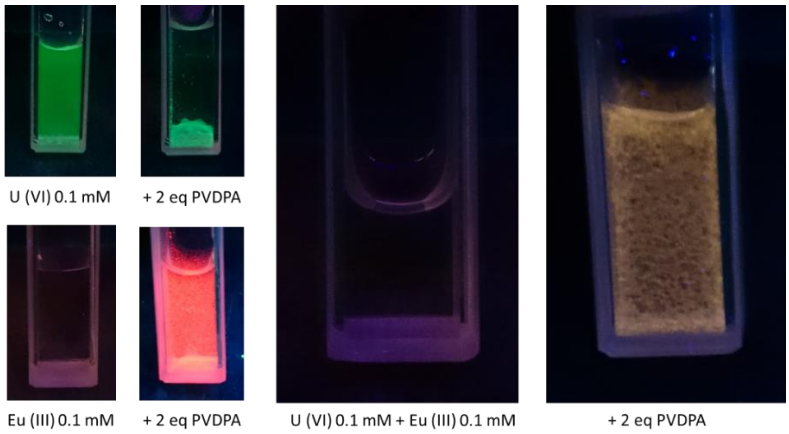

Figure IV-23. PVDPA interaction with U(VI), Eu(III) and both

To a mixed solution of U(VI) and Eu(III) at 0.1 mM each at pH~7, two equivalents of PVDPA were added as shown in figure 23 (right), causing a precipitation with a yellowish fluorescence when seen under a 254 nm UV lamp. Keeping in mind that the PVDPA - U(VI) complex is green (figure 23 top left) and that PVDPA-Eu(III) complex is red (figure 23 bottom left), we believe that the yellow precipitate is actually a mixed PVDPA - U(VI) / Eu(III) complex.

To prove this hypothesis, we looked at the fluorescence spectra of a mixed U/Eu solution before and after adding two equivalents of PVDPA, excited at 405 nm, as shown in figure 24.

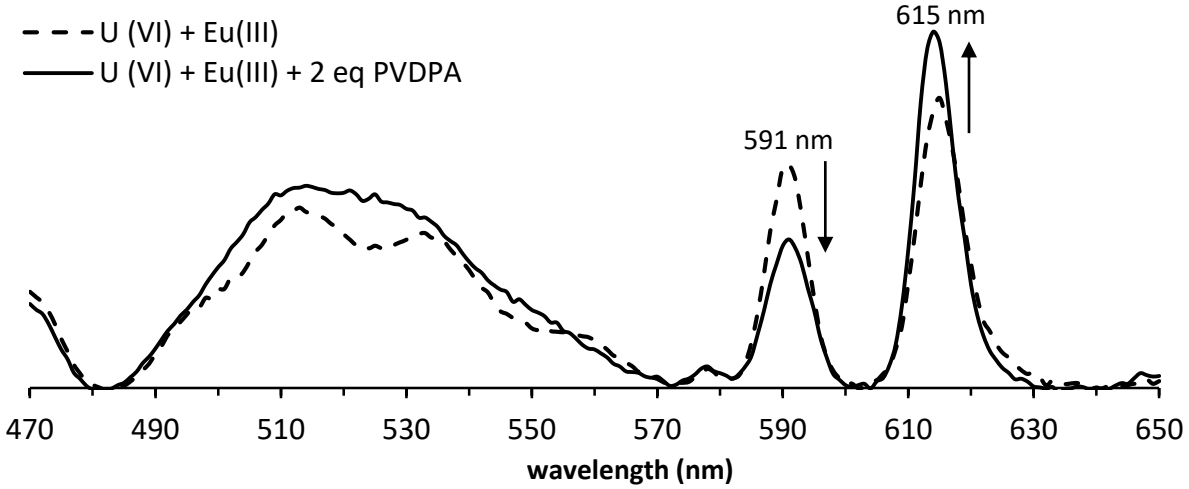

Figure IV-24. Emission spectra of a mixed U(VI)/Eu(III) solution with or without PVDPA

The change in U(VI) emission band shape between 480 and 570 nm on one side, and the Eu(III) 591/615 nm bands ratios on the other side (figure 24), both show that PVDPA is indeed interacting with both U(VI) and Eu(III) simultaneously, under the used conditions.

In another experiment, a mixed solution of U(VI) and Nd(III), at 0.1 mM each in simulated seawater, was prepared. Two equivalents of PVDPA were added and the solution filtered to remove the precipitated complexes. The relative concentrations of U(VI) and Nd(III) were then measured by ICP-MS. For a better comparison, U(VI) complexation in the absence of Nd(III) was taken from figure 18. The overall results are shown in figure 25. Nd(III) results were divided by 0.172 to account for the relative isotopic abundance of Nd-146.

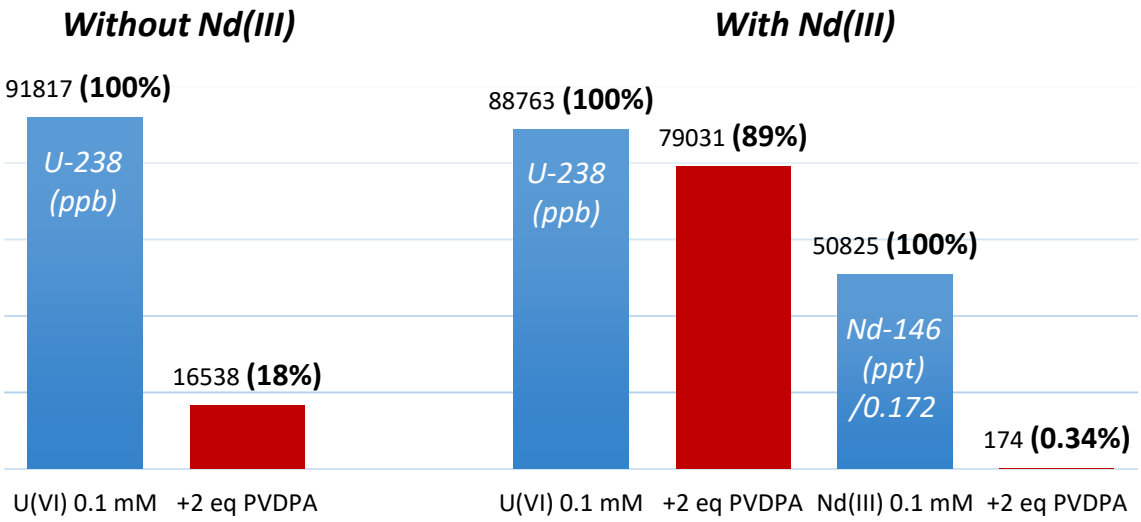

Figure IV-25. PVDPA interaction with a mixed U(VI) / Nd(III) solution

When only U(VI) was present, its relative concentration went down to 18% after treatment with PVDPA. When Nd(III) was introduced, we can see in figure 25 the competition between U(VI) and Nd(III) for the binding of PVDPA. The relative concentration of U(VI) went down slightly to 89% while Nd(III) relative concentration dropped to an impressive 0.34% when compared to the non-treated solution. These results show that, at neutral pH, the formation of PVDPA - Nd(III) complex is favored over PVDPA - U(VI).

It should be mentioned that this was the case when only 2 equivalents of PVDPA were added. Nevertheless, it is expected that when 4 equivalents of PVDPA are added, the majority of both species is trapped.

IV.6.2. PVDPA interaction with cesium and strontium

In order for the PALEX process to work, the PVDPA-based materials should have a higher affinity towards actinides/lanthanides over other major fission products. Herein, we assess the interaction between PVDPA and both cesium (I) and strontium (II) ions. Into a 0.25 mM solution of PVDPA, Cs(I) and Sr(II) were added in increasing ratios. Most importantly, no precipitation was seen. UV absorption spectra were registered at each point as shown in figure 26.

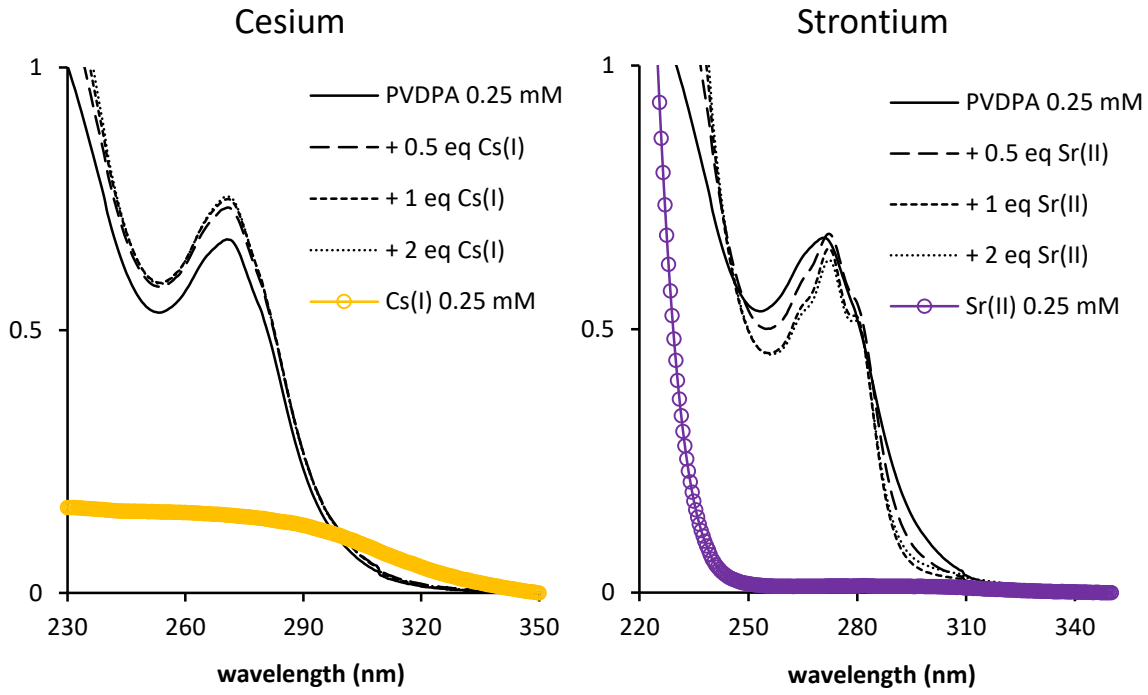

Figure IV-26. UV absorption spectra of PVDPA interaction with Cs(I) and Sr(II)

As seen in figure 26 (left), the addition of Cs(I) in increasing ratio doesn't seem to change the shape and position of the UV absorption spectrum of PVDPA. The PVDPA-Cs(I) spectra are identical at 0.5, 1 and 2 equivalents of added Cs(I). This is a sign of a minimal interaction between PVPDA and Cs(I).

In the case of strontium (figure 26 right), the addition of Sr(II) changed the shape of PVDPA's spectrum to the extent of a Sr(II)/PVDPA ratio of 1. This means that Sr(II) has a stronger effect on PVDPA than Cs(I). It's hard though to further understand the interaction of Cs(I) and Sr(II) with PVDPA and more studies would be needed. Unfortunately, these studies were not made on time.

However, literature data suggests that carboxylate ligands have minimal interaction of Cs(I) in water, followed by Sr(II) and both behind actinides like thorium (IV), uranium (VI) and plutonium (IV) and lanthanides like Eu(III). Carboxylate ligands were found to have metal affinities in the order of Pu(IV) > Eu(III) > Sr(II) > Cs(I) with a 0.1 M $NaNO_3$ concentration sufficient to prevent Cs(I) and Sr(II) complexation [21-23]. Picolinate ligand was found to have metal affinities in the order of Th(IV) > U(VI) > Sr(II) > Cs (I) [24].

These observations suggests that the interaction of PVDPA with Cs(I) and Sr(II) in water should be minimal if existent. Furthermore, the precipitation of PVPDA - Ln(III) and PVDPA-U(VI) complexes should enhance even more the selectivity of PVDPA towards actinides and lanthanides. Future in-depth studies should tackle this subject.

IV.6.3. Simulation of the PALEX concept

Finally, we wanted to simulate a nuclear spent fuel treatment using the PALEX concept. The complexity of such study and our limited resources made it impossible for us to use real samples, in addition to the fact that this was done towards the end of this thesis, preventing advanced analysis to be done on time. Based on all of the above observations and conclusions, we tried at least to prove visually the feasibility of the PALEX concept.

A mixed solution of U(VI), Eu(III), Sr(II) and Cs(I), at 1 mM each, was prepared. Into this solution, 4 equivalents of PVDPA were added to ensure that both U(VI) and Eu(III) are trapped and, within seconds, a white precipitate is formed. Under a 254 nm UV lamp, this precipitate exhibits a yellow fluorescence as seen in figure 27. This precipitate is believed to be a mixed PVDPA - U/Eu complex, especially when compared with earlier observations (figure 23). At this point, a simple filtration allows the isolation of the PVDPA-U/Eu complex as first step of the PALEX concept. It's worth mentioning that the same experiment was repeated at neutral (pH~7) or acidic (0.1 mM HNO_3) pH, with the same result in both cases.

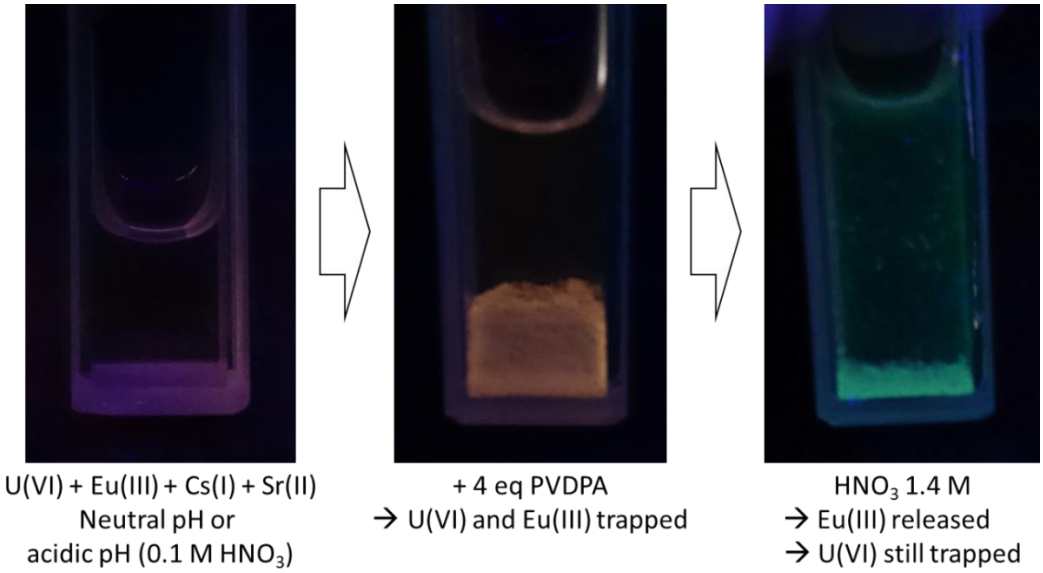

Figure IV-27. A simulation of the PALEX concept

In the second step of the PALEX concept, concentrated nitric acid was gradually added and around 1.4 M, the yellow precipitate turned green (figure 27), a sign of the PVDPA-U(VI) complex as seen earlier in figure 23. We believe that at this moment, Eu(III) is released back into the solution and U(VI) is still trapped by PVDPA. Herein, a simple filtration should be able to separate the trapped U(VI) from the released Eu(III). However, in this simulation, the used quantities were too small to actually do the filtration at each step. Thus, to have a better idea on the separation of U(VI) and Eu(III), the same experiment was repeated, this time using the (PVC-co-CPVC)-*g*-PVDPA fibers, which are easier to remove from the solution. Results are shown in figure 28.

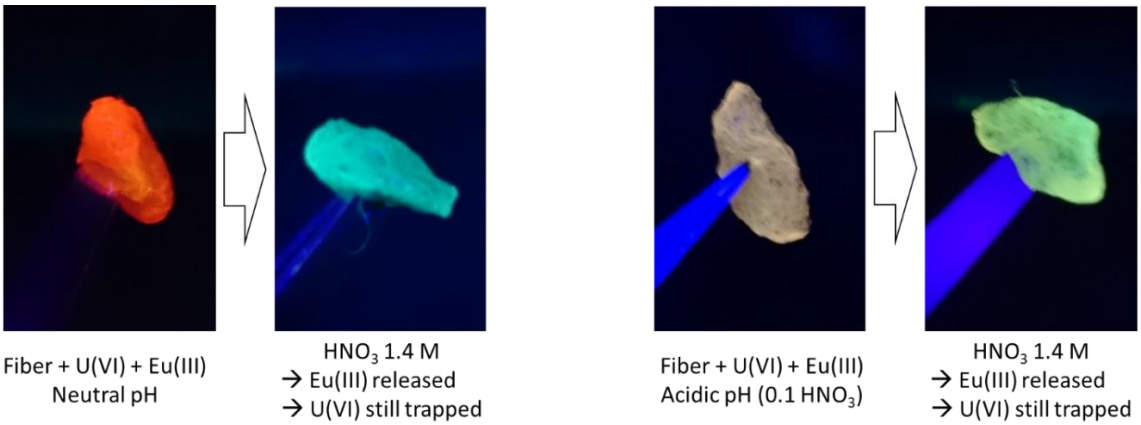

Figure IV-28. Sorption of U(VI) and Eu(III) on (PVC-co-CPVC)-g-PVPDA at neutral and acidic pH

Herein, (PVC-co-CPVC)-*g*-PVDPA fibers were dipped in a mixed U/Eu/Cs/Sr solution then taken out and seen under a UV lamp. Interestingly, when PVDPA-functionalized fibers were used instead of the free PVDPA polymer, the complexation behavior at neutral pH (figure 28 left) was different from that which took place in an acidic medium (figure 28 right).

At neutral pH, the fibers surface exhibits a red fluorescence, typical of a PVPDA - Eu(III) complex (figure 28 left). This means that Eu(III) may be predominantly trapped, in agreement with higher lanthanides affinity seen before in figure 25. When washed with a 1.4 M nitric acid solution, the fibers turned green, a sign of PVDPA - U(VI) complex. This means that even though the fibers were red fluorescent, uranium was also trapped and left on the surface after the nitric acid wash stripped off Eu(III).

In the second case, when the fibers were dipped in a mixed U/Eu/Cs/Sr solution at acidic pH (figure 28 right), the yellow fluorescence was a sign of a mixed PVDPA-U/Eu complex, similar to that seen earlier in figure 27. Here also, the nitric acid wash turned the fibers green, meaning again that Eu(III) was stripped off the fibers surface and U(VI) was still trapped.

To conclude, both U(VI) and Eu(III) were trapped by the PVDPA-functionalized fibers and a nitric acid wash is indeed releasing Eu(III), keeping U(VI) trapped on the PVPDA surface. Furthermore, pH seems to play an important role in deciding the PVDPA affinity towards U(VI) and Eu(III). Future studies should focus on understanding how pH tuning should be used to customize the PVDPA selectivity towards different metals and the metal releasing behavior as a function of pH, including actinides and lanthanides other than uranium and europium, in addition to other fission products.

IV.7. Conclusion

The interactions of PVDPA with different metal species were investigated. PVDPA showed high performance in trapping lanthanides (III) and uranium (VI) ions in aqueous media. PVDPA-based materials are promising candidates in application fields related to the nuclear industry. They can be used to harvest uranium from seawater as a future renewable source of clean energy. It should be noted that we actually tried to deploy a set of adsorbent fiber in the Mediterranean near the Lebanese shores but unfortunately they were lost in a storm. We hope though that this experiment would be reattempted in future studies. Furthermore, PVDPA can also be used in nuclear spent fuel recycling through the PALEX concept. It is also a strong ligand that can be used in the field of radiodecontamination and detoxification following nuclear accidents.

Even though a full assessment of PVDPA's usability in each of those fields requires further in-depth investigations, we think of this thesis as a precursor work that encourages future projects and collaborations with academic and industrial partners. Other applications can also be imagined for PVDPA-based materials, from fluorescent probes in biomedical imaging and counterfeit detection to heterogeneous catalysis.

Two scientific papers were submitted following the work on P4VP (one published and the other one pending) and two international PCT patent applications followed the work on the new PVDPA polymer and were submitted in France at the Institut National de la Propriété Industrielle (INPI) under the reference numbers PCT/FR2017/052705 and PCT/FR2017/052706.

IV.8. References

1. YANG, Q., et al., *Synthesis of Eu (III) and Tb (III) complexes with novel pyridine dicarboxylic acid derivatives and their fluorescence properties.* Journal of Central South University (Science and Technology), 2007. **4**: p. 020.
2. Tao, C., et al., *Pyridine-2, 6-dicarboxylic acid for the sensitization of europium (III) luminescence with very long lifetimes.* RSC Advances, 2015. **5**(72): p. 58936-58942.
3. Binnemans, K., *Interpretation of europium (III) spectra.* Coordination Chemistry Reviews, 2015. **295**: p. 1-45.
4. Lis, S., *Luminescence spectroscopy of lanthanide (III) ions in solution.* Journal of alloys and compounds, 2002. **341**(1-2): p. 45-50.
5. Barkleit, A., et al., *Americium (III) and europium (III) complex formation with lactate at elevated temperatures studied by spectroscopy and quantum chemical calculations.* Dalton Transactions, 2014. **43**(29): p. 11221-11232.
6. Kimura, T., et al., *Comparative study on the hydration states of Cm (III) and Eu (III) in solution and in cation exchange resin.* Journal of alloys and compounds, 1998. **271**: p. 719-722.
7. Kim, J., et al., *A study of the carbonate complexation of CmIII and EuIII by time-resolved laser fluorescence spectroscopy.* Journal of alloys and compounds, 1994. **213**: p. 333-340.
8. Moulin, C., et al., *Uranium speciation in solution by time-resolved laser-induced fluorescence.* Analytical Chemistry, 1995. **67**(2): p. 348-353.
9. Grenthe, I., et al., *Chemical thermodynamics of uranium*. Vol. 1. 1992: North-Holland Amsterdam.
10. Xu, C., et al., *Complexation of U (VI) with dipicolinic acid: Thermodynamics and coordination modes.* Inorganic chemistry, 2013. **52**(5): p. 2750-2756.
11. Eliet, V., et al., *Characterisation of hydroxide complexes of uranium (VI) by time-resolved fluorescence spectroscopy.* Journal of the Chemical Society, Faraday Transactions, 1995. **91**(15): p. 2275-2285.
12. Eliet, V., I. Grenthe, and G. Bidoglio, *Time-resolved laser-induced fluorescence of uranium (VI) hydroxo-complexes at different temperatures.* Applied spectroscopy, 2000. **54**(1): p. 99-105.
13. Meinrath, G., et al., *Lifetime and fluorescence quantum yield of uranium (VI) species in hydrolyzed solutions.* Journal of alloys and compounds, 2000. **300**: p. 107-112.
14. Burrows, H. and T. Kemp, *The photochemistry of the uranyl ion.* Chemical Society Reviews, 1974. **3**(2): p. 139-165.
15. Sachs, S., V. Brendler, and G. Geipel, *Uranium (VI) complexation by humic acid under neutral pH conditions studied by laser-induced fluorescence spectroscopy.* Radiochimica Acta, 2007. **95**(2): p. 103-110.
16. Gabriel, U., et al., *Uranyl surface speciation on silica particles studied by time-resolved laser-induced fluorescence spectroscopy.* Journal of colloid and interface science, 2001. **239**(2): p. 358-368.
17. Watanabe, C.N. and M.H. Gehlen, *Luminescence quenching of uranyl ion adsorbed in nafion membrane by alcohols and vinyl monomers.* Journal of Photochemistry and Photobiology A: Chemistry, 2003. **156**(1): p. 65-68.
18. Burrows, H.D., et al., *Mechanistic studies on uranyl ion initiated photopolymerization of acrylamide.* Berichte der Bunsengesellschaft für physikalische Chemie, 1992. **96**(5): p. 712-717.
19. Ivanov, A.S., et al., *Origin of the unusually strong and selective binding of vanadium by polyamidoximes in seawater.* Nature communications, 2017. **8**(1): p. 1560.
20. Blasse, G., et al., *Quenching of the luminescent state of uranium in oxides by metal ions.* Journal of Inorganic and Nuclear Chemistry, 1977. **39**(8): p. 1339-1341.
21. Rifi, E., F. Rastegar, and J. Brunette, *Uptake of cesium, strontium and europium by a poly (sodium acrylate-acrylic acid) hydrogel.* Talanta, 1995. **42**(6): p. 811-816.
22. Macášek, F., I.S. Shaban, and L. Mátel, *Cesium, strontium, europium (III) and plutonium (IV) complexes with humic acid in solution and on montmorillonite surface.* Journal of radioanalytical and nuclear chemistry, 1999. **241**(3): p. 627-636.
23. Sadhu, B., M. Sundararajan, and T. Bandyopadhyay, *Water-mediated differential binding of strontium and cesium cations in fulvic acid.* The Journal of Physical Chemistry B, 2015. **119**(34): p. 10989-10997.
24. Reinoso-Maset, E., P.J. Worsfold, and M.J. Keith-Roach, *Effect of organic complexing agents on the interactions of Cs+, Sr2+ and UO22+ with silica and natural sand.* Chemosphere, 2013. **91**(7): p. 948-954.

V. Conclusion and perspectives

In roughly a century, conventional reserves of uranium should dry out, making it inevitable to reconsider uranium harvesting from seawater to fuel future generation nuclear reactors. The extremely low uranium concentration and the complexity of seawater matrix make adsorption by chelating polymers the most promising method for uranium recovery from seawater in terms of simplicity of operation, operating cost, environmental risk and uptake capacity. Adsorbents with amidoxime functional groups are the most promising adsorbents because of their high affinity in chelating uranyl ions in seawater. However, they suffer from vanadium outcompeting uranium for binding sites and the need to use a hydrophilic comonomer. Our new water soluble and selective PVDPA polymer proved to be promising in solving these problems.

The other challenge facing nuclear industry is the recycling of spent fuel. In future reactors, all actinides will be recycled together and integrated in a new energy production cycle. The PVDPA polymer will be proven capable of simultaneously trapping actinides and lanthanides in aqueous solution and later release lanthanides back into an acidic solution. We thus provided the first experimental results of a polymer assisted spent fuel recycling concept we called PALEX.

The PVDPA polymer is also a promising candidate as an agent for radiodecontamination and radiodetoxification, following nuclear accidents.

The nuclear fuel cycle was first described in chapter I and the relation between our project and different aspects and challenges of the nuclear industry was established. Then, the main techniques and strategies to be employed in this work were reviewed. Different controlled polymerization techniques were described, and the adopted Supplemental Activation Reducing Agent Atom Transfer Radical Polymerization (SARA ATRP) was explained.

SARA ATRP polymerization offered several advantages. The non-stable copper (I) catalyst, used in conventional ATRP will be replaced by the stable copper (II) and the catalyst load will be reduced by a factor of 100, the reaction will be achieved in green solvents and at room temperature, minimizing the energy consumption and eventually the overall cost of post-purification. Thanks to metallic copper, the reaction is oxygen tolerant and no prior degassing. A green solvent is also used. These advantages made the synthesis of PVDPA easy, fast and cheap, both in solution and from different solid substrates.

In chapter II, 4-vinylpyridine (4VP) served as a model monomer and helped us investigating the SARA ATRP experimental conditions. P4VP was synthesized in solution and the SEC analysis proved the livingness and the control over chain length distribution. Furthermore, P4VP chains were successfully built from both an organic (PET) and inorganic (Silica) substrates. PET surface was pretreated by aminolysis with PEI, followed by the grafting of the BnCl radical initiator. On the other hand, the synthesized APTES-BnCl allowed the direct grafting of the radical initiator onto the silica surface. P4VP was then successfully built from both surfaces and studied by different surface analysis techniques, proving the covalent bonding between P4VP and both substrates. P4VP-modified silica powder was then used for oil/water separation, thanks to the pH-switchable wettability of P4VP.

In chapter III, the VDPM monomer synthesis was simplified and optimized. Its SARA ATRP polymerization was investigated in solution and the reaction livingness was evidenced, though the control over chain lengths distribution was not achieved on time. Styrene/VDPM copolymerization was then conducted with great success, allowing the synthesis of statistical, gradient and block copolymers. Monodisperse core-shell nanoparticles were also prepared using the water soluble VDPA monomer with styrene. Afterwards, PVDPM chains were successfully built from PET surfaces. Later on, PVC-based substrates took over and the surface functionalization strategy was reduced into a unique step allowing the fast preparation of functional surfaces with several micrometers thick PVDPM outerlayer.

In chapter IV, the prepared materials were hydrolyzed to obtain the water soluble PVDPA, either as a free polymer in aqueous solution or in the form of (PVC-co-CPVC)-g-PVDPA fibers. In both forms, PVDPA-based materials showed a high performance in scavenging targeted radionuclides in water. Several lanthanides along with uranium were successfully trapped and the solutions were "decontaminated". Furthermore, the high ionic strength and the presence of competing elements like vanadium, cesium and strontium didn't seem to compromise the trapping performance of PVDPA.

The high uranium and lanthanides trapping capacity in aqueous media makes PVDPA-based materials excellent candidates for different applications related to the nuclear industry. They can be used for uranium harvesting from seawater and are potentially more advantageous than the known amidoxime-based materials. They are potential candidates for nuclear spent fuel recycling through the proposed PALEX concept and can be further used in the field of environment decontamination and detoxification of living organisms including humans, following nuclear accidents.

Future efforts should focus on many aspects not enough tackled in this thesis. First of all, the control over PVDPM chain length distribution should be achieved and the polymerization kinetics further studied. The copolymerization of VDPM with comonomers other than styrene should be investigated and polymer compositions and architectures further developed. The surface-initiated polymerization should also be extended to other organic and inorganic substrates.

The interactions between PVDPA and different metals should be further studied. PVDPA's affinities towards different lanthanides, actinides and transition metals should be quantified, compared and the complexation mechanisms further understood. The preparation of PVDPA-based surfaces should be further optimized and the conditions for best performance determined.

Concerning the uranium harvesting from seawater, expeditions should be organized, PVDPA-based materials should be deployed in real ocean water and the uranium uptake determined in order to guide further developments. When for the PALEX concept, further studies should be conducted and PVDPA performance analyzed in simulated then real spent fuel samples.

The structural modification on PVDPM, before and after polymerization, could also be investigated. The ester moieties offer endless possibilities and can be replaced with many chemical

functions allowing to the physico-chemical properties of the resulting polymer to be tailored and thereby extending its usability in targeting specific metals in aqueous or organic media, and in other application fields like pyridine-based heterogeneous catalysis. When coupled to different metals, especially lanthanides, PVDPA complexes fluorescence can be used in biomedical imaging and counterfeit detection.

In this exploratory thesis, we tried to make a small contribution in solving several challenges facing the nuclear energy industry. Most importantly, we tried to avoid complex and expensive strategies in order to keep our approach economically viable. This project is hopefully first of many and by submitting two international patent applications, we hope that this work will encourage future developments and generate collaborations with experts in different related fields of research, both in academia and industry.

VI. Materials and methods

VI.1. Characterization techniques

VI.1.1. Nuclear magnetic resonance (NMR)

NMR measurements were done using Bruker's DPX250, DRX300 and AV360 spectrometers. Sample concentrations were fixed at a 10 mg/mL for ^{1}H-NMR and at 40 mg/mL for ^{13}C-NMR.

VI.1.2. Size exclusion chromatography (SEC)

SEC analysis was performed in *N*,*N*-dimethylformamide (DMF) for P4VP using a Styragel column (HR 4E, 5 µm, 4.6 x 300 mm) from Waters and refractive-index detector. The experiments were performed at a flow rate of 0.3 mL/min and the injection volume was 50 µL (1 mg/mL). PMMA standards were used to estimate the average molar masses and dispersities of analyzed samples. PS and P(S-co-VDPM) were analyzed with THF as eluent (1 mL/min) in a ViscoGELTM column (7.8 x 300 mm, GMHH R-H) provided by Viscotek and equipped with a Waters 410 refractive index detector, molar masses and dispersities were determined using polystyrene standards.
PVDPM samples were analyzed in DMF (+ LiBr, 1 g/L) at 60°C, at a flow rate of 0.8 mL/min and a polymer concentration from 2 to 5 mg/mL. The steric exclusion was carried out on two PSS GRAM 1000 Å columns (8 x 300 mm; separation limits: 1 to 1000 kg/mol) and one PSS GRAM 30 Å (8 x 300 mm; separation limits: 0.1 to 10 kg/mol) coupled with three detectors (Viscotek, TDA 305): a differential refractive index (RI) detector, a viscosimeter detector and a light scattering (LS) detector (laser λ = 670 nm at 7° and 90°). The OmniSEC 4.6.2 software was used for data acquisition and data analysis. Molar masses and dispersities (Đ) were calculated with a calibration curve based on narrow PMMA standards (from Polymer Standard Services), using only the RI detector. Light scattering (LS) molar masses were estimated using a dn/dc of 0.16 mL/g.

VI.1.3. Static water contact angle measurements (WCA)

Water contact angle (WCA) were carried out using a DS100 Kruss goniometer. The contact angle was measured within 10 s of placing a 3µL droplet of milliQ water on the surfaces and an average of at least 4 measurements was reported.

VI.1.4. Colorimetric measurement of amine functions

The masses of PET substrates were precisely measured prior to colorimetric assays, which then allowed to determine the exact surface area knowing the surface to mass ratio. Orange II method [1] was used to quantify the amount of exposed amine groups on the PET surfaces. The amino-covered films were immersed in 2 mL of dye solution (15 mg/mL) in acidic solution (Milli-Q water adjusted to pH 3 with 1 M HCl) for 30 min at 40 °C. The samples were then intensively rinsed several times using the acidic solution (pH 3) to remove unbound dye. Once air-dried, the colored films were immersed in 1 mL of alkaline solution (Milli-Q water adjusted to pH 12 with a 1 M NaOH solution). The pH of the solution containing the desorbed dye was adjusted to pH 3 by adding 1% v/v of 12 M HCl. The absorbance of the solution was then measured at 484 nm.

VI.1.5. Attenuated total reflection infrared spectroscopy (ATR-FTIR)

Infrared analysis were carried out on Bruker IFS 66 equipment with an ATR module with a diamond crystal from Pike technologies. 150 scans were performed with a resolution of 4 cm^{-1}. Absorbance spectra were registered between 600 and 4000 cm^{-1}.

VI.1.6. X-ray photoelectron spectroscopy (XPS)

XPS measurements were performed on a K-Alpha spectrometer from ThermoFisher, equipped with a monochromated X-ray Source (Al Kα, 1486.6 eV). A spot size of 400 mm was employed. The hemispherical analyzer was operated in CAE (Constant Analyzer Energy) mode, with a pass energy of 200 eV and a step of 1 eV for the acquisition of surveys spectra, and a pass energy of 50 eV and a step of 0.1 eV for the acquisition of high-resolution spectra. A “dual beam” flood gun was used to neutralize the charge build-up. The spectra obtained were treated by means of the “Avantage” software provided by ThermoFisher. A Shirley-type background subtraction was used and the peak areas were normalized using the Scofield sensitivity factors in the calculation of elemental compositions.

VI.1.7. Atomic Force Microscopy (AFM)

Tapping mode topography and phase imaging was accomplished using di Innova AFM Bruker with NanoDrive v8.02 software. Tapping mode images were acquired using silicon tips from

Nanosensors (PPP NCSTR) with a resonance frequency ranging between 76 and 263 kHz. Images were processed using Gwyddion software, freely available on the internet.

VI.1.8. Time-of-flight secondary ion mass spectrometry (ToF-SIMS)

ToF-SIMS measurements were carried out using a ToF-SIMS 5-100 (IONTOF GmbH) equipped with two sources; Bismuth liquid-metal ion source for spectroscopy analysis and an Argon ion source for sputtering, both with an incident angle of 45 degrees to the surface of the sample. Spectra of positive ions were collected from an area of 500 x 500 μm^2 from each sample using a pulsed 0.07pA Bi_3^+ beam, at 25 keV energy, and by keeping the primary ion dose (<2x 10^{11} ion/cm^2) below the secondary ion mass spectroscopy static limits. The secondary ions were extracted, with 2 keV energy, passing throw a single stage reflector before hitting a single micro channel plate detector. Low energy flood gun was used for the surface charge compensation**.** For in depth profiling, a 2.5 to 25 keV (depending on sample) Ar_{1500} cluster ion beam was used repeatedly for sputtering through the film with a current of 0.3 nA and a raster size of 1000×1000 μm^2 and a 25 keV Bi_3^+ beam (0.07 pA, 500x500 μm^2, 128x128 pixels) to analyze between each sputtering. The data were acquired and processed with SurfaceLab 6.6 software from IONTOF GmbH.

VI.1.9. Scanning electron microscopy (SEM)

SEM was performed using a field emission gun scanning electron microscope (FEGSEM) (ZEISS SUPRA 55 VP) at low voltage (1 kV) and low current (a few pA) and a very short working distance in order to be able to observe samples without coating them with a conductive layer. These conditions were selected to ensure the observation of only the top surface of the samples without any coating and to be able to combine or compare more efficiently SEM images with AFM ones.

VI.1.10. Matrix-assisted laser desorption/ionization time of flight mass spectrometry (MALDI-ToF)

The highest grade available of *trans*-2-[3-(4-ter-Butylphenyl)-2-propenylidene] malonitrile (DCTB), used as the matrix for MALDI-TOF MS, was purchased from Sigma Aldrich and used without further purification. MALDI-TOF MS analysis were performed using an UltrafleXtreme mass spectrometer (Bruker Daltonics, Bremen). Acquisitions were performed in reflector positive ion mode. The laser intensity was set just above the ion generation threshold to obtain peaks with

the highest possible signal-to-noise (S/N) ratio without significant peak broadening. The mass spectrometer was externally calibrated using PEG1500 and PEG4500. All data were processed using the FlexAnalysis software (Bruker Daltonics, Bremen).

VI.1.11. UV-Vis absorption spectroscopy

UV-vis spectra were recorded over 300-800 nm range with 0.5 nm resolution using a Carry 1E UV-vis spectrophotometer.

VI.1.12. Time-resolved laser-induced fluorescence spectroscopy (TRLFS)

TRLFS of uranium (VI) was conducted at room temperature, using a tunable OPO Panther® Continuum pulsed laser at incident wavelength of 430 nm and 3 mJ energy. The detection was made by means of a Spectra-Pro®-300 monochromator (Acton Research Corporation® coupled with a Princeton Instruments® CCD Camera). Spectra were recorded between 450 and 600 nm using 2 mL quartz glass cuvettes. Decay curves of uranium (VI) were obtained with a gate width of 0.5 µs and delay range between 0.2 and 200 µs. For each delay time, each luminescence spectrum was recorded four times, and for each spectrum 100 accumulations were averaged. Fluorescence lifetimes were calculated by *fi*tting the decay to an exponential decay function using the OriginPro® software:

$$I\,(t) = \sum_i Ii_0 \exp(-t/\tau_i)$$

$\boldsymbol{I(t)}$ being the total luminescence intensity at time **t**, $\boldsymbol{Ii_0}$ the luminescence intensity of the species ***i*** at the time t = 0, and $\boldsymbol{\tau_i}$ the corresponding lifetime.

For europium (III), the excitation wavelength was set at 466 nm and 7.5 mJ energy, the spectra recorded between 470 and 720 nm and decay curves obtained with a gate width of 5 µs and delay range between 2 and 1000 µs.

VI.1.13. Inductively coupled plasma mass spectrometry (ICP-MS)

Samples were diluted 100 times in ultrapure 1% nitric acid. Ultrapure commercial standards were used for calibration of U, V and Nd at 1 ppt, 10 ppt, 100 ppt, 1 ppb, 10 ppb and 100 ppb. Measurements were performed using a ThermoScientific HR-ICPMS Element XR at 50 µl/min direct injection.

VI.2. Synthesis of VDPM

VI.2.1. Dimethyl 4-chloropyridine-2,6-dicarboxylate [2]

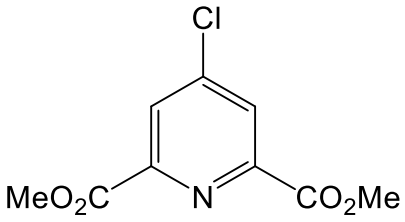

dimethyl 4-chloropyridine-2,6-dicarboxylate

In a round bottom flask, $PhPOCl_2$ (13 mL, 100 mmol, 4 eq) was slowly added to 4-hydroxypyridine-2,6-dicarboxylic acid (known as chelidamic acid or 4-hydroxy dipicolinic acid) hydrate (4.58 g, 25 mmol, 1 eq) while cooling in an ice bath. The reaction was then refluxed at 120 °C for 2 hours then slowly cooled back to room temperature. MeOH (75 mL) was added and the solution stirred for an additional 1 hour at room temperature. The solution is concentrated and DCM (100 mL) was added. This solution was washed with water (2 x 100 mL), $NaHCO_3$ (100 mL) then water (100 mL) again. The organic layer was dried over $MgSO_4$, filtrated then concentrated. Dimethyl 4-chloropyridine-2,6-dicarboxylate (M = 229.62 $g.mol^{-1}$) was then re-crystallized in hot MeOH, filtrated and dried (yield = 87%)

^1H NMR ($CDCl_3$, 360 MHz), δ (ppm): 3.99 (s, 6H, $CO_2C\mathbf{H_3}$), 8.26 (s, 2H, C**H***ar*).

VI.2.2. Dimethyl 4-iodopyridine-2,6-dicarboxylate [3]

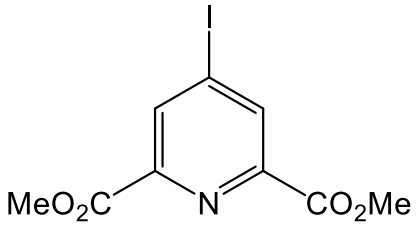

dimethyl 4-iodopyridine-2,6-dicarboxylate

Dimethyl 4-chloropyridine-2,6-dicarboxylate (4.04 g, 17.6 mmol) and NaI (26 g, 174 mmol, 9.9 eq) were solubilized in 120 mL and sonicated for 20 minutes. MeCOCl (4.16 g, 53 mmol, 3 eq) was then slowly added, the yellow solution turned dark brown. This solution was then sonicated for 30 minutes then concentrated then re-solubilized in DCM and neutralized with a 5% K_2CO_3 solution. The organic DCM layer was washed with a $Na_2S_2O_3$ solution, water, then dried over $MgSO_4$, filtrated and concentrated. The product was then re-crystalized in hot MeOH was washed with Et_2O to obtain the dimethyl 4-iodopyridine-2,6-dicarboxylate crystals (M = 321.07 $g.mol^{-1}$, yield = 90%)

^1H NMR ($CDCl_3$, 360 MHz), δ (ppm): 3.98 (s, 6H, $CO_2C\mathbf{H_3}$), 8.64 (s, 2H, C**H***ar*).

VI.2.3. Dimethyle 4-vinylpyridine-2,6-dicarboxylate (VDPM) [4]

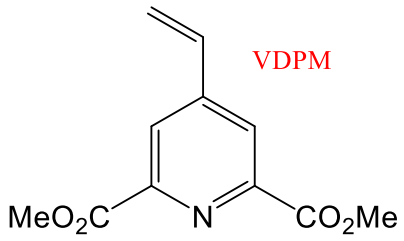

dimethyl 4-vinylpyridine-2,6-dicarboxylate

Dimethyl 4-iodopyridine-2,6-dicarboxylate (1.99 g, 6.2 mmol) was put in round bottom flask with 263 mg (1 mmol) of triphenylphosphine and 74 mg (0.33 mmol) of Palladium acétate. These reagents were solubilized in 20 mL of THF / water solvent mixture (9/1). 6.19 g of cesium carbonate (19 mmol) and 1.01 g of potassium vinyltrifluoroborate (7.5 mmol) were then added. The reaction was allowed to proceed at 85 °C for 8 hours with stirring, then cooled and filtrated. The white residue is washed with ethyl acetate then concentrated. The obtained solution is purified over silica gel, and eluted with a petroleum ether / ethyl acetate (3/1), then concentrated. Dimethyl 4-vinylpyridine-2,6-dicarboxylate (dimethyl 4-vinyl dipicolinate - VDPM) (M = 221.21 $gmol^{-1}$) was then recrystallized from a DCM / petroleum ether (1/10) mixture (yield = 70-80%).

^{1}H NMR ($CDCl_3$, 250 MHz), δ (ppm): 3.98 (s, 6H, $CO_2C\mathbf{H_3}$), 5.63 (d, 1H, *J* = 11.1 Hz, C=C**H** *trans*), 6.14 (d, 1H, *J* = 17.4 Hz, C=C**H** *cis*), 6.75 (dd, 1H, *J* = 17.4 Hz, *J* = 11.1 Hz, C**H**=CH_2), 8.24 (s, 2H, C**H***ar*).

^{13}C NMR ($CDCl_3$, 250 MHz), δ (ppm): 53.38 (s, **C**O_2CH_3), 121.57 (s, CH=**C**H_2), 125.11 (s, **C**H*ar*), 133.49 (s, **C**H=CH_2), 147.85 (s, **C**-CH=CH_2), 148.91 (s, **C**-CO_2CH_3), 165.37 (s, **C**=O).

ESI-MS: $[M+H]^+$ = 222.075

VI.3. SARA ATRP of 4VP in solution

The monomer (4VP, 1.0 mL, 9.27 mmol), initiator (BnCl, 8 µL, 0.0927 mmol), Cu^0 (l = 2 cm, d = 1 mm), catalyst ($CuCl_2$, 0.625 mg, 4.65 µmol), ligand (TPMA, 6.25 mg, 0.022 mmol) and 2-propanol (1.0 mL) were added to a 10 mL tube. The tube was sealed and placed in a water bath at 30 °C without prior degassing. After a predetermined time, an aliquot was taken for ^1H NMR measurement in MeOD. The solvent was evaporated, DCM was added to re-solubilize the content, and the resulting solution was precipitated in 200 mL of cold diethyl ether while stirring. The polymer was isolated by filtration and dried under vacuum at room temperature. The monomer conversion was determined by ^1H NMR in MeOD.

VI.4. SARA ATRP of VDPM in solution

In a typical reaction, the VDPM (M = 221.2 $g.mol^{-1}$) monomer's initial concentration was kept at 0.5 M in acetonitrile, and the copper wire at 1 cm/mL. The monomer (100 eq), $CuCl_2$ (0.01 eq), TPMA (0.4 eq) were dissolved in DMSO or acetonitrile in a 10 mL tube, the copper wire was added and the BnCl initiator (1 eq) added and the tube closed at placed in an oil bath for a predetermined time at 30 °C or 50 °C, without prior degassing. After a predetermined time, an aliquot was taken for ^1H NMR measurement in $CDCl_3$ to determine monomer conversion. The reaction was then diluted with an equal volume of DCM then the PVDPM polymer precipitated in THF, filtrated and dried.

The PVDPM polymer can be then hydrolyzed in NaOH to yield the poly(4-vinyl dipicolinic acid) polymer PVDPA for complexation studies.

VI.5. SARA ATRP of styrene

VI.5.1. Bulk SARA ATRP with Cu^0 as reducer agent

A solution of $CuCl_2$ (2.3 mg), TPMA (50 mg) and 10 mL styrene was prepared (St / $CuCl_2$ / TPMA = 100 / 0.02 / 0.2). 3 mL of this solution was placed in a 10 mL tube with 3 cm copper wire and 30 µL of BnCl initiator (DP = 100). The tube was closed and placed in an oil bath at 60 °C and aliquots were periodically taken and analyzed by NMR to determine the monomer conversion. The reaction solution was then diluted with DCM and the polymer precipitated in MeOH, filtrated and dried under vacuum.

Styrene monomer conversion was determined from NMR spectra. Below is an example at ~67 % monomer conversion:

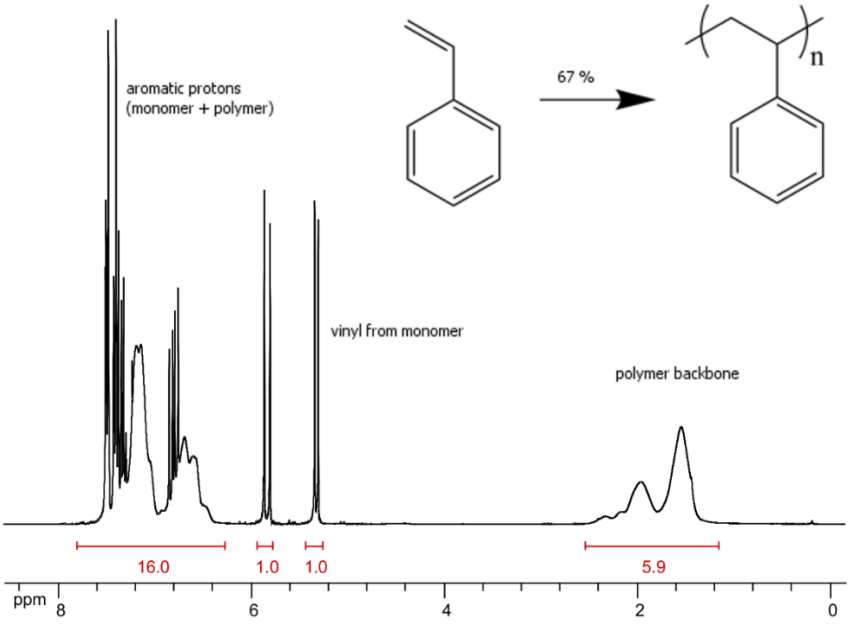

Using the vinyl doublets at 5.33 and 5.84 ppm as references for 1 protons each, the monomer conversion was calculated using the peak area $\mathcal{A}$ in the region between 6.3 ppm and 7.8 ppm as follows:

$$monomer\ conversion\ (\%) = \frac{\mathcal{A}_{6.3-7.8\ ppm} - 6}{\mathcal{A}_{6.3-7.8\ ppm} - 1} \times 100$$

VI.5.2. SARA ATRP with Cu^0 as reducer and sulfolane or sulfolane/water as solvent

For the polymerization in sulfolane or sulfolane / water as solvent. 2 mL of the same styrene/$CuCl_2$/TPMA solution was placed in a 10 mL tube with 1 mL of solvent, either pure sulfolane of sulfolane / water (9/1) mixture. 2 cm of a copper wire and 20 µL of BnCl initiator (DP = 100) was added, and the tube was closed and placed in an oil bath at 60 °C and aliquots were periodically taken and analyzed by ^{1}H NMR to determine the monomer conversion. The reaction solution was then diluted with DCM and the polymer precipitated in MeOH, filtrated and dried under vacuum.

VI.5.3. SARA ATRP with $Na_2S_2O_4$ as reducer agent and sulfolane / water as solvent

Styrene (1 ml), TPMA (5.0 mg), $CuCl_2$ (8.3 µL of a 137.9 mg in 985 µL water solution) and $Na_2S_2O_4$ (15.9 mg) were placed in a 10 mL tube with 0.5 mL sulfolane. 10 µL of the BnCl initiator (DP = 100) was added and the tube closed and placed in an oil bath at 60 °C. Aliquots were periodically taken to determine the monomer conversion. The reaction solution was then diluted with DCM and the polymer precipitated in MeOH, filtrated and dried under vacuum.

Styrene / BnCl / CuCl2 / TPMA = 100 / 1 / 0.1 / 0.2

VI.5.4. Styrene graft polymerization using PVC macroinitiator

PVC powder (82 mg), styrene (3 ml), CuCl2 (3.6 mg), TPMA (8.3 mg), sulfolane (1 ml) and Cu0 (3 cm) were put in a 10 mL tube. The tube was closed and put in an oil bath at 60 ºC for a predetermined time. The solution was then precipitated in MeOH to yiel the PVC-g-PS polymer.

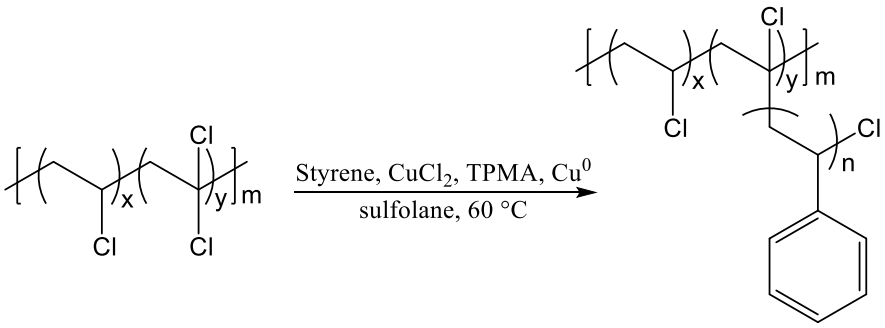

PVC - co - CPVC

PVC - *graft* - PS

To determine the amount of labile chlorine, the non-modified PVC powder (500 mg) was put in a round-bottom flask with an excess phenol (24 g) and agitated at 60 ºC for 4 days. The phenolized PVC was then precipitated in MeOH and filtrated.

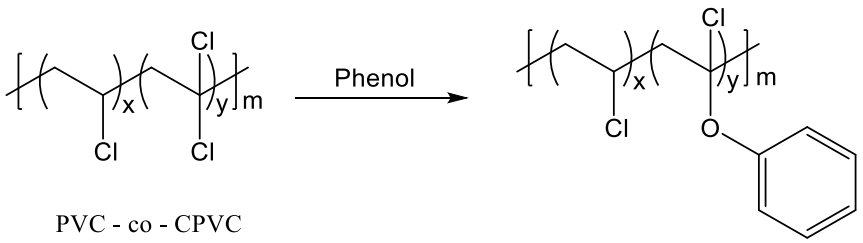

PVC - co - CPVC

The ^{1}H NMR spectrum then allowed the determination of labile chlorine (**y**).

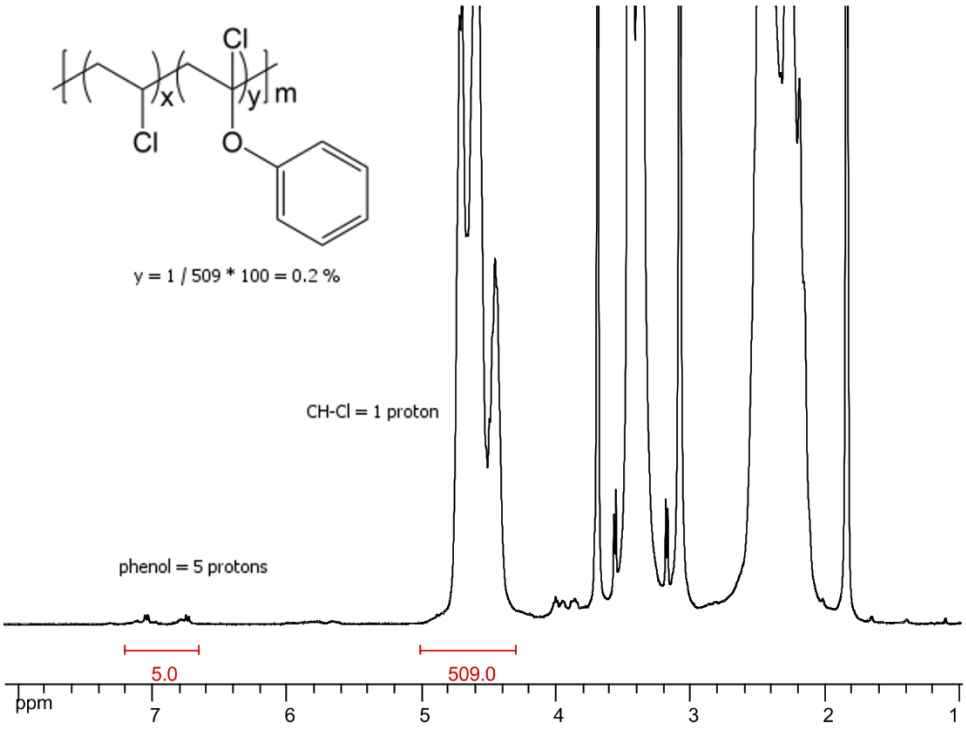

VI.6. Copolymerization of styrene with VDPM

VI.6.1. Statistical copolymer

Styrene (75 µL), VDPM monomer (147 mg), TPMA (7.5 mg), $CuCl_2$ (0.164 mg), sulfolane (0.68 mL), Cu^0 (2cm) were placed in a 10 mL tube. 128 µL of a 5.8 µL BnCl in 1 mL sulfolane solution was added and the tube closed and placed in an oil bath at 60 °C. Aliquots were periodically taken to determine the monomer conversion. The reaction solution was then diluted with DCM and the polymer precipitated in MeOH, filtrated and dried under vacuum.

Styrene / VDPM / BnCl / $CuCl_2$ / TPMA = 50 / 50 / 1 / 0.2 / 4

VI.6.2. Gradient copolymer

Styrene (1.33 mL), VDPM monomer (147 mg), TPMA (15 mg), $CuCl_2$ (0.164 mg), sulfolane (0.68 mL), Cu^0 (2 cm) were placed in a 10 mL tube. 13.4 µL of the BnCl initiator was added and the tube closed and placed in an oil bath at 60 °C. Aliquots were periodically taken to determine the monomer conversion. The reaction solution was then diluted with DCM and the polymer precipitated in MeOH, filtrated and dried under vacuum.

Styrene / VDPM / BnCl / $CuCl_2$ / TPMA = 95 / 5 / 1 / 0.01 / 0.44

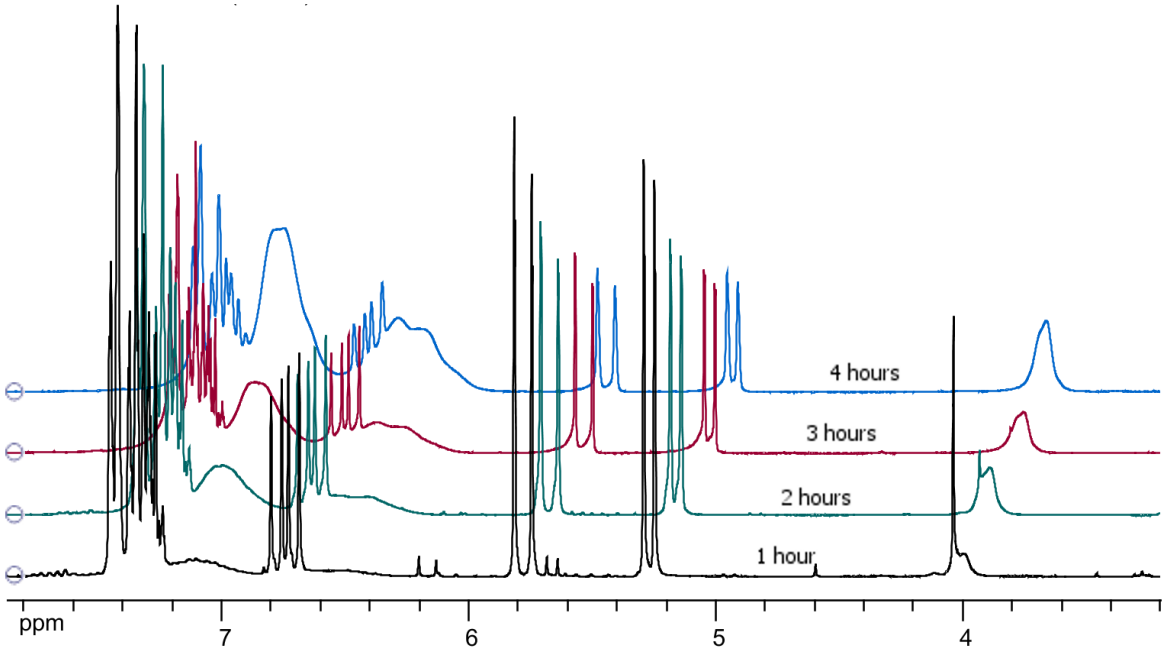

Individual comonomer conversions were determined using the following equations:

$$VDPM\ comonomer\ conversion\ (\%) = \frac{\mathcal{A}_{3.9-4.1\ ppm} - 6}{\mathcal{A}_{3.9-4.1\ ppm}} \times 100$$

Vinyl's doublets at 5.66 and 6.17 ppm were used as 1 proton references for VDPM comonomer.

$$Styrene\ comonomer\ conversion\ (\%) = \frac{\mathcal{A}_{6.25-7.80\ ppm} - 0.33 * \mathcal{A}_{3.9-4.1\ ppm} - 6}{\mathcal{A}_{6.25-7.80\ ppm}} \times 100$$

Vinyl's doublets at 5.27 and 5.78 ppm were used as 1 proton references for styrene comonomer.

VI.6.3. Block copolymer:

VDPM monomer (110.6 mg), TPMA (5.8 mg), $CuCl_2$ (0.135 mg), DMSO (0.3 mL) and Cu^0 (1 cm) were placed in a 10 mL tube. 5.8 µL of the BnCl initiator was added and the tube closed and placed in an oil bath at 60 °C. After 30 minutes, NMR showed no traces of unreacted VDPM. 2.3 mL of styrene were injected with 0.5 mL sulfolane. One hour after styrene injection, we took a small aliquot and did a simple precipitation test, the sample precipitated in THF, meaning that the PVDPM block is still predominant, or maybe the styrene didn't even polymerize. After 2 hours, an aliquot was completely soluble in THF, meaning that polystyrene was successfully being built on the PVDPM block. Another 0.5 mL of sulfolane were added and the reaction kinetics monitored by NMR. At each point, an aliquot was precipitated in MeOH, filtrated and dried under vacuum.

Styrene / VDPM / BnCl / $CuCl_2$ / TPMA = 400 / 10 / 1 / 0.02 / 0.4

VI.7. Surface-initiated SARA ATRP of 4VP on PET

VI.7.1. Aminolysis of PET surface [5]

PET films (2 x 1 cm^2) were washed prior to modification in H_2O / EtOH (1/1 v/v) for 10 minutes followed by 10 minutes in absolute acetone, then dried under vacuum at room temperature. Films were then immersed in DMSO for couple of minutes then put in a solution of 10 w/w of PEI in DMSO for a predetermined time in a water bath preheated at 50 °C. Treated PET was then washed in DMSO for 10 minutes before being put again in fresh DMSO and left overnight on a rotary table to remove any adsorbed PEI. It was then washed in copious amount of distilled water to wash off DMSO and remaining PEI. This step is crucial and was monitored by UV-Vis until no absorption at 216 nm was observed, indicating that DMSO and unreacted/unbound PEI were completely removed. Substrates were then washed in absolute acetone and dried under vacuum at room temperature for several hours.

VI.7.2. Grafting of radical initiator

Immediately after aminolysis, ATRP initiator was introduced onto the surface. PET films were immersed in diethyl ether for couple of minutes then put in a 1M solution of 4-(chloromethyl)benzoyl chloride in diethyl ether. 1.5 molar equivalent of Et_3N was then added and the reaction left overnight on a rotary table. Films were then extensively washed with dichloromethane and acetone successively, then dried under vacuum at room temperature for several hours. WCA was then performed and the reaction yield was determined by measuring the remaining unreacted amine functions on the surface with Orange II method.

VI.7.3. Surface-initiated SARA ATRP of 4VP

P4VP chains were built from the modified PET substrate by means of SI-SARA ATRP. PET films were introduced in a modified glass container where several substrates can be treated at once. 35 cm (7 x 5 cm) of a copper wire (d = 1mm) were washed successively with HCl (1M) / MeOH (1/1 v/v), MeOH and 2-propanol (IPA) then put in. 5 mL of a catalyst/ligand solution (0.625 mg $CuCl_2$ + 6.25 mg TPMA per 1 mL IPA) were added, followed by 40 mL of IPA and 5 mL of monomer (4VP). Reaction vessel was quickly sealed and put in a water bath preheated at 30 °C. After a

predetermined time, the vessel was opened, and the films were washed with copious amount of ethanol then acetone and dried under vacuum at room temperature for several hours then analyzed.

The overall strategy is described below:

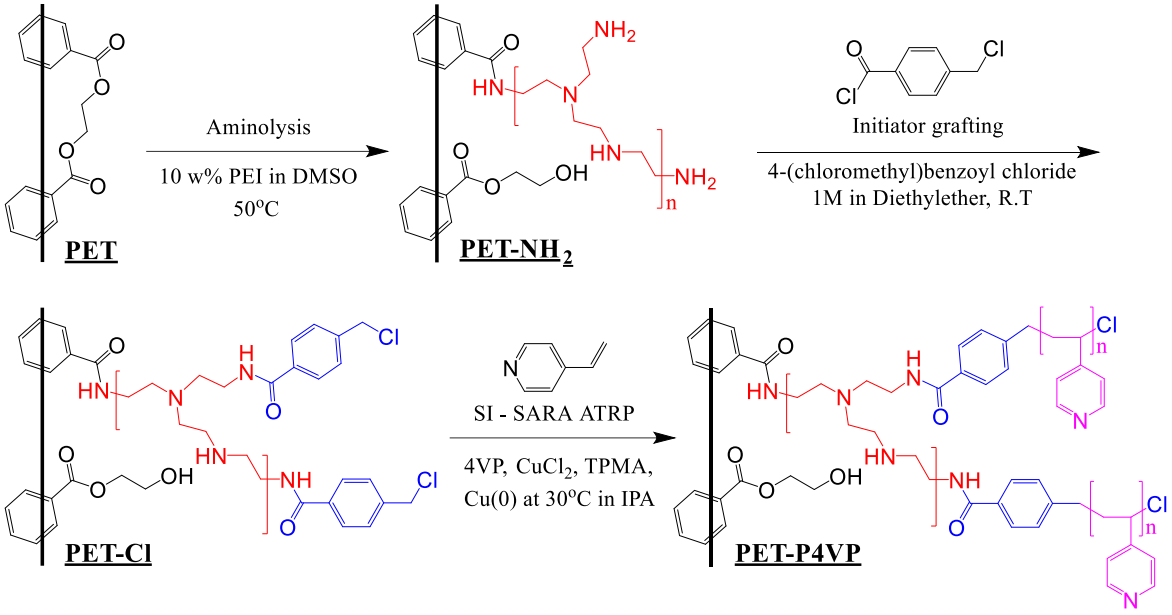

VI.8. Surface-initiated SARA ATRP of 4VP on silica

VI.8.1. Synthesis of APTES-BnCl

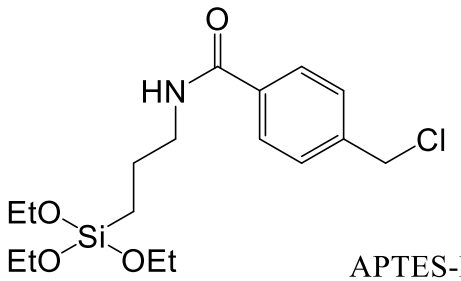

APTES-BnCl

In a round flask, 5 g of 4-(chloromethyl)benzoyl chloride (26.5 mmol) was dissolved in 20 mL of dry DCM under argon at 0°C. 4.5 mL of triethylamine (43.4 mmol), then 6.2 mL of 3-aminopropyltriethoxysilane (APTES) (26.5 mmol), were added dropwise. The reaction was allowed to proceed for 1 hour at room temperature and monitored by TLC. The reaction was diluted with 20 mL of DCM, washed with HCl (1M). The organic phase was dried with $MgSO_4$, filtered and concentrated under vacuum. The resulting transparent oily product was dried under vacuum over night to obtain 8.57 g (87%) of APTES-BnCl.

^{1}H NMR ($CDCl_3$, 360 MHz), δ (ppm): 0.69 (t, 2H, *J* = 7.8 Hz, C**H**$_2$Si), 1.21 (t, 9H, *J* = 6.9 Hz, C**H**$_3$CH$_2$OSi), 1.74 (m, 2H, *J* = 7.3 Hz, C**H**$_2$CH$_2$Si), 3.45 (m, 2H, *J* = 6.4 Hz, NHC**H**$_2$), 3.8 (m, 6H, *J* = 7.0 Hz, CH$_3$C**H**$_2$OSi), 4.58 (s, 2H, C**H**$_2$Cl), 6.53 (s, 1H, N**H**), 7.42 (d, 2H, *J* = 8.0 Hz, **H** *ar*), 7.75 (d, 2H, *J* = 8.0 Hz, **H** *ar*).

VI.8.2. Initiator grafting

Silicon wafer cut into 18 × 8 mm^2 was immersed in piranha solution (H_2SO_4 / H_2O_2 7/3 v/v) for 30 minutes, rinsed with copious amounts of distilled water until neutral pH, dried under a stream of argon and baked in a clean oven at 90 °C for 15 minutes, resulting in silanol-terminated silica surface. Immediately after piranha treatment, the dried substrates were immersed in a freshly prepared APTES-BnCl solution 2% (v/v) in anhydrous toluene for 1 hour at 70 °C, followed by thorough rinsing with toluene to remove any excess reagent, rinsed successively with methanol and distilled water. Finally, the substrates were baked in a clean oven at 90 °C for 30 minutes.

VI.8.3. Surface initiated SARA ATRP of 4VP

Due to the low stability of silanized films, surfaced initiated SARA ATRP of 4VP was performed on APTES-BnCl modified surfaces immediately after initiator grafting as follows:

In a modified glass container, substrates were placed along with 35 cm (5 × 7 cm) of a copper wire (d = 1 mm) (activated with HCl (1M) / MeOH then dried). 5 mL of a catalyst / ligand solution (0.625 mg $CuCl_2$ + 6.25 mg TPMA per mL dry 2-propanol) were added, followed by 40 mL dry 2-propanol and 5 mL of monomer (4VP). The container was quickly sealed with a septum and placed in a water bath at 30 °C for 22 hours. The vessel was then opened, and the films were washed successively with copious amount of ethanol, rinsed with diluted HCl (0.1 M) to remove potentially adsorbed copper catalyst, and washed with acetone. The films were dried under vacuum at room temperature for several hours then analyzed.

The overall strategy is described below:

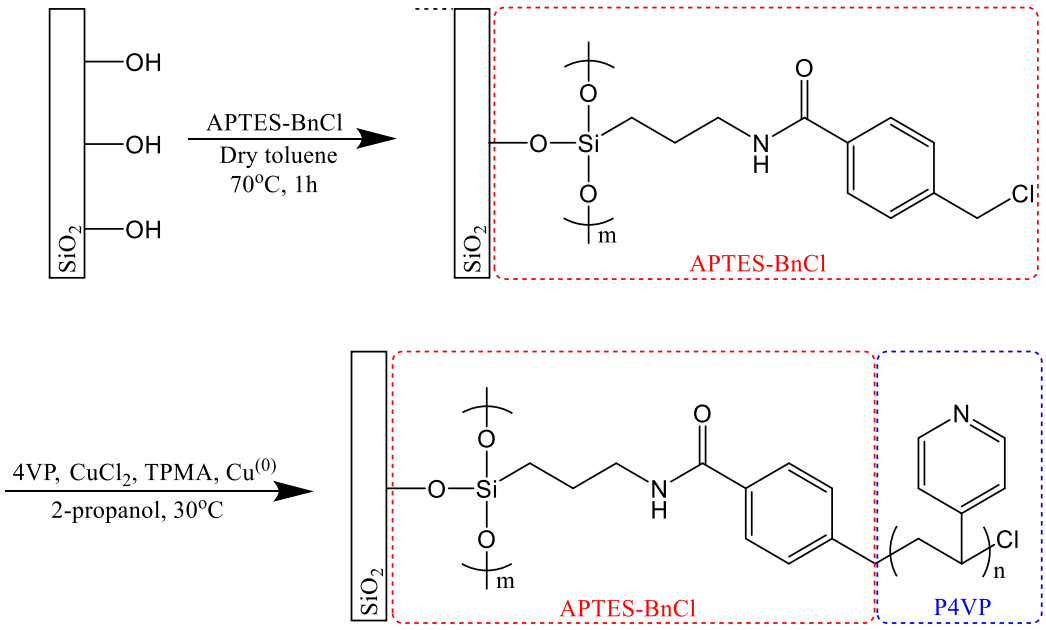

VI.9. Surface initiated SARA ATRP of VDPM on PET

Similar to the surface initiated SARA ATRP of 4VP on PET, the PET substrates were aminolyzed, the initiator grafted and the surface initiated SARA ATRP of the VDPM monomer was realized. The strategy is described as follows:

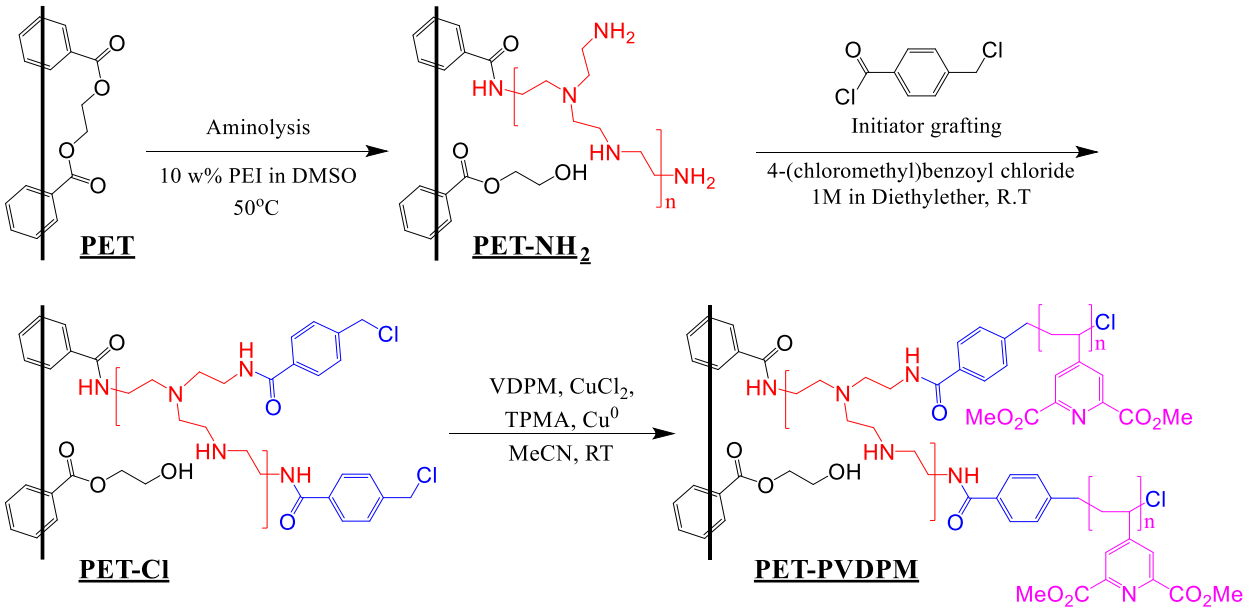

PET-Cl (film or fiber) was placed in a small vial containing a solution of VDPM/$CuCl_2$/TPMA (100 / 0.1 / 4) in acetonitrile. Monomer initial concentration was at 0.5 M. The vial was then closed and placed at a rotary table at room temperature for a predetermined time. The substrate was then washed over night in acetonitrile several times then dried and weighted to determine the weight gain. Only just before using the fibers in the complexation experiments, they were hydrolyzed in a NaOH 1 M solution overnight at room temperature.

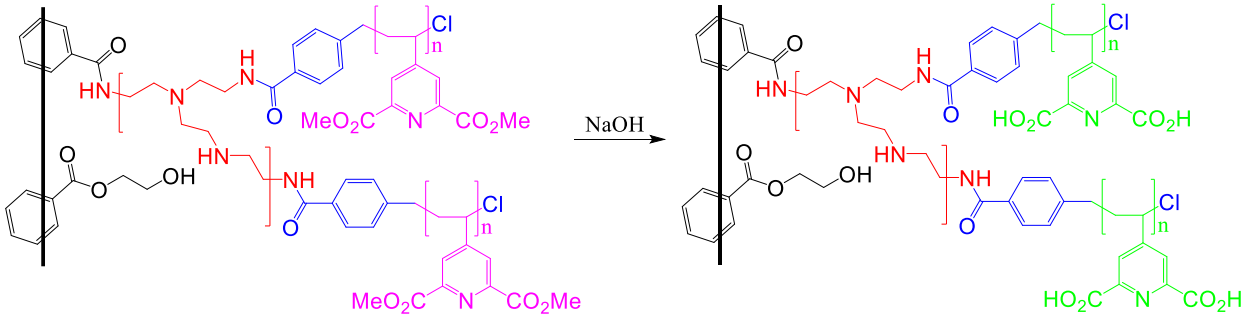

VI.10. Surface initiated SARA ATRP of VDPM on PVC substrates

VI.10.1. General strategy

When a PVC-based substrate was used, the surface initiated SARA ATRP of VDPM was directly applied, the strategy is described as follows:

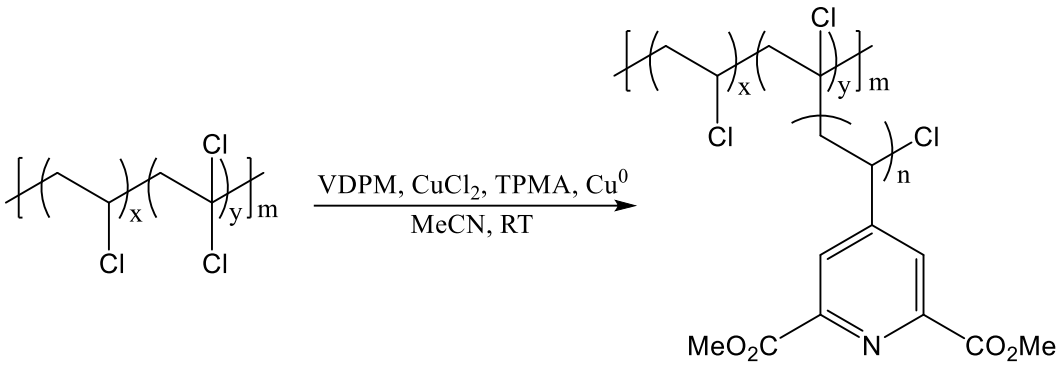

PVC - co - CPVC

(PVC-co-CPVC) - *graft* - PVDPM

VI.10.2. PVDPM on PVC powder

Precisely weighted PVC powder was placed in a 10 mL tube containing a solution of VDPM / $CuCl_2$ / TPMA (100 / 0.1 / 4 molar ratios) in acetonitrile. Monomer initial concentration was kept at 0.5 M. The tube was then closed and placed in an oil bath at 50 °C for a predetermined time. The powder was then washed with acetonitrile several times then dried and weighted to determine the weight gain. Only just before using the powder in the complexation experiments, it was hydrolyzed in a NaOH 1M solution overnight at room temperature.

VI.10.3. PVDPM on CPVC-coated PP films

Innovia™ CPVC-coated PP films (2 x 1 cm^2) were placed in a small vial containing a solution of VDPM / $CuCl_2$ / TPMA (100 / 0.1 / 4) in acetonitrile. Monomer initial concentration was at 0.5 M. The vial was then closed and placed at a rotary table at room temperature for a predetermined time. The films was then washed over night in acetonitrile several times then dried. Only just before using the fibers in the complexation experiments, they were hydrolyzed in a NaOH 1M solution for one hour at room temperature.

VI.10.4. On PVC-co-CPVC fibers

Precisely weighted Rhovyl™ PVC-co-CPVC fibers were placed in a small vial containing a solution of VDPM / $CuCl_2$ / TPMA (100 / 0.1 / 4) in acetonitrile. Monomer initial concentration was at 0.5 M. The vial was then closed and placed at a rotary table at room temperature for a predetermined time. The fibers was then washed over night in acetonitrile several times then dried and weighted to determine the weight gain. Only just before using the fibers in the complexation experiments, they were hydrolyzed in a NaOH 1M solution overnight at room temperature.

VI.11. Complexation studies

When the free polymer was used, an aqueous 5 mM solution of PVDPA was prepared in distilled water. A proper volume of this solution was added to a metal salt (nitrate or chloride as a counter anion) aqueous solution of known initial concentration and prepared in distilled water or in simulated seawater. Simulated seawater was prepared by dissolving 25.6 g NaCl and 193 mg $NaHCO_3$ in 1 L of distilled water.

The same technique was used for PVDPA-functional surfaces by replacing the free polymer solution with the proper PVDPA-modified substrate.

The used metals are:

Vanadium (Z = 23)	Strontium (Z = 38)	Cesium (Z = 55)
Lanthanum (Z = 57)	Neodymium (Z = 60)	Samarium (Z = 62)
Europium (Z = 63)	Ytterbium (Z = 70)	Uranium (Z = 92)

VI.12. References

1. Noel, S., et al., *Quantification of primary amine groups available for subsequent biofunctionalization of polymer surfaces.* Bioconjugate chemistry, 2011. **22**(8): p. 1690-1699.
2. Iglesias, C.P., et al., *Effect of a halogenide substituent on the stability and photophysical properties of lanthanide triple-stranded helicates with ditopic ligands derived from bis (benzimidazolyl) pyridine.* Journal of the Chemical Society, Dalton Transactions, 2000(13): p. 2031-2043.
3. Picot, A., et al., *Synthesis, structures, optical properties, and TD-DFT studies of donor-π-conjugated dipicolinic acid/ester/amide ligands.* Tetrahedron, 2008. **64**(2): p. 399-411.
4. Molander, G.A. and A.R. Brown, *Suzuki− Miyaura Cross-Coupling Reactions of Potassium Vinyltrifluoroborate with Aryl and Heteroaryl Electrophiles.* The Journal of organic chemistry, 2006. **71**(26): p. 9681-9686.
5. Jiang, L., Y. Jin, and R.K. Marcus, *Polyethylenimine modified poly (ethylene terephthalate) capillary channeled-polymer fibers for anion exchange chromatography of proteins.* Journal of Chromatography A, 2015. **1410**: p. 200-209.

VII. Résumé en français

D’ici la fin du siècle, les réserves naturelles d'uranium devraient s'assécher, il faudra alors envisager une alternative. La récupération de l'uranium de l'eau de mer, qui représente environ 4500 millions de tonnes (environ 100 fois supérieure à la réserve naturelle terrestre), deviendrait alors inévitable pour assurer le bon fonctionnement des réacteurs nucléaires. Cependant, la concentration extrêmement faible (3,3 ppb) et la complexité de la solution océanique font que cette source est extrêmement difficile à exploiter. L'adsorption par des fibres à base de poly(amidoxime) de cet uranium, est la stratégie actuellement la plus prometteuse, en raison de sa simplicité et de la forte affinité de ces fibres pour les ions uranyles. Cependant, ces fibres captent également les ions vanadiums. La compétition uranium/vanadium associée à une faible hydrosolubilité du poly(amidoxime) fait que cette solution n’est pas encore totalement satisfaisante. Au cours de cette thèse, nous avons développé nouveau polymère, le poly(acide 4-vinyldipicolinique) (PVDPA), qui est soluble dans l'eau et qui s'est révélé prometteur pour résoudre le problème de compétition entre l’uranium et le vanadium.

L'autre défi auquel l'industrie nucléaire est confrontée est le recyclage du combustible usagé. Dans les futurs réacteurs, tous les actinides seraient recyclés ensemble et réintégrés dans un nouveau cycle de production d'énergie. Le polymère PVDPA s’est révélé capable de piéger simultanément les actinides et les lanthanides en solution aqueuse et est capable de relarguer ensuite les lanthanides dans une solution acide, assurant ainsi la séparation des actinides des autres produits de fission. Nous avons ainsi fourni les premiers résultats expérimentaux d'un nouveau concept de recyclage du combustible usagé que nous avons appelé le procédé PALEX.

Le PVDPA serait également un candidat prometteur qui pourrait être utilisé en tant qu'agent de radio-décontamination et de radio-détoxification, qui ferait suite à des accidents nucléaires.

Le cycle du combustible nucléaire a d’abord été décrit dans le premier chapitre, la relation entre notre projet et les différents défis de l'industrie nucléaire a aussi été établie. Ensuite, les principales techniques et stratégies à utiliser dans ce travail ont été passées en revue. Différentes techniques de polymérisation contrôlées ont été décrites, la réaction de polymérisation de type SARA ATRP que nous avons employée dans ce travail a été expliquée et commentée.

La SARA ATRP offre plusieurs avantages. Le catalyseur Cu (I) non stable, utilisé dans l'ATRP classique est remplacé par le Cu(II) et le Cu(0), formes les plus stables de ce métal. La quantité de catalyseur est employée dans cette polymérisation est réduite d'un facteur 100 par rapport à la

polymérisation ATRP classique réduisant éventuellement le coût global de la post-purification. Grâce au cuivre métallique, la réaction est tolérante à l'oxygène et réalisable sans dégazage préalable. La réaction est réalisée dans des solvants plus écologiques et à température ambiante, ce qui minimise la consommation d'énergie. Ces avantages facilitent la synthèse du PVDPA, à la fois en solution et à partir de différents substrats solides.

Dans le chapitre II, la 4-vinylpyridine (4VP) a servi de monomère modèle et nous a permis d'étudier les conditions expérimentales de la SARA ATRP. Le P4VP a été synthétisé en solution et l'analyse SEC a mis en évidence le contrôle de la structure des polymères synthétisés. De plus, le P4VP a été greffé sur des substrats organiques (PET) et inorganiques (Silice). La surface de PET a été prétraitée par aminolyse avec de la polyéthylèneimine (PEI) suivie par le greffage de l'amorceur radicalaire BnCl. D'autre part, l'APTES-BnCl synthétisé a permis le greffage direct de l'amorceur radicalaire sur la surface de la silice. Le 4VP a ensuite été polymérisé sur les deux surfaces et les surfaces résultantes ont été caractérisées par différentes techniques d'analyse de surface mettant en évidence la liaison covalente entre le P4VP et les deux substrats. La poudre de silice modifiée avec le P4VP a ensuite été utilisée pour la séparation d'une émulsion d'huile dans l'eau, grâce à la modularité du P4VP en fonction du pH.

Dans le chapitre III, la synthèse du monomère VDPM a été réalisée et optimisée. Sa polymérisation par SARA ATRP a été étudiée en solution et la conservation des extrémités des chaînes a été mise en évidence, bien que le contrôle de la distribution des longueurs de chaîne n'ait pas été réalisé à temps. La copolymérisation styrène / VDPM a ensuite été menée avec succès, permettant la synthèse de copolymères statistiques, à gradient et à blocs. Des nanoparticules cœur – coquilles monodisperses ont également été préparées en utilisant le monomère VDPA hydrosoluble et le styrène. Ensuite, le VDPM a été polymérisé à partir des surfaces de PET. Les surfaces à base de PVC ont également été étudiées, et l'utilisation de cette surface à permis de réduire la stratégie de fonctionnalisation à une seule étape, permettant la préparation rapide de surfaces fonctionnelles avec des couches de PVDPM de plusieurs micromètres d'épaisseur.

Dans le chapitre IV, les matériaux à base de PVDPA, soit sous la forme libre en solution aqueuse soit sous la forme de fibres (PVC-co-CPVC) -g-PVDPA, ont été évalués vis-à-vis des différentes applications proposées. Dans les deux formes, le PVDPA a été capable de récupérer les radionucléides ciblés dans l'eau. Plusieurs lanthanides et l'uranium ont été piégés avec succès et

les solutions ont été « décontaminées ». De plus, la force ionique élevée et la présence d'éléments concurrents tels que le vanadium, le césium et le strontium ne semblent pas compromettre les performances de « piégeage » du PVDPA.

La forte capacité de piégeage de l'uranium et des lanthanides dans les milieux aqueux, fait des matériaux à base de PVDPA d'excellents candidats pour différentes applications liées à l'industrie nucléaire. Ils peuvent être utilisés pour la récupération de l'uranium de l'eau de mer et sont potentiellement plus avantageux que les matériaux à base d'amidoxime. Ils sont aussi des candidats potentiels pour le recyclage du combustible nucléaire avec le concept PALEX proposé et peuvent être utilisés dans le domaine de la décontamination de l'environnement et de la désintoxication des organismes vivants, y compris des humains, qui ferait suite à des accidents nucléaires.

Dans cette thèse, nous avons tenté d'apporter une contribution à la résolution de plusieurs défis auxquels l'industrie de l'énergie nucléaire est confrontée. Nous avons essayé d'éviter des stratégies complexes et coûteuses afin de maintenir notre approche économiquement viable. Nous espérons que ce projet encouragera des développements futurs et générera des collaborations avec des experts de différents domaines de recherche aussi bien dans le milieu académique que dans l'industrie.

Titre : Surfaces fonctionnalisées pour la radiodécontamination

Mots clés : Polymérisation contrôlée, Surfaces fonctionnalisées, radionucléides

Résumé : L'énergie nucléaire est l'un des moteurs de notre société moderne et, malgré des controverses, est considérée comme la forme d'énergie la plus efficace et la plus écologique. Néanmoins, elle est également à l'origine de nombreuses craintes : de part les déchets fortement radio-toxiques produits par les réacteurs et aussi les risques éventuels d'accidents nucléaires qui posent, sur la santé publique et l'environnement, de graves problèmes. Dans ce contexte, l'objectif de ce projet était de proposer de nouveaux matériaux innovants, capables de piéger efficacement les radionucléides dans les milieux aqueux contaminés.
Un nouveau polymère chélatant hydrosoluble, dérivé de l'acide dipicolinique, est décrit et a été synthétisé à la fois en solution en utilisant la polymérisation radicalaire contrôlée de type Cu^0-CRP mais également à partir de différents substrats comme le PET et le PVC, ce dernier s'étant révélé le plus efficace.
Ces nouveaux matériaux ont ensuite été testés et se sont avérés très performants dans le piégeage de l'uranium et de nombreux lanthanides dans l'eau. Ces résultats ont de nombreuses applications potentielles dans l'industrie nucléaire. Ils peuvent être utilisés pour récupérer l'uranium de l'eau de mer comme une future source d'énergie renouvelable. Ils peuvent également contribuer à l'industrie de la gestion des déchets nucléaires grâce à un procédé, baptisé PALEX, qui permet d'extraire les actinides et/ou lanthanides des effluents radioactifs. En plus, ces matériaux sont prometteurs dans le domaine du traitement des eaux radiocontaminées et la radiodétoxification des organismes vivants, y compris les humains.

Title : Functional surfaces for radiodecontamination

Keywords : Controlled polymerization, Functional surfaces, radionuclides

Abstract: Nuclear energy is the true engine of our modern day society and seen as the most efficient and clean form of energy. At the same time, it is the source of many concerns, with its highly radiotoxic waste produced by nuclear reactors and the public health and environmental risks that follow nuclear accidents. In this context, the aim of this project was to come up with new innovative materials, capable of efficiently trap radionuclides in contaminated aqueous media.
A new water soluble chelating polymer, based on dipicolinic acid, is reported and synthesized in solution as a free polymer, using the easy, cheap and fast metallic copper-mediated controlled radical polymerization (Cu^0-CRP). The new polymer was also built from different substrates like PET and PVC, the latter being the most efficient.
These new materials were later put to test and proved to be highly performing in trapping uranium and many lanthanides in water. These results have many implications in the nuclear industry. They can be used to harvest uranium from seawater as a future renewable energy source. They can also help the nuclear waste management industry through a proposed polymer assisted actinide/lanthanide extraction process, baptized PALEX. They are also a potential candidate for treating radiocontaminated environments and for radiodetoxification of living species, including humans.

Université Paris-Saclay
Espace Technologique / Immeuble Discovery
Route de l'Orme aux Merisiers RD 128 / 91190 Saint-Aubin, France